UNIVERSITY OF NAPLES FEDERICO II

Polytechnic and Basic Sciences School

Ph.D. School in Chemical Sciences

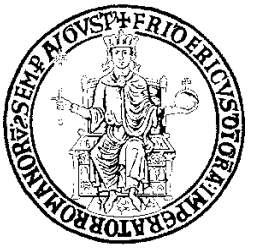

Multiscale Modelling of Heterogeneous Interfaces for Energy Conversion and Storage

Francesca Fasulo

Supervisors

Prof. Michele Pavone

Prof. Ana B. Muñoz García

Examiner

Prof. Roberto Centore

XXXV Cycle 2019/2023

Coordinator Prof. Angelina Lombardi

Abstract

Over the years, great efforts have been devoted to promising energy technologies, such as batteries, photoelectrochemical, and perovskite solar cells, for conversion and storage of clean renewable energy. Despite the advances achieved in developing these devices, several crucial issues related to phenomena occurring at heterogeneous interfaces are still open, leaving room to improve both device stability and sustainability. Interfaces, with exceptionally unique features, are the locus of the major physico-chemical processes that affect the functionalities of these technologies. In this framework, the complexity of interfacial chemistry often requires computational investigations to provide valuable insights into reactivity, structural and electronic behavior of constituent materials, and to optimize the design of the most suitable ones. Nevertheless, the computational study of such complex systems is not straightforward and a reliable description of each occurring phenomenon is not feasible with a unique approach. An in-depth understanding of interface reactivity and chemistry calls for new strategies beyond the standard computational approach. To this end, this Ph.D. thesis focuses on several challenges in energy technologies, identifying the most suitable ab-initio approaches to account for external variables of in-operando conditions, e.g. electric field and solvent, and to address reactivity at heterogeneous interfaces, across different space and time scales.

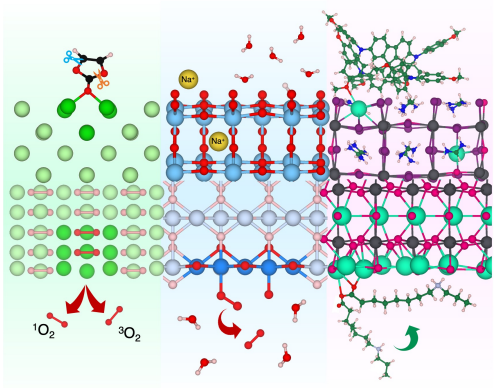

Table of Contents

CHAPTER 1 – INTRODUCTION

The current fossil fuel energy economy is widely affected by the ongoing rise in oil demand and simultaneous depletion of these resources. A further critical aspect is the progressive increase of gas emissions and pollution over time (Figure 1.1). The effective use of electric and renewable energies is, thus, one of the most crucial challenges to achieve a sustainable society.

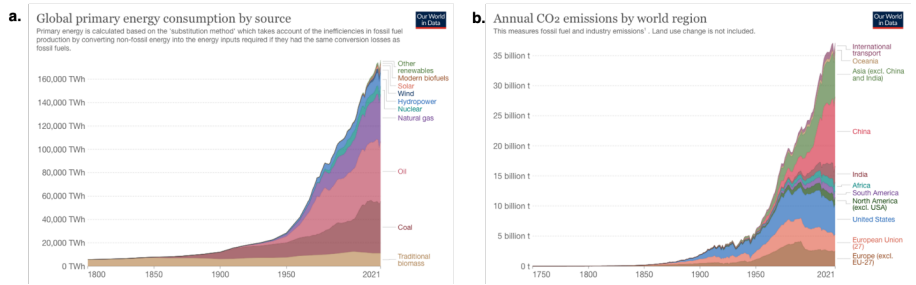

Figure 1.1 *Graphic of* ***(a)*** *global primary energy consumption by source and* ***(b)*** *annual CO_2 emissions by world region according to Our World in Data.*

In this framework, investigations on electric and solar energy technologies have been attracting growing interest.[1–3] On one hand, depending on the types, rechargeable batteries can be a power source for a wide range of applications, from portable electronics to large-scale electric grids and transportation.[4–6] On the other, sunlight is one of the major renewable sources available on our world, encouraging the research and popularity of solar cells.[7–9] Due to the intermittent nature of renewable resources, active research has also been focusing on solar energy storage, achievable by the conversion of sunlight into a chemical fuel via photoelectrochemical cells (PECs).[10,11] The main benefits of these electric and solar technologies are the high theoretical energy densities, that can be reached, and zero or low carbon dioxide (CO_2) emission. As a result, these devices are an

attractive strategy for producing clean energy with minimal environmental impact, and the development of new electrochemical and photovoltaic technologies can play a key role in both energy conversion/storage and pollution reduction.[3]

Generally, batteries consist of two electrodes, a negative electrode (anode) and a positive electrode (cathode) sandwiched around an electrolyte. After oxidation and reduction processes occurring at electrode-electrolyte interfaces, the electrons go through an external circuit, creating a flow of electricity.[6] Solar cells produce electricity through the photovoltaic effect, for which voltage and current are generated by light adsorption.[8] Like the solar cells, the PECs are based on sunlight harvesting, but in these devices further electrochemical reactions at photocatalyst interfaces mimic the photosynthesis process allowing storage of solar energy as high energy chemicals also known as solar fuels.[10] As it turns out, all these devices are made up of solid materials in contact with solvents, electrolyte solutions, molecules or other materials. Some energy device functionalities are so frequently influenced by chemistry and properties of these heterogeneous interfaces, which have extremely unique characteristics, often quite different from those of bulk materials.[12–15] An everyday example is the water in contact with heavier items, that float on top due to the high surface tension of the water surface.

It is well-known that energy technologies rely mostly on physico-chemical processes that take place at heterogeneous interfaces. Processes involving ion/electron transfer, molecular/ion adsorption/desorption/reactivity, and complex interface restructuring can lead to irreversible modifications and undermine the whole device performance. Thus, low efficiency, poor long-term cyclability and stability can affect the promising applications of these devices. A detailed understanding of interfacial phenomena and processes is thus crucial to improve sustainability and durability of energy conversion technologies. Plus, the use of abundant, non-toxic, and non-expensive constituents can require the

design of new efficient materials, other than optimization and control of processes occurring at the complex interfaces. Thus, heterogeneous interface chemistry has been attracting great interest in both academic and industrial research along with enhancement of clean energy production and storage, and material design. In this framework, material sciences and computational chemistry can allow for a deeper knowledge and further improvement of these technologies.

Due to the numerous variables present in any real system, experimental techniques frequently cannot achieve the degree of details at an atomistic scale. Experiments can often need support of theoretical approaches to unveil interface complexity and reaction mechanisms, to assess structure-function relationships and to perform the rational design of new better performing materials.[16–18] Over the years, computational investigations have provided valuable insights on heterogeneous interfaces. Nevertheless, the computational study of such complex systems is not straightforward, and a sufficiently accurate description of all the occurring phenomena is not easily achievable within a unique approach. Moreover, different features of in operando conditions must often be considered and a multi-scale strategy is needed to disentangle the many processes so to identify the most suited materials for each elementary step.[18]

Object & Outline. Aiming to push forward different computational tools and identify the most suitable ab-initio approach to each specific aspect of chemistry at heterogeneous interfaces, in this Ph.D. thesis, we focus on several cases of study in the field of electric and solar technologies. We also aim to unveil new insights on relevant challenges and complex processes, occurring at heterogeneous interfaces in aforementioned energy technologies: batteries, PECs, and perovskite solar cells (PSCs).[8,9,15] In particular, we address:

- in the field of batteries, the effect of external electric field on Na ion intercalation at anatase (TiO_2) interfaces upon NIBs charge-discharge

cycle by application of a sawtooth potential; the singlet oxygen release from the lithium peroxide (Li_2O_2) surface, a deteriorative process for Li-air battery cyclability, by means of an electrostatic embedding method at CASPT2 level of theory; and the early steps of promising SEI formation at Li-metal anode by vinylene carbonate (VC) via Density Functional Embedding Theory (DFET);

- concerning the PECs devices, the oxygen evolution at iridium oxide (IrO_2) interface by means of an electrostatic embedding method at NEVPT2 level of theory; and the dynamic of water on TiO_2 surface at low coverage through metadynamics approach at Density Functional Tight Binding (DFTB) level of theory;
- for PSCs, the changing and passivation of $CsPbBr_3$ perovskite by in situ formation of zwitterionic ligands considering solvent effect via a cluster approach; the charge transfer processes occurring between SPIRO and two kinds of perovskite, the widely used MAPI and triple-cation perovskite via a projection-operator diabatization (POD) approach; the design of new HTLs and harvesting materials by means of Density Functional Theory (DFT).

The following chapters are so organized: in Chapter 2 we introduce the general theoretical backgrounds, while we discuss the cases of study concerning batteries, PECs, and PSCs in Chapters 3, 4, and 5, respectively. Each case of study is discussed following the scheme: introduction, models and computational details, results and discussion. Finally, in Appendix A we report other cases of study carried out in the field of solar energy and catalysis, but not concerning processes at heterogeneous interfaces.

CHAPTER 2 – METHODS

In this chapter we briefly present the theoretical backgrounds, starting from the electronic problem, sections 2.1 Hartree-Fock (HF) and post-HF methods, 2.2 Density Functional Theory (DFT), 2.3 solution for periodic system; 2.4 Density Functional Tight Binding (DFTB); 2.5 embedding approaches, 2.6 basis set and pseudopotential, to consideration on charge partitioning methods (2.7), external electric fields and solvent (2.8), and finishing with consideration on dynamics, section 2.9 Molecular, Ab-initio Dynamics (MD, AIMD) and metadynamics approaches

Computational chemistry exploits methods of theoretical chemistry, implemented into efficient computer programs, to unveil structures, interactions, and properties of molecules and materials.

In quantum mechanics the state of a system is described by a function of spatial, spin and time coordinates, named wave function $\Psi(r,s,t)$. The time evolution of a quantum state is given by solving the Schrödinger equation:

$$i\hbar\frac{\partial\Psi}{\partial t} = \widehat{H}\Psi \qquad (2.1)$$

here $\widehat{H}$ denotes the Hamiltonian, the observable corresponding to the total energy of a system, and $\hbar$ is the reduced Planck constant. As Newton second low in classical mechanics, this equation allows to find the future state of a quantum-mechanical system from knowledge of its present state.

When the potential energy is constant in time, one can assume separation of the spatial and time dependencies of wave equation, $\Psi(r,s,t) = T(t)\psi(r,s)$, and derive the time-independent Schrödinger equation:

$$\widehat{H}\psi(r,s) = E\psi(r,s) \qquad (2.2)$$

where E is a constant and has the dimension of energy, while $\psi(r,s)$ are named stationary states, with time-independent probability density.

Neglecting relativistic interactions, the general Hamiltonian of a physical system can be written as:

$$\hat{H}(r,R) = \hat{T}_e + \hat{T}_N + \hat{V}_{e-e} + \hat{V}_{e-N} + \hat{V}_{N-N} \qquad (2.3)$$

where $\hat{T}_e$ and $\hat{T}_N$ are respectively the electron and nuclear kinetic energy operators, $\hat{V}_{e-e}$ electron-electron interaction, $\hat{V}_{e-N}$ electron-nuclei interaction, and $\hat{V}_{N-N}$ core-core interaction operators. Thus, the eigenvalue of the Hamiltonian is the total energy of the system under investigation and all the chemical information can be given by solving this eigenvalue equation. Since the electrons are lighter than the nuclei, the electronic and nuclear motion are strongly separated on time scales, so that the wave functions of atomic nuclei and electrons in a system can be treated separately. The wave function can be written as the product of a nuclear ($\phi_n(R)$) and electronic ($\phi_e(r,R)$) wave function, that depends parametrically on nuclear positions (R), other than on electron coordinates (r).Within the Born–Oppenheimer (BO) approximation, the electronic wavefunction ($\phi_e(r,R)$) can be solved for a fixed nuclear configuration:

$$\hat{H}_e\phi_e(r,R) = \{\hat{T}_e + \hat{V}_{e-e} + \hat{V}_{e-N}\}\phi_e(r,R) = E_e(R)\phi_e(r,R) \qquad (2.4)$$

and the electronic energy obtained contributes a potential term ($E_e(R)$) to the motion of the nuclei:

$$\hat{H}_N\phi_N(R) = \{\hat{T}_N + \hat{V}_{N-N} + E_e(R)\}\phi_N(r,R) = E_{tot}\phi_N(R) \qquad (2.5)$$

In this approximation, the nuclei move on a potential energy surface (PES) obtained by solving the electronic problem (*2.4*). Generally, the equilibrium geometry is achieved through an iterative process. The electrical problem (2.4) is solved for fixed positions of the nuclei in order to determine the term $E_e(R)$, which is used in equation (2.5). Then, the forces acting on the nuclei are assessed.

The total energy E_{tot} in nuclear equation (*2.5*) is the total energy of the system, and can be approximated as the sum of translational, rotational, vibrational, and electronic energies:

$$E \approx E_{tr} + E_{rot} + E_{vib} + E_{el} \qquad (2.6)$$

The most difficult step is to determine electronic energy: most theoretical investigations are focused on alternative strategies for the solution of the electronic problem. There are two types of approaches to solving the electronic Schrödinger equation: the empirical/semi-empirical or ab-initio methods, based on the inclusion or not of empirical parameters, respectively. Due to different computational cost, each method embraces several phenomena spanning different time and space scales (Figure 2.1).

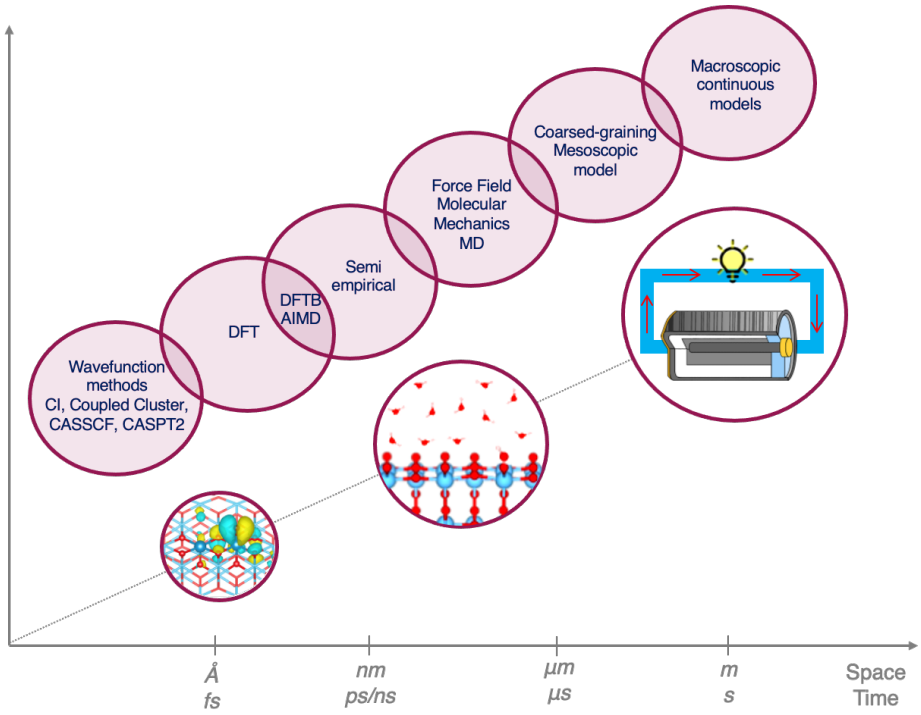

Figure 2.1 *Space and time scales of simulation methods in chemistry and material science.*

2.1. Hartree-Fock (HF) Method

The prototype of ab-initio methods is the Hartree-Fock method (HF)[19]. The peculiarity of this method is that the wave function is the best possible one written as a Slater determinant of spin orbitals. This latter is an anti-symmetrized linear combination of spin orbitals products (ϕ_i) between an *i*-th electron spatial orbital (φ_i) and an *i*-th electron spin function (α or β) ($\phi_i = \varphi_i\ \alpha_i/\beta_i$):

$$\psi(r_1, r_2, .., r_N) = \frac{1}{\sqrt{N!}} \begin{bmatrix} \phi_1(r_1) & \cdots & \phi_N(r_1) \\ \vdots & \ddots & \vdots \\ \phi_1(r_N) & \cdots & \phi_1(r_N) \end{bmatrix} \qquad (2.1.1)$$

where *r* stands for spatial and spin coordinates.

In closed-shell system, where all spatial orbitals are doubly occupied, a single molecular orbital, called restricted, is used twice, one multiplied by the α spin function and the other multiplied by the β spin function in the Slater determinant. Basing on the variational principle, this wave function, resulting from the Slater determinant, is optimized by minimizing the corresponding energy:

$$E_0 = \langle \psi_0 | \hat{H} | \psi_0 \rangle \qquad (2.1.2)$$

With this approach, the HF energy is computed, which for closed-shell system assumes the form:

$$E_{HF} = 2 \sum_{i=1}^{n/2} \varepsilon_i \qquad (2.1.3)$$

ε_i is the orbital energy, obtained by solving the one-electron differential equation:

$$\hat{F}(1)\phi_i(1) = \varepsilon_i \phi_i(1) \qquad (2.1.4)$$

where $\hat{F}$ is a one-electron operator, known as Fock-operator.

Explicating this operator, one gets:

$$E_{HF} = 2 \sum_{i=1}^{n/2} \varepsilon_i = 2 \sum_{i=1}^{n/2} H_{ii}^{core} + \sum_{i=1}^{n/2} \sum_{j=1}^{n/2} (2J_{ij} - K_{ij}) + V_{NN} \qquad (2.1.5)$$

$$J_{ij} = \left\langle \phi_i(1)\phi_j(2) \middle| \frac{1}{r_{12}} \middle| \phi_i(1)\phi_j(2) \right\rangle \quad K_{ij} = \left\langle \phi_i(1)\phi_j(2) \middle| \frac{1}{r_{12}} \middle| \phi_j(1)\phi_i(2) \right\rangle$$

J_{ij} is a coulomb integral, the electrostatic energy of repulsion between an electron with probability density function $|\phi_i|^2$ and an electron with $|\phi_j|^2$. The factor 2 avoids counting inter-electronic repulsion twice. K_{ij} is instead the exchange integral term, deriving from the prerequisite of the wave function to be anti-symmetric with respect to electron exchange. The Coulomb operator ($\hat{J}_j(\vec{x}_i)$) and the corresponding potential are local, whereas the exchange operator ($\widehat{K}_j(\vec{x}_i)$) is non-local. The result of the first operator on a spin orbital depends only on the value of this orbital at position $\vec{x}_i$, while exchange potential depends on the value of all points of space. The term H_{ii}^{core} is the sum of kinetic and potential energies for the attraction between *i*-th electron and the nuclei:

$$H_{ii}^{core} = \left\langle \phi_i(1) \middle| -\frac{1}{2}\nabla_1^2 - \sum_\alpha \frac{Z_\alpha}{r_{1\alpha}} \middle| \phi_i(1) \right\rangle \qquad (2.1.6)$$

A step forward in the practical application of the HF-method was made with Roothaan's proposal to expand the spatial orbital ϕ_i as linear combinations of one-electron basis functions χ_s:

$$|\phi_i\rangle = \sum_{s=1}^{b} c_{si} |\chi_s\rangle \qquad (2.1.7)$$

Substitution of the expansion into Hartree-Fock equation gives:

$$\sum_{s=1}^{b} c_{si}(F_{rs} - \varepsilon_i S_{rs}) = 0 \quad r = 1,2,\dots,b \qquad (2.1.8)$$

$$F_{rs} = \langle \chi_r | \hat{F} | \chi_s \rangle \quad S_{rs} = \langle \chi_r | \chi_s \rangle$$

The equation is a series of simultaneous linear homogeneous equations in the unknown c_{si} that describe the molecular orbital ϕ_i.

For a nontrivial solution, one must have:

$$det(F_{rs} - \varepsilon_i S_{rs}) = 0 \qquad (2.1.9)$$

This is known as secular equation whose roots give the orbital energies.

The Hartree-Fock-Roothaan equations *(2.1.8)* must be solved by an iterative process until convergence of the orbital energies; the process is known as Self-Consistent-Field (SCF) method. To turn the partial differential equations into algebraic equations suitable for efficient implementation in computational software, the first step is to guess for the occupied-molecular orbital (ϕ_i) expressions as linear combinations of basis functions (μ):

$$|\phi_i\rangle \approx \sum_\mu c_{\mu i}|\mu\rangle \qquad (2.1.10)$$

where the expansion coefficients are given by

$$c_{\mu i} = \sum_\upsilon \langle\mu|\upsilon\rangle^{-1}\langle\upsilon|\phi_i\rangle \qquad (2.1.11)$$

This set of functions defines a basis set. In the linear combination of atomic orbitals approach (LCAO), such basis set is composed of atomic orbitals. Several types of these atomic orbitals and other basis set are described in Section 2.6. The initial basis set is so used to compute the Fock-operator. The matrix elements can be computed, and the initial set of energies can be obtained by solving the secular equation. These are then used to solve for an improved set of coefficients, giving an improved set of the orbitals. The later are employed to compute an improved Fock-operator, continuing until no further improvement in molecular orbital coefficients and energies occurs from one cycle to the next (Figure 2.1.1).

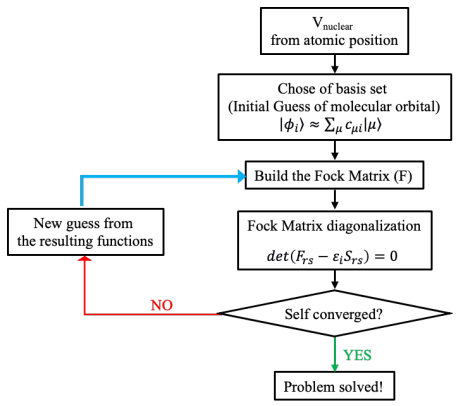

Figure 2.1.1 *Hartree-Fock self-consistent-cycle.*

2.1.1. HF Limits & Electronic Correlation

The limits of Hartree-Fock method are the employment of finite number of basis functions and the absence of electronic correlation. In order to represent the molecular orbitals exactly, the basis functions should form a complete set and this would require an infinite number of basis functions. Only starting from an infinite set of basis functions and performing a high number of cycles, one would get the exact solution to this problem. Of course, this is not possible. The numerical solutions will always contain truncation errors, and the energy will be greater than the real one. In practice, with current computing power, use of very large basis sets is feasible, and one can obtain wave functions that differ negligibly from the true HF wave function, while addressing the correlation problem requires a different approach. The electronic correlation generally indicates how much the movement of one electron is influenced by the presence of others. This introduces an error in the wave function and the energy. Thus, the correlation energy is the difference between the true energy and the Hartree-Fock energy in a complete basis ("Hartree-Fock limit"):

$$E^{corr} = E^{exact} - E^{HF}_{limit} \qquad (2.1.12)$$

In particular, one can usually distinguish between dynamic and static correlation. The first is due to the replacement of electron-electron repulsion with an average electron charge cloud in HF method, while the second to HF mono-determinantal ground state inappropriate to describe excited state, biradical and open-shell systems.

For these molecules with unpaired electrons, it is also known that the restricted spin-orbital are unsuited, because the spatial orbitals are constrained to be identical for alfa and beta spin. Open-shell $\varphi_i\alpha$ and $\varphi_i\beta$ electrons experiment different effective potentials and they are better described with different spatial orbitals, called unrestricted. The use of these different orbitals for α and β

electrons in the Hartree–Fock method gives a pair of Roothaan equations, known as the Pople–Nesbet–Berthier equations:

$$F^{\alpha}C^{\alpha} = SC^{\alpha}\varepsilon^{\alpha} \qquad F^{\beta}C^{\beta} = SC^{\beta}\varepsilon^{\beta} \qquad (2.1.13)$$

where S is the overlap matrix of the basis functions, while $F^{\alpha/\beta}$, $C^{\alpha/\beta}$ and $\varepsilon^{\alpha/\beta}$ are the matrices for the α and β orbitals of Fock, of coefficients and of orbital energies, respectively.

This so-called unrestricted HF method (UHF) can generally give the ground state of radicals or to any excited state, represented by a single determinant wave function. Nevertheless, for these systems different electronic configurations are often close in energy and mix heavily, so that a quantum chemical method, which account for the multiconfigurational nature of the electronic structure, is essential. Ab-initio methods, which account for the multiconfigurational nature of the electronic structure, are the so-called post Hartree-Fock.

2.1.2. Post Hartree-Fock Methods: CI & CASSCF

Using a basis set of K spatial functions, the solution of the Hartree-Fock eigenvalue problem yields a set of 2K orthonormal spin orbitals $\{\phi_k\}$ with energies $\{\varepsilon_k\}$. These are divided into two subsets:

- the N occupied lowest energy spin orbitals $\{\phi_a\}$;
- the 2K-N unoccupied orbitals $\{\phi_r\}$, namely virtual.

The HF ground state wave function is the Slater determinant ($|\Psi_0\rangle$), formed by the N occupied orbitals, but it is only one of many possible determinants. The number of single determinants, which are possible with 2K spin orbitals and N electrons (2K>N), is given by the binomial coefficient:

$$\binom{2K}{N} = \frac{(2K)!}{N!(2K-N)!} \qquad (2.1.14)$$

The HF ground state is considered the reference state and the other are classified by replacing ϕ_a with ϕ_r orbitals, so that they could rapresent excited states of the system. For istance, the following expression rapresents singly (S) and duobly (D) excited determinant, respectively:

$$|\Psi_a^r\rangle = |\phi_1\phi_2\phi_3 \dots \phi_r\phi_b \dots \phi_N\rangle \quad |\Psi_{ab}^{rs}\rangle = |\phi_1\phi_2\phi_3 \dots \phi_r\phi_s \dots \phi_N\rangle \quad (2.1.15)$$

Here one and two electrons in $\phi_{a,b}$ orbitals are promoted to $\phi_{r,s}$.

The importance of these determinants, as approximate rapresentations of the system true states, diminishes with increasing of excited electron. However, the exact wave function for ground and exited states can be written as a linear combination of all these possible N-electron determinants, which costitute a complete set:

$$\Psi^{CI} = c_0|\Psi_0\rangle + \sum_{ra} c_a^r|\Psi_a^r\rangle + \sum_{\substack{a<b \\ r<s}} c_{ab}^{rs}|\Psi_{ab}^{rs}\rangle + \cdots \qquad (2.1.16)$$

This procedure is called configuration interaction (CI)[19], because each $|\Psi_i\rangle$ determinant specifies a 'configuration' of spin orbitals. Particularly, with a complete set, the method is known as full-CI and the exact energy of ground and excited states are the eigenvalues of the Hamiltonian matrix, with elements:

$$\langle\Psi_i\,|\widehat{H}|\Psi_i\rangle \qquad (2.1.17)$$

Unfortunately, even for small systems and minimal basis sets, the number of determinants, that must be included in this calculation, is extremely large and too computationally expensive. Researchers have questioned if all these configurations are needed. It is known that many configurations have almost zero weight and the important configurations use only a limited set of molecular orbitals. Thus, the idea has been to divide the molecular orbital space into three subspaces, active, inactive and external orbitals. The latter two subspaces are doubly and not occupied, respectively, while the remaining electrons occupy a set of active orbitals, where a full-CI defines the wave function (Figure 2.1.2).

Such an approach is well-known as the Complete Active Space SCF multiconfigurational method (CASSCF).[20]

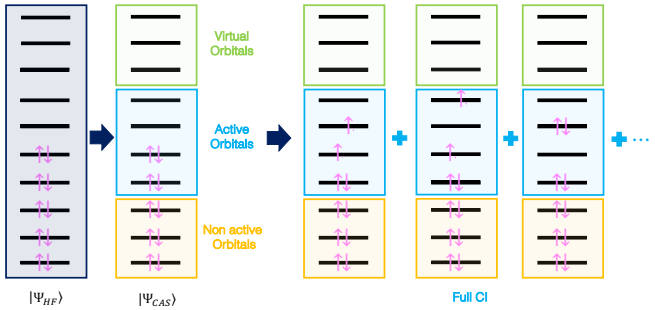

Figure 2.1.2 *Schematic representation of CASSCF approach.*

Using this method, the wave function is constructed as a linear combination of all configurations in the active space (Figure 2.1.2):

$$|\Psi^{CAS}\rangle = \sum_m c_m |m\rangle \qquad (2.1.18)$$

with molecular orbitals (MOs) and configuration (c_m) coefficients optimized during research of energy stationary value, using the variational principle. Thus, the CASSCF energy is given by:

$$E = \langle \Psi^{CAS} \left| \hat{H} \right| \Psi^{CAS} \rangle = \sum_{pq} h_{pq} D_{pq} + \sum_{pqrs} g_{pqrs} P_{pqrs} \qquad (2.1.19)$$

considering the non relativistic Hamiltonian in the second quantization formalism:

$$\hat{H} = \sum_{pq} h_{pq} \hat{E}_{pq} + 1/2 \sum_{pqrs} g_{pqrs} (\hat{E}_{pq} \hat{E}_{rs} - \delta_{qr} \hat{E}_{ps}) \qquad (2.1.20)$$

with $\hat{E}_{pq}$ excitation operator, which promotes an electron from p to q orbital.

In the (2.1.19) MO coefficients appear in the one- and two-electron integrals h_{pq} and g_{pqrs}, while CI coefficients in the first (D_{pq}) and second (P_{pqrs}) reduced density matrix:

$$D_{pq} = \langle \Psi^{CAS} \left| \hat{E}_{pq} \right| \Psi^{CAS} \rangle \;\; P_{pqrs} = \langle \Psi^{CAS} \left| \hat{E}_{pq}\hat{E}_{rs} - \delta_{qr}\hat{E}_{ps} \right| \Psi^{CAS} \rangle \quad (2.1.21)$$

Moreover, through state averaged CASSCF method it is possible to average the energies of M states, with identical orbitals, but different CI coefficients:

$$E_{aver} = \sum_{i=1}^{M} w_i E_i \quad (2.1.22)$$

In this way CASSCF method includes static correlation and CASSCF wave functions give a good qualitative description of the electronic structure. However, it is not accurate enough for a quantitative assessment of relative energies, e.g. excitation energies. Dynamic correlation is required and it could be included by second-order perturbation theory, given the so called Complete Active Space Perturbation Theory (CASPT2)[21], or the N-Electron Valence State Perturbation Theory (NEVPT2). [22]

2.1.3. CASPT2 & NEVPT2 Approaches

In the formalism of second-order perturbation theory, to solve the eigenvalue problem:

$$\hat{H}|\Psi_i\rangle = \varepsilon_i|\Psi_i\rangle \quad (2.1.23)$$

we could relate the unknown eigenvalues and eigenfunctions to the known solutions of the Schrödinger equation, with $\hat{H}_0$ Hamiltonian, which slightly differs to $\hat{H}$. This difference is so-called perturbation ($\hat{V}$) and the strength is governed by a parameter λ:

$$\hat{H} = \hat{H}_0 + \lambda\hat{V} \quad (2.1.24)$$

The exact eigenvalues and eigenfunctions are expanded similarly in a Taylor series in λ:

$$\varepsilon_i = E_i^{(0)} + \lambda E_i^{(1)} + \lambda^2 E_i^{(2)} + \cdots \quad (2.1.25)$$

$$|\Psi_i\rangle = \left|\Phi_i^{(0)}\right\rangle + \lambda \left|\Phi_i^{(1)}\right\rangle + \lambda^2 \left|\Phi_i^{(2)}\right\rangle + \cdots \quad (2.1.26)$$

where E_i^k and $\left|\Phi_i^{(k)}\right\rangle$ are the nth-order energy and wave function corrections, respectively, while E_i^0 and $|\Phi_i^0\rangle$ are eigenvalues and eigenfunctions of unperturbed system ($\widehat{H}_0 \left|\Phi_i^{(0)}\right\rangle = E_i^0 \left|\Phi_i^{(0)}\right\rangle$). The first-order wave function is given by linear combination of zeroth-order functions:

$$\left|\Phi_i^{(1)}\right\rangle = \sum_n c_n \left|\Phi_n^{(0)}\right\rangle \qquad (2.1.27)$$

while the second-order energy is:

$$E_i^{(2)} = \sum_{m \neq n} \frac{\left|\left\langle \Phi_m^{(0)} \middle| \hat{V} \middle| \Phi_n^{(0)} \right\rangle\right|}{E_n^{(0)} - E_m^{(0)}} \qquad (2.1.28)$$

A similar approach can also be used in the multiconfigurational case, leading to the CASPT2 and NEVPT2 approaches.[21,22]

These post Hartree-Fock methods are based on the use of CASSCF wave function as the zeroth-order approximation wave function, while the zeroth-order Hamiltonian is defined as:

$$\hat{H}_0 = \hat{P}_0 \hat{X} \hat{P}_0 + \hat{P}_{SD} \hat{X} \hat{P}_{SD} + \hat{P}_X \hat{X} \hat{P}_X \qquad (2.1.29)$$

where $\hat{P}_0$, $\hat{P}_{SD}$ and $\hat{P}_X$ are projection operator into reference function ($|\Psi^{CAS}\rangle$), singly and doubly excited space ($\hat{E}_{pq}\hat{E}_{rs}|\Psi^{CAS}\rangle$) and the rest of CI space, respectively.

Concerning the CASPT2 approach[21], $\hat{X}$ in (2.1.29) is the Fock operator $\hat{F}$:

$$\hat{F} = \sum_{p,q} \hat{f}_{pq} \hat{E}_{pq} \qquad (2.1.30)$$

and the first-order wave function is:

$$|\Phi^1\rangle = \sum_{p,q,r,s} c_{pqrs} \hat{E}_{pq} \hat{E}_{rs} |\Psi^{CAS}\rangle \qquad (2.1.31)$$

Only singly (S) and doubly (D) excited states are included and the different functions, which contributes to SD space, are linearly indipendent. Therefore, the first order equation for the coefficients C is:

$$(F - E_0 S)C = -V \qquad (2.1.32)$$

where *F* is the Fock matrix in the SD space, *S* the corresponding overlap matrix, *C* the vector of coefficients, and *V* is the vector representing the interaction between excited and referent functions. It foresees so the construction of the matrixes, diagonalitation and iterative equation solver. Furthermore, multistate (MS)-CASPT2[23] uses a multi-dimensional reference space, which is spanned by two or more state-average CASSCF single state (SS)-CASSCF. It is expected that the MS approach will be important when the CASSCF wave function is not a good reference state for the perturbation calculation due to strong interaction between close lying electronic states.

Meanwhile, the NEVPT2 method developed by Angeli et al.[22] employs the bielectronic Dyall Hamiltonian[24] as the zeroth-order Hamiltonian ($\hat{X}$) in (2.1.29):

$$\hat{H}^D = \hat{H}_i^D + \hat{H}_v^D + C \qquad (2.1.33)$$

here $\hat{H}_i^D$ is a one-electron (diagonal) operator in the nonactive (core and external) subspace, $\hat{H}_v^D$ is a two-electron operator confined to the active space and C is a constant to ensure that $\hat{H}^D$ is equivalent to the full Hamiltonian within the CAS space, exactly:

$$\hat{H}_i^D = \sum_i^{core} \varepsilon_i \hat{E}_{ii} + \sum_r^{virt} \varepsilon_r \hat{E}_{rr} \qquad (2.1.34)$$

$$\hat{H}_v^D = \sum_{ab}^{act} h_{ab}^{eff} \hat{E}_{ab} + \frac{1}{2}\sum_{abcd}^{act} \langle ab|cd\rangle \langle \hat{E}_{ac}\hat{E}_{bd}|\delta_{bc}\hat{E}_{ad}\rangle \qquad (2.1.35)$$

$$C = 2\sum_i^{core} h_{ii} + \sum_{ij}^{core} 2\langle ij|ij\rangle - \langle ij|ji\rangle - 2\sum_i^{core} \varepsilon_i \qquad (2.1.36)$$

$$h_{ab}^{eff} = h_{ab} + \sum_j (2\langle aj|bj\rangle - \langle aj|jb\rangle) \qquad (2.1.37)$$

where labels i,j a,b and r denote core, active and virtual orbitals of complete active space, respectively, $\varepsilon_{i/r}$ are the orbital energies of the involved orbitals, and $\hat{E}_{mm}$ are the excitation operators. Thus, in contrast to CASPT2, this approach is free of intruder states and parameters such as the IPEA shift, an empirical correction to the zeroth-order Hamiltonian, which is introduced to account for systematic errors in the calculation of CASPT2 dissociation energies.

The zeroth-order wave functions external to the CAS space are named the "perturber functions". Writing the CAS wave function as an antisymmetrized product of an inactive part (Φ_c) and of a valence part (Ψ_m^v):

$$|\Psi_m^0\rangle = |\Phi_c \Psi_m^v\rangle \qquad (2.1.38)$$

the perturber wavefunctions can be written as

$$\left|\Psi_{l,\mu}^k\right\rangle = \left|\Phi_l^{-k} \Psi_\mu^{v+k}\right\rangle \qquad (2.1.39)$$

where Φ_l^{-k} and Ψ_μ^{v+k} are an orbital product with n_c-k inactive (core or virtual) orbital electrons and a multireference valence function with n_v-k electrons, respectively. The number k represents the number of electrons promoted from the inactive to the active space at second order: $-2 \leq k \leq 2$.

Based on the first-order wavefunction expansion and zeroth-order Hamiltonian, the NEVPT2 exists in different formulations: totally uncontracted NEVPT2, the partially (PC-) and the strongly (SC-) contracted NEVPT2. In the former, the perturber wavefunctions are defined into space S_l^k of determinants with the same inactive part and all the possible active parts:

$$S_l^k \stackrel{\text{def}}{=} \left\{\left|\Phi_l^{-k} \Psi_l^k\right\rangle\right\} \qquad (2.1.40)$$

The simplest way to obtain the perturbers consists of the Hamiltonian diagonalization:

$$\hat{P}_{S_l^k} \hat{H} \hat{P}_{S_l^k} \left|\Phi_l^{-k} \Psi_\mu^{v+k}\right\rangle = E_{l,\mu} \left|\Phi_l^{-k} \Psi_\mu^{v+k}\right\rangle \qquad (2.1.41)$$

where $\hat{P}_{S_l^k}$ is the projector onto the space S_l^k.

Because a diagonalization of the true Hamiltonian must be performed for each determinant space, this procedure is unpractical. On one hand, a way to simplify the problem consists in finding a subspace of S_l^k spanned by wavefunctions interacting with $\left|\Psi_m^{(0)}\right\rangle$, consistent with the philosophy of contracted CI and CASPT2, leading to the PC-NEVPT2. On the other hand, one can choose a single function for each space S_l^k, leading to the strongly contracted SC-NEVPT2 scheme. In this latter approach, the strongly contracted perturber function and the energy of the perturber function are:

$$\Psi_l^k = \hat{P}_{S_l^k} \hat{H} \Psi_m^{(0)} \qquad (2.1.42)$$

$$E_l^{(k)} = \frac{\left\langle \Psi_l^{(k)} \middle| \hat{H}^D \middle| \Psi_l^{(k)} \right\rangle}{\left\langle \Psi_l^{(k)} \middle| \Psi_l^{(k)} \right\rangle} \qquad (2.1.43)$$

Overall, by incorporating both static and dynamic electronic correlation, these post-HF methods achieve a reliable description of strongly correlated systems, excited states, and open-shell systems. Nevertheless, due to the reliance on the number of electrons, HF and post-HF methods are extremely expansive, and only a small system, can be described by these approaches. In the following Section 2.2-2.4, we describe several methods to solve the electronic problem for large systems.

2.2. Density Functional Theory (DFT)

In the past years, the Density Functional Theory (DFT)[25] has become the workhorse method in first-principles calculations aimed to describe or predict structural and electronic properties in a vast class of systems, ranging from

molecules, simple crystals to complex extended systems, such as interfaces in electrochemical devices. In DFT the $\hat{V}_{e-N}$ electron-nuclei interaction of Hamiltonian (2.4) is represented with $V_{e-N}[\rho]$ functional:

$$V_{e-N}[\rho] = \int \rho(r)v(r)dr \qquad (2.2.1)$$

where $v(r)$ is the external potential and $\rho(r)$ the electronic density. In fact, DFT is a ground-state theory in which the relevant physical quantity is the electronic density. At the base of this method there are the two Hohenberg-Kohn theorems. The first theorem establishes that, from a given $\rho(r)$, one can uniquely determine $v(r)$ and so the position of the nuclei. Because also the kinetic energy of electrons and electron-electron interactions are uniquely determined by electronic density, with this approach the energy of the system is expressed as a unique functional of the ground state total density:

$$E[\rho] = T_e[\rho] + V_{e-N}[\rho] + V_{e-e}[\rho] \qquad (2.2.2)$$

Thus, all properties of a system derive from the electron density. For the second Hohenberg-Kohn theorem, the functional that delivers the ground-state energy of the system gives the lowest energy if and only if the input density is the true ground-state density. In other words, the energy content of the Hamiltonian reaches its absolute minimum (the ground state), when the ρ is that of the ground state. Like the HF theory, DFT is based on the variational principle, thus the density of ground state can be calculated, exactly in principle, by minimizing the total energy of a guess electron density ($\tilde{\rho}$):

$$E_o \leq E[\tilde{\rho}] = T[\tilde{\rho}] + V_{e-N}[\tilde{\rho}] + V_{e-e}[\tilde{\rho}] \qquad (2.2.3)$$

To compute the total energy of a system it is not necessary to have the full 3N dimensional wave function. The DFT is based on the idea that only knowledge of the electron density is required to obtain an exact solution of the ground state energy.

Considering equation (2.2.2), it is possible decompose the term V_{e-e} as:

$$V_{e-e}[\rho] = V_H[\rho] + E_{xc}[\rho] \qquad (2.2.4)$$

where V_H is the classical Coulomb energy of repulsion between electrons, and E_{XC} collects all contributions due to non-classical electron-electron interactions.

So, we obtain:

$$E[\tilde{\rho}] = T_e[\tilde{\rho}] + V_H[\tilde{\rho}] + V_{ext}[\tilde{\rho}] + E_{XC}[\tilde{\rho}] \qquad (2.2.5)$$

while V_H and V_{ext} are exactly computable, this is not possible for T_e and E_{XC}.

For the exchange-correlation energy, another definition could be given by hole-formalism.[25] The relationship between the interacting system and a fictitious, noninteracting system, could be also studied considering the interaction $\frac{\lambda}{|r-r'|}$ and varying λ from 0 (noninteracting system) to 1 (physical system) in the presence of an external potential, V_λ, such that the ground state of the Hamiltonian:

$$\hat{H}_\lambda = \hat{T} + \hat{V}_{e-N} + \hat{V}_\lambda + \lambda\hat{V}_{ee} \qquad (2.2.6)$$

has density $\rho(r)$ for all λ. In this way, the E_{XC} of interacting system can be expressed in terms of an integral over a coupling constant (λ):

$$E_{XC} = \frac{1}{2}\int \rho(r)dr \int \frac{1}{|r-r'|}\rho_{XC}(r, r'-r)dr' \qquad (2.2.7)$$

$$\text{with} \quad \rho_{XC}(r, r'-r) = \rho(r')\int_0^1 (g(r, r', \lambda) - 1)d\lambda \qquad (2.2.8)$$

The function $g(r, r', \lambda)$ is the pair-correlation function of the system with density $\rho(r)$ and Coulomb interaction $\lambda\hat{V}_{e-e}$. The exchange-correlation hole $\rho_{XC}(r, r'-r)$, describes the effect of the interelectronic repulsions, as the fact that an electron being at the point r reduces the probability of finding one at r'. Therefore, the E_{XC} may then be viewed as the energy resulting from the interaction between an electron and its exchange-correlation hole. This functional is an extremely complex mathematical object whose exact form has

not been known yet and finding the best possible approximation to E_{XC} is the main aim of DFT.

Due to unknown T_e and E_{XC} terms, some approximations must be done. The most commonly exploited ones are based on the Kohn Sham method. To reduce the errors generated by the approximation of these terms, Kohn and Sham have proposed an approach that consists in replacing the electron density with a pseudo-orbital picture of independent particles (the electrons):

$$\rho(r) = \sum_i |\psi_i(r)|^2 \qquad \langle \psi_i | \psi_j \rangle = \delta_{iJ} \tag{2.2.9}$$

This system is characterized by the same density as the real one, and with an external potential $V_{KS}[r]$:

$$E_{KS}[\tilde{\rho}] = T_S[\tilde{\rho}] + V_H[\tilde{\rho}] + V_{e-N}[\tilde{\rho}] + E_{XC}[\tilde{\rho}] \tag{2.2.10}$$

here $T_S[\tilde{\rho}]$ is the kinetic energy for the non-interacting electron system, which can be computed accurately:

$$T_S[\tilde{\rho}] = -\frac{\hbar^2}{2m} \sum_i \int \psi_i(r)^* \nabla^2 \psi_i(r) dr \tag{2.2.11}$$

and $V_H[\tilde{\rho}]$ is the Hartree energy, due to electrostatic interactions:

$$V_H[\tilde{\rho}] = \frac{e^2}{2} \int \tilde{\rho}(r)\tilde{\rho}(r')/|r - r'| dr dr' \tag{2.2.12}$$

The exchange-correlation functional $E_{XC}[\tilde{\rho}]$ collects the contributions due to the exchange energy, the correlation energy, and to the term that serves to correct T_S for recovering T_e. All-in-all, within the Kohn-Sham formalism, the energy of the actual many interacting electrons system is shown to be equivalent to that of a fictitious system of independent electrons within an effective potential involving the interaction with the nuclei complemented by the electron-electron Coulomb interaction and the exchange-correlation functional E_{xc}. Applying the variational theorem, the solution is thus obtained by minimization of the energy with respect to ψ_i, satisfying the following Kohn-Sham (KS) equation:

$$\hat{H}_{KS}\psi_i(r) = \left(-\frac{\hbar^2}{2m}\nabla^2 + \hat{V}_H(r) + \hat{V}_{XC}(r) + \hat{V}_{e-N}\right)\psi_i(r) = \epsilon_i\psi_i(r) \quad (2.2.13)$$

where the Hartree ($\hat{V}_H$) and exchange-correlation ($\hat{V}_{XC}$) potentials:

$$\hat{V}_H(r) = \frac{\delta E_H[\rho(r)]}{\delta\rho} = e^2 \int \frac{\rho(r\prime)}{|r-r\prime|} dr'; \; \hat{V}_{XC}(r) = \frac{\delta E_{XC}[\rho(r)]}{\delta\rho} \quad (2.2.14)$$

depend self-consistently upon the ψ_i via the charge density. The energy can be rewritten in an alternative form using the Kohn-Sham eigenvalues ϵ_i:

$$E = \sum_i \epsilon_i - E_H[\rho(r)] - \int \rho(r)V_{XC}(r)dr + E_{XC}[\rho(r)] \quad (2.2.15)$$

Furthermore, the density, normalized to the number of electrons ($\rho(r)$), is obtained from the individual orbitals ($\psi_k(r)$):

$$\rho(r) = \sum_k f_k|\psi(r)|^2 \quad (2.2.16)$$

where f_k are the occupation number of orbitals.

The Kohn-Sham Hamiltonian ($\hat{H}_{KS}$) depends thus on the orbitals via the density and must hence be solved self-consistently. In a self-consistent approach, we need to find the self-consistent charge density (or potential), performing the following operations (Figure 2.2.1): calculate the potential from the charge density; diagonalize the Kohn-Sham equations at fixed potential and then calculate the charge density from Kohn-Sham orbitals.

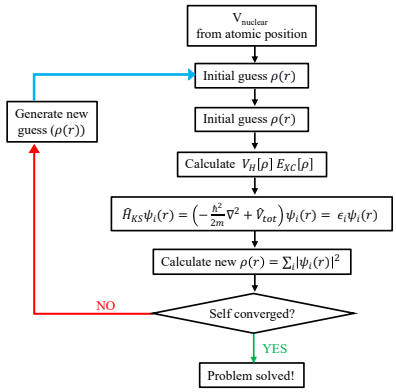

Figure 2.2.1. *DFT self-consistent-cycle.*

While the Kohn-Sham equation is mathematically very similar to the HF equation, it formally incorporates the electron-electron correlation. On the opposite, the HF energy must be complemented by a wave function type many-body correlation contribution based on multiconfigurational schemes. Plus, conversely to many-body wavefunctions which are functions of coordinates in space R^{3N}, the electronic density is only a function of variables in R^3. Hence, the resolution of the Kohn-Sham equation is much simpler and computationally much more efficient than CI type schemes, which explains the success of DFT. The main theoretical problem of DFT is that the exchange-correlation functional remains unknown.

2.2.1. Approximation of Exchange-Correlation Functional

First, note that spin-polarized extension of functional can be simply described by assuming a unique quantization axis for spin, thus the energy functional is:

$$E[\rho_+(r), \rho_-(r)] = T_S + E_H + \int \rho(r)V(r)dr + E_{XC}[\rho_+(r), \rho_-(r)] \quad (2.2.17)$$

and minimization of the above functional yields the following Kohn-Sham equations:

$$\left(-\frac{\hbar^2}{2m}\nabla^2 + \hat{V}(r) + \hat{V}_{XC}^{\sigma}(r) + \hat{V}_H\right)\psi_i^{\sigma}(r) = \epsilon_i^{\sigma}\psi_i^{\sigma}(r) \quad (2.2.18)$$

Exchange-correlation potential and charge density are thus defined:

$$\hat{V}_{XC}^{\sigma}(r) = \frac{\delta E_{XC}}{\delta \rho_{\sigma}(r)} \qquad \rho_{\sigma}(r) = \sum_i f_i^{\sigma} |\psi_i^{\sigma}(r)|^2 \quad (2.2.19)$$

Many methods have been proposed to approximate the E_{XC} functional, the first one was the Local Density Approximation (LDA). This approach assumes that the electron density in a very small volume of space can be approximated as a uniform electron gas. In other words, a general system with inhomogeneous density is considered locally homogeneous:

$$E_{XC}^{LDA} = \int \rho(r)\varepsilon_{XC}^{LDA}[\rho]dr \qquad (2.2.20)$$

Because of this, the LDA tends to over-estimate the exchange-correlation energy. It is a good approximation for metals, but is much less suitable for molecular systems, whose properties are substantially dependent on the non-homogeneity of the charge distribution along chemical bonds. For this reason, several approaches have been developed in which the exchange-correlation contribution is dependent on the density value and on its gradient at one point. These are known as the family of General Gradient Approximation (GGA) density functionals. In this case, the functional E_{XC} takes the form:

$$E_{XC}^{GGA} = \int f[\rho, \nabla\rho]dr \qquad (2.2.21)$$

Some GGA functional are parameterized by fitting to experimental data, but there are also some GGA functionals that achieve the inclusion of gradient correction without experimentally fitted parameters. One example of such a parameter-free GGA functional is the one developed by Perdew, Burke and Ernzerhof (PBE).[26,27] It is known for its general applicability and accuracy for a wide range of systems. Potentially more accurate than the GGA functionals are the meta-GGA functionals, which include the second derivative of the electron density (the Laplacian).

The difficulties in expressing the exchange part of the energy can also be relieved by including a component of the exact exchange energy calculated from Hartree-Fock theory:

$$E \approx \alpha E + \beta E^{GGA} \qquad (2.2.22)$$

where the coefficients α and β can be determined with reference to a system for which exact results are known. This kind of functional are known as hybrid functionals. Among these, the most used one are the B3LYP (Becke, 3-parameter, Lee–Yang–Parr)[28,29], PBE0[30] and HSE (Heyd-Scuseria-Ernzerhof)[31] exchange-correlation functional. The former is given by:

$$E \approx E^{LDA} + 0.2(E^{Fock} - E^{LDA}) + 0.72\,\Delta E^{B88} + 0.81\,\Delta E^{PW91} \quad (2.2.23)$$

were ΔE^{B88} and ΔE^{PW91} are the widely used GGA corrections to the LDA exchange and correlation energies respectively. Meanwhile, the PBE0[30] functional mixes 75% of PBE exchange energy and 25 % of Hartree-Fock exchange energy, and the HSE functional[31] uses an error function screened Coulomb potential to calculate the exchange portion of the energy in order to improve computational efficiency, especially for metallic systems. The general expressions for these functionals are:

$$E_{XC}^{PBE0} = \frac{1}{4}E_X^{HF} + \frac{3}{4}E_X^{PBE} + E_C^{PBE} \quad (2.2.24)$$

$$E_{XC}^{HSE} = a\,E_X^{HF,SR}(\omega) + (1-a)E_X^{PBE,SR}(\omega) + E_X^{PBE,LR}(\omega) + E_C^{PBE} \quad (2.2.25)$$

where E_X^{HF} is the Hartree–Fock exact exchange functional, E_X^{PBE} is the PBE exchange functional, and E_C^{PBE} is the PBE correlation functional, while for HSE a and ω are the mixing parameter and an adjustable parameter controlling the short-range of the interaction. Referred to as HSE06, standard values of a and ω are 0.25 and 0.2 respectively, which gives good results for most systems.

Due to computing the exact HF exchange energy, these hybrid functionals are computationally demanding. Otherwise, the correlated nature of d and f electrons is a source of error in DFT calculation, due to the self-interaction error (SIE), which arises from the unphysical Coulomb interaction of an electron with itself, not completely canceled in most exchange-correlation functionals.[32] A possible alternative to the more expensive hybrid functionals is the DFT+U Hubbard-like correction scheme of the DFT functionals.[33–36] Such an approach is one of the most used methods for improving the description of d and f electrons, mainly for strongly correlated electron materials, including middle-to-late transition metal oxides, with tightly localized d and f electrons. Within the DFT+U scheme, the intra-atomic interactions between the strongly correlated electrons are introduced

in the calculations by addition of an "on-site" potential.[35] At the LDA+U level, the total energy is given by:

$$E_{LDA+U}[\rho(r)] = E_{LDA}[\rho(r)] + E_{Hub}[\{n_m^{I\sigma}\}] - E_{DC}[\{n^{I\sigma}\}] \quad (2.2.26)$$

where $n_m^{I\sigma}$ are the occupations number of m orbital with spin σ for the atom I. The E_{Hub} is the Hubbard term, and E_{DC} the "double-counting" term.

2.2.2. Dispersion Energy

Another well-known limitation of commonly used DFT functionals is an accurate description of van der Waals (vdW) interactions, also known as dispersive forces, which play an important role in many molecular systems and heterogeneous interfaces. They control, for example, the structures of DNA and proteins, the packing of crystals, the formation of aggregates, and the orientation of molecules on surfaces.[37,38] Within the framework of DFT calculations, Grimme[39,40] proposed an effective method for obtaining a correct description of such interactions, consisting of a semi-empirical dispersion correction energy (E_{disp}) added to the KS-DFT result, so that the total energy becomes:

$$E = E_{DFT} + E_{disp} \quad (2.2.27)$$

This dispersive energy is described by damped pair-wise interatomic potentials of the form of C_6R^{-6}, in which R is the interatomic distance and C_6 is the dispersion coefficient. The resulting functionals, that consider the dispersion energy in this way, are called DFT-D, or even Grimme corrections. In the DFT-D3 functional the dispersion correction, E_{disp}, is a sum of two- and three-body energies:

$$E_{disp} = E^{(2)} + E^{(3)} \quad (2.2.28)$$

$$E^{(2)} = \sum_{ij} \sum_{n=6,8,10\ldots} s_n \frac{C_n^{ij}}{r_{ij}^n} f_{d,n}(r_{ij}) \quad E^{(3)} = \sum_{ijk} E^{ijk} f_{d,(3)}(r_{ijk}) \quad (2.2.29)$$

where

$$f_{d,n}(r_{ij}) = \frac{1}{1+6(r_{ij}/R_0^{ij}s_{r,n})^{-\alpha_n}} \qquad (2.2.30)$$

Here, the first sum is over all atom pairs in the system, C_n^{ij} denotes the averaged isotropic n^{th}-order (n=6, 8, 10) dispersion coefficient for atom pair ij, and r_{ij} is their internuclear distance. A further correction has been given by the introduction of the "BJ-damping term" in D3 version of Grimme's functional, known as DFT-D3(BJ)[40], in the following form (n≥6):

$$E_{disp} = -\frac{1}{2}\frac{\sum_{i\neq j} C_n^{ij}}{R_{ij}^n + const} \qquad (2.2.31)$$

This BJ-damping term give a constant contribution of E_{disp} to the total correlation energy from each spatially close pair of atoms. The BJ-damping requires one fit parameter more for each functional but has the advantage of avoiding repulsive interatomic forces at shorter distances. In fact, a disadvantage of the zero-damping approach is that at small and medium distances the atoms experience a repulsive force which may lead to longer interatomic distances with dispersion correction than without. In addition, according to the thermodynamic benchmarks, BJ-damping is the most accurate DFT-D approach, especially for medium-range electron correlation problems, and only small and practically insignificant double-counting effects are observed.

In 2009, Tkatchenko and Scheffler[41] developed and assessed a different scheme to determine the C_6 coefficients and vdW radii from the mean-field ground-state electron density. In this scheme, the effective coefficient (C_{6AA}^{eff}) for an atom in a molecule (A) is determined in the following way:

$$C_{6AA}^{eff} = \frac{\eta_A^{eff}}{\eta_A^{free}}\left(\frac{\eta_A^{eff}}{\eta_A^{eff}}\right)\left(\frac{\kappa_A^{free}}{\kappa_A^{eff}}\right)^2 C_{6AA}^{free} \qquad (2.2.32)$$

taking advantage of the direct relation between polarizability (α) and volume (V)[42], employing the Hirshfeld partitioning[43] of the electron density for the latter:

$$\frac{\kappa_A^{eff}}{\kappa_A^{free}}\frac{\alpha_A^{eff}}{\alpha_A^{free}} = \frac{V_A^{eff}}{V_A^{free}} = \frac{\int r^3 \omega_A(r)\rho(r)d^3r}{\int r^3 \rho_A^{free}(r)d^3r} \quad (2.2.33)$$

$$\omega_A(r) = \frac{\rho_A^{free}(r)}{\sum_B \rho_B^{free}(r)} \quad (2.2.34)$$

here κ_A is the proportional constant between volume and polarizability for the free-atom and atom-in-A- molecule, $\omega_A(r)$ is the Hirshfeld atomic partitioning weight for the atom A, r^3 is the cube of the distance from the nucleus of an atom A, $\rho(r)$ is the total electron density, $\rho_A^{free}(r)$ is the electron density of the free atom A, and the sum in (2.2.34) goes over all atoms in the system. Both $\rho(r)$ and $\rho_A^{free}(r)$ are calculated from DFT. Meanwhile η_A^{eff} in (2.2.32) is an effective frequency. Since the C_6 coefficients are additive, the intermolecular C coefficient, C_6^{mol}, is given by the sum of all interatomic contributions:

$$C_6^{mol} = \sum_{A\in M_1}\sum_{B\in M_1} C_{6AB}^{eff} \quad (2.2.35)$$

where M_1 and M_2 refer to the first and the second molecule, respectively.

2.3. Solid-State Periodic Systems.

From the computational point of view, formidable challenge is the description of an object with an infinite extension; DFT can be conveniently employed to exploit solid-state periodic properties. To this aim, one must introduce a basis of wave functions with the properties:

- each of these wave functions represents an energy eigenstate
- each of these wave functions is a Bloch wave, having the form:

$$\psi_{nk}(r) = e^{ikr}u_{nk}(r) \quad (2.3.1)$$

where u_{nk}, Bloch's function, has the same periodicity as the atomic structure of the crystal, and *k* is a vector of real numbers, known as the crystal wave vector.

In other words, Bloch wave derives from multiplying a plane wave e^{ikr} by a periodic function u_{nk}. This is known as Bloch's theorem and is a way to describe the electron variable in a crystal.[44,45] There are two important consequences of this theorem:

I. The translated wave function is equal to the original one times a phase:

$$\psi_{nk}(r + R) = e^{ikR}\psi_{nk}(r) \qquad (2.3.2)$$

II. It is possible to solve the Kohn Sham orbitals of the entire crystal by considering the information of only one unit cell, the first Brillouin zone, a uniquely defined primitive cell in reciprocal space.

The reciprocal space is often used to describe solid state. A reciprocal lattice is composed of K points set:

$$K = K_1 b_1 + K_2 b_2 + K_3 b_3 \qquad (2.3.3)$$

in which b_1, b_2 and b_3 are the primitive vectors of the reciprocal lattice:

$$b_1 = 2\pi \frac{a_2 x a_3}{|a_1 \cdot a_2 x a_3|} \qquad b_2 = 2\pi \frac{a_3 x a_1}{|a_1 \cdot a_2 x a_3|} \qquad b_3 = 2\pi \frac{a_1 x a_2}{|a_1 \cdot a_2 x a_3|} \qquad (2.3.4)$$

Here a_1, a_2 and a_3 are the primitive vectors of the direct lattice: there is a bi-univocal relationship between direct lattice and reciprocal lattice: each direct lattice corresponds to one and only one reciprocal lattice. While the direct lattice vectors have the dimension of distance, those of the reciprocal lattice are wave vectors. Thus, the Schrödinger equation for a periodic solid can be conveniently solved in the reciprocal space via DFT approach. Another consideration concerns the Born-von Karman boundary conditions (Periodic Boundary Conditions, PBC), which impose the restriction that a wave function must be periodic on a certain Bravais lattice. The condition can be stated as:

$$\psi(r + N_i a_i) = \psi(r) \qquad (2.3.5)$$

where i runs over the dimensions of the Bravais lattice, the a_i are the primitive vectors of the lattice, and the N_i are integers (assuming the lattice has N cells where $N=N_1N_2N_3$). This definition can be used to show that:

$$\psi(r+T)=\psi(r) \qquad (2.3.6)$$

for any lattice translation vector T such that:

$$T=\sum_i N_i a_i \qquad (2.3.7)$$

The consequence of using this periodic condition is, therefore, discretization of the space of wave vector, k. In practice, calculations are performed on a grid of points belonging to the first Brillouin zone, called "k-points".

For analysis purposes, one often plots the total density of states (DOS) $g(\varepsilon)$, defined by the following equation, where $\varepsilon_{i,k}$ is the energy of given states i:

$$g(\varepsilon)=\sum_{i,k}\delta(\varepsilon-\varepsilon_{i,k}) \qquad (2.3.8)$$

From the DOS, one can define the conduction property of materials (Figure 2.3.1).

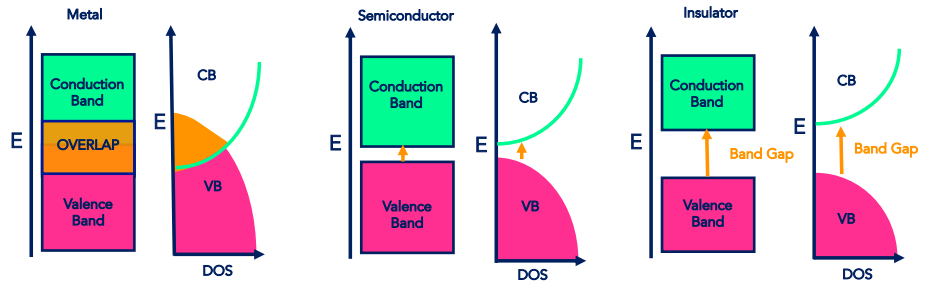

Figure 2.3.1 *Schematic representation of density of states (DOS) for metal, semiconductor and insulator materials.*

2.3.1. Metallic Systems

While in semiconducting or insulating material, a finite number of bands (N) are fully occupied (valance band VB) and separated from unoccupied states (conduction band (CB) by an energy gap, for a metallic system the bands are partially occupied (Figure 2.3.1). Plus, at finite temperature some electrons in a metal will be in excited states, since there is no energy gap in a metal that could prevent such excitations. The occupation numbers can be functions of temperature, $f_i(T_e) = f(\varepsilon, T_e)$. One can approximate the average energy level at which an electron is present with the Fermi-Dirac distribution function:

$$f(\varepsilon, T_e) = \frac{1}{1+e^{(\varepsilon - E_F)/(k_B T_e)}} \qquad (2.3.9)$$

here T_e is the temperature of the electronic system, k_B is the Boltzmann constant, and E_F is the Fermi energy which can be regarded as the chemical potential of the electrons, as well as the highest occupied energy level of a material at absolute zero temperature. In order to mimic the behavior of a metal, one uses a "smearing" technique, where T_e is set to a high value (typically a few tenth of eV or an order of magnitude higher than the physical temperature) to have a smooth transition of the occupation numbers between 1 at low energies and 0 at high energies.[46] From a computational perspective, one can choose an occupation function, e.g Fermi-Dirac or a gaussian function, also because, working with a finite number of k-points, the electronic eigenvalue spectrum in a calculation is discrete. Thus, a broadening "smearing" scheme is often used to find the Fermi level and to occupy the Kohn-Sham eigenstates. Feasible options for the occupation type are a Fermi-Dirac or a gaussian broadening function, or the generalized gaussian-type distribution functions of Methfessel and Paxton[47], mainly applied to metallic systems.

2.3.2. Slab Supercell Approach

Concerning the heterogeneous interfaces, the focus of this thesis, one need to consider the modeling of periodic crystal facets, the place where molecules from the gas or liquid phase come into contact with the materials.

A family of lattice planes (crystal facets), (Figure 2.3.2) are named from the three Miller indices, h, k, ℓ, (hkℓ). The plane intercepts to the main crystallographic axes of the solid (a,b,c) are defined as following:

$$\frac{a}{h} \quad \frac{b}{k} \quad \frac{c}{l} \tag{2.3.10}$$

Note that for hexagonal and rhombohedral lattice systems, a i index, obeying the constraint h+k+i=0, is often specified: (hkiℓ).

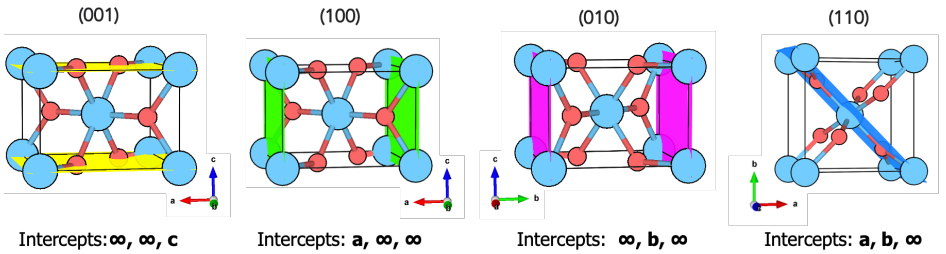

Figure 2.3.2 *Several examples of lattice plane defined by Miller indexes. Intercepts to the main crystallographic axes of the solid is also reported.*

Surfaces are generated by cutting a bulk crystal along specific directions, defined by the Miller indices. The created surface has two-dimensional periodicity and due to the changed coordination, the surface geometry will relax or possibly even reconstruct, to let surface atoms find new equilibrium positions.

For surface, the most notable model is the supercell slab approach, where surfaces are mimicked by a slab with a finite number of parallel atomic layers.[48] In principle, there is no periodicity in the direction normal to the surface, thus

including a vacuum along this direction is the more efficient choice (Figure 2.3.3). The resulting slab in the supercell is so infinite and periodic in the directions parallel to the surface, but finite in the direction perpendicular to the surface. To avoid unwanted interactions between periodic copies of the repeated slab, one needs to include a sufficiently large vacuum region. The thickness of this vacuum region is a parameter that should be tested; as a starting point, one typically uses 10-15 Å of vacuum. The layer numbers in a surface slab are also defined by convergence test on the surface energy, computed as follows:

$$\gamma = \frac{E_{slab} - NE_{bulk}}{2A} \qquad (2.3.11)$$

where A is the area exposed by the surface, E_{slab} is the total energy of the surface slab, E_{bulk} is the total energy of the bulk, and N is the number of formula units (f.u.) contained in the surface slab. Enough layers are often needed to have bulk behavior in the inner layer, as better model of the nanoparticle facets.

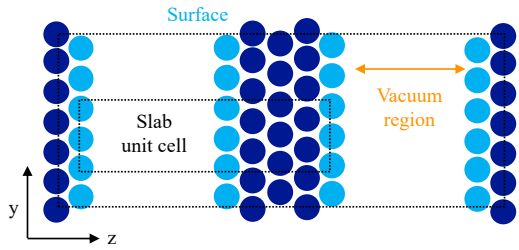

Figure 2.3.3 *Schematic representation of surface slab supercell along x-direction. The large and small box indicate the supercell and slab unit cell, respectively. Vacuum region (orange arrow); Surface atoms (light blue), bulk atoms (dark blue).*

If the two facets of slab have different type of termination, the workfunctions of these two surfaces are generally different, and therefore the electrostatic potential in the vacuum must reach different values depending on whether one samples it at a position far outside the front or the back surface. Several DFT codes allow

the user to account for this physically meaningful possibility by including a jump of the electrostatic potential with adjustable magnitude right in the middle of the vacuum region. This jump corresponds to the electrostatic potential of an infinitesimally thin dipole layer positioned in the middle of the vacuum region, which is exactly balanced by a dipole density of equal size, but opposite sign, built up via the electronic density inside the slab. It is also important to note that the electrons cannot propagate through the vacuum layer, and hence there is no k-point dependence. Therefore, one uses a two-dimensional k-point grid in the (kx , ky) plane and sets kz = 1.

2.4. Density Functional Tight Binding (DFTB)

Although the wide advantages in material sciences, study of an extremely large system, e.g. realistic size nanoparticles in a complex environment, with an appropriate time-space scale, is not feasible by means of DFT calculations. Further reduction of computational cost can be given by the Self-Consistent Charge Density Functional Tight Binding theory (SCC−DFTB).[49,50] Such an approach, collocated between semi-empirical methods (Figure 2.1), has shown to provide reliable results on structures, electronic features, and energetics for different interfaces, in qualitative agreement with DFT ones, but at a much-reduced computational cost.

The standard Tight Binding (TB) method works by expanding eigenstates of a Hamiltonian in an orthogonalized basis of atomic-like orbitals and representing the exact many-body Hamilton operator with a parametrized Hamiltonian matrix, where the matrix elements are fitted to the band structure of a suitable reference system. The eigenstates of the system are then obtained by solving the characteristic equation:

$$(H - E_n S)C_n = 0 \qquad (2.4.1)$$

The method used to obtain the energy distinguishes the variety of tight-binding methods. In the DFTB approach[49], the DFT is used to solve the equation (2.4.1) and several assumptions are done:

- only valence electrons are treated explicitly;
- Kohn-Sham orbitals are expanded with the LCAO approximation by minimal localized pseudoatomic Slater orbitals. The effective one-e-Kohn-Sham potential of many-atom system is constructed using a superposition of unperturbed neutral (pseudo)atomic densities. Molecular reference density (ρ_0) is given by a superposition of densities (ρ_a), from the neutral atoms 'a' that compose the molecule or solid;
- the charge density is substituted by a superposition of a reference density and a small fluctuation:

$$\rho_0' = \rho_0(\vec{r}') \quad \delta\rho' = \delta\rho(\vec{r}') \tag{2.4.2}$$

The DFT total energy is so expanded in a Taylor series around this reference density up to a specific order:

$$E[\rho] = E^0[\rho_0] + E^1[\rho_0, \delta\rho] + E^2[\rho_0, (\delta\rho)^2] + E^3[\rho_0, (\delta\rho)^3] + \cdots \tag{2.4.3}$$

In the SCC−DFTB approach [49], the Taylor series $E[\rho]$ is truncated at the second order, and expansion of the Kohn-Sham total energy with respect to charge density fluctuations is computed as following:

$$E_{tot} = \sum_{i\mu\nu} c_\mu^i c_\nu^i H_{\mu\nu}^0 + E_{rep} + \frac{1}{2}\sum_{a,b}^{M} \gamma_{ab}\Delta q_a \Delta q_b \tag{2.4.4}$$

where $H_{\mu\nu}^0$ are the elements of the Hamiltonian matrix, c_μ^i and c_ν^i are the wave function expansion coefficients, E_{rep} approximates the short-range repulsion term, and Δq_a and Δq_b are the charge fluctuation terms for atoms a and b, respectively.

The letter term is neglected in the traditional zeroth-order non-SCC TB approach. It is known as electrostatic-interaction term for the charge fluctuations, and is given by:

$$\gamma_{ab} = \frac{1}{\sqrt{R_{a,b}^2 + 0.25(1/U_a + 1/U_b)^2}} \qquad (2.4.5)$$

with U_a and U_b are the atomic Hubbard parameters, linked to the chemical hardness of atom a and b. Meanwhile, the Hamiltonian matrix in the first term of (2.4.4) is given by:

$$H_{\mu v}^0 = \begin{cases} \varepsilon_\mu^{neutral\ free\ atom} & if\ \mu = v \\ \langle \varphi_\mu^a | \hat{T} + \hat{V}_0^a + \hat{V}_0^b | \varphi_v^b \rangle & if\ a \neq b \\ 0 & otherwise \end{cases} \qquad (2.4.6)$$

Since a and b indicate the atoms on which the wavefunctions and potentials are centered, only two-center Hamiltonian matrix elements are treated and explicitly evaluated in combination with the two-center overlap matrix elements. In other words, the nondiagonal Hamiltonian matrix elements ($H_{\mu v}^0$) are derived via a two-center approximation, whereas the diagonal elements correspond to the calculated atomic orbital energies. Finally, the repulsive term is approximated as the sum over all pairs of atom-atom potentials, which in turn are determined as a difference between the SCC-DFTB electronic energy and DFT total energy as a function of interatomic distance for properly chosen reference systems, as following:

$$E_{rep}R) = \left\{ E_{LDA}^{SCF}(R) - \sum_i^{occ} n_i \varepsilon_i(R) \right\}\Big|_{reference\ structure} \qquad (2.4.7)$$

All-in-all, the computational efficiency of the SCC-DFTB method originates from the use of tabulated values of Hamiltonian and overlap matrix elements over a large number of interatomic distances that allow to obtain interpolated values at any distance and to skip the computationally intensive explicit

evaluation of two-center integrals. Therefore, the DFTB is based on parameter set, which are contained in the Slater-Koster files and consist of:

- electronic part: matrix elements of the Hamiltonian and overlap operators between basis functions centered on two atoms, tabulated for different distances;
- repulsive part: approximated as a sum of pair potentials, represented by spline functions or by polynomials (needed for elements with a direct covalent bond).

The parameters are stored in files X-X, X-Y, Y-X and Y-Y, with X, Y being the available parametrized elements. The homonuclear X-X files additionally contain the atomic parameters for the given atom type. The successful SCC-DFTB parametrization implies that the main properties of reference systems are well reproduced with respect to DFT. Using these parameters, the DFTB program does not have to perform any integral evaluation during the program runtime. The DFTB approach is so characterized as a semi-empirical (SE) method, requiring moderate number of parameters rather than molecular mechanic (MM) approaches. In this way, it is useful to gain up dynamic simulation to 2 orders of magnitude in speed compared to standard DFT, allowing to study structure and dynamic of solvents interfaces (see Section 2.9), and also reactivity.[51–55]

Even though the DFT provides a great balance between computational effort and accuracy, especially in material science, this method is a ground state theory, and such as HF, lacks static correlation. There are a number of well-known situations where DFT is inadequate, e.g. strongly correlated systems, excited states, and open-shell systems, and high computational multireference methods are required to achieve reliable description by incorporating both static and dynamic electronic correlation.[56,57] Nevertheless, the region of interest in complex systems, as electrocatalytic heterogeneous interfaces, often is only a small part of the whole system. To achieve a reliable description of these localized processes in an extended system, embedded cluster approaches can provide a trustworthy description of chemical environment.[58–64]

2.5. Embedding Cluster Approaches

The basic idea of embedding cluster methods is the partition of the total system in two regions (Figure 2.5.1):

- the active region of interest, named cluster, given by small number of atoms where the phenomena is localized. The cluster is treated with accurate, high-level quantum mechanics methods, e.g via the expensive DFT with hybrid functional, CASPT2 and NEVPT2 approaches.
- the environment, consisting in the extended crystal atoms, not included in the cluster. This region is treated with low-level calculation.

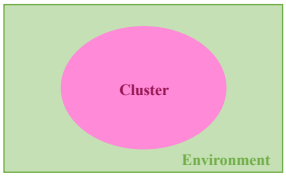

Figure 2.5.1 *Embedded approaches: partitioning of system in cluster (pink) and environment (green).*

Different embedding methods can be distinguished by formalism used to describe the cluster-environment interaction. In the following section, we present a brief overview of the simple electrostatic embedding approach, and the more rigorous quantum embedding theory based on the density functional, (DFET). Other fromalism based on quantum mechanics are the density matrix embedding (DMET) and Green's function embedding (QDET). For more details and complete vision of these methods, see ref [58].

2.5.1. Electrostatic Embedding Approach

Among the embedding theories, the simplest method is to incorporate the effect of periodic nature of heterogeneous interfaces by mimicking the environment in an array of point charges, which generate the exact electrostatic field of the extended crystalline (Figure 2.5.2).[63] Such an approach has been already demonstrated to be a reliable solution for the description of adsorption processes and complex reactions on surfaces, especially for ionic or quite-ionic covalent metal oxides.[60–62,64]

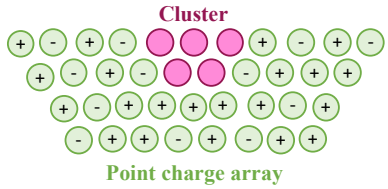

Figure 2.5.2 *Electrostatic embedded approach scheme: cluster (pink) in the point charge array (green).*

Conceptually, in the electrostatic embedded cluster calculation, the quantum system (QM) region interacts only with the atomic point charges of the surrounding, so the energy of the whole embedded system is composed of the following terms:

$$E_{QM/q} = E_{QM} + E_q + E_{int} \qquad (2.5.1)$$

where E_{QM} is the electronic energy of the quantum system, E_{int} is the energy of interaction of the electrons and nuclei of the quantum system with the embedding charges, and E_q is the electrostatic energy of the embedding charges. More specifically, E_q is the energy of interaction between the charges:

$$E_q = \sum_{a=1}^{N_{emb}} \sum_{b>a}^{N_{emb}} \int \int \frac{q_a(r-R_a)q_b(r\prime-R_b)}{|r-r\prime|} dr' \qquad (2.5.2)$$

Meanwhile, in atomic units, the interaction term is given by:

$$E_{int} = -\sum_{m}^{N_{emb}} q_m \int \frac{\rho(r)}{|r-R_m|} dr + \sum_{m}^{N_{emb}} \sum_{n}^{N_{QM}} \frac{q_m Z_n}{|R_n-R_m|} \qquad (2.5.3)$$

here, the first term is the Coulomb energy of interaction between the electronic density $\rho(r)$ and the embedding charges, while the second term is the Coulomb energy of interaction between N_{emb} embedding charges q_a (nuclei with atomic number Z_n). In the presence of the embedding charges, the electronic density is polarized accordingly, the Hamiltonian thus becomes:

$$\hat{H}_{QM/q} = \hat{T} + \hat{V} + \hat{V}_{emb} \qquad (2.5.4)$$

where

$$\hat{V}_{emb}(r) = \sum_{a=1}^{N_{emb}} \int \frac{q_a(r\prime-R_a)}{|r-r\prime|} dr' \qquad (2.5.5)$$

To avoiding artificial drift of electron density from the anions onto their nearby positive point charges, effective core potentials (ECPs) or ab initio model potentials were placed at the boundary between the terminating anions of the cluster and the point charges to simulate the electrostatic and Pauli repulsions between the cluster and the environment.[65,66] In ECP the core electrons of a molecule are kept frozen and represented by a set of atomic effective potentials, while only the valence electrons are explicitly handled in the quantum mechanical calculation.[66] Pseudopotential methods are deeply described in Section 2.6.4

2.5.2. Density Functional Embedding Theory

Concerning the more rigorous fromalism based on quantum mechanics, the density-based embedding theories (DFET)[59,67,68], typically consists in the partitioning of the total system density (ρ_{tot}) into an embedded cluster (ρ_{clu}) and environment densities (ρ_{env}) (Figure 2.5.3):

$$\rho_{tot} = \rho_{clu} + \rho_{env} \qquad (2.5.6)$$

The total energy functional so can be decomposed as:

$$E_{tot}[\rho_{tot}] = E_{clu}[\rho_{clu}] + E_{env}[\rho_{env}] + E_{int}[\rho_{clu}, \rho_{env}] \qquad (2.5.7)$$

where E_{clu} and E_{env} are the energy functionals associated with the embedded cluster and the environment, respectively, and E_{int} is the cluster-environment interaction energy functional.

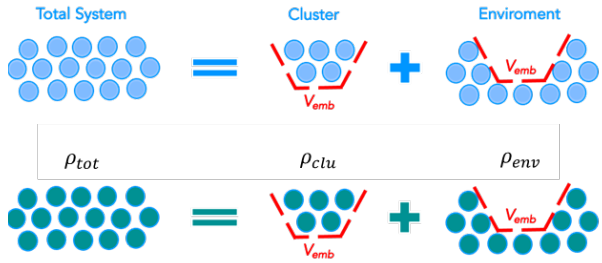

Figure 2.5.3 *DFET approach scheme from ref [69]. Top panel: partition of periodic system into a periodic environment and a finite-sized cluster. Their interaction is given by an embedding potential, V_{emb} (red). Bottom panel: partition of total density (ρ_{tot}) in the sum of cluster (ρ_{clu}) and environment (ρ_{env}) density.*

The embedding potential for the cluster due to the environment, and vice-versa, is the functional derivative of the interaction energy with respect to the cluster (environment) electron density:

$$V_{emb}^{clu} = \delta E_{int}[\rho_{clu}, \rho_{env}]/\delta\rho_{clu} \text{ and } V_{emb}^{env} = \delta E_{int}[\rho_{clu}, \rho_{env}]/\delta\rho_{env} \qquad (2.5.8)$$

In principle, the embedding potential dependents on how the total system is partitioned. Nevertheless, fixing the number of electrons in each subsystem and introducing the following constraint on the embedding potential:

$$V_{emb}^{clu} = V_{emb}^{env} \tag{2.5.9}$$

it is shown that the cluster and the environment share a common embedding potential, which is unique.[67] Such V_{emb} is solved so that the sum of the cluster and environment densities matches the total density:

$$\rho_{clu}[V_{emb}](r) + \rho_{env}[V_{emb}](r) = \rho_{tot} \tag{2.5.10}$$

The embedding potential satisfying this requirement can be solved by maximizing an extended Wu−Yang functional (W) known from Optimizing Effective Potential (OEP) theory[70]:

$$W[V_{emb}] = \tilde{E}_{clu}[\rho_{clu}, V_{emb}] + \tilde{E}_{env}[\rho_{env}, V_{emb}] - \int \rho_{tot}(r) V_{emb}(r)\, dr \tag{2.5.11}$$

where the subsystem energy $\tilde{E}_K[\rho_K, V_{emb}]$ (K=clu,env) includes the interaction with the embedding potential $E[\rho] + \int \rho\,(r) \cdot V\,(r) dr$. The extended Wu-Yang OEP problem is solved in an iterative way; at each iteration, the W functional is maximized via the gradient:

$$g(r) = \frac{\delta W}{\delta V_{emb}(r)} = \rho_{clu} + \rho_{env}(r) - \rho_{tot}(r) \tag{2.5.12}$$

where the cluster and environment densities are computed in the formalism of Kohn Sham, as:

$$\rho_{clu}(r) = \sum_j f_j^{clu} \left|\psi_j^{clu}(r)\right|^2 \tag{2.5.13}$$

$$\rho_{env}(r) = \sum_j f_j^{env} \left|\psi_j^{env}(r)\right|^2 \tag{2.5.14}$$

Firstly, the ρ_{tot} , ρ_{clu}, and ρ_{env} are often calculated with a low-level method (e.g., KS-DFT-LDA/GGA), thus the obtained V_{emb} is at the accuracy of this low-level theory. The electronic structure of the cluster is later refined by performing

high-level calculations on the cluster, with embedding potential designed to represent the environment influence on this active region:

$$(\widehat{H}_{clu} + V_{emb})\Psi_{clu} = E_{clu}\Psi_{clu} \qquad (2.5.15)$$

where $\widehat{H}_{clu}$ is the electronic Hamiltonian, E_{clu} is the energy, and Ψ_{clu} is the wave function of the cluster.

Due to cluster and environment partitioning, the DFET is highly performing when the boundary between these two regions is physically easy to define, e.g for several metals and semiconductors, while difficulties emerge with application on systems with covalent bonding character. In principle, if we employ the exact XC functional, dangling bonds can be treated exactly, but approximate local or semilocal XC functionals are used to build the embedding potential. Therefore, numerical and theoretical challenges for computing embedding potentials arise in covalent system because of dangling bonds with unpaired electrons. A simple scheme for performing covalent embedding in DFET is a direct partition of the boundary atoms, e.g. a carbon atom is split into a hydrogen and a boron atom, an oxygen atom is split into a hydrogen and a nitrogen atom, and so on.[71] Another strategy is the so-called density-matrix functional embedding theory (DMFET), which is based on use of one-particle density matrix as the target to reproduce, leading to introduction of nonlocal embedding potential form.[72]

2.6. Basis Sets

In all the methods described above, a basis set is used to represent the electronic wave function or the electron density and solve the electronic Schrödinger equation. Hereby, we describe several types of basis set employed in HF/post-HF and DFT, DFTB approaches.

2.6.1. Gaussian Type Orbitals (GTOs)

Among the kind of atomic orbitals basis set, the Gaussian Type Orbitals (GTOs) are widely used.[19] General expression of these functions is:

$$G_{ijk}^{\alpha,R}(r) = N_{ijk}^{\alpha}(x - R_1)^i(y - R_2)^j(z - R_3)^k e^{-\alpha(r-R)^2} \qquad (2.6.1)$$

Contracted functions (CGTO) are obtained from a linear combination of the entire basis function set, known as the Primitive GTO (PGTO):

$$\chi(CGTO) = \sum_i^k a_i \chi(PGTO) \qquad (2.6.2)$$

The degree of contraction is the number of PGTOs included in a CGTOs. To indicate a basis set in terms of primitive and contracted functions, the notation (10s4p1d / 4s1p) → [3s2p1d / 2s1p] is used. Here the functions in round parentheses are the number of PGTOs and those in square brackets are the CGTOs. In this notation, the functions used for heavy atoms are listed before the slash, and those employed for hydrogen atoms are listed after the slash.

The smallest basis sets, in which a single basis function is used for each orbital, are called minimal basis sets. The most common minimal basis sets, known as STO-nG, are derived from a minimal Slater-type orbital (STO) basis sets, represented by n number of Gaussian primitive functions (nG). This set is fine for atoms in the gas-phase, but additional functions, named polarization functions, are needed to describe the polarization of the electron density in molecules. Another common addition to GTO basis sets are diffuse functions.

These are extended Gaussian basis functions with a small exponent, which give flexibility to the atomic orbitals far away from the nucleus. Diffuse basis functions are important for description of anions or dipole moments, but they can also be important for accurate modeling of intra- and intermolecular bonding. Basis sets with multiple basis functions corresponding to each valence atomic orbital are called valence double, triple, quadruple-zeta, and so on, e.g. the triple-zeta plus polarization, TZVP basis set, where triple-zeta specifics that there are three basis functions for valence electron. Among these basis sets, the Ahlrichs def2 basis set family (def2-XVP)[73] and Dunning cc-pVnZ[74] are very appealing. The latter are optimized by means of correlated wavefunctions and include successively larger shells of polarization (correlating) functions (d, f, g, etc.), thus the name correlation consistent (cc) polarized valence n zeta (cc-pVnZ) basis sets.

2.6.2. Numeric Atom-Centered Basis Functions (NAO)

Particularly advantageous choice is numeric atom-centered orbital (NAO) basis functions[75] of the form:

$$\varphi_i(r) = \frac{u_i(r)}{r} \Upsilon_{lm}(\Omega) \tag{2.6.3}$$

because the radial shape $u_i(r)$ is numerically tabulated and fully flexible. Here, $\Upsilon_{lm}(\Omega)$ are the spherical harmonics. The utility of NAOs is that the numerical solutions of Schrödinger-like radial equations can been chosen:

$$\left[-\frac{1}{2}\frac{d^2}{dr^2} + \frac{l(l+1)}{r^2} + v_i(r) + v_{cut}(r)\right] u_i(r) = \epsilon_i\, u_i(r) \tag{2.6.4}$$

Therefore, each radial function is defined by two parts: a potential $v_i(r)$ which defines the main behavior of $u_i(r)$, and a steeply increasing confining potential $v_{cut}(r)$, which ensures a smooth decay of each radial function to be strictly zero outside a confining radius r_{cut} (Figure 2.6.1). In this formalism, one can include

a minimal basis consists of the core and valence functions of spherically symmetric free atoms, by simply setting $v_{cut}(r)$ to the self-consistent free-atom radial potential (v_{at}^{free}). This minimal basis greatly facilitates the all-electron treatment because it naturally accounts for wave function oscillations near the nucleus, where the nuclear Z/r potential dominates. Plus, the addition of a confining potential $v_{cut}(r)$ to all basis functions prevents any extended, slow-decaying analytical or numerical radial function tails. Overall, different spatial regions of large systems are strictly separated from one another, enabling near-O(N) scaling of numerical integrations and the electron density update with system size N. The shape $v_{cut}(r)$ must be choose so to ensure a smooth decay of all basis functions and their derivatives to zero.

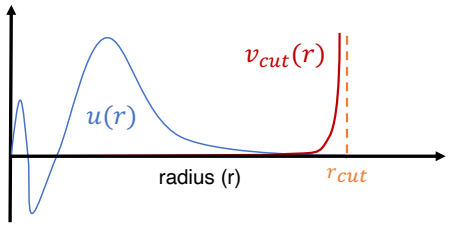

Figure 2.6.1 *Radial shape* $u_i(r)$ *of NAO basis function (blue line), confining potential* $v_{cut}(r)$ *(red line) and radius* r_{cut} *(orange line)*

Calculations using both these finite basis sets, GTO and NAO, are susceptible to basis set superposition error (BSSE). To understand the BSSE, one can consider that two interacting molecules, approaching one another, are subject to an overlap of their basis functions. It is like each molecule borrows functions from the other, effectively increasing its basis set and improving the calculation of derived properties such as energy.[76] If the total energy is minimized as a function of the system geometry, the short-range energies from the mixed basis sets must be compared with the long-range energies from the unmixed sets, and this

mismatch introduces an error, known as BSSE. An approach to compute this BSSE is the counterpoise method (CP), based on re-performing all the calculations using a mixed basis set, realized by introducing "ghost orbitals", basis set functions, which have no electrons or protons.[77] The error is then subtracted a posteriori from the uncorrected energy.

2.6.3. Plane Wave Basis Set

Contrary to the localized basis sets GTO and NAO, previously described and widely used for molecular systems, the plane-wave basis set does not exhibit the BSSE.[78,79] However, such basis set are less well suited to gas-phase calculations than localized basis sets, due to the assumption of periodic boundary conditions. Based on the formalism of Block waves (see section 2.3), a PW basis set for states of wave vector k is defined as:

$$|k+G\rangle = \frac{1}{\sqrt{\Omega}} e^{i(k+G)r} \qquad (2.6.5)$$

where Ω is cell volume, G is the reciprocal lattice vector. In a PW basis set one works with Fourier components ($c_{i,k+G}$)

$$|\varphi_i\rangle = \sum_G c_{i,k+G} |k+G\rangle \qquad (2.6.6)$$

$$c_{i,k+G} = \langle k+G|\varphi_i\rangle = \frac{1}{\sqrt{\Omega}} \int \varphi_i(r)\, e^{-i(k+G)r} dr = \tilde{\varphi}_i(k+G) \qquad (2.6.7)$$

and only certain plane waves will appear in the Fourier expansion of Block waves (2.3.1). In principle, one still need infinite number of plane waves. However, the coefficients, c_{k+G}, for the plane waves with small kinetic energies ($|k+G|^2$) are more important than those with large kinetic energies, thus one can truncate the expansion at some value of $|k+G|$ lower than a kinetic energy cutoff (E_{cut}):

$$\frac{\hbar^2 |k+G|^2}{2m_e} \leq E_{cut} \qquad (2.6.8)$$

In other words, only the reciprocal lattice vectors whose kinetic energy lower than a predefined maximum cutoff energy (E_{cut}) are kept in the expansion, while the rest of the coefficients are set to zero. A schematic representation is showed in Figure 2.6.2 The PW basis set is so complete only for $E_{cut} \rightarrow \infty$, and large E_{cut} are computationally demanding. For an accurate calculation, this value is often given by convergence test on the total energy. Beyond the absence of the BSSE, this basis set is given by delocalized basis functions, and due to its definition is only adopted in quantum-chemical simulations of periodic systems. In particular, PW basis set can be computationally expensive due to use of similar accuracy to describe the vacuum region, which can be useful to simulate isolated molecules and heterogeneous interfaces. Another aspect of PW basis set that can affect the computational cost is that core electrons tend to be concentrated very close to the atomic nuclei. This behavior results in large wavefunction oscillations and density gradients near the nuclei, which are not easily described by a plane-wave basis set unless a very high energy cutoff. Thus, to reduce the computational cost associated with the description of core electron, plane-wave basis sets are often used in combination with an "effective core potential" or pseudopotential, so that the plane waves are only used to describe the valence charge density. In the following section, we describe the main types of pseudopotentials.[80]

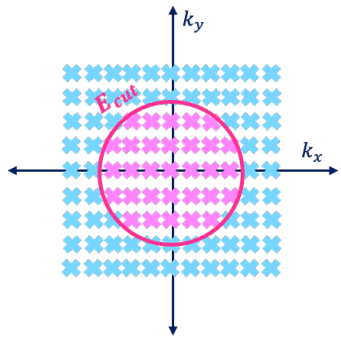

Figure 2.6.2 *Schematic rapresentation of plane wave basis function in reciprocal space (k_y,k_x) with the kinetic energy cutoff (E_{cut}).*

2.6.4. Pseudopotentials

To define a pseudopotential (PP), a linear operator $\hat{T}$ is introduced to connect all-electron orbitals $|\psi_i\rangle$ to pseudo-orbitals $|\tilde{\psi}_i\rangle$:

$$|\psi_i\rangle = \hat{T}|\tilde{\psi}_i\rangle \qquad (2.6.9)$$

The operator $\hat{T}$ can be defined in terms of its action on atomic waves. Considering $\tilde{\phi}_l$ corresponding set of atomic pseudo-waves and ϕ_l set of atomic all-electron waves, beyond some suitable "core radius" R_l, $\tilde{\phi}_l = \phi_l(r)$, while for $r < R_l$, $\tilde{\phi}_i$are smooth functions. If the sets are complete in the core region, the operator $\hat{T}$, can be written as:

$$|\psi_i\rangle = \hat{T}|\tilde{\psi}_i\rangle = |\tilde{\psi}_i\rangle + \sum_l \left(|\phi_l\rangle - |\tilde{\phi}_l\rangle\right)\langle\beta_l|\tilde{\psi}_i\rangle \qquad (2.6.10)$$

where the β_l "projectors" are atomic functions, having the properties $\langle\beta_l|\tilde{\phi}_m\rangle = \delta_{lm}$ and $\beta_l = 0$ for $r > R_l$. The pseudopotential is written as a nonlocal operator, $\hat{V}$, in terms of the β_l projectors:

$$\hat{V} \equiv V_{loc}(r) + \sum_{lm} |\beta_l\rangle D_{lm} \langle\beta_m| \qquad (2.6.11)$$

where $V_{loc}(r)$contains the long-range Coulomb part ($-Ze^2/r$). The (valence) charge density is no longer the simple sum of $|\tilde{\psi}_i|^2$, but:

$$\rho(r) = \sum_i f_i \left|\tilde{\psi}_i(r)\right|^2 + \sum_i f_i \sum_{lm} \langle\tilde{\psi}_i|\beta_l\rangle\, Q_{lm}(r) \langle\beta_m|\tilde{\psi}_i\rangle \qquad (2.6.12)$$

$$Q_{lm}(r) = \phi_l^*(r)\phi_m(r) - \tilde{\phi}_l^*(r)\tilde{\phi}_m(r) \qquad (2.6.13)$$

The $Q_{lm}(r)$ is known as augmentation charges and is zero for $r > R_l$, also known as the cut-off radius. One wants the pseudopotential and pseudo-orbitals to be as smooth as possible so that expansion into plane waves is convenient (low E_{cut}) and are as close as possible to true ("all-electron") orbitals outside the core region, for all systems containing a given atom.

Within this PAW formalism, we can describe the several kinds of PP[81,82]:

- In the full PAW scheme (PAW-PP), the augmentation functions are calculated and stored on a radial grid, centered at each atom. The charge density is composed of a "smooth" term expanded into plane waves, and an "augmentation" term calculated on the radial grid;
- If $Q_{lm}(r) = 0$, we obtain the norm-conserving PPs (NC-PP) in the separable, nonlocal form proposed by Hamann, Schlüter, Chiang in 1982.[83] The NC-PP takes the following form:

$$\hat{V}_{ps}(r) = \sum_l \sum_m |Y_{lm}\rangle V_{lm}(r) \langle Y_{lm}| \qquad (2.6.14)$$

  where $|Y_{lm}\rangle$ projects a one-particle wavefunction, such as one Kohn-Sham orbital, to the angular momentum labeled by {l,m}, while $V_{lm}(r)$ is the pseudopotential that acts on the projected component. Inside the cut-off radius the norm of each pseudo-wavefunction be identical to its corresponding all-electron wavefunction, while all-electron and pseudo wavefunctions are identical outside cut-off radius. Such PPs do not give any important information about the orbitals close to the nucleus and are relatively hard, leading to very high plane-wave cutoffs (70 Ry and up).
- In the Ultrasoft PP scheme are based on the norm-conservation constraint, but the localized atom-centered augmentation charges are introduced. However, these PPs give less information about the orbitals close to the nucleus then the PAW-PP. The augmentation charges here are pseudized to allow an efficient treatment of the augmentation charges on a regular grid. The pseudized augmentation charges are usually treated on a regular grid in real space, which is not necessarily the same as the one used for the representation of the wave functions. With the Ultrasoft PP core radii R_l can be pushed to larger values, and cutoffs of 25 to 35 Ry are usually good for most cases.

2.7. Charge Partitioning Methods

Atom charges analysis is often useful for an in-depth understanding of structural features and reactivity of molecules and materials. By means of quantum mechanics approaches one can compute the electronic charge density, but the partition of electrons in system components is not straightforward. To this aim, several charge partitioning methods are proposed. One can distinguish between approaches based on electronic orbitals (e.g. Mulliken[84] and Löwdin[85] population analysis) or on charge density (e.g. Hirshfeld[43] and Bader[86,87] analysis).

In atomic orbital basis set, the number of electrons N can be define as:

$$N = \sum_{\mu}(\mathbf{PS})_{\mu\mu} \tag{2.7.1}$$

where **P** and **S** are the density and overlap matrix, respectively, and the sum runs over all basis functions (μ). The product $(\mathbf{PS})_{\mu\mu}$ can be interpret as the number of electrons associated with the basis function (ϕ_{μ}). With atom-centered basis functions, considering only μ centered on atom A ($\mu \in A$), with nuclear charge Z_A, the Mulliken charge [84] of A is so defined:

$$q_A^{Mulliken} = Z_A - \sum_{\mu \in A}(\mathbf{PS})_{\mu\mu} \tag{2.7.2}$$

Assigning the electron density using the Löwdin symmetrically orthogonalized basis set, [85] one obtains the Löwdin q_A charge, as following:

$$q_A^{\text{Löwdin}} = Z_A - \sum_{\mu \in A}(\boldsymbol{S}^{1/2}\mathbf{P}\boldsymbol{S}^{1/2})_{\mu\mu} \tag{2.7.3}$$

Another definition of atomic charges is based on the Hirshfeld atomic partitioning weight for atom A ($\omega_A(r)$ in (2.2.34)).[43] Via a self-consistent computation of both the entire system ($\rho(r)$) and its separated atomic densities ($\rho_{A/B}^{free}(r)$ in (2.2.34)), the Hirshfeld charges are computed as:

$$q_A^{\text{Hirshfeld}} = Z_A - \int \omega_A(r)\rho(r)dr \qquad (2.7.4)$$

Although the less basis set dependence than Mulliken and Lowdin population analysis, within this method, the computed charges and dipole moments are typically underestimated.

The Bader approach, also independent from the basis set, can be used with plane wave as well as atomic basis functions and the computed charges are more reliable.[86,87] Based on the electronic charge density, the atomic region around a certain nucleus or atomic basin (Ω_A) lies between all zero-flux surfaces surrounding the nucleus, on which the charge density is a minimum perpendicular to the surface ($\nabla\rho(r)n = 0$, with n the normal vector). Thus, a system is partitioned in spatial regions, that define the atoms. The electron population of the atom A is then determined by integrating the electron density within the atomic basin, and the Bader charge of atom A is computed:

$$q_A^{\text{Bader}} = Z_A - \int_{\Omega_A} \rho(r)dr \qquad (2.7.5)$$

A disadvantage of this approach is the computational cost of the three-dimensional integration of the electron density in the atomic basin, necessary to determine the atomic charge.

2.8. Other Aspects in Electrochemical Heterogeneous Interfaces

The in-depth understanding of electrochemical reactions at complex heterogeneous interfaces often relies on accurate computational methods able to describe and predict the undergoing processes in operando conditions. Several aspects, such as the effects of an external electric field or solvents in most electrochemical devices, need to be included in ab-initio simulations. Hereby, we describe the several methods used in this thesis to include these aspects.

2.8.1. External Electric Field: Sawtooth Potential Approach

The chemical interactions and electronic features, specially at electrode surfaces in batteries devices, may be sensibly affected when an external bias comes into play. For 2D periodic materials, e.g. interfaces where electrochemical phenomena take place, the inclusion of a sawtooth potential has enabled include the effect of this external field.[88–94] In standard Local-Density Functional (LDF) equations, to include the dielectric response of electrons in a complex many-body problem of a solid placed into an external field, the one-electron Schrödinger equations can be written in the following way:

$$\left(\hat{T} + \hat{V}_H + \hat{V}_{XC} + \hat{V}_{ion} + \hat{V}_{ext}\right)\psi_i(r) = \epsilon_i\psi_i(r) \qquad (2.8.1)$$

where the potential external to the system of electrons is separated into a part due to the nuclei alone, $\hat{V}_{ion}$, from the one giving the field external to solid, $\hat{V}_{ext}$. This latter is named bare perturbation. Physically in the simplest case, with a time-independent field constant in space, the potential V_{ext} corresponding to constant bare field is a monotonic function (V_{mon} in Figure 2.8.1a), that makes the crystal potential no longer periodic. Such potential V_{ext} tends to move all electrons to ∞, where they would have the lowest energy.

In the 1980, Rest and Kunc[91,92]demonstrated the possibility of circumventing these contradictions between periodic system and aperiodic potential within the

LDF method and have shown how to deal directly with the dielectric response of a solid to a macroscopic field. The idea is to simulate an electric field along the longitudinal axis and perpendicular to the interface plane, by using a sawtooth-like potential (V_{saw} in Figure 2.8.1a) added to the bare ionic potential. Thus, the V_{ext} has a translational periodicity of some superlattice, satisfying the periodic condition, and a small fraction of each supercell will perceive a constant field.

Considering then a surface slab as region of interest, in a supercell with large vacuum region, the applied sawtooth potential spans throughout the supercell with a constant slope ($\vec{F}$), and then reaches the middle of the vacuum region where the slope is reversed to ensure periodicity (Figure 2.8.1b,c). This is equivalent to the application of a constant electric field in the main region of the periodic cell, the slab. Taking advantages of its simplicity, this approach has applied in numerous studies, from unveiling field effects on oxygen vacancy migration at the anatase surface and Cu migration in SiO_2 cristobalites, to model the interface between a solid-state electrolyte, i.e., $Li_9N_2Cl_3$, and the Li metal under charging conditions, to study how an external electric field can affect the separation of photogenerated electron–hole pairs in semiconductors.[88–90,94]

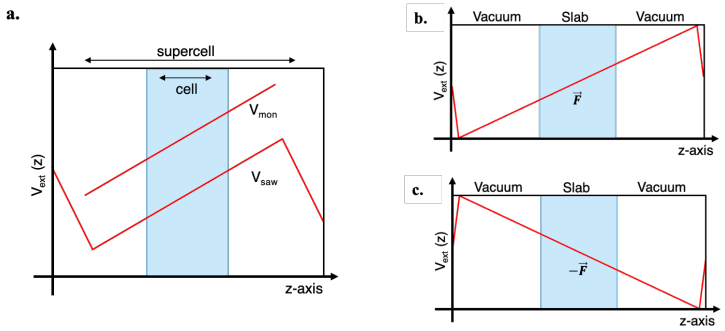

Figure 2.8.1 (a) *Aperiodic monotonic (V_{mon}) and periodic sawtooth-like (V_{saw}) potentials applied to a supercell along z-axis to simulate the external potential V_{ext} (as in ref [91,92]).* ***(b)*** *Positive and* ***(c)*** *negative $\pm\vec{F}$ sawtooth-like potentials applied to a slab to describe the external electric field. The red line is the potential.*

2.8.2.Solvent: Implicit & Explicit Model

Another important aspect is that several processes in electrochemical devices occur in solvent means. Accounts for the behavior of solvated systems can be possible through the implicit or explicit solvent models.[95] When a solute is immersed in a solvent, its charge distribution interacts with the solvent one. Continuum or implicit solvation methods are generally computationally efficient and can provide a reasonable description of the solvent behavior.[96] In a continuum model, rather than representing the charge distribution of the solvent explicitly, it can be approximated by a continuous electric field. The main parameter is thus the dielectric constant (ε), defining the degree of polarizability of the solvent. This field is usually called the 'reaction field' in the regions of space occupied by the solute, since it derives from reaction of the solvent to the presence of the solute. The electric field at a given point in space is the gradient of the electrostatic potential φ at that point, and the work required to create the charge distribution may be determined from the interaction of the solute charge density ρ with the electrostatic potential. Generally, a calculation proceeds by encapsulating a solute in a cavity. This cavity containing the solute is embedded in homogeneously polarizable continuum describing the solvent. The solute charge distribution meets the continuous dielectric field at the surface of the cavity and polarizes the surrounding medium, which causes a change in the polarization on the solute. In ab-initio theoretical investigations, a perturbation, given by implicit solvent, is added to the solute Hamiltonian, as following:

$$\widehat{H}_{tot}(r_m) = \widehat{H}_{mol}(r_m) + \hat{V}_{mol+solvent}(r_m) \qquad (2.8.2)$$

where $\hat{V}_{mol+solvent}(r_m)$ interaction operator includes the following terms (2.8.3): V_{cavity} cavity creation; a term accounting for the energy spent to build a cavity in the solvent of suitable size and shape to house the solute; $V_{electrostatic}$ the electrostatic energy, dealing with the polarization of the solute and solvent;

$V_{repulsion}$ an approximation for the quantum mechanical exchange repulsion; and $V_{dispersion}$ quantum mechanical dispersion energy.

$$V_{mol+solvent} = V_{cavity} + V_{electrostatic} + V_{repulsion} + V_{dispersion} \quad (2.8.3)$$

Most of implicit solvent methods are based on the Poisson-Boltzmann equation, which is an expansion of the original Poisson's equation:

$$\nabla(\varepsilon\nabla\Phi(r)) = -4\pi\rho(r) \quad (2.8.4)$$

In the widely used Polarizable Continuum Model (PCM)[97], $\hat{V}_{mol+solvent}$ is written in terms of apparent point charges placed at the center of small surface elements on the cavity surface. Other methods such as Solvation Model based on Density (SMD) model solves the Poisson-Boltzmann equation analogously to PCM but using a set of specifically parametrized radii which construct the cavity.[98] Meanwhile, the Multipole Expansion (MPE) implicit solvation approach expands the dielectric response of the solvent in a multipole series.[99] The basic idea of MPE is to expand the electrostatic polarization potential in terms of regular and irregular solid harmonics.

All-in-all, in the implicit model, no explicit solvent molecules are present and so explicit solvent coordinates are not required. Include explicit solvent molecules in the calculation usually are done by application of molecular mechanics (MM), based on force fields which are generally empirical, parametrized functions which can efficiently calculate the properties and motions of large system (Figure 2.1). Meanwhile, due to increasing of computational cost with number of atoms, ab-initio calculations are often applied on small, solvated clusters of molecules. To describe and predict the solvent effects, one must include the motions of explicit solvent molecules. Basic principles of dynamics simulations are described in the following section.

2.9. Molecular Dynamics

Molecular-dynamics (MD) simulations generate a detailed information of the system at the microscopic level, leading large sampling of system positions (q) and momenta (p) as function of time (t). Useful information on the macroscopic level is provided by means of statistical mechanics.[95] Thus, in molecular dynamics one evaluates the average quantities by performing time averaging along the generated trajectory in phase-space. Considering some macroscopic equilibrium property A, a microscopic, instantaneous value A(q,p) can be defined for a given t. If the system has a constant temperature, volume, and number of particles (NVT ensemble), due to ergodic hypothesis, the time and ensemble average are equal:

$$\langle A \rangle_{time} = \langle A \rangle \qquad (2.9.1)$$

$$\langle A \rangle_{time} = \lim_{T\to\infty} \frac{1}{T} \int_0^T A(x(t))dt \quad and \quad \langle A \rangle = \int\int A(q,p)P(q,p)dqdp \qquad (2.9.2)$$

where P(q,p) is the probability of being at a particular phase-space point (q,p).

To study the time evolution of a chemical system, in classical molecular-dynamics (MD) simulations Newton equation of motion is solved:

$$M_I \ddot{R}_I = F_I \qquad (2.9.3)$$

In practice, to propagate the atoms, a small discrete time step Δt is introduced and a numerical step-by-step integration of the equations of motion is carried out. Taking the Taylor series expansion in Δt gives:

$$R_I(t + \Delta t) = R_I(t) + \Delta t \dot{R}_I(t) + \frac{1}{2}\Delta t^2 \ddot{R}_I(t) + \cdots \qquad (2.9.4)$$

$$\dot{R}_I(t + \Delta t) = \dot{R}_I(t) + \Delta t\, \ddot{R}_I(t) + \cdots \qquad (2.9.5)$$

The time evolution of the system is followed by applying integration algorithms into an MD computer program, as via velocity Verlet integrator:

$$R_I(t + \Delta t) = R_I(t) + \dot{R}_I(t)\Delta t + \frac{F_I(t)}{2M_I}\Delta t^2 \qquad (2.9.6)$$

$$\dot{R}_I(t+\Delta t) = \dot{R}_I(t) + \frac{F_I(t+\Delta t)+F_I(t)}{2M_I}\Delta t \qquad (2.9.7)$$

The new positions $R_I(t+\Delta t) = R_I$ can thus be calculated from the current positions $R_I(t)$, velocities $\dot{R}_I(t)$ and forces $F_I(t)$. Similarly, the new velocities can be obtained from knowledge of current velocities and forces $F_I(t)$, and from the new forces which are available as soon as the new positions are calculated. The time step used to discretize the time evolution must be smaller than the fastest motion in the system under investigation.

Traditional molecular dynamics simulations take advantages from pre-defined analytical potentials. The most commonly used potentials are the pairwise additivity approximation by the empirical MM force field ($U^{MD}(R_{IJ})$ potential between each set of atoms I and J). From the analytical potentials the forces are then obtained by taking the derivatives with respect to the positions:

$$F_I = -\frac{\partial U(R_I)}{\partial R_I} = -\sum_J \frac{\partial U^{MD}(R_{IJ})}{\partial R_{IJ}} \qquad (2.9.8)$$

Employing the classical force fields in the MD allow to span large timescale from nano to microseconds. Nevertheless, these MM potentials fail to describe processes where electronic degrees of freedom play an important rule, e.g in excited states and chemical reactions. To achieve reliable dynamic description of such processes, electronic behavior needs to be included from first principles method, such as the DFT. This approach is well-known as Ab Initio Molecular Dynamics (AIMD).[100]

2.9.1. Ab-initio Molecular Dynamics (AIMD)

In the ab-initio molecular dynamics (AIMD), the forces are computed on-the-fly by means of accurate electronic structure calculations. Within the Born–Oppenheimer approximation, the potentials are obtained by solving a time-independent quantum chemical electronic structure problem as:

$$U(R_I) = min_{\{\psi\}} E[\{\psi\}; R_I] \qquad (2.9.9)$$

Thus, to provide the forces for calculating the next step, the Schrödinger equation with an optimized electronic wavefunction ψ at current nuclear position R_I can be solved by ab-initio methods. Because the increased accuracy and predictive power of AIMD simulations comes at significant computational cost, the less expensive DFT and DFTB approaches[49] are to date the most commonly employed electronic structure theory. In this formalism of Born-Oppenheimer MD (BOMD),[100] the potential energy $E[\{\psi\}; R_I]$ is minimized at every MD step with respect to $\{\psi_i\}$ under the holonomic orthonormality constraint $\langle\psi_i|\psi_j\rangle = \delta_{ij}$. This leads to the following Lagrangian:

$$\mathcal{L}_{BO} = \frac{1}{2}\sum_{I=1}^{N} M_I \dot{R}_I^2 - min_{\{\psi_i\}} E[\{\psi_i\}; R] + \sum_{i,j} \Lambda_{ij}\big(\langle\psi_i|\psi_j\rangle - \delta_{ij}\big) \qquad (2.9.10)$$

where Λ_{ij} is a Hermitian Lagrangian multiplier matrix. By solving the corresponding Euler-Lagrange equations:

$$\frac{d}{dt}\frac{\partial \mathcal{L}}{\partial \dot{R}_I} = \frac{\partial \mathcal{L}}{\partial R_I} \text{ and } \frac{d}{dt}\frac{\partial \mathcal{L}}{\partial \langle\dot{\psi}_i|} = \frac{\partial \mathcal{L}}{\partial \langle\psi_i|} \qquad (2.9.11)$$

one obtains the associated equation of motion (EOM):

$$M_I \ddot{R}_I = -\hat{H}_e\langle\psi_i| + \sum_i \Lambda_{ij}\big(|\psi_j\rangle\big) \qquad (2.9.12)$$

Another AIMD approach was proposed in the 1985 by Car and Parrinello[101], taking direct advantages of the quantum mechanical adiabatic time scale separation of fast electronic (quantum) and slow nuclear (classical) motion. The two-component quantum-classical system is mapped into a two component purely classical problem with two separate energy scales at the expenses of losing the intrinsic time dependence of the electronic sub-systems. In Car-Parrinello MD (CPMD) a coupled electron-ion dynamics is performed, where the electronic degrees of freedom are added to the Lagrangian as classical ones:

$$\mathcal{L}_{CP} = \underbrace{\frac{1}{2}\sum_I M_I \dot{R}_I^2 + \sum_i \mu_i \langle \dot{\psi}_i | \dot{\psi}_i \rangle}_{kineti\ energy} - \underbrace{\langle \Psi_0 | \hat{H}_e | \Psi_0 \rangle}_{potential\ energy} + \underbrace{\sum_{i,j} \Lambda_{ij} \left(\langle \psi_i | \psi_j \rangle - \delta_{ij} \right)}_{constraints} \quad (2.9.13)$$

where the electronic degrees of freedom are an artificial inertia commonly known as the fictitious mass parameter μ_i, whose units is energy×time^2, and $\{\dot{\psi}_i\}$ are the orbital velocities. Once again, applying the Euler-Lagrange equations (2.9.11) lead to the following EOM:

$$M_I \ddot{R}_I = -\frac{\partial}{\partial R_I} \langle \Psi | \hat{H}_e | \Psi \rangle \quad \mu_i \ddot{\psi}_i(t) = -\frac{\delta}{\delta \psi_i^*} \langle \Psi_0 | \hat{H}_e | \Psi_0 \rangle + \sum_i \Lambda_{ij} \left(|\psi_j\rangle \right) \quad (2.9.14)$$

where $-\frac{\partial E}{\partial \langle \psi_i |}$ are the electronic forces for propagating the electronic degrees of freedom in time within a fictitious Newtonian dynamic along the nuclei.

For the case of Kohn–Sham DFT, the above equations became:

$$M_I \ddot{R}_I = -\nabla \langle \psi_0 | \hat{H}_e^{KS} | \psi_0 \rangle \quad \mu_i \ddot{\phi}_i(t) = -\hat{H}_e^{KS} \phi_i + \sum_i \Lambda_{ij}\, \phi_j \quad (2.9.15)$$

Because no SCF cycles are required to ensure the consistent with the instantaneous energy and to force the electrons to adiabatically follow the nuclei, the computational cost to compute the nuclear forces in each CPMD step is much reduced with regards of BOMD. However, the achievable length and time scales are still one of AIMD major limitations. Due to the cost of treating the electronic degrees of freedom, the computational cost of these simulations is far higher than classical molecular dynamics. In a typical AIMD simulation one needs to use a time step of the order of femtoseconds (i.e., 10^{-15} seconds) to correctly integrate the equations of motions. For this reason, AIMD methods are typically limited to smaller systems and shorter times. Unfortunately, interesting events often take place on a much longer timescale. The achievable timescale is still severely limited also in MD simulations. For example, a small, denatured protein needs about 10^{-4} seconds to sample the rugged energy landscape and find its folded state. To explore this process, also with MD are needed about 10^{11} time steps.

To address the drop of computational time, in the last few years, a large variety of methods have been proposed. These are often referred as enhanced sampling techniques, one of them is the metadynamis.

2.9.2. Metadynamics

Metadynamics belong to a class of methods in which sampling is facilitated by the introduction of an additional bias potential, added to the Hamiltonian of the system, that acts on a selected number of degrees of freedom, often referred to as collective variables (CVs).[102,103] From a mathematical point of view, the CVs can be defined as functions, generally nonlinear, of the atomic coordinates R: $s(R) = (s_1(R), s_2(R), .., s_d(R))$. At time t, the bias potential can be written as a sum of Gaussians deposited along the system trajectory in the CVs space:

$$V_G(S,t) = \int_0^t dt' \, \omega \, exp\left(-\sum_{i=1}^{d} \frac{(S_i(R) - S_i(R(t')))^2}{2\sigma_i^2}\right) \qquad (2.9.16)$$

where ω is an energy rate and σ_i is the width of the Gaussian for the ith CV. The energy rate is constant and usually expressed in terms of a Gaussian height W and a deposition stride τ_G:

$$\omega = \frac{W}{\tau_G} \qquad (2.9.17)$$

This bias discourages the system from revisiting configurations that is already sampled. Thus, metadynamic simulations:

- accelerate the sampling of rare events by pushing the system away from local minima;
- allows exploring new reaction pathways as the system tends to escape the minima passing through the lowest free-energy saddle point.

- explores the low free-energy regions first, not requiring a priori knowledge of the landscape. After sufficient time, the bias potential V_G provides an unbiased estimate of the underlying free energy ($F(S)$):

$$V_G(S, t \to \infty) = -F(S) + C \qquad (2.9.18)$$

where C is an additive constant, and $F(S)$ is defined as

$$F(S) = -\frac{1}{\beta} ln\left(\int dR\delta(S - S(R))\, e^{-\beta U(R)}\right) \qquad (2.9.19)$$

Where $\beta = (k_B T)^{-1}$, T the temperature of the system, and U(R) the potential energy function.

In a single run, V_G oscillates around the free energy, so that the bias potential overfills the underlying FES and pushes the system toward high-energy regions of the CVs space, and it is not trivial to decide when to stop a simulation. If one is interested in reconstructing the FES, it should be stopped when the motion of the CVs becomes diffusive in the region of interest (Figure 2.9.1). A solution is provided by well-tempered metadynamics[104], in which the bias deposition rate decreases over simulation time via a different expression for the bias potential:

$$V(S, t) = k_B \Delta T ln\left(1 + \frac{\omega N(S,t)}{k_B \Delta T}\right) \qquad (2.9.20)$$

where $N(S, t)$ is the histogram of the S variables collected during the simulation, and ΔT an input parameter with the dimension of a temperature. With respect to standard metadynamics, the bias deposition rate decreases as 1/t, the dynamics of all the microscopic variables becomes progressively closer to thermodynamic equilibrium as the simulation proceeds. Plus, the bias potential does not fully compensate the FES, but it converges to:

$$V_G(S, t \to \infty) = -\frac{\Delta T}{T + \Delta T} F(S) + C \qquad (2.9.21)$$

Nevertheless, contrary to standard metadynamics, the bias converges to its limiting value in a single run.

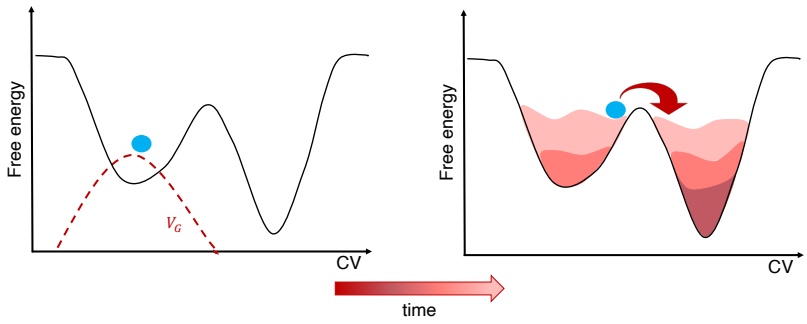

Figure 2.9.1 *Schematic representation of the progressive filling of the underlying free energy surface (FES) (black line).*

Another downside is identification of a set of CVs appropriate for description of complex processes is far from trivial. CVs are function of the microscopic coordinates of the system. To assure an effective application of metadynamics, the CVs must respect the following guidelines:

- Choosing a correct set of CVs to distinguish between the initial and final state and describe all the relevant intermediates;
- CVs should include all the slow modes of the system, in other words, those variables that cannot be satisfactorily sampled in the timescale of the simulations;
- Low number of CVs is desirable to obtain a low-dimensional FES.

Within the field of material science, metadynamics has been widely used to shed light on various diffusion processes.[105–108]

In the following chapters, we identify the most suitable ab-initio approaches, above all these discussed here, to each specific aspects of chemistry at heterogeneous interfaces in batteries, photoelectrochemical cells and perovskite solar cells.

CHAPTER 3 – NEXT GENERATION BATTERIES

After the first commercial release in the early 1990s by the Sony Corporation, the Lithium-Ion Batteries (LIBs) are widely studied and developed for portable electronics.[6,109] The LIB working principle is well-known based on Li-ion (Li^+) intercalation and diffusion processes.[110] Upon discharge, the Li^+ is removed from the negative electrode and injected into the positive one, while opposite processes occur during charging of battery (Figure 3.1a). The constituent electrodes are so intercalating materials, placed in lithium-ion conducting electrolytes. Despite the numerous benefits related to the high open circuit voltage, low self-discharge rate, and high energy-to-weight ratios, the high cost and limited availability of lithium pose a serious threat to large-scale applications of Li-ion devices.[6,110] In this framework, similar operating principles with LIBs have encouraged research and development of Na-ion batteries (NIBs).[4,111–113] This type of battery with cheaper and affordable materials may be used in grid infrastructure and electric transportation. Nevertheless, while benefiting the diffusion through liquid electrolytes, the large Na^+ radius hinders a convenient reversible intercalation into the structure of the LIBs commonly adopted electrodes.[111,114–118] The hunt for different NIBs constituent materials is so still a major concern. Another alternative to LIBs to boost the deployment of electric vehicles, are the Li-air batteries, discovered by Abraham in 1996[119], due to enhanced specific capacity and reduced cell weight.[120–122] This latter feature is mostly determined by the anodic materials, as the cathode is mainly composed of lightweight porous material that hosts the gaseous O_2 coming from the outside. The working principle relies on the oxygen reduction reaction (ORR) and oxygen evolution reaction (OER) occurring upon, respectively, discharge and charge processes (Figure 3.1b). Ideally, from the reaction of one kilogram of O_2 with lithium metal, it is possible to achieve an amount of energy equal to that supplied by gasoline, which is about 14.5% of the theoretical energy density of Li-air

batteries.[121] In practice, major challenges including long-term stability and performance issues need to be addressed to scale up Li-air technologies as viable solutions for electric transportation. On one hand, despite the theoretical reversibility of the accepted cathode reaction, which main product is the lithium peroxide (Li_2O_2)[122] (see Figure 3.1b), less than 90% of discharge-consumed O_2 evolves upon charging, and the ratio of electrons to O_2 deviates from the ideal values ($2e^-/O_2$) during a single battery cycle. Several secondary reactions, especially at cathode material, severally limit the Li-air batteries rechargeability and provided energy.[120–123] Great research efforts have, thus, been focused on unveiling the effective reversibility of Li-air battery cathode upon charge-discharge cycling. On the other, the use of Li metal anode has been gainful due to its low electrochemical potential, ultrahigh theoretical specific capacity, and low density.[124–126] Nevertheless, uncontrolled dendritic growth at the metal electrode/electrolyte interface upon cycling can lead to severe safety hazards. A promising strategy to overcome dendritic growth is the formation of protective and stable layers between the Li metal and the electrolyte, namely the Solid Electrolyte Interphase (SEI) (Figure 3.1b).[127,128] This layer, given by degradation processes at electrolyte/electrode interfaces, must allow the continuous Li ion deposition-dissolution mechanism, and also must limit the further decomposition of active material and dendritic growth. In this context, due to complexity of electrolyte/electrode reactivity, an in-depth atomistic understanding of SEI formation mechanism is required to enhance the whole performances of typical Li metal batteries (LMBs).

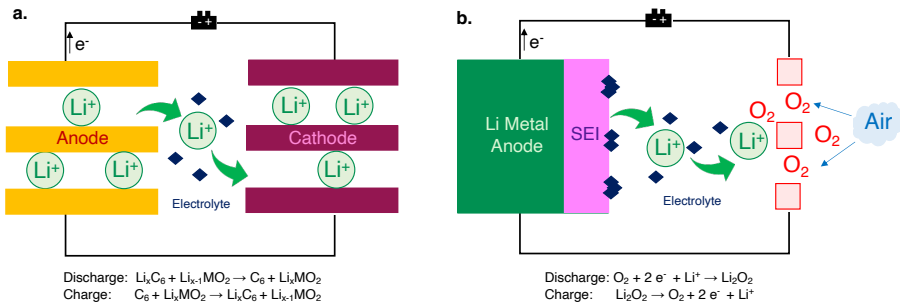

Figure 3.1 *Schematic representation of* ***(a)*** *Li-ion and* ***(b)*** *Li-air batteries. The general discharge/charge reactions are also reported. We consider the LIBs common anodic and cathodic material (graphite and metal oxide, able to host the* Li^{+}*)* [110] *and for Li-air the widely accepted formation of the lithium peroxide (*Li_2O_2*) upon discharge.* [122] *In Li-air devices, the Solid Electrolyte Interface (SEI) between Li metal anode and electrolyte is also shown (pink box).*

Overall, as emerged from the above dissertation, several issues related to electrode/electrolyte(ion) interfaces undermine the development and distribution of the promising Na-ion, Li-air and Lithium Metal batteries. In this framework, an atomistic perspective can be helpful to an in-depth understanding of interfacial electrochemical processes. To this aim, in this chapter, we identify a proper computational strategy to cover the aforementioned major challenges at next-generation batteries heterogeneous interfaces: the Na ion uptake under electric field at promising anode material for NIBs, the origin of secondary reaction occurring at Li_2O_2 interfaces in Li-air batteries, and the formation of stable SEI at LMBs interfaces.

3.1 Structural and Electronic Effects of External Electric Field on Na Uptake at TiO_2 Interfaces.

Introduction. Among many investigated systems as NIBs anodes, titanium dioxide (TiO_2) represents a sustainable choice for the overall balance of performance, stability, and cost. Titania-based compounds are versatile functional materials in several energy conversion technologies, from solar cells to water-splitting photocatalysis and also Li-based batteries.[129–132] Thus, nanostructured TiO_2-based materials have recently been attracting great interest as NIBs negative electrodes.[118,133,134] However, several experimental investigations have highlighted the morphology-dependent performance of anatase electrodes employed in Na-cells. In particular, the facets of TiO_2 nanoparticles (NPs) show different activity, with the (100) and (001) terminations significantly more effective than the most stable (101) one.[133,135,136] This morphology-dependent activity of anatase facets was recently explained by a reliable first-principle model for Na^+ adsorption/insertion at anatase surfaces.[137] It is suggested that the crystalline facets act as intercalation sites into subsurface layers and their different behaviour can be ascribed to a convenient accommodation of Na^+ without significant lattice distortion for the (100) surface, and to an easy insertion through the subsurface layer favoured by a large lattice window for the (001) termination. Nevertheless, a significative aspect in battery devices, but neglected in these standard DFT simulations, is the effect of electric fields on the chemical interactions and electronic features of electrodes. A truthful computational strategy is so required for an in-depth understanding of electrochemical reactions occurring at electrode surfaces. To this end, in this section, we report a structure and electronic characterization of Na/TiO_2 interfaces under an external field via the worthwhile sawtooth-like potential approach (see Chapter 2 – section 2.8.1 for further details on this method).[91–94]

We aim to unveil how the direction and the intensity of the applied field can affect Na^+ adsorption and intercalation into TiO_2 facets.

Methods & computational details. Our structural models consisted of 10-layer supercells 1x2x1, 2x1x1, 2x2x1 for the (101)-, (100)- and (001)- TiO_2 surfaces (Figure 3.1.1) with 15 Å of vacuum along c. Concerning the sawtooth potential, we reversed the slope in a small region (~0.5 a_0) in the middle of the vacuum to ensure periodicity. Calculations were performed with $|\vec{F}|$ = -5 × 10^{-3}, 0, 5 × 10^{-3} Ha (1Ha = 51.4 V/Å). For Na^+ adsorption, we also considered $|\vec{F}|$ = -2.5 × 10^{-3}, 2.5 × 10^{-3} Ha. Hereafter, we named the field positive or negative depending on its direction against the z-axis ($\vec{F}$ and $-\vec{F}$, see Chapter 2 - Section 2.8.1 Figure 2.8.1b). For all the calculations, we used spin-polarized periodic DFT+U approach[35] within PW basis sets, as implemented in Quantum Espresso (QE).[138] We used the PBE functional, plus an effective U_{eff} = 3.3 eV parameter for *d* electrons of Ti atoms.[139] The PAW potentials were taken from QE repository[140] and the wave functions (augmented charge density) was expanded in plane waves with a 70 (280) Ry cutoff. We used the 2x2x1 k-point sampling based on a Monkhorst-Pack grid scheme as implemented in QE.[141] All the geometry optimizations consisted of full atomic-position relaxation until forces on the ions were below 0.05 eV/Å. Convergence threshold on total energy was 10^{-6} a.u.

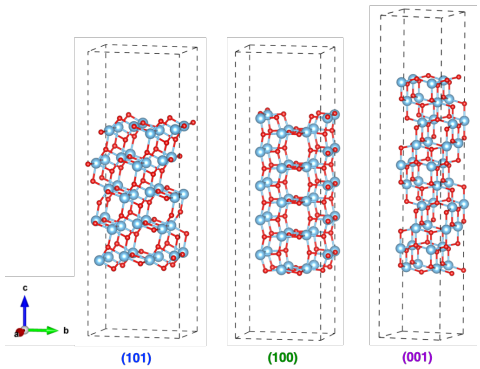

Figure 3.1.1 *TiO_2 anatase surfaces: (101), (100), (001). Color code: Ti (cyan), O (red).*

Field structural and energetic effects on Na adsorption. The resulting minimum-energy structures of Na-adsorbed states (Na^{OUT}) on top of TiO_2 anatase surfaces, (101), (100) and (001), under the influence of external electric fields, are featured in Figure 3.1.2 with remarkable distances between Na and surface O atoms (Na-O). For all the surfaces, under a positive field Na-O bonds undergo elongation, while decreasing under a negative field. The former effect is most relevant on the (001) surface, with a Na-O bond variation of ~0.6Å against the 0.4Å and 0.2Å for (101) and (100) interfaces, respectively. Meanwhile, all surfaces are slightly affected by the negative fields. In this case, an asymptotic value is reached at high negative fields for the Na^{OUT}-(001) interface. This structural analysis highlights that the field direction can affect the structural arrangements of Na^{OUT}-TiO_2 interfaces, exactly positive and negative fields lead Na adsorption sites farther and closer from the surfaces, respectively.

For all these minimum energy structures, we analyzed the energetic behavior computing the adsorption energies, E_{ads}:

$$E_{ads} = E_{Na^{OUT}} - E_{slab} - \frac{1}{2}E_{Na} \qquad (3.1.1)$$

where $E_{Na^{OUT}}$, E_{slab} and E_{Na} are the total energies of Na^{OUT} states, pristine surface slabs and metallic sodium, considering the *bcc* 2-atoms cells[142], respectively. On one hand, the adsorption energy trends in Figure 3.1.3a reveals that the previous zero-field surface activity (E_{ads} (001) > (101) > (100))[137] is unchanged under both positive and negative fields. On the other, we found that in a positive field E_{ads} drop of 0.4/0.6 eV, favoring the Na adsorption, while the negative fields increase E_{ads} of 0.2 eV. To in-depth understand of field effects, we dissected the E_{ads} in terms of interaction (E_{int}) and distortion energies (E_{dis}),:

$$E_{int} = E_{Na^{OUT}} - E_{surf}^{Na^{OUT}} - E_{Na}^{Na^{OUT}} \qquad E_{dis} = E_{surf}^{Na^{OUT}} - E_{surf}^{surf} \qquad (3.1.2)$$

where $E_{surf}^{Na^{OUT}}$ and E_{surf}^{surf} are the total energies of each surface slab at the Na-adsorbed geometry and in their minimum-energy structures, respectively, while

$E_{Na}^{Na^{OUT}}$ is the total energy of the sodium atom at the Na^{OUT} geometry, computed at each field strength and direction.

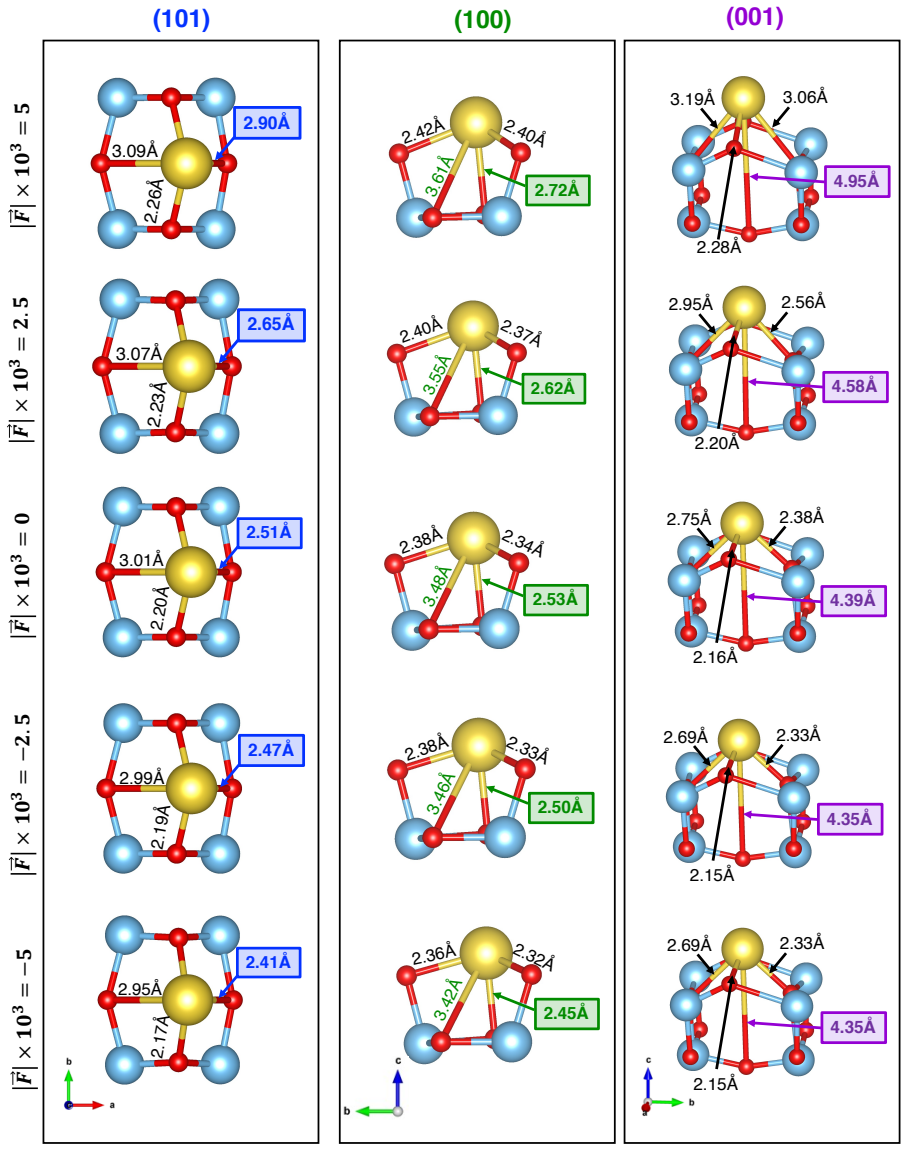

Figure 3.1.2 *Na-adsorbed states (Na^{OUT}) on top of TiO_2 surfaces (from left to right: (101), (100) and (001)) obtained at PBE+U level of theory with external electric fields. Color code: Na (yellow), Ti (cyan) and O (red).*

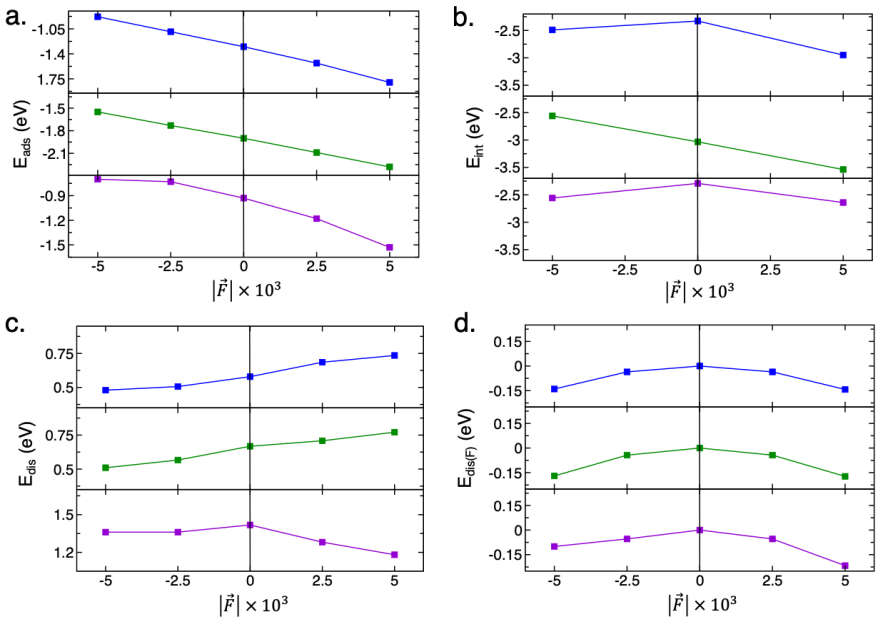

Figure 3.1.3 *Energy contributions at Na^{OUT}-TiO_2 interfaces:* ***(a)*** *adsorption, E_{ads},* ***(b)*** *interaction, E_{int},* ***(c)*** *distortion, E_{dis}, and* ***(d)*** *field-derived distortion, $E_{dis(F)}$, energies (eq. 3.1.1 to 3.1.3). Color code: Na^{OUT}-(101), blue; Na^{OUT}-(100), green; Na^{OUT}-(001), violet.*

Analyzing the resulting energetics plotted in panels b and c of Figure 3.1.3, we found no effect by electric field polarization on Na-TiO_2(001) interaction (Figure 3.1.3b), but E_{int} equally drop at both positive and negative fields. For this termination, we can thus ascribe at slight lattice distortion (Figure 3.1.3c) the more favorable E_{ads} under positive field. Meanwhile, in the case of (101) and (100) facets, Figure 3.1.3b shows extremely stabilizing interactions at positive fields, which balance the increased distortion energies and can explain the more favorable E_{ads}. To examine possible effect of bias on lattice distortion, we also computed the surface distortion energies upon the application of the external field $E_{dis(F)}$ as:

$$E_{dis(F)} = E_{surf}^{surf(F)} - E_{surf}^{surf(F0)} \qquad (3.1.3)$$

where $E_{surf}^{surf(F)}$ and $E_{surf}^{surf(F0)}$ are the total energies of the surface slabs in their minimum-energy structures at positive/negative fields and zero-field, respectively. The overall negative $E_{dis(F)}$ values (Figure 3.1.3d) reveal that the field slightly stabilizes all the surfaces, so that the different distortions can be ascribed to the lattice reorganizations aiming to accommodate a Na atom. Finally, to account for the mere structural field effects, we calculated the difference between energies (with no bias) of geometries obtained under positive/negative fields and of zero-field ones. We obtained a similar contribution of ~ 0.1 eV for all the surfaces and fields. The only exception is the Na^{OUT}-(001) state at the positive field, which has a higher amount of this distortion energy (0.25 eV) due to the further position of Na atom with regard to zero-field structure (Figure 3.1.2). These energetic analyses demonstrate that positive fields would benefit adsorption processes on all surfaces due to improved Na-TiO_2 interactions at (101) and (100) surfaces and due to reduced lattice distortion at (001) one. Plus, merging the structural and energetic characterizations, we found that the Na adsorption sites are further from the surface in the lowest energy Na^{OUT} states at positive fields.

Field electronic effect on Na adsorption. Analysis of the charge density difference (CD plot) between positive/negative and zero fields (Figure 3.1.4) reveals that under positive and negative fields the surface Ti atoms present electron accumulation and depletion, respectively. This is also confirmed by the variation of average magnetization and Löwdin charges on Ti atoms in the two topmost layers (Table 3.1.1). Noteworthy, the O and Ti charges are far from the ionic limits, due to the well-known strong hybridization of Ti d and O p state,[137] also underlined by the computed projected density of states (pDOS) in Figure 3.1.5. This further analysis on electronic structure of Na^{OUT} systems reveals a population of the TiO_2 conduction band states with adsorption of Na atom. This validates our model to simulate the interaction between a Na cation and an n-type semiconductor, as required for the NIB electrode.

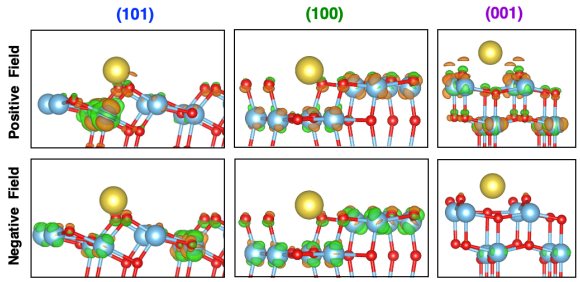

Figure 3.1.4 *Charge density difference plots calculated between positive (top) / negative (bottom) and zero field on top of Na^{OUT} geometries obtained at zero field at PBE+U level of theory. Isodensity value: 0.001 a.u. Color code as in Figure 3.1.2; electron gain (green surface), electron deplation (orange surface).*

Table 3.1.1 *Average magnetization ($M_{Ti\text{-}2L}$) and Löwdin charges ($q_{Ti\text{-}2L}$) of the Ti atoms within two topmost layers (Ti-2L) of the Na^{OUT} systems at each field value ($|\vec{F}|$).*

$\lvert\vec{F}\rvert$ (Ha)	$M_{Ti\text{-}2L}$ (m_B/cell)			$q_{Ti\text{-}2L}$ (e^-)		
	(101)	**(100)**	**(001)**	**(101)**	**(100)**	**(001)**
+ 5 x 10^{3}	0.50	0.28	0.12	1.45	1.46	1.45
0	0.22	0.16	0.15	1.44	1.45	1.44
- 5 x 10^{-3}	0.01	0.08	0.00	1.43	1.44	1.44

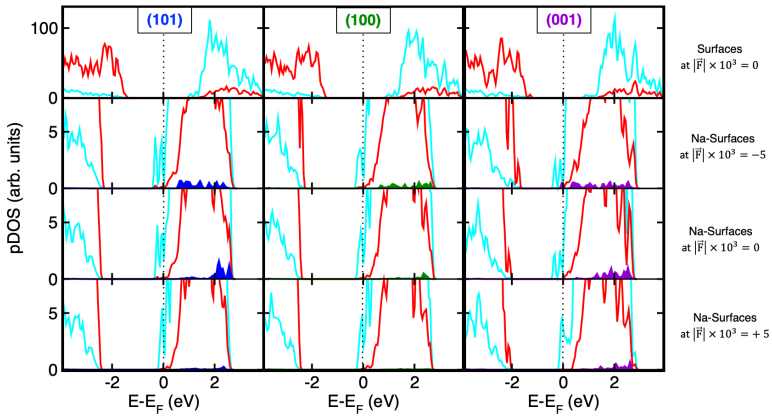

Figure 3.1.5 *Projected density of states (pDOS) for pristine surfaces at zero-field; Na^{OUT} at negative field, zero-field and at positive field. Color code: Ti d states, cyan; O p states, red; Na s states, blue, green, and violet for (101), (100) and (001) surfaces, respectively.*

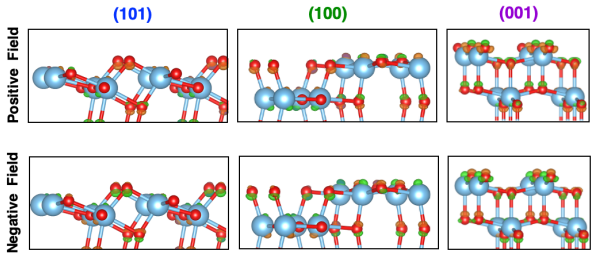

Figure 3.1.6 *Charge density difference plots calculated between positive/negative and zero-field for pristine TiO_2 surfaces at PBE+U level of theory. Isodensity value: 0.001 a.u. Color code as in Figure 3.1.2 and 3.1.4.*

Finally, analysis of the CD plots for the pristine anatase surfaces upon application of the field (Figure 3.1.6) shows no charge density variation, so that the main source of charge transfer is the Na adsorption at a given field polarization. Overall, the electronic analysis suggests that the field polarization affects the interfacial electronic features, inducing a reduction/oxidation of Ti atoms. Since the $Ti^{4+/3+}$ redox pair is directly involved during the Na^+ intercalation reaction[134,143], one could associate the field direction to the battery charge-discharge processes. In particular, the sawtooth-like potential with positive slope can simulate the anode desodiation and simultaneous Ti oxidation occurring upon discharge in the low-voltage range.

Field effect on Na insertion. Because subsurface insertion appears to be more appropriate to model intercalation of Na at anatase interfaces,[137] we also investigated the field effects in Na-inserted states at the subsurface layer of TiO_2 surfaces (Na^{IN}) (Figure 3.1.7). Due to the high screening of surface layer toward the applied potential, the energetics and structure of Na^{IN} states remain practically unchanged under positive and negative field. Nevertheless, the field effects on E_{ads} are reflected on IN-OUT energy gap (Figure 3.1.8). In particular, these energy gaps decrease under negative field, with lowest energy variation for the (001) surface.

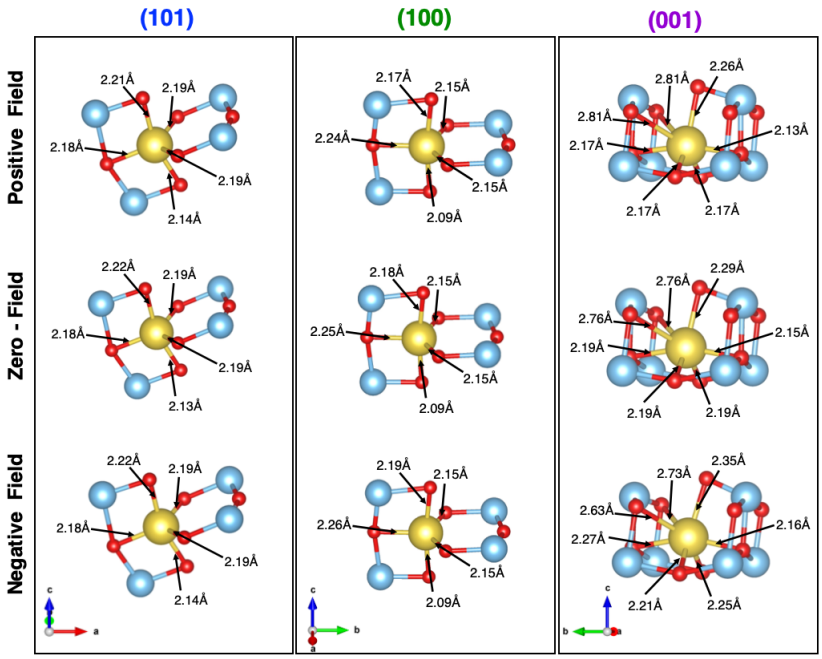

Figure 3.1.7 *Na^{IN} states at the subsurface layers of TiO_2 surfaces obtained at PBE+U level of theory with positive, zero, negative field. Color code Figure 3.1.2*

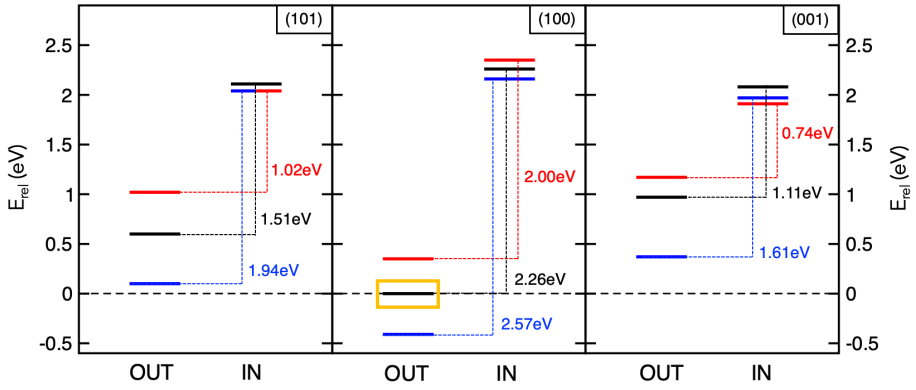

Figure 3.1.8 *Insertion and adsorption energetics for Na^{IN} and Na^{OUT} states at TiO_2 surfaces at PBE+U level of theory. All energy values, E_{rel}, are referred to Na-adsorbed on (100) surface with zero-field (yellow box). Color code: zero-field (black lines), positive and negative field ($|\vec{F}| \times 10^3 = \pm 5$ Ha) in blue and red lines, respectively.*

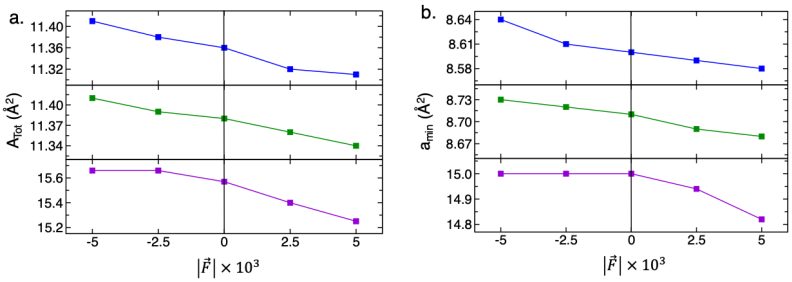

Figure 3.1.9 *Electric field effects on* ***(a)*** *total (A_{Tot}) and* ***(b)*** *minimum accessible (a_{min}) areas of the lattice windows, defined as ref [*137*]. Color code: Figure 3.1.2.*

In line with previous results [137] and zero-field, the trend for the energy gap ($E_{IN} - E_{OUT}$) is (100) > (101) > (001) at both negative and positive fields. The further analysis in Figure 3.1.9 of surface lattice windows, defined in ref [137] and ascribed as limiting factor for Na^+ uptake at TiO_2 interfaces, reveals a higher variation of this structural parameter under the negative field. Overall, structural and energetic effects of electric field suggest that the negative polarization can facilitate Na^+ insertion into TiO_2 NPs, in particular on the (001) surface. This negative field, leading to Ti reduction and favoring Na intercalation, can so be representative of the sodiation upon NIBs charging.

To sum up, our findings reveal that field polarization influences titania electrical properties as well as Na^+ absorption, boosting redox reactions within Ti atoms, as in battery charge/discharge cycles. In particular, the (001)-TiO_2 facet shows high activity under both negative and positive fields, also suggesting the reversibility upon charge/discharge processes. Beyond that, this study highlights the straightforward application of the sawtooth potential approach as a computational strategy to consider the effects of external field in battery operando conditions on electrochemical processes at electrode interfaces.

This work is published on Journal of Materials Research [144] and is reproduced with permission from Springer Nature.

3.2 Unveiling Singlet Oxygen Release at Lithium Peroxide Interface.

Introduction. In 2016, the formation of singlet oxygen, namely the first excited state ($^1O_2$: $^1\Delta_g$) of triplet dioxygen ($^3O_2$: $^3\Sigma_g$), has been found to play a key role on the Li-air battery components degradation.[145–147] Electron paramagnetic resonance spectroscopy revealed that the $^1O_2$ reacts with aprotic electrolyte leading to the same secondary products of Li-air battery, and the use of $^1O_2$ quencher increased batteries reversibility.[145] The singlet oxygen is found especially from the Li_2O_2 decomposition upon charge, starting from 3V to higher voltages, and due to its high reactivity, it leads to degradations of the electrolyte, undermining the performance and the long-term stability of the Li-air battery.[146] The $^1O_2$ release was hitherto ascribed to electrochemical oxidation of Li_2O_2 with a $2e^-$ oxidation process (Figure 3.1b) above the voltage of 3.55,[145,148] but electrochemical experiments on metal-O_2 cell and ab-initio DFT study have recently recognized the superoxide disproportionation as the source of $^1O_2$.[147,149,150] Upon charging, the dissolved peroxide deposited on the cathode would lead to a superoxide-like species by a one-electron oxidation (eq 3.2.1). Thus, the oxygen can be released by disproportion of these superoxide species (eq 3.2.2) or by a second electron oxidation (eq 3.2.3):

$$Li_2O_2 \leftrightarrows Li^+ + 1\,e^- + LiO_2 \qquad (3.2.1)$$

$$2\,LiO_2 \rightarrow Li_2O_2 + O_2 \qquad (3.2.2)$$

$$LiO_2 \leftrightarrows Li^+ + 1\,e^- + O_2 \qquad (3.2.3)$$

The superoxide disproportion is asserted as the main pathway for the second electron transfer from superoxide to peroxide in discharge process, and for oxygen evolution with two-step one-electron oxidation process upon charge.[149,151–153] In aprotic media, superoxide disproportionation with significant amount of $^1O_2$ relies on the higher stability of the peroxide with strong Lewis

acids.[152] Ab-initio DFT study also revealed that disproportionation dominates O_2 evolution for most mediators and always yields some $^1O_2$, but the mediators with high redox potentials above 3.5 V versus Li/Li^+ can also drive $^1O_2$ evolution from superoxide oxidation.[154] Singlet oxygen release from disproportion or oxidation of superoxide species is still under debates. Due to instability of superoxide at Li_2O_2 potential, it could be an unstable specie during charging, difficult to detect experimentally, and it can be instantly oxidated, so that also a two-electron oxidation can be observed. In particular, it was found that the theoretical differences in the standard potentials of a reaction resulting in triplet or singlet oxygen is 0.96 V and 0.48 eV in the case of one transferred electron and two transferred electrons, respectively.[147] Despite the broad literature and the great advances on the mechanism of singlet oxygen release by superoxide disproportion at molecular level, less is known about $^1O_2$ evolution from peroxide/superoxide oxidation at cathode interfaces. The facets of Li_2O_2 nanoparticles, the main discharge product in Li-air batteries, are expected to be the locus of reaction during charge reactions and the oxygen release from oxides and dissolved species can be quite different from the gas phase processes. Atomistic investigations should thus not disregard the role of Li_2O_2 interfaces. To this end, we studied the release of triplet- and singlet-oxygen species from the $(11\bar{2}0)$-Li_2O_2 surface, one of the most exposed facets under the most reducing and oxidizing conditions.[155] The multireference nature of involved species has also called for investigations via more accurate CASPT2 method.[150,156,157] At this level of theory, Houchins et. al.[150] found that singlet oxygen can be largely released in disproportionation reactions involving free superoxide anions, also suggesting a singlet oxygen release via superoxide dissolution from cathode surfaces. Meanwhile, the analysis of different bond lengths ($d_{O\text{-}O}$) and oxygen distances from Li atom ($d_{O\text{-}O,Li}$) via CASPT2 approach revealed that the $d_{O\text{-}O}$ variation influences the energetics of oxygen release and nature of the molecule ground state.[156,157] However, the high computational cost

of CASPT2 approach hinders the study on extended surfaces, requiring computational strategy beyond the standard ones. Due to the ionic feature of lithium peroxide material and localized nature of oxygen release process, we thus proposed the simpler electrostatic embedded cluster approach at the CASPT2 level of theory[62–64] (see Chapter 2 section 2.5.2 and 2.1.3, respectively for further details) to study the underlying process at Li_2O_2 interfaces. Such an approach can provide a reliable description of the involved multireference species, e.g. superoxide and singlet oxygen, not neglecting the rule of interfaces.

Models & computational details. We considered a supercell 2x2 of 5 layers slab for the $(11\bar{2}0)$ surface, with 15 Å of vacuum along the c direction (Figure 3.2.1a). We performed spin polarized periodic DFT calculations as implemented in the Vienna Ab initio Simulation Package (VASP, ver. 5.4.1)[158–160] using the PBE functional.[26,27] Core electrons were described by PAW potentials obtained from the VASP repository.[82] Pseudo-wave functions were expanded in a PW basis set with a kinetic energy of 600 eV and 2x2x1 Γ-centered k-point mesh for sampling the Brillouin zone, that we determined from convergence tests until the total electronic energy was below 1 meV/f.u. Taking into account dipole correction as implemented in VASP code[141], we carried out geometry optimization of surface, in terms of atomic positions until the maximum forces acting on each atom were below 30 meV/Å. Due to computational cost of multireference methods, a stoichiometric cluster, that includes the released molecule and the nearest 8 lithium atoms with other 3 peroxide molecules, was carved from Li_2O_2 surface, while a large point charge array mimicked extended crystal surface (Figure 3.2.1b). A supercell of 7.64 Å x 8.28 Å x 6.58 Å with 729 Li (+1 charge) and O (-1 charge) point charge assure neutrality of all system. To compute the electrostatic embedding, we used the OpenMolcas software. [161] The cc-PVTZ basis set were employed for cluster atoms, while ECPs[66] for Li atoms bonded to the terminating O, but not included in the cluster, to prevent artificial

drift of the anion electron density onto the surrounding positive charges. We computed the energy of the first five states.

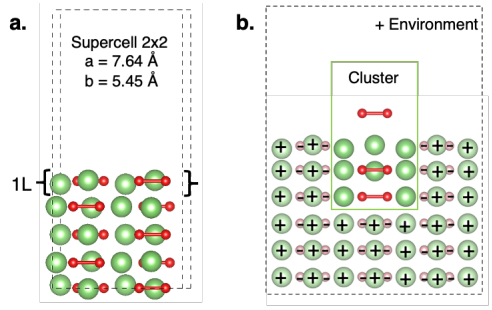

Figure 3.2.1 *Structural models for DFT- and CASPT2- approaches:* ***(a)*** *the 2x2 supercell and* ***(b)*** *the embedded cluster of* $(11\bar{2}0)$ *– Li_2O_2 surface. Color code: Li (green), O (red).*

Oxygen release at DFT-PBE level of theory. Based on previous works,[156,157] we first studied via periodic DFT the oxygen release from the $(11\bar{2}0)$-facet setting up a rigid scan in the following O_2 bond lengths (d_{O-O}) and released molecule-surface distances (d_{O-Surf}) (in Figure 3.2.2):

d_{O-O} (Å): 1.205, 1.208, 1.210, 1.215, 1.220, 1.225, 1.230, 1.235, 1.250, 1.300,

1.350, 1.400, 1.450, 1.500, 1.550, 1.600

d_{O-Surf} (Å): 1.00, 1.15, 1.25, 1.50, 1.75, 2.00, 2.25, 2.50, 2.75, 3.00, 3.25, 3.50,

3.75, 4.00, 4.50, 5.00

For O−O distances, we considered the peroxide molecular (O_2^{2-}) bond length on Li_2O_2 surface topmost layer ($d_{O-O,Surface}$ 1.55 Å), the typical superoxide (O_2^-) distance (1.35Å) and both DFT-PBE ($d_{O-O,T/S}$= 1.235 Å) and experimental values ($d_{O-O,T}$ = 1.2075 Å $d_{O-O,S}$= 1.215 Å) of $^3O_2/^1O_2$ bond lengths.[162] Figure 3.2.2 shows the resulting triplet- and singlet-oxygen release potential energy surfaces (PESs) at DFT-PBE level of theory. We, hereafter, identified PESs as S/T-PES, where S/T indicates singlet/triplet spin multiplicity, thus S/T-(d_{O-Surf}, d_{O-O}) are

points of S/T-PESs. Close to surface (low d_{O-Surf}), all system retains the singlet multiplicity of lithium peroxide surface, while triplet is the low-energy state when the released molecule is ~2Å far from the surface. At this d_{O-Surf}, we also found a reorganization of d_{O-O} from 1.55Å to 1.35Å, which is the typical bond distance of superoxide molecule. The magnetization moment of ~0.4 on each oxygen atom of released molecule confirms that superoxide is formed at this point (exactly at T-(2.00Å; 1.35Å)). Increasing d_{O-Surf}, further decrease of bond length occurs from 1.35Å to 1.25Å and the oxygen molecule is formed. Far from surface, the singlet PES lies ~0.7 eV above triplet. These results reveal that the charging mechanism of oxygen release can occur at Li_2O_2 interface via the formation of superoxide species preferring the triplet oxygen release. We also found that the oxygen bond length could be a key descriptor to predict the formation of the superoxide and O_2 release, in agreement with previous molecular studies. [156,157]

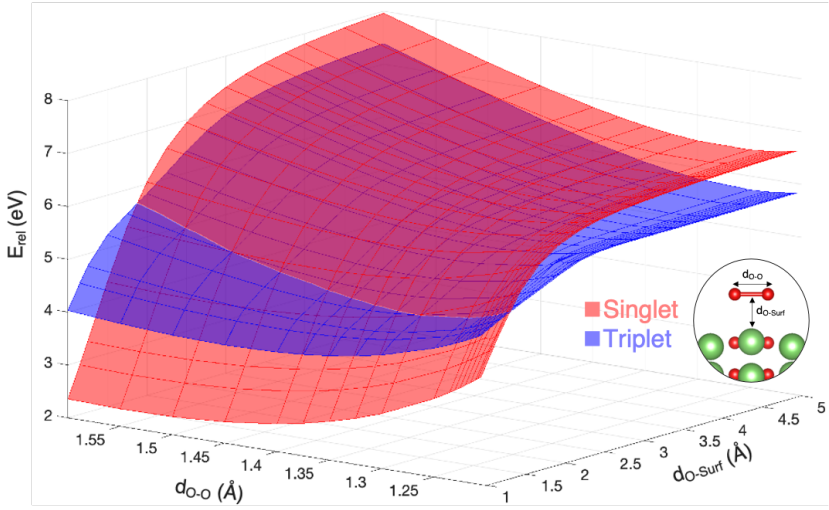

Figure 3.2.2 *Singlet/Triplet potential energy surfaces (PES) at DFT-PBE level of theory of oxygen release from* $(11\bar{2}0)$*- Li_2O_2 surface in the two coordinates: released O_2 bond length (d_{O-O}) and its distances from surface (d_{O-Surf}), shown in the insert. E_{rel} is $E_{dO-Surf,dO-O} - E_{0.0,1.55}$, where $E_{0.0,1.55}$ is the energy of pristine surface.*

Oxygen release at CASPT2 level of theory. Further reliable analysis on radical superoxide species and elusive singlet oxygen state are provided by the electrostatic embedded-cluster approach at CASPT2 level of theory. The choice of active space is due to preliminary CASPT2 calculations on the isolated triplet ($^3O_2$) and singlet ($^1O_2$) dioxygen. The Table 3.2.1 shows that both bond distances ($d_{O\text{-}O}$) and excitation energy ($\Delta E_{S\text{-}T}$) converge with the active space CAS(12e,10o), including the 12 electron of O_2 in the ten MOs: $\sigma_s\ \sigma_s^*\ \sigma_p\ \pi\ \pi^*\sigma_p^*$, plus 2 unoccupied MOs. Thus, to simulate the Li-air battery charging process (Figure 3.2.3a), we optimized the CASSCF wavefunctions in an active space CAS(14e,12o), adding two orbitals localized on topmost Li atoms to the aforementioned CAS(12e,10o) (Figure 3.2.3b).

Table 3.2.1 *Bond distances ($d_{O\text{-}O}$) for isolated singlet ($d_{O\text{-}O,S}$) and triplet ($d_{O\text{-}O,T}$) dioxygen and excitation energy ($\Delta E_{S\text{-}T}$) at CASPT2 level of theory with different active spaces.*

	CAS(8e,6o)	CAS(10e,8o)	CAS(12e,10o)	CAS(12e,12o)
$d_{O\text{-}O,S}$ (Å)	1.22	1.23	1.23	1.23
$d_{O\text{-}O,T}$ (Å)	1.21	1.22	1.22	1.22
$\Delta E_{S\text{-}T}$ (eV)	0.95	1.24	1.04	1.02

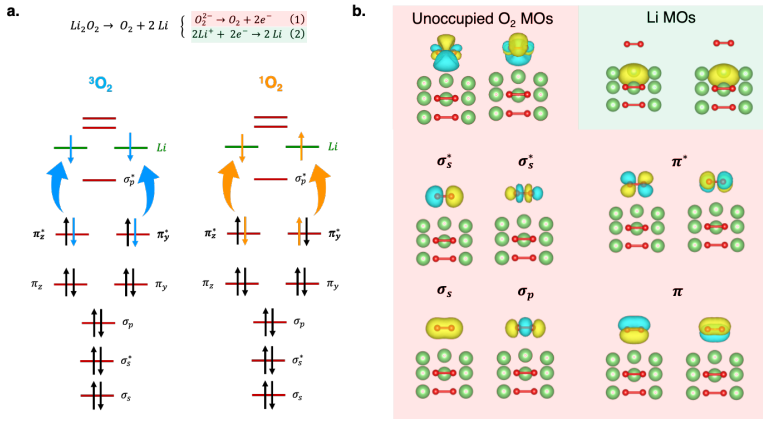

Figure 3.2.3 (a) *Li-air batteries charge process and schematic peroxide oxidation to $^3O_2$/$^1O_2$ and lithium reduction.* ***(b)*** *Orbitals in the active space CAS(14e,12o). Color code as Figure 3.2.1. Isodensity positive (yellow) and negative (cyan) values (0.05 a.u).*

Figure 3.2.4 shows the color energy maps of oxygen release triplet- and singlet-PESs by means of both periodic DFT and embedded-cluster CASPT2 approaches. We compared the PESs in the range 1.25Å-1.55Å and 1.0Å-2.5Å for $d_{O\text{-}O}$ and $d_{O\text{-}Surf}$, respectively. As found by DFT-PBE approach, on topmost of surface, the released molecule has the equilibrium bond length of the peroxide (1.55 Å), while increasing $d_{O\text{-}Surf}$, $d_{O\text{-}O}$ shrinks. Furthermore, at low $d_{O\text{-}Surf}$, the system preserves the total singlet spin multiplicity of the lithium peroxide surface.

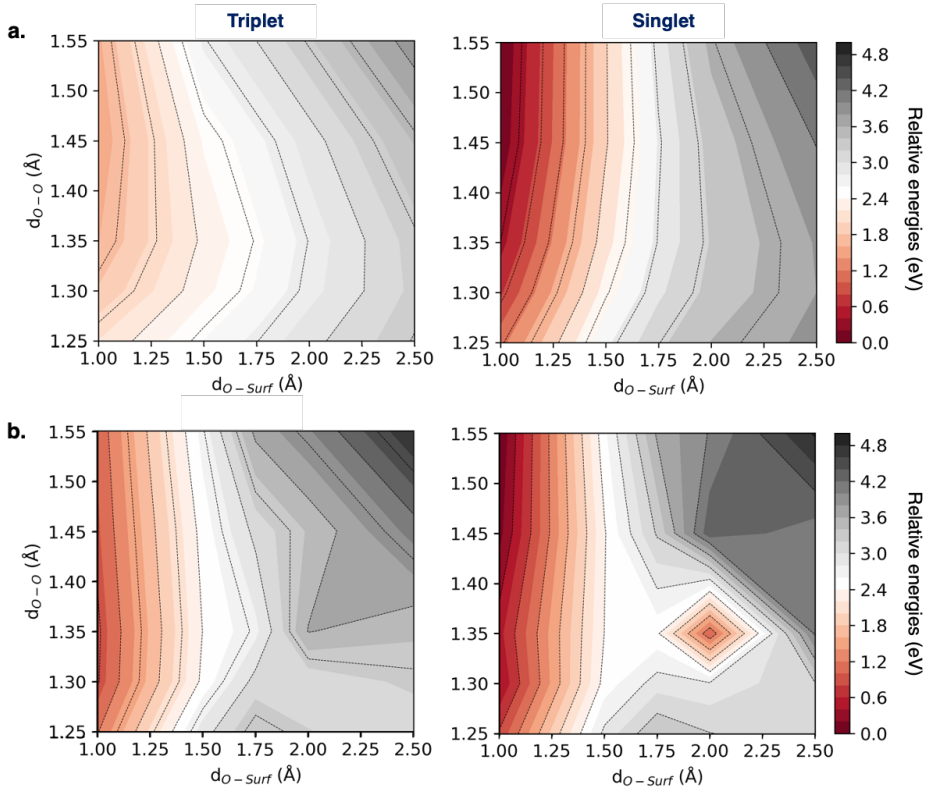

Figure 3.2.4 *Color Energy (eV) maps of O_2 release from periodic surface* ***(a)*** *at DFT-PBE level of theory and embedded-cluster* ***(b)*** *at CASPT2 level of theory. Triplet(left)/singlet(right) spin multiplicity. Relative energies are referred to* $E_{1.00,1.55}$.

Analysis of the O_2 π^* and Li orbitals electron occupation (Figure 3.2.5) reveals that the released molecule loses one electron, that occupied one Li orbital, at ~1.75Å from surface, with a decrease of bond length from 1.55Å to 1.35Å. These MOs occupancy and structural reorganization denote a one-electron oxidation of released molecule from peroxide to superoxide.

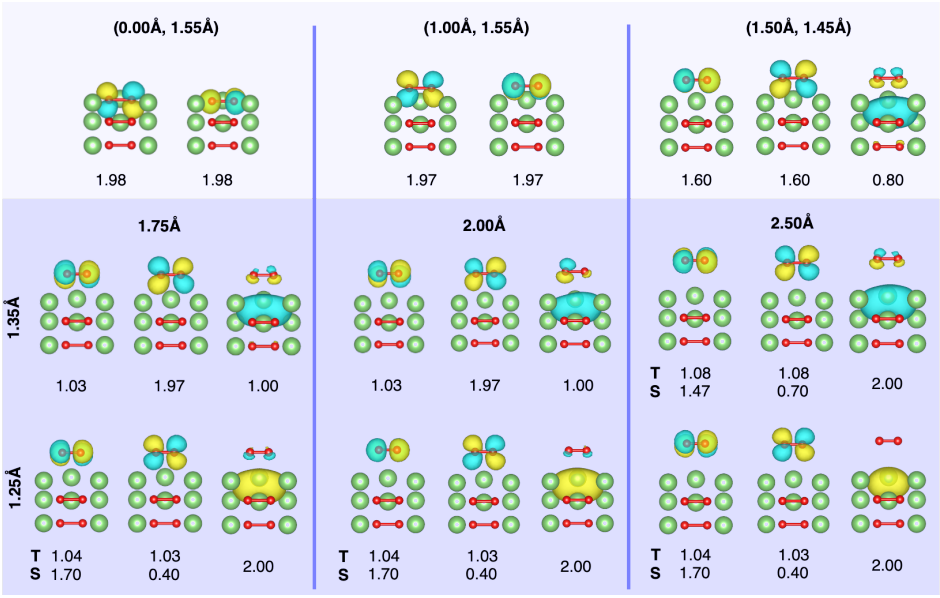

Figure 3.2.5 *Occupation of natural MOs in the active space CAS(14e,12o) at most noteworthy points ($d_{O\text{-}Surf}$,$d_{O\text{-}O}$) of CASPT2 S/T-PES. Color code as Figure 3.2.1 and 3.2.3*

Therefore, going from S-(0.0Å,1.55Å)/S-(1.0Å,1.55Å) to S-(1.75Å,1.35Å)/S-(2.0Å,1.35Å), a superoxide specie is formed. After this first electron oxidation, the oxygen release derives from further oxidation of superoxide specie. A second electron occupies the Li orbital or with a further decrease of $d_{O\text{-}O}$ from 1.35Å to 1.25Å at $d_{O\text{-}Surf}$ 1.75Å, 2.0Å and 2.5Å (Figure 3.2.5) or preserving $d_{O\text{-}O}$ of superoxide (1.35Å) at 2.5Å far from surface. Mulliken population analysis also

confirms the oxidation of release molecule to superoxide/dioxygen. The negative charge of peroxide specie changes when the molecule moves away from surface, exactly from -0.5 at (0.0Å,1.55Å) to -0.3 at (1.75Å,1.35Å)/(2.0Å,1.35Å) to 0.0 at (1.75Å,1.25Å)/ (2.0Å,1.25Å)/(2.5Å,1.25Å).

Overall, these findings suggest that both DFT-PBE and CASPT2 level of theory can predict the oxidation of peroxide to superoxide and then further oxidation to dioxygen. Nevertheless, the multireference approach reveals that the ground electronic state of the superoxide is an open-shell singlet diradical, as proven for MO_2^- trimer.[156] Plus, this level of theory predicts a local minimum of superoxide specie at S-(2.0Å,1.35Å), which is absent in DFT-PES. Such superoxide released occurs overcoming an energy barrier of ~2.40 eV, in close agreement with previous outcomes on molecular systems.[157]

To unveil the nature of this energy barrier, we also built up the PES for a cluster with a Li vacancy. Thus, the resulting system has a positive charge (+1) and double spin multiplicity, as the superoxide O_2^-. Figure 3.2.6 shows the resulting color energy maps by means of PBE and CASPT2 approaches. Again, we found a local minimum, which is absent in DFT-PES on Li-vacancy surface, but at lower $d_{O\text{-}Surf}$ (1.5Å,1.35Å) than stoichiometric system. Analysing the occupation of the O_2 π^* and Li MOs in the active space along the PES of defective cluster (Figure 3.2.7), we found that released molecule loses one electron, that occupies Li orbital, closer to the surface (at 1.5Å). As for the stoichiometric cluster, this oxidation occurs with a decrease of $d_{O\text{-}O}$ from 1.55Å to 1.35Å and overcoming an energy barrier of ~1.78 eV. Conversely, the second oxidation occurs at 2.0Å far from surface, with no bond reorganization. These findings reveal that lithium peroxide oxidation to superoxide can be favourite on defective surfaces, as already highlighted by previous ab-initio DFT study on Li_2O_2 surfaces.[163] As a result, the local minimum can be ascribed to formation of stable superoxide species by one-electron peroxide oxidation and oxidation of lithium peroxide.

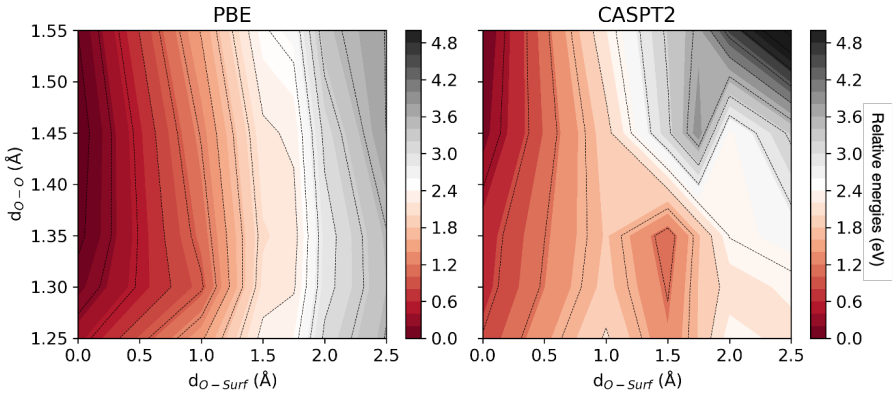

Figure 3.2.6 *Color Energy (eV) maps of O_2 release from periodic defective surface* ***(a)*** *at DFT-PBE level of theory and embedded- defective cluster* ***(b)*** *at CASPT2 level of theory. Triplet(left)/singlet(right) spin multiplicity. Relative energies are referred to* $E_{0.00,1.55}$.

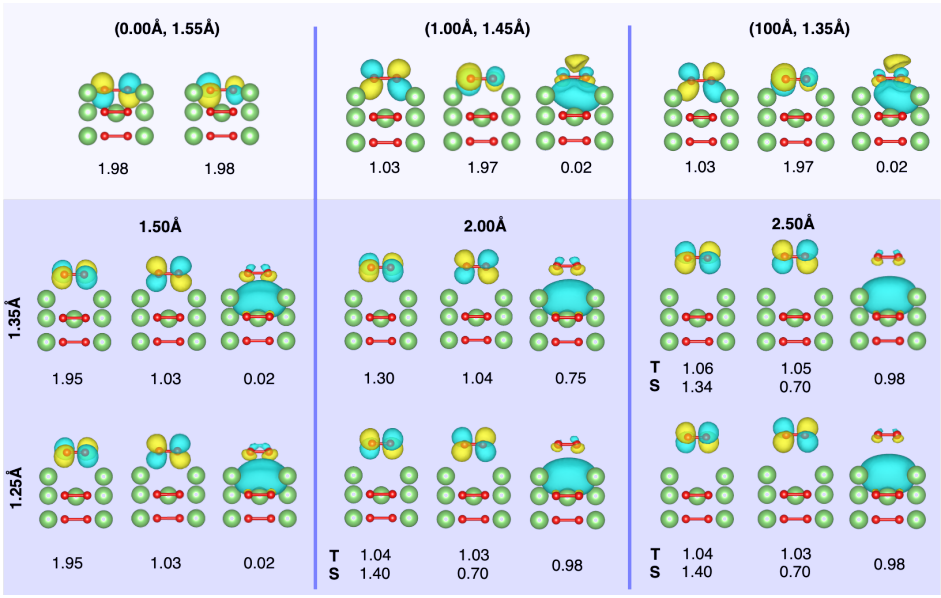

Figure 3.2.7 *Occupation of natural MOs in the active space CAS(14e,12o) at the most noteworthy point ($d_{O\text{-}Surf}$,$d_{O\text{-}O}$) of defective cluster at CASPT2 level of theory. Color code as Figure 3.2.1 and 3.2.3*

Further details analysis on energetic for singlet/triplet oxygen release from stochiometric and defective cluster are featured in Figure 3.2.8.

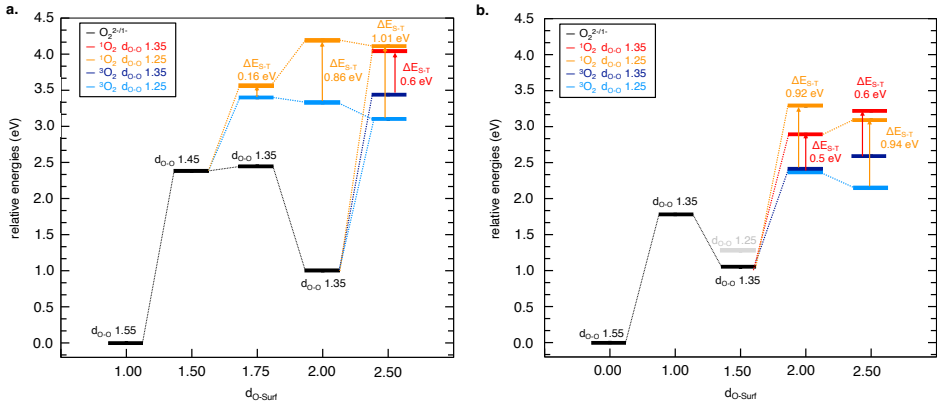

Figure 3.2.8 *Energetics of singlet/triplet O_2 release from stochiometric* ***(a)*** *and defective* ***(b)*** *cluster via CASPT2 embedded method. Relative energies are referred to $E_{1.0,1.55}$ and $E_{0.0,1.55}$, respectively. Color code: peroxide/superoxide (black), singlet oxygen with $d_{O\text{-}O}$ 1.35Å (red) and with $d_{O\text{-}O}$ 1.25Å (orange), triplet oxygen with $d_{O\text{-}O}$ 1.35Å (dark blue) and $d_{O\text{-}O}$ 1.25Å (light blue).*

From both stochiometric and defective cluster, we found that after formation of stable superoxide at 2.0Å and 1.5Å, respectively, further oxidation can occur or preserving the bond length of superoxide species (1.35Å) or with the structural reorganization (exactly, $d_{O\text{-}O}$ drops from 1.35Å to 1.25Å). On one hand, following the former oxidation of O_2^- without reorganization of bond length (at $d_{O\text{-}O}$ 1.35Å), the difference energy between $^1O_2$ and $^3O_2$ is ~0.60 (Figure 3.2.8). On the other hand, from both systems, the O_2^- oxidation with decrease of bond length is favourite with predominant release of $^3O_2$, which lies ~1.0 eV lower than $^1O_2$. Overall, oxidation of stable superoxide species drives quite low release of singlet dioxygen, which requires higher voltage than triplet state. Nevertheless, the energy difference between peroxide at S-(1.0Å,1.55Å) and

oxygen formed at 1.75Å ((1.75Å,1.25Å)) is ~3.5 eV for stochiometric embedded cluster. Therefore, high potential can induce the formation of unstable superoxide-like species at ~1.75Å and, after decrease of bond length oxygen molecule can be released. Following this path, $^1O_2$ lies only 0.16 eV above $^3O_2$ (Figure 3.2.8a). These results reveal that, upon Li-air battery charge, high voltage can drive the oxidation of peroxide to an unstable superoxide-like species, that can instantly be oxidate to O_2, releasing slight amount of singlet oxygen close to cathode.

In conclusion, our findings show that the electrostatic CASPT2 embedded method, that predicted a local minimum, absent in DFT approach, provides an in-depth description of the peroxide to superoxide oxidation at lithium peroxide interfaces. Such an approach also reveals that upon Li-air battery charge, the $^1O_2$ release at cathode interfaces can rely on relative stability of dissolved superoxide species, with the unstable superoxide as the main source of oxygen in the excited singlet state. Beyond that, this case of study paves the rote for further application of the embedded approaches to investigate complex molecule reactivity at electrode interface.

This case of study is object of a manuscript under revision.

3.3 Reactivity of Vinylene Carbonate at Lithium Metal Surface.

Introduction. Recently, the addiction of vinylene carbonate (VC) into common electrolytes, e.g. ethylene (EC) and diethyl/dimethyl (DEC/DMC) carbonate, has shown to form a stable SEI, limiting the uncontrolled electrolyte/electrode decomposition.[164–167] The peculiarity features of this additive can rely on ability to polymerize on Li metal surfaces, other than undergo reductive decomposition as the common electrolytes. Several experimental studies have shown that the SEI given by VC-containing electrolytes consist of poly(vinylene carbonate) (poly(VC)), mostly accompanied by CO_2 release, with rather low or even neglectable development of CO and C_2H_2.[164–166,168] A microscopic investigation also has revealed a mosaic-like SEI formation exhibiting Li_2O and Li_2CO_3 domains, probably due to VC-decomposition.[169] Despite these remarkable advances in morphology and structure of VC-derivative SEI, the mechanisms are far from trivial due to complexity of in situ observation at electrode-electrolyte interface upon battery cycle. To this aim, theoretical investigations can support the experimental efforts and give new insight on VC reactivity at atomistic level. DFT simulations at molecular level revealed that reductive cleavage of a vinyl ester C-O bond into the O-C=O moiety is kinetically the most likely scenario with respect to the breaking of vinyl ether C-O bond into the O-C=C moiety.[170–172] Nevertheless, the product of the latter, the •CH=CH-O-COO- radical anion, leading to overcome of an energy barrier of ~0.8 eV, has been regarded as the radical initiator toward VC polymerization. [170–172] In this framework, we aimed to analyze how the Li metal anode interface can affect the VC open-ring reductive reaction, which can be the starting point for further polymerization processes. Thus, we proposed an ab-initio approach to investigate the adsorption and dissociation of VC molecule on the most stable Li metal surface, the (001) lattice termination.[173] Noteworthy, periodic DFT simulation requires the use of hybrid functional for reliable description of the VC decomposition products with

localized electron density, but simultaneously the GGA functional is the best choice for metallic systems, e.g. Li metal surface, for which the former often fails.[14,174] To overcome this limitation of DFT methods in modelling localized interactions between reacting molecules and metal surfaces, the most suitable computational strategy is so the DFET (see Chapter 2 section 2.5.2 for further details).[67,68] Despite the lithium peroxide in 3.2, in this case we cannot use the simpler electrostatic embedding due to the unfeasibility into defining charge for Li metal atoms. Meanwhile, DFET approach allows to characterize the primary VC/Li metal interactions by the HSE06 hybrid functional, without losing accuracy on environment description, solving the unique embedding potential (V_{emb}) at PBE level of theory.[26,27] Note that to simplify the model and unveil the main effect of Li metal interfaces, in this first study via DFET of Li/VC interaction, we neglected the effect of solvent.

Models & computational details. We adopted a 4x4 supercell as structural model for the VC interfaced to Li(001) metal surface with 15 Å of vacuum along the c direction (Figure 3.3.1a**)**. The number of layers were selected by a convergence test on surface energy as function of thickness. Spin-polarized DFT calculations were performed within PBC by employing PW basis sets as implemented in the VASP.[158–160] We used the PBE functional with the D3 correction to account for van der Waals (vdW) forces at the interface.[26,40,175] Core electrons were described by PAW potentials obtained from the VASP repository,[82] with pseudo-wave functions expanded in a PW basis set with a kinetic energy of 600 eV, and 4x4x1 Monkhorst-Pack k-point mesh for sampling the Brillouin zone. The Methfessel-Paxton method of the first order with 0.2 eV smearing width was used for Li surface.[47] Geometry optimization was carried out by relaxing the atomic positions within the two topmost layers of the Li(001) slab until the maximum forces acting on each atom were below 30 meV/Å, while all the other coordinates were kept constant. For all the calculations, the convergence threshold for energy was set to 10^{-5} eV.

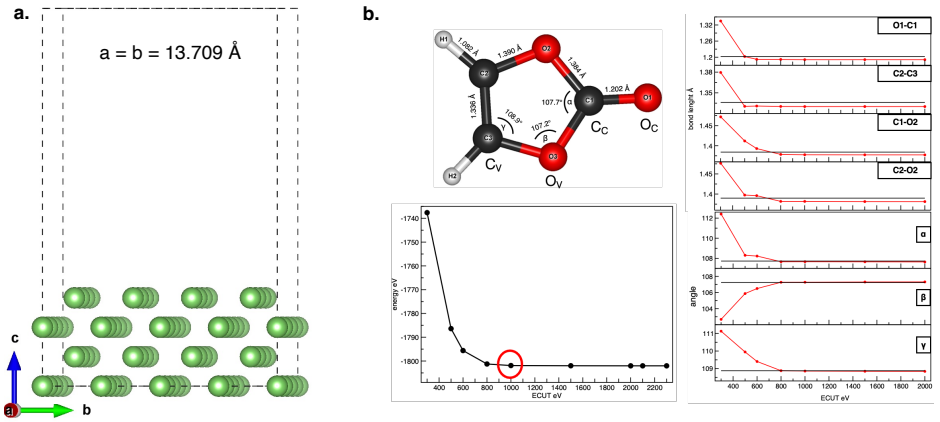

Figure 3.3.1 (a) *Structural model of Li (001) 4x4 4L-slab.* ***(b)*** *Minimum-energy structure of VC molecule obtained with VASP-based methods at the PBE-D3 level of theory; Convergence tests of kinetic energy cutoff on the VC total energy and structural parameters performed with ABINIT code (the black horizontal line are the experimental values from [176], ABINIT-derived values (red lines), VASP-derived values (black continuous lines)). Color code: O (red), C (black), H (white), Li(green).*

In the DFET approach, the HSE06 hybrid functional[31] was employed, and the HSE06-in-PBE energies within DFET were calculated as:

$$E = E^{PBE}_{Li-VC,PBC} - E^{PBE}_{Li-VC,cluster}[V_{emb}] + E^{HSE06}_{Li-VC,cluster}[V_{emb}] \quad (3.3.1)$$

where $E^{PBE}_{Li-VC,PBC}$ was the DFT-PBE energy of the system within PBC, while $E^{PBE}_{Li-VC,cluster}[V_{emb}]$ and $E^{HSE06}_{Li-VC,cluster}[V_{emb}]$ were the energies of the cluster system at, respectively, PBE and HSE06 level of theory, that were computed in a PBE-derived embedding potential, V_{emb}. The Kohn-Sham equations for clusters and environments were solved with a local DFET implementation within a modified ABINIT program that treats the embedding potential as an external potential.[177] This modified ABINIT version was provided by Professor Chen Huang at Florida State University. We used the NC pseudopotential[83] given by the fhi98PP program for all the atoms[178], and a kinetic energy cutoff of 1000 eV as determined from convergence tests on the total energy and the structural

parameters of VC molecule, placed in a 10Å-cubic cells. As showed in Figure 3.3.2b, the energy cutoff (ECUT) converges at 1000 eV. The structural parameters are also in good agreement with experimental values.[176]

VC adsorption at (001) Li metal surface. We first investigated the adsorption processes of VC molecules at (001) Li metal surface, which is the initial step for all possible further reactions toward the SEI formation. Based on previous theoretical studies on EC and PC/Li interactions[179,180], we analyzed several interaction modes by considering side, parallel and perpendicular arrangements of the VC molecule toward the Li surface. The side position exposing two oxygen atoms, named carbonyl and vinylic oxygen, O_C and O_V, towards the Li surface, leads to a stable bidentate configuration, the Li[O_CO_V] hereafter. Meanwhile, on one hand, the parallel arrangement leads to two tilted configurations, forming two or one Li-O bonds via the O_C atom, thus named as "bridged tilted" and "end-on" configurations, respectively (Li[O_C]$_{e,t}$ and Li[O_C]$_{b,t}$); on the other, the O_C of VC perpendicularly to the surface points towards the Li surface and binds either in an "bridged perpendicular" or "end-on" coordination modes (Li[O_C]$_{b,p}$ and Li[O_C]$_{e,p}$), according to the number of Li -O_C interaction. The resulting minimum energy geometry at PBE-D3 level of theory are featured in Figure 3.3.2 within the computed adsorption energies, as following:

$$E_{ads} = E_{VC-Li} - E_{Li} - E_{VC} \qquad (3.3.2)$$

where the E_{VC-Li}, E_{Li} and E_{VC} are the total energies of, respectively, the VC molecule adsorbed on Li(001) slab, the pristine Li(001) surface, and the isolated VC molecular systems, respectively.

Analysis of energetic trend reveals that the bidentate mode, Li[O_CO_V], is the most favorable interaction, followed by the two bridged states, Li[O_C]$_{b,t}$ and Li[O_C]$_{b,p}$, and then by the end-on ones, Li[O_C]$_{e,t}$ and Li[O_C]$_{e,p}$, in perfect agreement with EC and PC adsorption trend on Li metal surfaces.[179,180] Considering the number

of molecule-surface interactions, this trend relies on an extra stabilization occurring in the two-bond configurations compared to the one-bond ones.

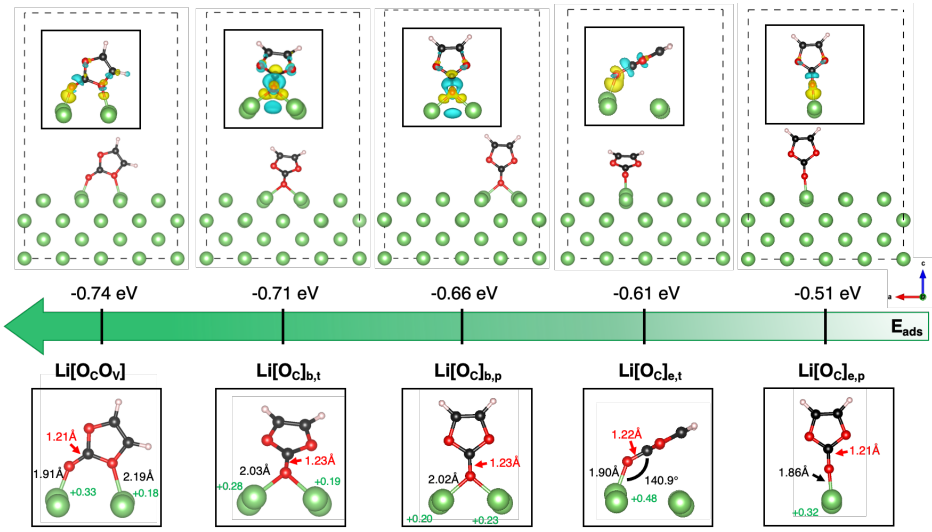

Figure 3.3.2 (top) *VC adsorption on Li metal: minimum-energy structures of VC-Li(001) adsorbed states in different configurations and corresponding adsorption energies calculated according to eq. 3.3.2 at the PBE-D3 level of theory. Insets: charge density difference plots (isosurface: 3 a.u.).* ***(bottom)*** *Relevant structural parameters: Li-O(VC) and C_C-O_C bond lengths and Li atom displacement along the z-axis. Color code: as in Figure 3.3.1, electron gain (yellow), electron loss (cyan).*

In all adsorption modes, we identified no significative variation of dihedral angle O_V,O_V-C=O, which can be representative of the possible pyramidalization at the C_C atom, when deviates from the ideal value of the planar geometry (180°) (Table 3.3.1). We only found a slight distortion (~5°) for the bidentate configurations Li[O_C]$_{b,t}$. Further structural analysis in Figure 3.3.2 highlights a displacement of Li atoms along the z-axis (~0.2-0.3) toward the VC molecule, accompanied by an elongation of the carbonyl C=O bond of ~0.02 Å. This slight surface and VC reorganization can rely on the quite strong Li-O interaction. The Li-O bond

lengths at the Li/VC interface (Figure 3.3.2) are comparable to those in the Li_2O solid phase, *i.e.*, 1.99 Å[181], suggesting that the VC adsorption on Li(001) surface exhibits an ionic-like nature. This finding is confirmed by the charge difference (CD) plot in Figure 3.3.2 and the positive/negative Bader charge variation on Li/O atoms ($\Delta q_{Li} > 0$ and $\Delta q_O < 0$ in Table 3.3.1), which reveals an electron depletion/accumulation at Li/VC side, in other words a charge transfer from surface to VC molecule. Plus, the negative charge variation on the whole VC molecule (Δq_{VC}) accounts for a reduction of the adsorbed VC with regard to the isolated molecule. We found the less negative Δq_{VC} and Δq_O for the lowest-energy bidentate $Li[O_CO_V]$ compared to the other two bridged $Li[O_C]_{b,t}$ and $Li[O_C]_{b,p}$ modes. Despite this lower electron transfer and reduction, the higher stability of this bidentate mode can rely on delocalization on the two oxygen atoms (O_C and O_V) bonded to the surface of transferred electron density. These findings highlight the direct relationship between the charge transfer degree and the thermodynamic stability of VC/Li interfaces, and also point to a key role for the Li metal surface in shifting the electron density on the VC molecule and prompting a VC-reduction.

Table 3.3.1 *The dihedral (O_V,O_V-C=O) angle for the VC molecule in each adsorption mode. Bader charge variation upon adsorption calculated on the whole VC molecule (Δq_{VC}), the Li (Δq_{Li}) and O (Δq_O) atoms involved in the Li-O bonds at the interface. The net charge on the oxygen atoms bonded to the surface in the final adsorbed state is also reported (q_O).*

	$Li[O_CO_V]$		$Li[O_C]_{b,t}$	$Li[O_C]_{b,p}$	$Li[O_C]_{e,t}$	$Li[O_C]_{e,p}$
Dihedral (O_V,O_V-C=O)	179.60°		174.67°	179.37°	179.64°	179.97°
Δq_{VC}	-0.26		-0.36	-0.31	-0.25	-0.19
Δq_{Li}	+0.86 (O_C)	+0.23 (O_V)	+0.70 / +0.87	+0.48 / +0.59	+1.13	+0.81
Δq_O	-0.13 (O_C)	-0.08 (O_V)	-0.28	-0.23	-0.14	-0.11
q_O	-1.24 (O_C)	-1.11 (O_V)	-1.34	-1.30	-1.26	-1.22

Following similar approaches employed for EC- and PC-Li systems [179,180], we calculated the projected Density of States (pDOS) to analyze the effect on the electronic structure, evaluating the energy gap between the LUMO and the Fermi energy ($E_{LUMO} - E_F$). Comparison of the pDOS of VC-Li interaction system with unbound one (VC molecule far away from the surface (*i.e.*, ~ 5 Å)) in Figure 3.3.3, reveals that the LUMO energy decreases with VC adsorption on Li(001) surface. We found a major effect on LUMO energy for the two bridged configurations, $Li[O_C]_{b,p}$ and $Li[O_C]_{b,t}$, where $\Delta E = E_{LUMO} - E_F = 0.66$ and 0.74 eV, respectively.

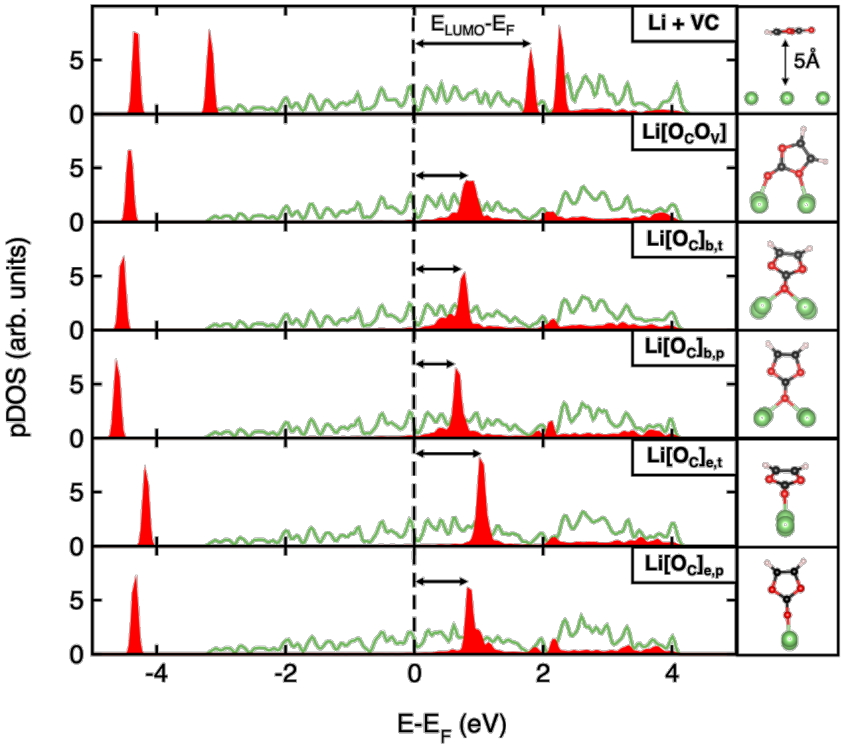

Figure 3.3.3 *Projected Density of States (pDOS) of the VC-adsorbed configurations on Li(001). Black arrows show the energy gap, $\Delta E = E_{LUMO} - E_F$. Color code: Li (green lines), VC molecule (red solid pattern). The corresponding structures are shown to the side for clarity.*

Because a lower $E_{LUMO} - E_F$ gap is a request for the SEI formation at the electrolyte/anode interface[182], these findings highlight that the two bidentate states can be the primary initiator for the reductive decomposition. Nevertheless, we selected only the $Li[O_C]_{b,t}$ for the following further study on open-ring reductive reaction due to the overall thermodynamic stability joined with the prominent surface reconstruction, slightly VC pyramidalization and enhanced charge transfer.

Reductive dissociation pathways towards VC decomposition. Following the previous studies on molecular systems[170–172], we considered both open-ring reductions along C_C-O_V or C_V-O_V bonds, leading to different products (Figure 3.3.4). Hereafter, we named the resulting first open-ring states as DISS(C_CO_V) and DISS(C_VO_V). These two states can undergo further decomposition with formation from the former of an acetylene molecule (C_2H_2) and lithium oxide cluster (Li_2O) accompanied by CO evolution; while from the latter of a lithium carbonate cluster (Li_2CO_3) with C_2H_2 release. Figure 3.3.4 shows the resulting minimum-energy structures of each reaction step with the corresponding energy formation from the previous one, computed as following:

$$\Delta E = E_n - E_{n-1} \qquad (3.3.3)$$

where E_n and E_{n-1} are the total energies of the nth and (n-1)th reaction intermediates along the corresponding pathway. Energetic analysis reveals that both mechanisms have overall largely favorable energy, exactly $\Delta E_{tot} = \Delta E_{3\text{-}0/2\text{-}0} = -5.29$ and -3.92 eV for C_C-O_V and C_V-O_V paths, respectively. Nevertheless, the final acetylene release contradicts the experimental evidence of low C_2H_2 amount[164–166], requiring further analysis.

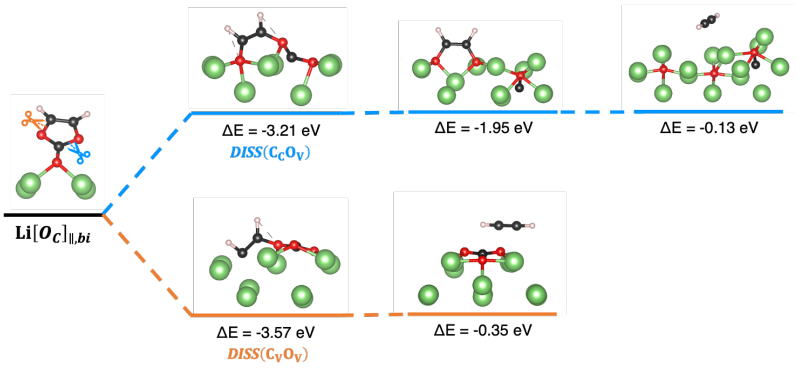

Figure 3.3.4 *Reductive VC ring-opening dissociation on Li(001) surface: minimum-energy structures along two possible reaction pathways obtained at PBE-D3 level of theory with their corresponding energetics, ΔE, calculated according to eq. 3.3.3. Color code as in Figure 3.3.1, C_C-O_V (light blue) and C_V-O_V cleavage (orange).*

On one hand, the structural analysis on the first dissociative state DISS(C_CO_V) and DISS(C_VO_V) in Figure 3.3.5 reveals a general displacement of Li atoms along the z axis of ~0.3-0.4 Å, accompanied with decrease of Li-O and elongation of VC bond lengths. On the other, CD plots and Bader charge analysis (Figure 3.3.5) highlight a charge transfer from surface to VC open ring products, with large negative charge variations localized on carbonyl (Δq = –1.97) and vinylic carbon atoms (Δq = –1.29) into DISS(C_CO_V) and DISS(C_VO_V), respectively. The latter state also presents a net negative charge (q_C = –0.85) on vinylic carbon atom, which can be related to a further reduction of the ˙CH=CH-O-COO- radical anion debated in the literature.[165,170,172] This high reactive specie could have a key role in several processes beyond the reductive ring-opening decomposition, which could also explain the low C_2H_2 release from SEI growth. For an in-depth understanding, we further investigated this reactive species formation proposing a mechanistic study of ring-opening reactions by means of the DFET, crucial to a reliable description of both Li metal environment and these species, which have a localized electron density.

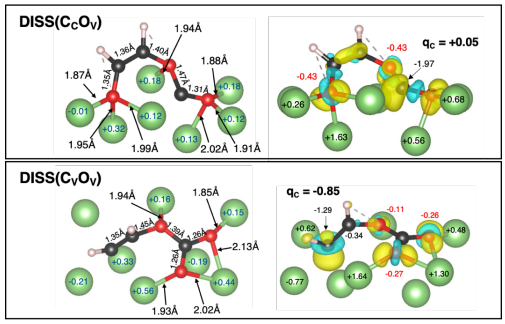

Figure 3.3.5 *Structural details of the first reaction intermediates, DISS(C_CO_V) and DISS(C_VO_V), Bader charge variation on Li (in black) and O (in red) atoms, Δq, and corresponding charge density difference plots (isosurface 1 meV/Å^3). The net charge on C_C and C_V carbon atoms is displayed in bold. Color code as in Figure 3.3.1*

VC-Li interaction by DFET: method validation. Before computing embedded-cluster energy at HSE06 level of theory, we validated the DFET approach, treating the cluster and environment at the DFT level with PBE functional (PBE-in-PBE). As a result, we should have the same cluster electron density as from periodic DFT-PBE calculation on the whole system, if the embedding potential was exact.[68] Plus, we solved the embedding potential (V_{emb}) for two clusters of different sizes (Figure 3.3.9a), given by partitioning of the 4x4 supercell of (001)-Li surface. In particular, we considered a small cluster, containing 8 Li atoms (*i.e.*, 8-Li), and an environment of 56 Li atoms; and a larger cluster, with 12 Li atoms (*i.e.*, 12-Li), and an environment of 52 Li atoms, also to choose the most accurate partition of the whole system. The Figure 3.3.6b shows the electron densities within embedded region projected on the b axis for the periodic system (black line), the 8-Li (red line) and 12-Li (orange line) clusters. We found a great agreement among the three projected electron densities within the explored b-axis range, with an average variation from the periodic density of 4x10^{-4} e$^-$/Å^3 and 3x10^{-4} e$^-$/Å^3 for the 8- and 12-Li clusters, respectively. This finding reveals no effect of cluster size on electronic

description of Li metal surface. Concerning the VC/Li interactive systems, we used the so-obtained V_{emb} from Li surface to perform DFET calculations on the two most favorite adsorption configurations, $Li[O_CO_V]$, $Li[O_C]_{b,t}$, and the two open-VC dissociated states, $DISS(C_CO_V)$ and $DISS(C_VO_V)$. We also solved the V_{emb} for the four VC_8-Li clusters and compared the projected electron densities with the other ones (green lines in Figure 3.3.6c). This latter case agrees better with periodic densities, but calculation of specific V_{emb} for each system is computational demanding. A great alternative is the V_{emb} from the 12-Li cluster, with a slight variation of $5x10^{-4}$ $e^-/Å^3$ from the periodic PBE density for all the explored states and low computational cost.

For these VC/Li interfaces, we, finaly, evaluated the relative energies of $DISS(C_CO_V)$ and $DISS(C_VO_V)$ with respect to $Li[O_C]_{b,t}$ as:

$$\Delta E = E_{DISS(C_CO_V)/DISS(C_VO_V)} - E_{Li[O_C]_{b,t}} \qquad (3.3.4)$$

and the adsorption/dissociation energies of the two adsorbed/dissociated states ($Li[O_CO_V]$, $Li[O_C]_{b,t}$ / $DISS(C_CO_V)$ and $DISS(C_VO_V)$) with respect to the unbound state, $E_{(Li+VC)}$, as follows:

$$E_{ads/dis} = E_{ads/diss-VC@Li} - E_{(Li+VC)} \qquad (3.3.5)$$

To unveil the accuracy of DFET on energetic of Li/VC interaction, all these computed relative energies were computed by means of periodic DFT within the PBE functional using both PAW and NC pseudopotentials, and from embedded cluster models at DFET-PBE level of theory ($E^{PBE}_{Li-VC,cluster}[V_{emb}]$) by using the embedding potential solved for 8-Li, 12-Li and VC_8-Li. The resulting values are plotted in Figure 3.3.6d. Again, the V_{emb} solved for the 12-Li clusters show the best agreement with periodic DFT-PBE results.

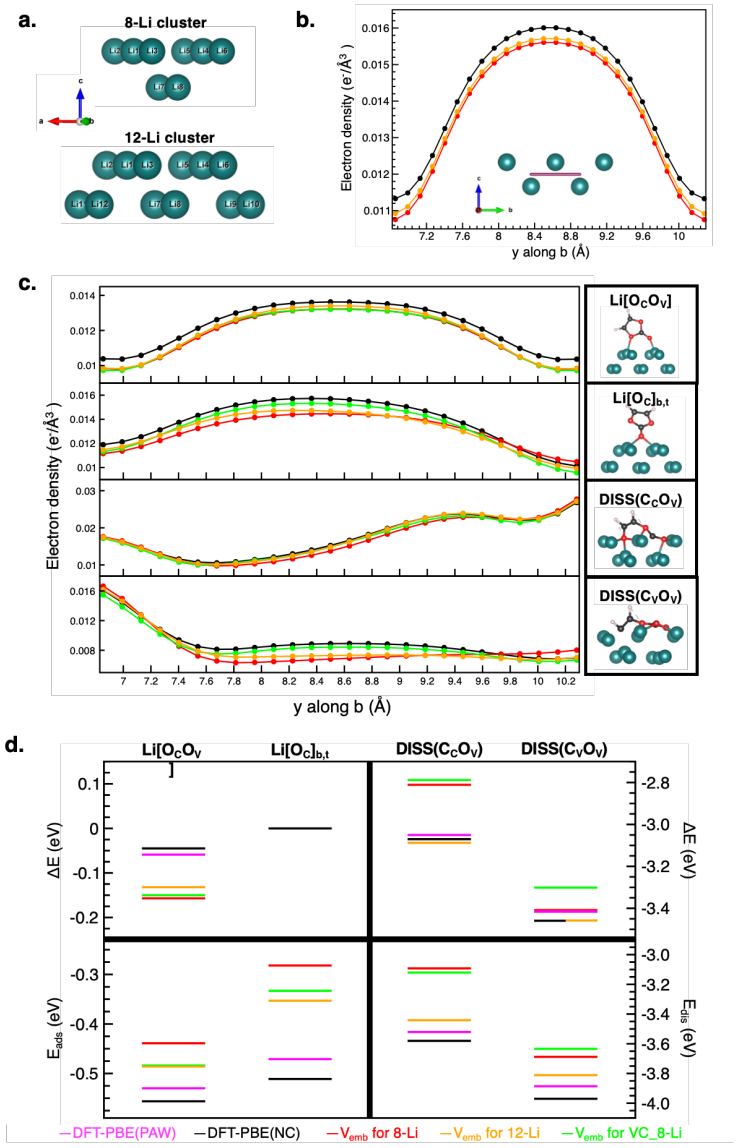

Figure 3.3.6 ***(a)*** *Different-sized clusters for Li surface. Plot of electron densities projected on b axis for Li surface* ***(b)*** *and for VC adsorbed/dissociated states on Li surface* ***(c)****: periodic DFT-PBE (black), 8-Li cluster DFET-PBE-in-PBE (red) and 12-Li cluster DFET-PBE-in-PBE (orange) using* V_{emb} *solved for corresponding Li surface clusters, green line refers to obtained with* V_{emb} *solved for each VC adsorbed/dissociated state on 8-Li.* ***(d)*** *Relative energies (top) and adsorption/dissociation energies (bottom) calculated according to equation 3.3.4 and 3.3.5.*

Overall, due to the optimal compromise between computational cost and electronic, energetic characterization of VC/Li interaction, the 12-Li cluster and the corresponding V_{emb} at PBE level of theory represents the best choice to further analysis on VC open-ring reaction by means of DFET approach.

VC-Li interaction by DFET: new insight on open-ring reaction. To our aim, we compared the different models and methods on the two most stable adsorbed configurations ($Li[O_CO_V]$, $Li[O_C]_{b,t}$) and the two possible open-VC dissociated states ($DISS(C_CO_V)$, $DISS(C_VO_V)$), evaluating the DFET energetics for adsorption/dissociation properties according to:

$$E_{ads/dis} = E_{ads/dis-VC@Li} - E_{Li} - E_{VC} \qquad (3.3.6)$$

where $E_{ads/dis-VC@Li}$ E_{Li} and E_{VC} are the total energies of the adsorbed/dissociated VC states at Li metal interface, the pristine Li surface, and the isolated VC molecule. Comparison of resulting values with DFT computed energies from PAW and NC pseudopotentials, employed in VASP and ABINIT, respectively, reveals that adsorption and dissociation energies drop at the HSE06-in-PBE level of theory, with no effect on the overall energy trend and higher stability of open-ring products (Table 3.3.2). At this level of theory, we also found a high negative Bader charge on vinylic carbon atom in $DISS(C_VO_V)$, confirming its localized anionic nature and the aforementioned promising reactivity.

Table 3.3.2 *The adsorption/dissociation energies, $E_{ads/diss}$, calculated according to eq. 3.3.6 for periodic (DFT-PBE(PAW) and DFT-PBE(NC)) and embedded cluster (DFET-HSE06-in-PBE) models of $Li[O_CO_V]$, $Li[O_C]_{b,t}$, $DISS(C_CO_V)$ and $DISS(C_VO_V)$.*

$E_{ads/dis}$ (eV)	$Li[O_CO_V]$	$Li[O_C]_{b,t}$	$DISS(C_CO_V)$	$DISS(C_VO_V)$
DFT-PBE(PAW)	-0.511	-0.556	-3.581	-3.970
DFT-PBE(NC)	-0.471	-0.530	-3.521	-3.886
DFET-HSE06-in-PBE	-0.266	-0.419	-3.227	-3.737

The ring-opening mechanisms were then further characterized by investigation of minimum energy paths (MEPs) via the Climbing Image-Nudged Elastic Band (CI-NEB) approach.[183] Starting from the considered adsorbed state $Li[O_C]_{b,t}$ (*i.e.*, i00) the MEPs toward the two final open-ring structure, $DISS(C_CO_V)$ or $DISS(C_VO_V)$, (*i.e.*, i06) consist of five intermediate states (i01-i05). All these states and corresponding energetic paths at DFT-PBE and DFET-HSE06-in-PBE levels of theory are featured in Figure 3.3.7.

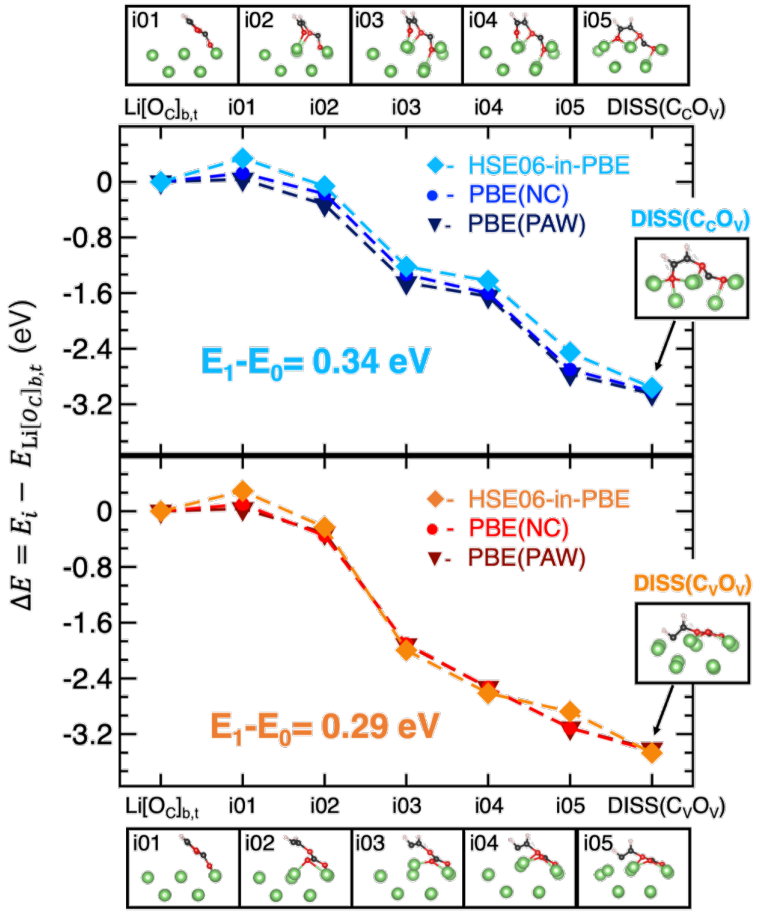

Figure 3.3.7 *Minimum energy paths (MEPs) for migration of VC molecule from its adsorbed to dissociated states, (top) DISS(C_CO_V) and (bottom) DISS(C_VO_V), computed via CI-NEB approach. The reaction intermediates (images i01-i05) are also displayed.*

The first remarkable result by means of the HSE06-in-PBE method is the prediction of an energy barrier of ~0.3 eV, not predicted with semi-local PBE-DFT approaches, associated with the formation of the high-energy i01 states along both MEPs.

To in-depth understanding of these energy barriers, we analyzed the structural variations and electronic behavior of these highest energy structures, *i.e.*, the i01-DISS(C_CO_V) and i01-DISS(C_VO_V) transition states (Figure 3.3.8a). The former analysis shows a decrease of O_V,O_V-C=O dihedral angle of ~38° and 30° for i01-DISS(C_CO_V) and i01-DISS(C_VO_V), respectively. Meanwhile, the Bader charge analysis on VC molecule (q_{VC}) merged with the spin density of the i00-ground state ($Li[O_C]_{b,t}$) and the two i01-transition states reveals that this structural reorganization occurs with a reduction of the VC molecule to a ketyl-like radical anion. These findings reveal that the energy barrier predicted by the HSE06-in-PBE approach can be ascribed to VC molecules pyramidalization at the carbonyl carbon atom at these i01-state and formation of radical anion. Among the two open-ring products, the i01-DISS(C_VO_V) shows a slightly lower structural and electronic reorganization, leading so to a slightly lower energy barrier. This result and the higher stability of the final open-ring product, DISS(C_VO_V) (Figure 3.3.5), can so suggest the cleavage of a vinyl ester C-O bond as slightly more accessible pathway, in line with previous works.[170,172] Nevertheless, we found a slightly lower barrier energies than those reported by Wang et al.[172] (~ 0.3 *vs.* 0.8 eV), suggesting that the Li metal surface, acting as an electron donor, has a key rule on VC open-ring reductive reactivity.

Detailed analysis of the Bader charge along the paths (Figure 3.3.9) shows a minor and more significant decrease of O_V and $C_{C/V}$ charges, respectively. In particular, we found more negative q_C values along the DISS(C_VO_V) than the DISS(C_CO_V), suggesting a more anionic nature of this open-ring product. The pDOS and spin density in Figure 3.3.8b also confirmed this result, highlighting the carbanion and radical nature of DISS(C_VO_V) and DISS(C_CO_V), respectively.

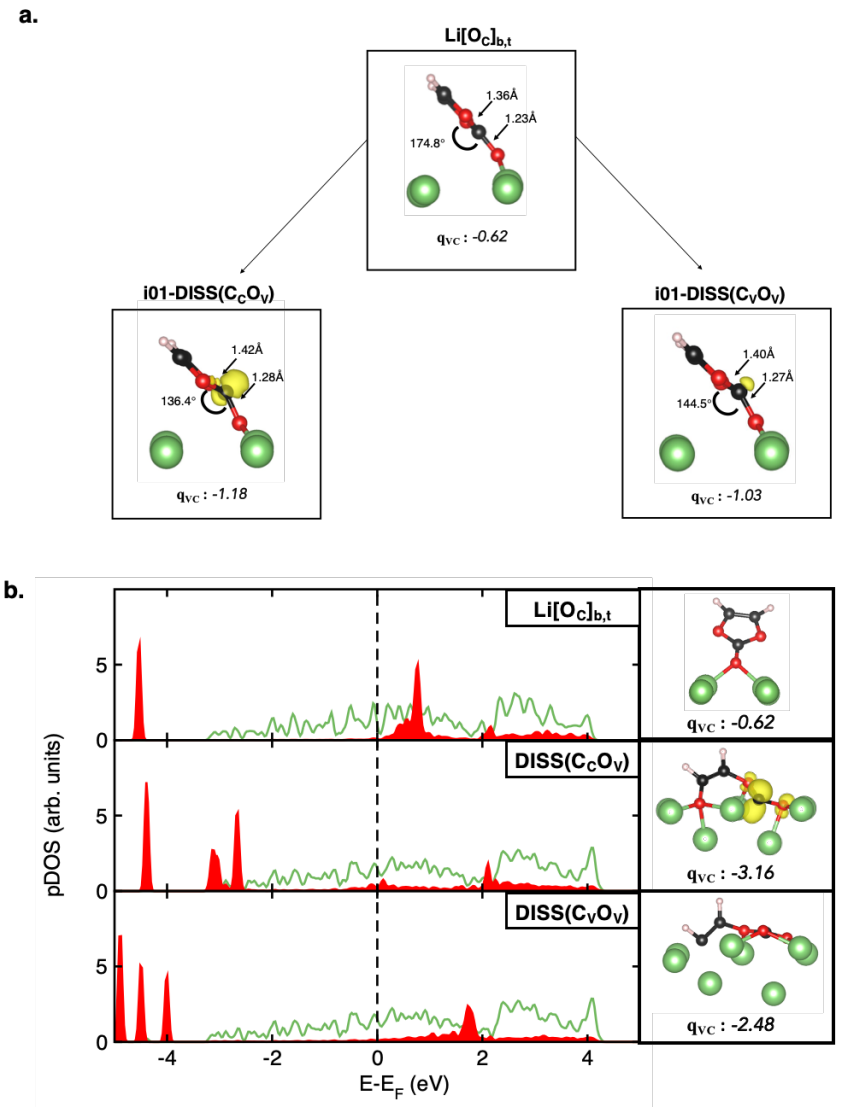

Figure 3.3.8 (a) *Structural details, spin density (isosurface 5×10^{-4} e^-/bohr^3) and total Bader charge on VC molecule of the i00- ($Li[O_C]_{b,t}$ adsorbed state) and i01-images ($DISS(C_CO_V)$ and $DISS(C_VO_V)$ dissociated states) along the MEPs.* ***(b)*** *Projected Density of States (pDOS), spin density (isosurface 0.05 e^-/bohr^3) and total Bader charge on VC molecule of the $Li[O_C]_{b,t}$, $DISS(C_CO_V)$ and $DISS(C_VO_V)$. Color code as in Figure 3.3.1*

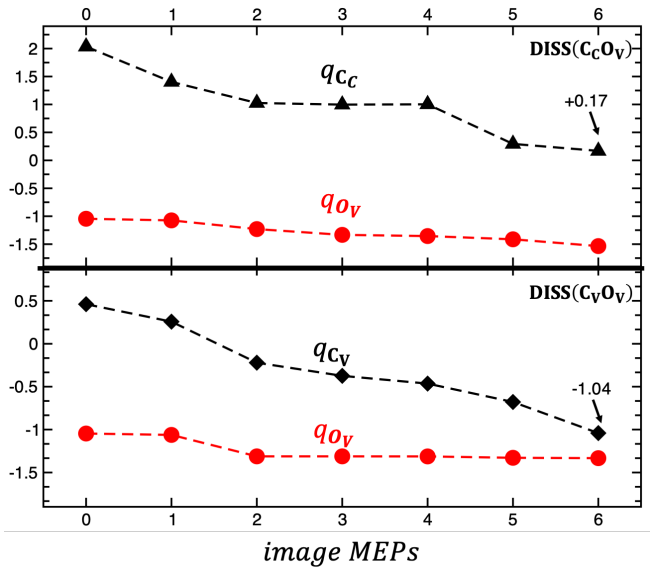

Figure 3.3.9 *Bader charges on the atoms involved in the dissociation processes, DISS(CcOv) (q_{C_C} and q_{O_V}) and DISS(CvOv) (q_{C_V} and q_{O_V}), along the MEPs obtained from CI-NEB calculations.*

To sum up, our findings via DFET approach reveal that further electron transfer from Li metal surface enhances the VC open-ring reductive reaction, which leads two products with different chemical nature and possible reactivity toward further reaction beyond the VC decomposition, e.g. polymerization. Among them, the cleavage at the vinyl ether C-O site (C_V-O_V) is found as the most likely scenario. Again, this case of study, as section 3.2, highlights the crucial rule of embedded approach to unveil molecule reactivity at electrode surface, and also the promising application of DFET method for metallic systems.

This work is object of a publication on Journal of Materials Chemistry A [184] and is reproduced with permission from Royal Society of Chemistry.

CHAPTER 4 –PHOTOELECTROCHEMICAL CELLS

Photoelectrochemical cells (PECs) have emerged as another promising strategy for storage of clean energy.[10,11] In these devices, via further electrochemical reaction at photoelectrocatalyst interfaces, harvested solar energy is converted into high-energy chemicals. This process, well-known as "artificial photosynthesis", has been mainly focusing on water splitting to H_2 as a renewable fuel (Figure 4.1a) or on the CO_2 reduction to liquid fuels with also the aim of CO_2 mitigation in the atmosphere (Figure 4.1b). [11]

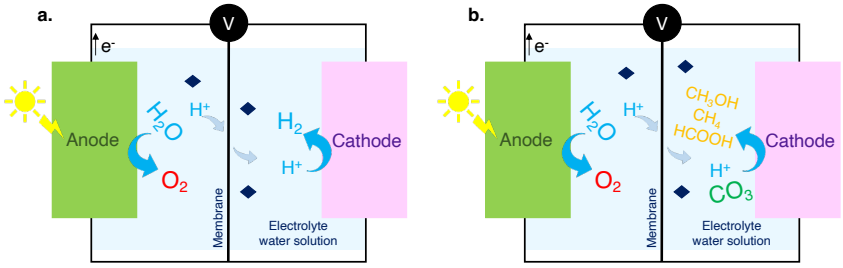

Figure 4.1 *Schematic representation of photoelectrochemical cells (PECs) based on* ***(a)*** *water splitting reaction ($H_2O \rightarrow O_2+H_2$) and* ***(b)*** *CO_2 reductive reaction to several fuels.*

For water-splitting devices targeting hydrogen production, nanostructured IrO_2 is a well-known highly efficient electrocatalyst toward the oxygen evolution reaction (OER).[185,186] The less active rutile phase of IrO_2 is known to be stable under the OER conditions, while its amorphous analogues exhibit higher activity for oxygen evolution, but lower stability. Nevertheless, the non-innocent role of the oxide sublattice can lead to destabilization of the oxide structure and result in dissolution of the catalyst.[185,187] Understanding the mechanisms driving the OER and catalyst degradation is, thus, essential for improving the performance of IrO_2 and IrO_2–based catalysts and for an efficient scale-up of these

technologies. The CO_2RR is, indeed, a thermodynamically non-selective process undergoing different products in aqueous electrolyte, thus the practical realization requires the development of catalysts with high selectivity toward a single product, at low overpotentials, while inhibiting the competing hydrogen evolution reaction. [11] Among the several potential photocatalysts, titania (TiO_2) has emerged as sustainable photo-electrode thanks to its low costs, stability and non-toxicity.[131,132] Nanostructured titania has demonstrated excellent performance in a wide range of photo-catalytic applications in aqueous solutions, including the photo-degradation of organic pollutants and water splitting.[131] After the finding in 1972 by Honda and Fushimi[188] that under sunlight a TiO_2 photoanode in an electrochemical cell causes the splitting of water into O_2 and H_2, the PECs based on water splitting and TiO_2 catalyst have attracted great interest and have been widely studied. Nevertheless, unveiling the mechanisms driving the water splitting and the CO_2 reductive reaction (CO_2RR) at catalyst interfaces still represents a grand challenge. Due to aqueous environment, elucidating the structure and reactivity of titania-water interfaces is also crucial for improving efficiency and selectivity of solar-to-fuel processes.

Despite the wide progresses on photocatalyst aqueous interfaces from ab-initio investigations, several aspects are still doubtful. Thus, in this chapter we address two issues concerning heterogeneous water/photocatalyst interface: the oxygen evolution from IrO_2 and the water dynamic on top of TiO_2 surface, suggesting computational strategies beyond the usual methods.

4.1 In-depth Understanding of Oxygen Evolution at Iridium Oxide Interfaces by Multireference Approach.

Introduction. At the experimental operating condition, the most exposed facet of IrO_2 nanoparticles (NPs), the (110), can be fully oxidated, forming a terminal Ir-Oxo species, with a radical character and electron deficiency.[185,189–191] These electrophilic species are susceptible to nucleophilic attack, providing the active sites to form the O−O bonds, essential for O_2 production.[192] In this framework, starting from these Ir-Oxo species, three mechanisms for the oxygen release are proposed (Scheme 4.1.1): the adsorbate evolving mechanism (AEM), the oxo-coupling mechanism (I2M) and lattice oxygen mechanism (LOM).[185,186] The AEM implies the formation of a hydroperoxide specie (Ir-OOH) and a proton-coupled electron transfer step (PCET) before O_2 release, while the O-O bond is formed by the coupling of two neighbour Ir-Oxo species or of an Ir-Oxo and lattice oxygen (O_{lat}) in the I2M and LOM, respectively.

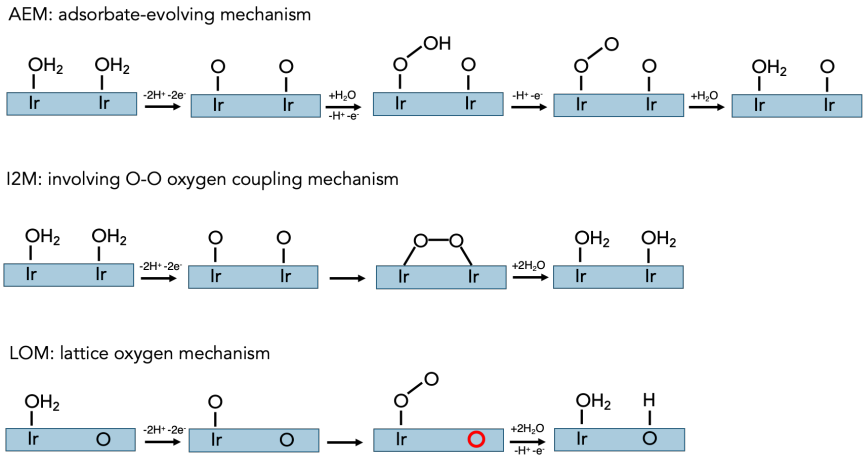

Schema 4.1.1. *Proposed mechanism for oxygen evolution from IrO_2. From top to bottom: adsorbate evolving mechanism (AEM), oxo-coupling mechanism (I2M) and lattice oxygen mechanism (LOM).*

The latter LOM mechanism appears to be less relevant, even though recent experiments highlight that the OER triggers an exchange of oxygen atoms in the first 2.5 nm of the rutile IrO_2 lattice.[193] If the LOM and I2M can compete with the AEM is still unclear. Ab-initio DFT study showed that the formation of metal vacancies due to catalyst dissolution can lead to lower OER overpotentials for the LOM, but defective IrO_2 is less LOM active than RuO_2 due to its greater stability under OER conditions.[194] Following the AEM path on top of the most stable (110) facet, a dynamic microkinetic model and DFT ab-initio study identified water dissociation as rate-determining step in AEM, but a quite similar energy barrier was found for the oxygen release.[191,195] This latter high barrier was first ascribed to the overbending of oxygen to surface given by the semi-local PBE functional and multireference nature of oxygen molecule and electrophilic Ir-Oxo species. Noteworthy, common functionals were shown to introduce significant errors into the overall energy for the ORR and OER[196] and a study of the binding O_2 to Heme revealed that the CASPT2 multireference method better reproduced the experimental binding energies, while GGA and hybrid functionals over- and under- bind the oxygen molecule, respectively. [197] As also reported for radical O–O coupling reaction in diferrate-mediated water oxidation, the DFT predicted a rather stabilized product, compared to the multireference approaches, affecting the characterization of the O_2 release mechanism.[198] All-in-all, unless the broad experimental and theoretical progress on OER paths at IrO_2 interfaces, an in-depth understanding of the high energy barrier to remove oxygen molecule is still required and multireference methods can allow to achieve a reliable description of both the electrophilic Ir-Oxo active site and of the oxygen triplet ground state. To this end, following the case of study in section 3.2 on singlet oxygen release from Li_2O_2, we proposed a systematic study via the electrostatic embedded approach at NEVPT2 level of theory.[22]

Model & computational details. To all the reaction intermediates upon O_2 release pathways, we adopted the 2x1 supercell of 5 layers – (110) surface (6.38

Å× 6.40 Å) with 15Å of vacuum along the c direction (Figure 4.1.1). All the geometry optimizations were performed by relaxing the atomic positions within the two topmost layers of surface until the maximum forces acting on each atom are below 30 meV/Å, while all the other coordinates were kept constant. We performed spin-polarized periodic DFT calculations as implemented in QE[138] at the PBE-D3(BJ) level of theory.[26,27,40] Core electrons were described by PAW potentials from QE repository[140], while the wave functions (augmented charge density) were expanded in PW with a 55 (220) Ry cutoff. We used the 2x2x1 k-point sampling based on the Monkhorst-Pack scheme and dipole correction as implemented in QE.[47,141] The Methfessel-Paxton method of the first order with 0.02 Ry smearing width was used due to metal character of IrO_2. Because the applied potential cannot affect the last O_2 evolution step[195], we considered no external field and study the OER at zero potential. For calculations at SC-NEVPT2 level of theory, we mimicked the extended crystal via a large point charge array (Ir +4 and O -2) by an electrostatic embedding, as implemented in ORCA.[199] We used the def2-TZVP basis set, while ECPs[66] were employed for Ir atoms bonded to the terminating O, but not included in the cluster.

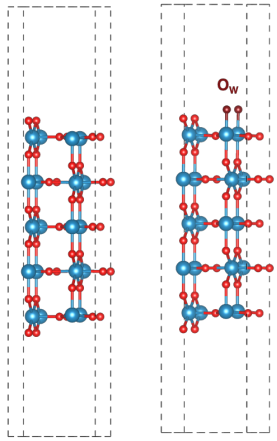

Figure 4.1.1 *The 2x1 supercell of stoichiometric 5L-(110) IrO_2 surface (left) and fully oxidated surface (right). Color code: Ir (light blue), O (red), water O_w (dark red).*

Oxygen release mechanisms via periodic DFT. We first reported a whole picture of the three mechanisms in Scheme 4.1.1 at PBE-D3(BJ) level of theory. All considered steps with corresponding energetics are shown in Figure 4.1.2. Hereafter, we enumerated the steps as (A/I/L)n, where A/I/L stays for AEM, I2M and LOM, respectively. For consistency, we considered the formation of oxygen-oxygen bond as step 2 in each path, so we named the first two steps of AEM, which are proton-coupled electron transfer steps (PCET), as A0 and A1. Because previous theoretical investigation revealed no further water molecule adsorption before full release of O_2, we considered as final step of the O_2 evolution, putting this molecule ~5Å far from surfaces. The step 0 is the (110)- IrO_2 surface with a full coverage of Ir-Oxo species (second step in Scheme 4.1.1, Figure 4.1.1), due to the well-known full oxidation of the iridium oxide facet occurring at the experimental operating condition[191], and high formation energy ((E_f) of -2.57 eV), computed as:

$$E_f = E_{(110)-Oxo} - E_{(110)} - 2E_{H2O} + 2E_{H2} \qquad (4.1.1)$$

where $E_{(110)-Oxo}$ and $E_{(110)}$ are the electronic energies for the fully oxidated and the stoichiometric (110) IrO_2 surfaces, while E_{H2O} and E_{H2} of water and hydrogen isolated molecules (i.e. inside a 10 Å-cubic cell so as to avoid intermolecular interactions), respectively.

After the formation of this electrophilic active sites (0), relative energies (E_r) of successive steps in Figure 4.1.2a are referred to this step zero, as follows:

$$E_r = E_n - E_{(110)-Oxo} (+ nE_{H2O} - nE_{H2}) \qquad (4.1.2)$$

where E_n is the electronic energies for the minimum-energy structure of step n. For step with no water adsorption (+H_2O) or proton-electron transfer (-H^+-e^-), the term in parentheses is equal to 0.

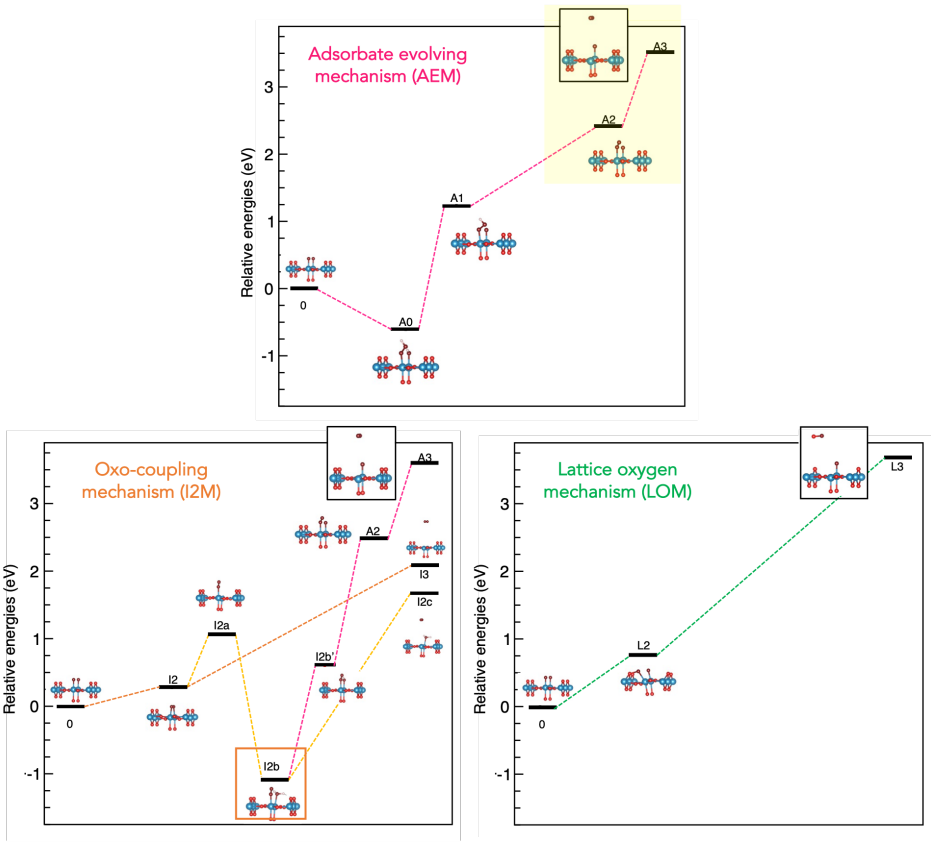

Figure 4.1.2 *Energetics and minimum-energy structures of the oxygen release paths on top of the full oxidized (110)-IrO_2 surface at PBE-D3(BJ) level of theory. Color code: AEM (magenta lines), I2M (orange/yellow lines), LOM (green lines).*

By looking at the first step of each mechanism (Figure 4.1.2), we found that a dissociative adsorption of water molecule on top of electrophilic species (A0 step) in AEM has a negative formation energy (-0.61 eV), while the Oxo-Oxo (I2 step) and Oxo-O_{lat} (L2 step) coupling require ~0.27 eV and ~0.76 eV, respectively. These results highlight that electron deficiency of Ir-Oxo species makes the oxygen susceptible to nucleophilic attack from another water molecule, that is dissociative adsorbed, favoring the adsorbate-evolving mechanism, consistent with previous theoretical studies. [191,192,194,200] As already

known, the two successive proton couple electron transfer from A0 to A1 and from A1 to A2 are the rate limited steps. Meanwhile, on one hand, the LOM is the most unlikely scenario, with the highest energy demand for oxygen release ($\Delta E_{L3-L2} \approx 2.93$ eV), probably due to great stability under OER conditions of IrO_2, as suggested by Zagalskaya et al. [194] On the other, the oxygen release via the oxo-coupling mechanism can follow different paths from the I2 state: by cleavage of both Ir-O_2 bonds (I3, orange path in Figure 4.1.2) or only one (I2a, yellow path in Figure 4.1.2). The latter involves less energy ($\Delta E_{I2a-I2} \approx 0.79$ eV vs $\Delta E_{I3-I2} \approx 1.81$ eV) and the saturation of Ir atom with further adsorption of H_2O, leading a local minimum, the I2b state (orange box in Figure 4.1.2). From this local minimum, the direct oxygen evolution (I2c, yellow path in Figure 4.1.2) is less favorite than the water oxidation (I2b' step). Following this path along the I2M, further water oxidation leads to the A2 state. These findings suggest that at high potential the I2M can result in the same last two steps of AEM (A2 and A3).

The A2 to A3 oxygen evolution takes place overcoming a high energy barrier of ~1.10 eV, in agreement with previous theoretical studies.[191] The released molecule at 5Å from surface (A3) is a triplet dioxygen, as shown by electronic characterizations in Figure 4.1.3. While the A2 state has a singlet spin multiplicity with total magnetization close to 0 (0.17 a.u.), the spin-resolved projected Density of States (pDOS) for the two states (Figure 4.1.3a) reveal difference between the two spin channels for the A3 state. This finding is confirmed by the spin density (Figure 4.1.3b) localized on O_2, that has a spin population of ~$2e^-$, and Ir-Oxo specie of ~$1e^-$, resulting in the whole system total magnetization of 3.26 a.u. Motivated by these results, we perform further analysis by means of method beyond standard DFT to achieving reliable description of released triplet dioxygen and radical species.

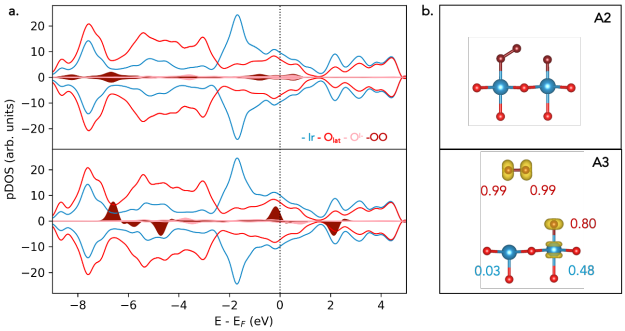

Figure 4.1.3 ***(a)*** *Spin-resolved projected density of state (pDOS) and* ***(b)*** *spin density with spin population of A2 and A3 states. Isosurface value 0.03 a.u. pDOS color code: Ir (blue),* O_{lat} *(red),* O_w *(dark red), Ir-Oxo (*O^L*) (pink). Atomic color code: as Figure 4.1.1*

Validate embedding method: cluster and environment size. Inspired by promising results in section 3.2, to unveil the nature of the energy barrier for oxygen release at (110)-IrO_2 surface, we proposed the computational strategy based on the electrostatic embedding approach.[62–64] Due to the high computational cost of multireference methods, we carve up small clusters, including the released O_2 molecule, preserving the interaction with the extended surface by mimicking the periodic surfaces with an extended point charge array. This is possible due to ionic-like nature of IrO_2 material. To validate our approach, we compared the periodic DFT and embedded clusters approach energy barrier of the last AEM step ($\Delta E_{A3\text{-}A2} = E_{A3}\text{-}E_{A2}$) at PBE-D3(BJ) level of theory. We also considered the effect of cluster and environment size (Figure 4.1.4a). Starting from the small cluster with only two Ir atoms, named Ir2, we can increase cluster size by adding two Ir atoms into the first layer. Addiction can be done along x or y direction, so that two cluster can be obtained: Ir4,x and Ir4,y. Further inclusion of one Ir atom on bottom layer of (110)-IrO_2 surface gives the Ir5,x and Ir5,y cluster, respectively. Finally, cluster Ir7 includes both 2 Ir atoms toward x and y direction and the one bottom Ir. Concerning the two charge fields (Figure 4.1.4b), one (Env-1) has ~3800 charges between Ir and O,

and the other (Env-2) is 10Å and 5Å larger in the x- and y- direction, respectively, so that the number of point charges is almost double up (~7100 charges). Table 4.1.1 reports the resulting energy barriers for the different-size clusters embedded in each charge array. Detailed analysis on $\Delta E_{A3\text{-}A2}$ reveals that the size of the charge array has a significative effect on the smallest Ir2 cluster. For this system, the energy barrier decreases of 0.66 eV when moving from the small to large array (Env-1 to Env-2), while the variation for the other clusters is utmost at ~0.2 eV. Overall, considering the large Env-2, the computed energy barriers for each cluster agree with previous periodic PBE-D3(BJ) result (PBC in Table 4.1.1). The minor error with periodic values are given by the largest cluster, Ir7, and Ir4,x cluster, followed by Ir2 and Ir5,y clusters.

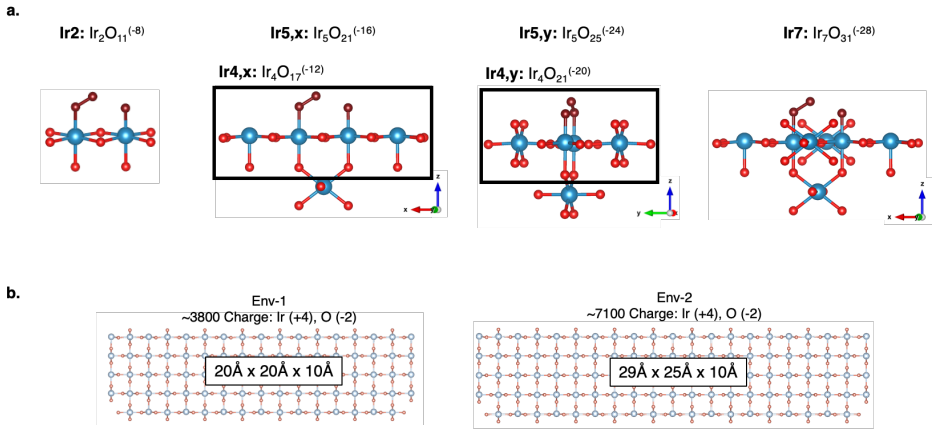

Figure 4.1.4 a. *Cluster and* ***b.*** *point charge array of different sizes carved from periodic (110)-IrO_2 surface. The clusters are named Ir(n), where n is the number of Ir atoms. Color code as Figure 4.1.1*

Table 4.1.1 *Energy difference ($\Delta E_{A3\text{-}A2}$) of clusters with the charge arrays in Figure 4.1.5*

$\Delta E_{A3\text{-}A2}$ (eV)	Ir2	Ir4,x	Ir4,y	Ir5,x	Ir5,y	Ir7	PBC
Env-1	1.67	0.95	1.22	1.13	1.05	1.20	1.10
Env-2	1.01	1.17	1.23	1.30	1.00	1.14	

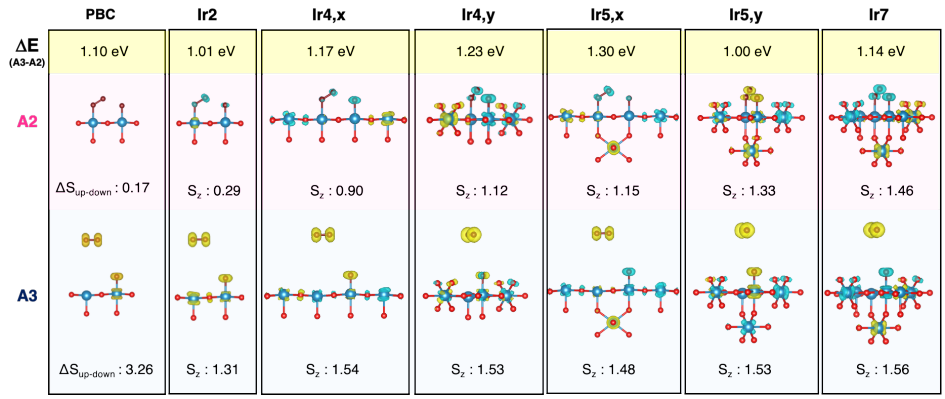

Figure 4.1.5 *Spin density with total magnetization ($\Delta S_{up\text{-}down}$) for periodic system (label: PBC) and with the spin number S_z for embedded clusters of A2 and A3 state at PBE-D3(BJ) level of theory. Isosurface 0.03 a.u. Color code: as Figure 4.1.2; spin up (yellow), spin down (cyan)*

Concerning the electronic structures for clusters in Env-2, Figure 4.1.5 shows the spin density, the total magnetization for periodic system (PBC), which is the difference between electron with spin up and down ($\Delta S_{up\text{-}down}$), and the spin number S_z for embedded clusters. Due to definition of these two quantities, the S_z should be half of periodic total magnetization. We found that the number of unpair electrons increases with cluster size by means of the embedded method. This further localization of Ir electrons can be ascribed to mimicking the IrO_2 metallic surface by clusters in a charge array and to use of localized basis set against delocalized PW in periodic DFT simulations. Noteworthy, the Ir2 cluster has S_{zA} of about 0.29 and 1.31 for A2 and A3, respectively, showing the best agreement with electronic structure of the periodic surface. We also computed the A3-A2 energy difference ($\Delta E_{A3\text{-}A2}$) by means of B3LYP-D3(BJ) functional. In close remark with previous calculation on small IrO_2 cluster model[191] and the well-known O_2 under-binding by hybrid functionall.[197], energy barriers (Figure 4.1.6) drop of ~0.7/0.8 eV for Ir2, Ir5,y and Ir7 clusters with regards of PBE-D3(BJ) values, while of ~0.5 eV for the Ir4,x cluster. Analysis of the spin density

(Figure 4.1.6) can explain this different behavior. By means of hybrid functional, less stable A3 state with a high spin state on Ir atoms is predict with Ir4,x cluster.

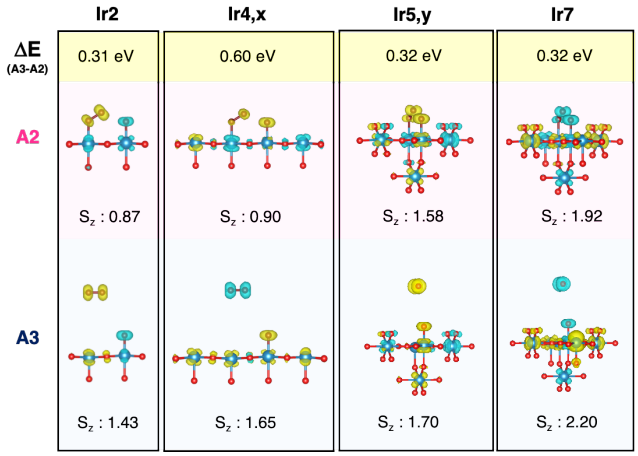

Figure 4.1.6 *Spin density with the spin number S_{zA} for embedded clusters of A2 and A3 state at B3LYP-3(BJ) level of theory. Isosurface 0.03 a.u. Color code: as Figure 4.1.2*

Overall, the smallest embedded- Ir2 gives the best compromise for both electronic and energetic description of (110)-IrO_2 surface, and also low computational demand. Thus, we chose this cluster Ir2 with Env-2 for further investigation on the oxygen evolution energy barrier at NEVPT2 level of theory.

NEVPT2 activation barrier of oxygen release. Concerning the orbitals in the active spaces:

- to describe the oxygen molecule, we considered the O_2 molecular orbitals (MOs). To clarify, the well-known orbital diagrams of O_2 MO are reported in Figure 4.1.7b.
- due to radical nature of Ir-Oxo[191] and inspired by previous theoretical study on Fe-O bound[198], we included 4 orbitals for Ir-Oxo specie, the $2\pi_{dp}$ and $2\pi^*_{dp}$ in Figure 4.1.7c. These orbitals are given by bound and

antibound π interaction of d_{xz}, d_{yz} of Ir atom with p_x, p_y of O. Plus, we found that when the oxygen molecule is bound to Ir atom (Ir_R), the Ir-Oxo π^*_{dpx} is combined with the π^*_z O_2 MO, forming the bound and antibound interactions, named $(\pi^*_{dpx}\pi^*_z)$ and $(\pi^*_{dpx}\pi^*_z)^*$ in Figure 4.1.7c.

- considering the A2 species, the π^*_y O_2 MO forms a π interaction with d_{yz} Ir_R orbital, leading to the two orbitals $\pi_{d\pi y}$,$\pi^*_{d\pi y}$ in Figure 4.1.7d.

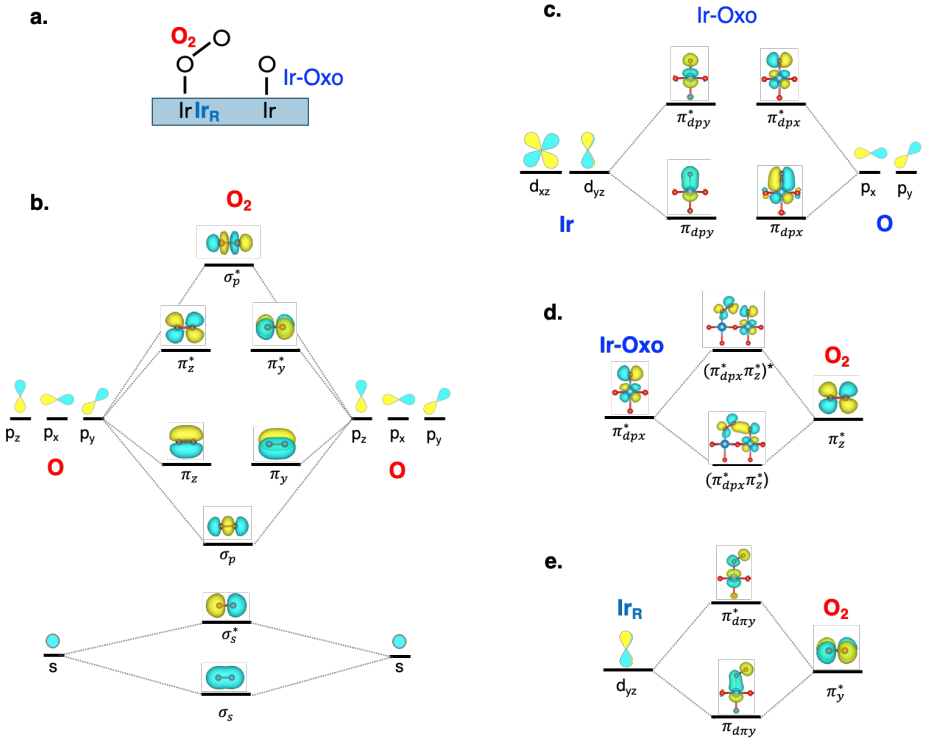

Figure 4.1.7 ***(a)*** *Schematic definition of Ir-Oxo, Ir_R and O_2. Orbital diagrams of* ***(b)*** *oxygen molecule,* ***(c)*** *interaction between the Ir d_{xz} and d_{yz} and p_xp_y O orbitals for Ir-Oxo species,* ***(d)*** *Ir-Oxo π^*_{dpx} with the π^*_z O_2 MO and for the € π^*_y O_2 MO with d_{yz} Ir_R orbital, leading to the two orbitals $\pi_{d\pi y}$,$\pi^*_{d\pi y}$. Color code: as Figure 4.1.2 Isodensity positive and negative values (0.03 a.u.) are in yellow and cyan, respectively.*

We started from a small active space with 4 electrons in the 4 orbitals, named CAS(4e,4o). This active space includes the $\pi_{d\pi y}$, $\pi^*_{d\pi y}$, $(\pi^*_{dpx}\pi^*_z)$ and $(\pi^*_{dpx}\pi^*_z)^*$ orbitals for the A2 state, while d_{yz} of Ir_R, π^*_y, π^*_z and π^*_{dpx} for A3. Then, we increased the active space arriving to the largest one with 18 electrons in 13 orbitals, CAS(18e,13o), given by the 4 ($2\pi_{dp}$ $2\pi^*_{dp}$) orbitals of Ir-Oxo specie, the 8 (σ_s $\sigma^*_s 2\pi$ $2\pi^*\sigma_p$ σ^*_p) molecular orbitals (MOs) of released O_2 and the d_{yz} orbital of Ir_R bound to O_2. In particular, we examined the following active spaces:

CAS(4e,4o), CAS(6e,6o), CAS(8e,7o), CAS(10e,8o), CAS(12e,9o), CAS(14e,11o) and CAS(18e,13o).

Analysis of occupation number of active orbitals reveals that A2 and A3 can have utmost four unpair electrons in the following orbitals: A2 in $\pi_{d\pi y}$, $\pi^*_{d\pi y}$, $(\pi^*_{dpx}\pi^*_z)$ and $(\pi^*_{dpx}\pi^*_z)^*$, while A3 in: the π^*_{dpx} of Ir-Oxo, the $2\pi^*$ of O_2 and the d_{yz} of Ir_R. This result suggests that A2 and A3 can be found in three possible states with singlet, triplet, and quintet spin multiplicity, indicated as ^{1}A2/3, ^{3}A2/3, ^{5}A2/3, respectively.

Figure 4.1.8 shows the CASSCF/NEVPT2 relative energy (E_{rel}) of A2 and A3 spin states for each active spaces. E_{rel}, is referred to the A2 singlet state (^{1}A2), as following:

$$E_{rel} = E_n - E_{1A2} \qquad (4.1.3)$$

where E_n and $E_{A2,S}$ are the energies of $^{3/5}$A2, $^{1/3/5}$A3 and ^{1}A2 states, respectively.

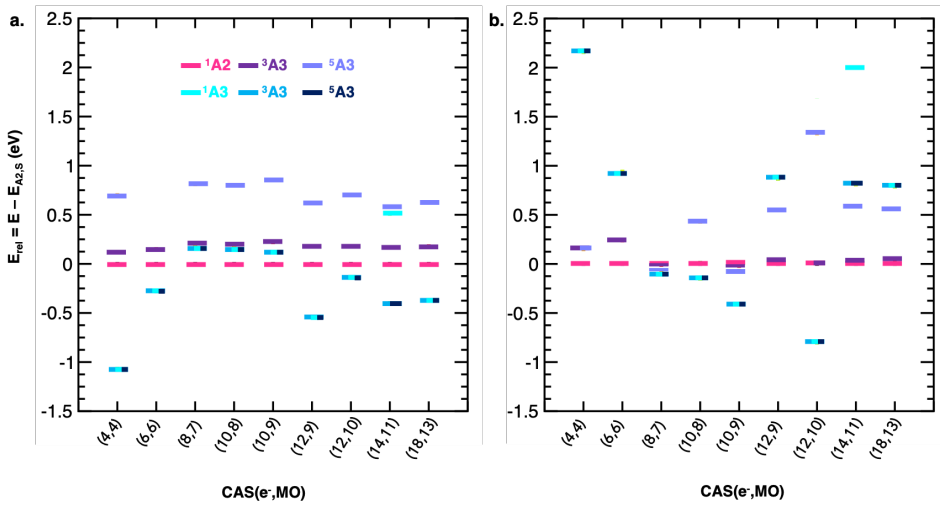

Figure 4.1.8 *Relative energies (eq. 4.1.3) of singlet, triplet and quintet A2 and A3 states at CASSCF (a) and NEVPT2 (b) level of theory. The active spaces are named CAS(n,m), where n and m are the number of electrons(e) and orbitals(o), respectively. Color code: ^{1}A2(magenta), ^{3}A2(violet), ^{5}A2(lilac), ^{1}A3 (cyan), ^{3}A3 (light blue) and ^{5}A3 (dark blue).*

Concerning A2, ^{3}A2 and ^{5}A2 lie ~0.2eV and ~0.6eV, respectively, at higher energies against ^{1}A2, which is the ground state at each active space. This difference between ^{1}A2 and ^{3}A2 decreases with larger active space at NEVPT2 level of theory, becoming quite degenerate (E_{rel} ~0.03eV). Meanwhile, the ^{1}A3, ^{3}A3 and ^{5}A3 are degenerate at both CASSCF/NEVPT2 levels of theory, except with the active space CAS(14e,11o), for which the singlet A3 state (^{1}A3) lies ~1.19 eV above $^{3/5}$A3. This energy difference can be ascribed to prediction of the first excited dioxygen state, the singlet close shell ($^1O_2$: $^1\Delta_g$), which lies exactly ~0.96eV above the triplet ground state ($^3O_2$: $^3\Sigma_g$).[162] Other than the energy difference, this result is confirmed by the MOs occupation numbers. Considering the triplet O_2, with two unpair electrons in π^* MOs, on one hand, the other two unpair electrons of Ir atom and Ir-Oxo can have opposite s_z values, leading to a singlet open shell surface and ^{3}A3 state. On the other hand, these two electrons can have both the same or opposite s_z value of the triplet O_2 unpair e^-, resulting

in the high and lower spin state ^{5}A3 and ^{1}A3, respectively (Figure 4.1.9a). These three states with triplet O_2 ^{5}A3, ^{3}A3 and ^{1}A3 are predicted to be degenerate via all active spaces. The only ^{1}A3 computed by CAS(14e,11o) presents one of oxygen π^* MOs double occupied, while the other has occupancy close to 0 (Figure 4.1.9b). Overall, the CAS(14e,11o) predict ^{1}A3 with singlet oxygen molecule in the excited $^1\Delta_g$ state, so that it lies at higher energy.

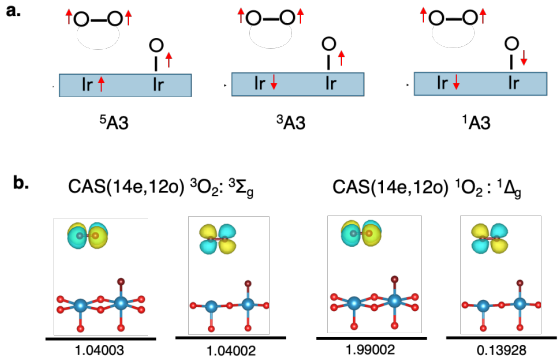

Figure 4.1.9 (a) *Possible ^{5}A3, ^{3}A3 and ^{1}A3 states with triplet oxygen molecule.* ***(b)*** *Occupation of the two O_2 π^* MOs for $^{5/3}$A3 and ^{1}A3 states with CAS(14e,11o).*

Considering the low energy states for A2 and A3, as found at DFT level of theory, the NEVPT2-embedded approach predicts A3 at higher energy, except for three active spaces CAS(8e,7o), CAS(10e,8o) and CAS(10e,9o), which show an opposite trend, with A3 more stable than A2 (Figure 4.1.8b). Detailed analysis of MOs in these three active spaces reveals that CAS(10e,8o) differs for A2 and A3, while the CAS(10e,9o) includes the two σ_p σ_p^* MOs and not the 2π MOs of O_2. Concerning the CAS(8e,7o), it includes more orbitals of Ir-Oxo species rather than oxygen molecule.

Overall, these results highlight that to reliable description of oxygen evolution, we need analogous active space for A2 and A3, which include more MOs of released oxygen molecule, in the exact order (Figure 4.1.7b).

Excluding the CAS(8e,7o), CAS(10e,8o) and CAS(10e,9o), active spaces, we found that the NEVPT2 energy barrier for oxygen release ((Figure 4.1.10a) converges to ~0.8 eV at large active spaces, CAS(14e,11o) and CAS(18e,13o). This energy barrier is only ~0.2 eV lower than DFT-PBE result. Nevertheless, considering the free energy correction from previous study ($\Delta G_{A3-A2} = 0.58\ eV\ vs\ \Delta E_{A3-A2} \approx 1.00\ eV$)[191], the multireference method predicts a free energy $\Delta G_{A3-A2} \approx 0.37\ eV$ closer to microkinetic value, based on experimental and theoretical studies ($\Delta G_{A3-A2} = 0.43\ eV$). [195]

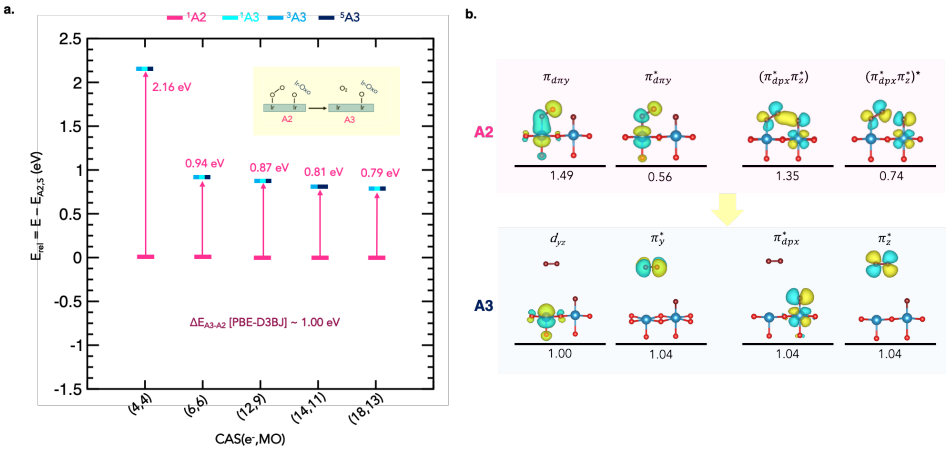

Figure 4.1.10 (a) *The energy barrier for oxygen release via NEVPT2-embedded methods with different active spaces CAS(n,m), where n and m are the number of electrons(e) and orbitals(o), respectively.* ***(b)*** *Occupation number of* $\pi_{d\pi y}$, $\pi^*_{d\pi y}$, $(\pi^*_{dpx}\pi^*_z)$ *and* $(\pi^*_{dpx}\pi^*_z)^*$ *orbitals in CAS(18e,13o).*

Analyzing the interaction between O_2 and IrO_2 surface in A2 state, given by the noteworthy $\pi_{d\pi y}$, $\pi^*_{d\pi y}$, $(\pi^*_{dpx}\pi^*_z)$ and $(\pi^*_{dpx}\pi^*_z)^*$ orbitals (Figure 4.1.10b) in all

the active spaces, we can suggest that the high energy barrier for evolving oxygen from IrO_2 surface can be due not only to the breaking of a π interaction between O_2 and Ir surface atom, and also of a further interaction with adjacent electrophilic Ir-Oxo species, that can be present at the experimental operating condition.[190,192,200] Different occupation and shape of the MOs are found at PBE-D3(BJ) level of theory, that could explain the slightly decrease of the energy barrier at NEVPT2 level of theory.

To conclude, our results reveal that the AEM and I2M can compete on top of fully oxidated (110)-IrO_2 surface, resulting in the same last two steps for the oxygen evolution. This oxygen release occurs after overcoming a high energy barrier, also predict by NEVPT2 approach, which also gives new insight on the nature of this barrier. Again, our findings highlight the potentialities of the electrostatic embedded approach for an in-depth understanding of complex localized phenomena at heterogeneous interfaces.

This case of study was carried out during a short-term scientific mission (STSM) at the research group of Professor Laura Gagliardi at University of Chicago, granted by the COST action 18234. The manuscript is under revision.

4.2 Dynamics of Water at TiO_2 Anatase (101) Interface at low Coverage.

Introduction. Great experimental and theoretical efforts have addressed the water reactivity on the most stable facet of anatase (TiO_2), the (101).[201–209] However, the water molecular *vs* dissociative adsorption is still under debate. At anatase interfaces, the coverage is defined as the number of water molecules per under-coordinated five-fold Ti surface species (Ti_{5C}) (θ = n° H_2O adsorbed / n° Ti_{5C}), so that a full water coverage (θ=1) consists of all the Ti_{5C} on topmost surface layer bound to a H_2O molecule, well-known as first water layer. An additional water layer, the second one, consists of water molecules that interact via H-bonding to the two-fold O_{2C} sites on the TiO_2 surface, with an average distance H···O_{2C} of ~1.9 Å.[201,202,204] After these two layers, no further interaction between water and anatase surface are found, but there are water-water interactions, that leads to bulk water far from the surface.[209] To unveil these liquid/solid interfaces at atomistic point of views, the molecular dynamic had a crucial rule. AIMD simulations based on DFT level of theory revealed that at low θ molecular adsorption is the most likely scenario, while dissociative water adsorption can be more favourite on oxygen-deficient surfaces, due to the increase basicity of the O_{2C} atoms.[202,209] These studies also highlighted that molecular adsorbed H_2O are coordinated with unsaturated Ti_{5C} sites via a dative bond (distances H_2O-Ti_{5C} ~2.3 Å), while the OH groups are covalently bound to Ti_{5C} (distances OH-Ti_{5C} ~1.8 Å). In the latter case, the dissociated H also binds the O_{2C} sites, thus forming two surface hydroxyl groups, the terminal hydroxyl on Ti_{5C} and a bridging hydroxyl, derived by protonation of O_{2C} (Scheme 4.2.1).[204]

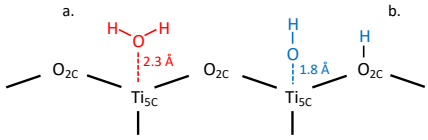

Scheme 4.2.1 *Schematic representations of* ***(a)*** *molecular (H_2O in red) and* ***(b)*** *dissociative (OH in blue) configurations at the anatase TiO_2 (101) surface.*

Noteworthy, all these theoretical simulations are at 160K, which is lowest temperature peak in the temperature-programmed desorption (TPD)[210], but spectra surface X-ray diffraction (SXRD)[211] and photoemission spectroscopy (XPS) data[212] have recently revealed mixed molecular adsorption and dissociation into the fist layer at TiO_2(101) anatase interfaces at room temperature. The former reveals that the topmost Ti_{5C} atoms bound 25% and 75% of H_2O and OH, respectively, while additional H_2O, from second to bulk layers, exhibited only further molecular adsorption above this mixt first layer.[211] In the latter, mixt first layer was detected at the stoichiometric TiO_2(101) interface in higher pressure of water (0.6−6.0 mbar), but not in ultrahigh vacuum UHV.[212] Therefore, these findings have undermined the well-accepted model of the water-stoichiometric anatase interface, calling for further investigation to unveil the elusive equilibrium between water adsorption and dissociation into the first monolayer on the pristine (101)-anatase surface. Recently atomistic investigations based on hybrid density functional and Reactive Force Field molecular dynamics have supported this dissociative adsorption. [213–216] These works have mainly addressed two interface structures, with only one water molecule and 25% of dissociated molecules. Nevertheless, experimental temperature dependence suggested that percentage of dissociated water molecules increases from 25% at 220 K to 75% at 300 K.[215] MD simulations have also revealed this variation with temperature, but never pushing forward the 50% of dissociated water molecules.[213] The complete characterization of

water/titania dynamics into the first layer thus requires further investigations, exploring all the possible hydroxylated TiO_2(101) surfaces (25%, 50%, 75% and 100%). In this framework, we studied the water adsorption and dissociation on the anatase TiO_2(101) surface at low (θ=0.25) and full (θ=1) coverage at 300K. To this aim, we proposed a computational strategy based on metadynamics simulation at SCC-DFTB level of theory, taking advantage from both approaches. The former method allowed to explore the water dissociative dynamics at the anatase TiO_2(101) stochiometric surface, despite the high free-energy barriers. Meanwhile, the DFTB reduced the computational demanding, but still provided reliable structural, electronic and energetic characterization of water-titania interface, in qualitative agreement with DFT ones.[208,217,218]

Model & computational details. The (101) anatase surface was modeled with 1x2 supercells of three-bilayers slab, including 20 Å of vacuum along c axis to avoid image interactions. The CP2K/Quickstep package[219] was used to perform static geometry optimizations and for the metadynamic simulations, combined with the PLUMED package.[220] A canonical sampling through velocity rescaling (CSVR) thermostat[221] with a target temperature of 300 K, a time constant of 0.05 ps was used to impose NVT conditions to the system, while a time step of 0.5 fs was used to ensure reversibility. The pre-equilibration simulation was run for 15 ps, then the systems were allowed to evolve for other 12 ns, to ensure convergence of FES. For these simulations, the Gaussian hills the sigma was 0.1 Å and 0.3 Å for dissociation at θ = 0.25, θ = 1 and adsorption processes, respectively. The height was 4.0 kJ/mol, while the biasfactor was 50 and the deposition rate 100 steps. The convergence of the electronic structure, and the forces were relaxed to less than 10^{-6} au with the Gamma-point k-sampling. For DFT study, we used the PBE functional[26,27] with Goedecker-Teter-Hutter (GTH) pseudopotentials for core electrons and DZVP as basis sets plus a PW with cutoff of 380 Ry. On selected geometries from metadynamic simulations, we also carried out single point energy calculations with the HSE06 hybrid functional.[31]

Water reactivity at anatase interface: method validation. To our aim, we selected the MATSCI parameterization of DFTB, which is widely employed in materials sciences and was also tested specifically for water-titania interface.[208,217,218] Before proceeding with dynamic simulations, we validated the accuracy of this parameter set against the DFT(PBE) and DFT(HSE06) by computing the dissociation reaction path for a single water molecule at the TiO_2(101) surface with the CI-NEB approach.[183] We addressed the dissociative path identifying 15 intermediate steps from molecular $(H_2O)_{ads}$ to dissociated (H-OH) adsorbed water. The Figure 4.2.1b shows the resulting energy variations (ΔE_{rel}), computed with respect to the lowest-energy state $(H_2O)_{ads}$, along the values of distances between surface oxygen O_{2C} and hydrogen water atom $d_{H\text{-}O2C}$ (Figure 4.2.1a). Comparing the minimum-energy geometries at DFTB(MATSCI) and DFT(PBE), we found a slight variation in the main distances between TiO_2 surface and water (Figure 4.2.1a). Both methods also predict the same energetic paths, with molecular adsorption state more favorite than the dissociative one (Figure 4.2.1b). On one hand, this latter state is quite less stable at DFT(HSE06) level of theory, leading to a slight increase of relative energy ΔE_{rel} (~0.6 eV) with respect to DFT(PBE) and DFTB(MATSCI) values (~0.5 eV). On the other, the activation energy for water dissociation is slightly higher for DFTB(MATSCI) level of theory (~0.2 eV) and DFT(HSE06) rather than for DFT(PBE). These results suggest that the DFTB(MATSCI) approach can reliably describe the structural and energetic features of water/titania interfaces. In particular, concerning the water dissociation energetic, such a level of theory agrees with the more accurate hybrid functional. Overall, DFTB(MATSCI) shows a balance between computational cost and accuracy, ensuring an efficient approach for further dynamic simulations. Plus, comparison of the adsorption and dissociation paths computed by NEB with DFTB(MATSCI) (Figure 4.2.1c) suggests that these two processes can occur at different time scales, due to the difference between the activation energies of

~0.2 eV. Thus, we can study individually the adsorption and dissociative processes, performing two distinct metadynamics simulations.

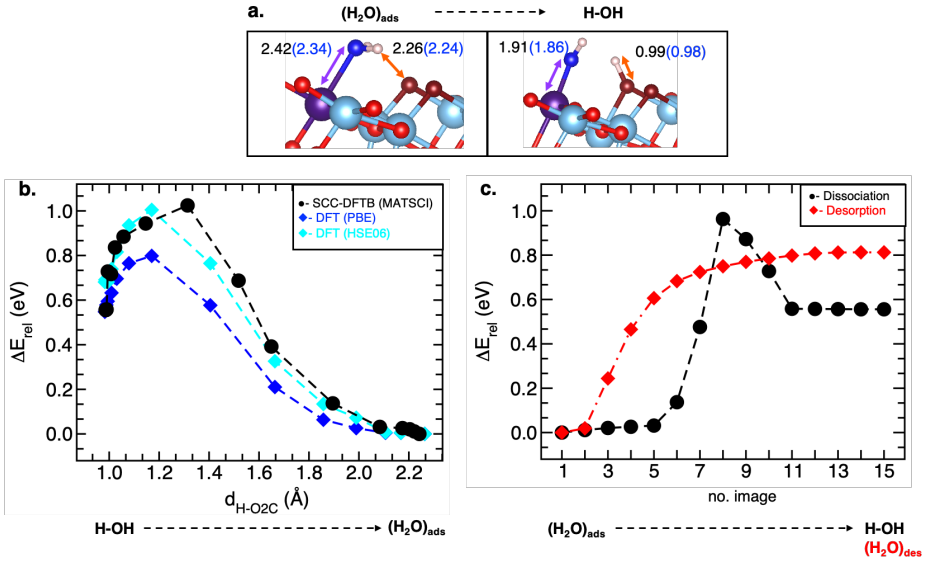

Figure 4.2.1 ***(a)*** *Molecular and dissociative adsorbed states. Color code: O (red), Ti (light blue), O_{2C} (dark red), Ti_{5C} (violet), water oxygen O_W (blu), H (white); the equilibrium distances (in Å) are reported for SCC-DFTB (MATSCI) (black font) and DFT(PBE) (blue font).* ***(b)*** *Dissociative reaction path computed with SCC-DFTB (MATSCI) (black circles), DFT(PBE) (blue diamonds) and DFT(HSE06) (cyan diamonds).* ***(c)*** *SCC-DFTB (MATSCI) results for desorption (red diamonds) and dissociation (black circles) reactions.*

Dynamics of water at anatase interface: choice of CVs. The collective variables (CVs) are the main significative parameters to set for metadynamic simulations (see Chapter 2 section 2.9.2 for further details). In our cases, the use of a rational switching function (with n parameter 8) implemented in PLUMED, allow to choose a generalized coordination number as CVs. On one hand, for the formation of first water adsorbed layer (Figure 4.2.2a), the most straightforward

CV, hereafter named n_d, is defined by the number of adsorbed but not dissociated water molecules onto the TiO_2(101) surface. In particular, we counted the number of molecules with distances from surface Ti_{5C} less than 3 Å (Figure 4.2.2b). This CV can so change from 0 to 4 when the 4 Ti_{5C} surface sites in our surface slab model bound the corresponding number of water molecules. In other words, CV=0 represents no adsorbed molecule, while CV=4 stays for the fully molecular adsorbed first water mono-layer. On the other, for the water dissociation at both low (θ=0.25) and full (θ=1) coverages, we should consider the O-H distances, exactly both the distance between water oxygen (O_W) and hydrogen atoms (d_1), and between surface oxygen O_{2C} and hydrogen water atoms (d_2) (Figure 4.2.2c). We so choose CVs, hereafter named n_{d1} and n_{d2}, which account for the d_1 and d_2 distances less than 1.3 Å, respectively. In this way, n_{d1} and n_{d2} can change from 2 to 1 and 0 to 1, respectively, when the H_2O molecule adsorbed but undissociated undergo a cleavage of the H-O bond.

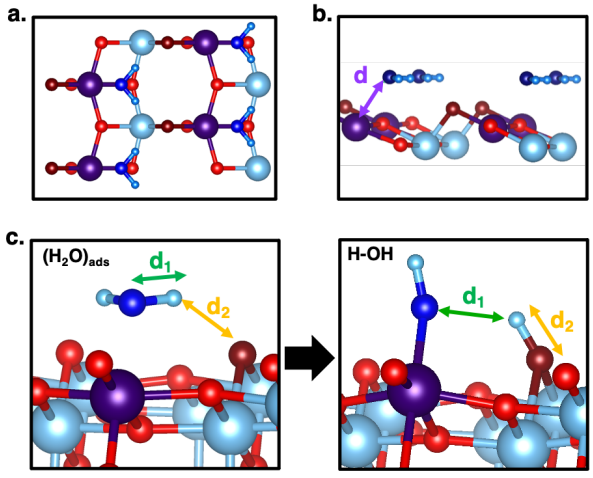

Figure 4.2.2 ***(a)*** *The full coverage (θ=1) view along c axis;* ***(b)*** *distance between Ti_{5C} and O_W (d violet arrow);* ***(c)*** *the distances between H with O_W (d_1 green arrow) and O_{2C} (d_2 orange arrow). Color code: as Figure 4.2.1*

Given the simplicity of this description, we can consider a simpler one-dimensional linear combination of these two variables ($c = 0.5\ n_{d1} - 0.5\ n_{d2}$), so that our CV c is 1 for molecular adsorption and 0 for dissociative. Considering the full coverage with a molecule for each of the Ti_{5C} ($\theta = 1$), the same CV c, goes from 0 (all dissociated) to 4 (no dissociated water). Noteworthy, assessment of transition barrier would require further investigation with more complex CV, accounting for both adsorption and dissociation processes due to possible interconversion process. However, these CVs can distinguish the different adsorbed and dissociated states, allowing to properly define the difference between states in the resulting distinctive free energy surfaces (FESs).

Dynamics of water at anatase interface: low & full coverage. At low coverage ($\theta = 0.25$), the analysis of the dissociative water FES confirms the NEB results that the undissociated adsorbed water is the lowest energy state (Figure 4.2.3). We found a $\Delta E_{diss\text{-}ads}$ of ~0.54 eV and an energy barrier for water dissociation of ~1.14 eV. Overall, these findings suggest the predominant molecular adsorption at the low coverage on the stoichiometric (101) anatase surface, in remarkable agreement with previous DFT calculations.[201,202,204,208] Further Mulliken population analysis at DFT(PBE) level of theory on several images along the resulting trajectory (Figure 4.2.3b) reveals an increase of positive and negative atomic charges on the H atoms that bound the surface (H_{Surf}) and on water oxygen atoms O_W (Figure 4.2.3c), respectively. This finding highlights a heterolytic dissociation of water at TiO_2(101) interface, consistent with water dissociation on other similar metal oxides.[222,223]

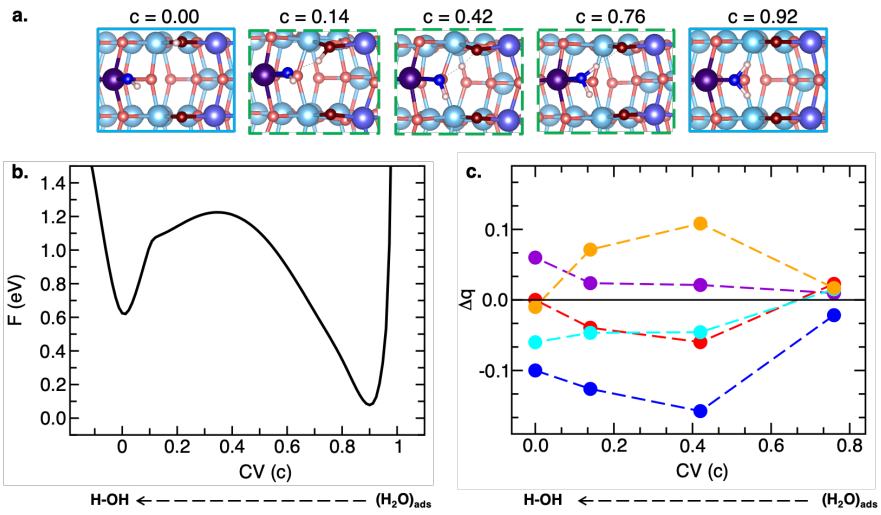

Figure 4.2.3 (a) *Selected image with values of the CV c from metadynamics dissociation trajectory at θ=0.25 (top view, color code: as Figure 4.2.1);* ***(b)*** *FES for dissociation process at θ=0.25;* ***(c)*** *Mulliken population analysis of atomic effective charges (q, at DFT-PBE level of theory) on Ti_{5C} (violet), O_{2C} (red), O_W (blue), H atom bond to O_W (light blue), H atom bond to O_{2C} (orange). Δq = [q at c] – [q at c = 0.92 $(H_2O)_{ads}$].*

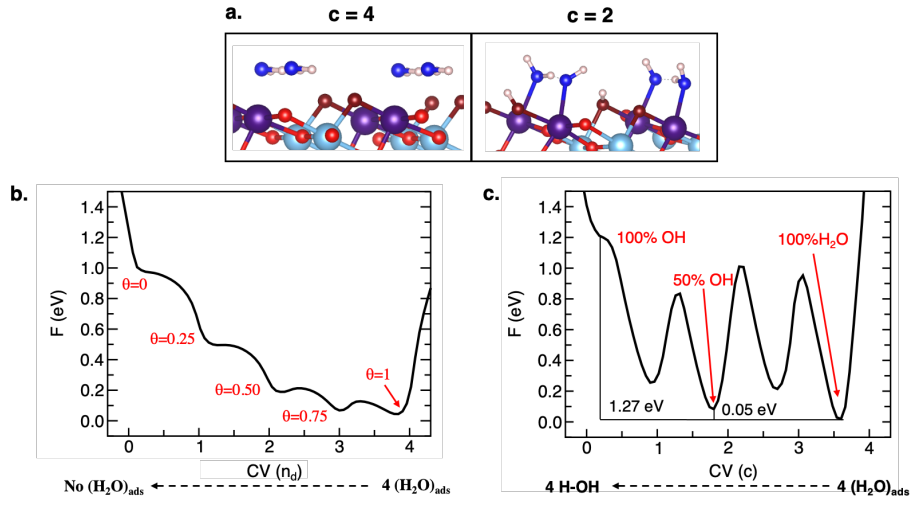

Figure 4.2.4 (a) *Selected image for CV c = 2 (mix state) and c = 4 (4 $(H_2O)_{ads}$);* ***(b)*** *FES for molecular adsorption process at coverage θ = 1;* ***(c)*** *FES for the dissociation process at coverage θ=1. Color code: as Figure 4.2.1*

Considering the adsorption of the first water layer (Figure 4.2.4a), despite the slight structural difference between DFTB(MATSCI) and DFT(PBE) minimum energy structure at c=4, we found the same adsorption energy per molecule (0.67 eV vs 0.69eV[201,202], respectively). Further analysis of FES in Figure 4.2.4c reveals a decrease of activation free energies for the adsorption of the second, third and fourth water molecules. The molecular adsorption toward the full coverage leads to a total adsorption free energy of ~0.9eV, in agreement with previous studies.[201] Therefore, these findings highlight the favorite molecular adsorption of the first water monolayer, with water molecules bound to the Ti_{5C} sites of the anatase (101) surface at room temperature. Nevertheless, a comparison of dissociative FESs at low (Figure 4.2.3b) and full coverage (Figure 4.2.4c) reveals that water dissociation is more likely to occur with an increase of the water molecules (θ=1). In this latter case, the FES shows a minimum at c≈4, which correspond to four molecular adsorbed water molecules, immediately followed by the dissociated state at c≈2 (50% of dissociated water), at only ~0.05 eV at higher energy. This finding suggests that the partial hydroxylated state is likely to be observed on the stoichiometric anatase interface at room temperature. Meanwhile, lying 0.20 eV and 1.27 eV above the minimum-energy state at c≈4 (Figure 4.2.4c), the other mixt dissociated states at c≈3 (25% dissociated molecule), c≈1 (75% dissociated molecule) and the full dissociated state (c=0) are the most demanding scenario. The strong stability of the mixed state (c≈2) can rely on the further h-bond interactions between water molecule and hydroxylate group (H_2O–OH) (Figure 4.2.4a), as previously highlighted for a hydroxylated surface.[214] Analyzing the variations of average Ti_{5C} – O_{2C} bond distances ($d_{Ti5C\text{-}O2C}$) along the trajectories of molecular adsorption and dissociative processes at full coverage (Figure 4.2.5), we also found that these structural parameters increase with water dissociation, going from 1.87 ± 0.02 Å (at CV c≈4) to 2.18 ± 0.05 Å (at CV c≈0), ascribable to protonation of O_{2C} sites. This elongation reaches the average $d_{Ti5C\text{-}O2C}$ value of 2.04Å at the partial

hydroxylated state (CV c≈2), in quantitative agreement with the SXRD data for the ultrathin water film on TiO_2(101) surface at room temperature.[211]

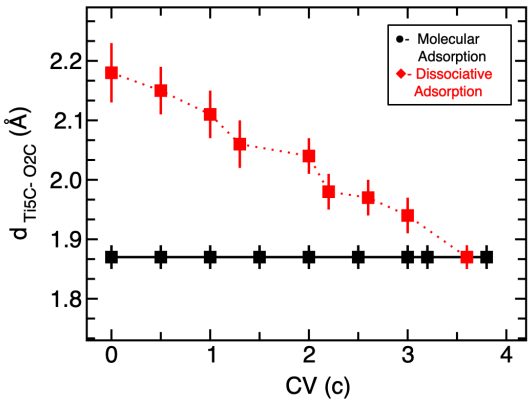

Figure 4.2.5 *The mean values of Ti_{5C} – O_{2C} distances ($d_{Ti5C\text{-}O2C}$, Å) vs CV (c) for dissociative (red line) and molecular (black line) adsorption metadynamics at θ = 1.*

To sum up, these findings suggest a non-zero probability to find partial hydroxylated stoichiometric TiO_2(101) surface at room temperature, in qualitative agreement with recent experimental and theoretical works.[211–216] The overcoming of dissociation barrier can rely on the strong Ti-O_W and H_2O-OH interactions. Despite the feasible partial hydroxylated structure of the aqueous titania interfaces, these new insights on water dynamics suggest the metadynamics simulations at DFTB level of theory, as a reliable and low computational demanding approach to dynamics of water/solid interfaces.

This case of study, object of a publication [224], was carried out during a short-term scientific mission (STSM) at the research group of Professor Michele Parrinello at Università della Svizzera Italiana (USI, Lugano), granted by the COST action 18234. Reprinted with permission from J. Phys. Chem. C 2022, 126, 37, 15752–15758. Copyright 2022 American Chemical Society.

CHAPTER 5 – PEROVSKITE SOLAR CELLS

Unlike batteries and PECs, solar cells are not based on chemical reactions, but convert sunlight radiations directly into electricity.[7,8] After light absorption, an electron is pushed to a higher energy state in the conduction band (CB) of the absorber material, and a hole is left in the valence band (VB), generating an electron-hole couple. The harvesting material is interfaced with charge transport layers (CTL) or materials (CTM), which are devoted to the extraction and collection of both photogenerated holes (HTL/M) and electrons (ETL/M).[8,15,225–227] Following this charge separation, the higher energy electron is moved toward electrodes and then in an external circuit (Figure 5.1a). Among these devices, the rapid development of perovskite solar cells (PSCs) has currently led to a power conversion efficiency (PCE) of 25.7%.[8,228] A perovskite is a material with a crystal structure having the formula ABX_3, where A and B are cations and X is generally an anion (e.g. halide I^-/Br^-) (Figure 5.1b).

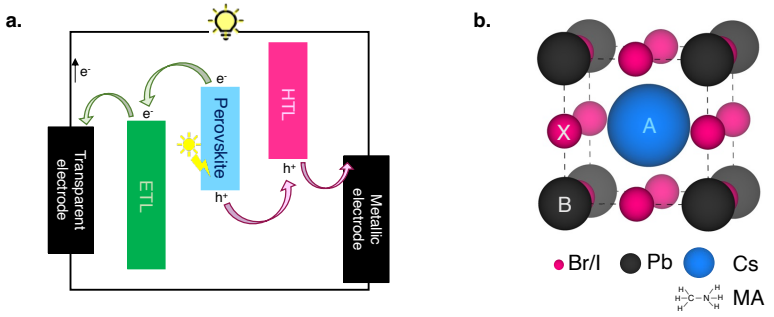

Figure 5.1 ***(a)*** *Schematic representation of a perovskite solar cell. After the generation of an electron (e^-)- hole (h^-) couple, these charges are transported through the electron (ETL) and hole (HTL) transport layers, respectively, to the collective electrodes (black box.)* ***(b)*** *Common structure of perovskite ABX_3. The specie A is Cs and the methylammonium (MA: CH_3NH_3) cations for $CsPbX_3$ and MAPI, respectively.*

The archetypal and most studied perovskites for PSCs are the inorganic $CsPbX_3$[229] and the hybrid methylammonium lead iodide $CH_3NH_3PbI_3$, well-known as MAPI (Figure 5.1b).[230] These lead-based perovskite materials have appealing features for solar cells, such as low exciton binding energy, high absorption coefficient, long charge carrier lifetimes.[8,9,228] However, on one hand, the huge potential of inorganic $CsPbX_3$ perovskite nanocrystals (NCs) is undermined by the ionic nature of the perovskite lattices, which induces highly dynamic bindings between the NC surface and organic capping ligands. On the other, degradation induced by environmental agents (heat, moisture, air) limits the whole PSCs stability.[8] These issues have so called for new passivation strategies of perovskite and the design of new harvesting materials. One well-established approach consists of the MAPI composition tuning, with addition of a larger formammidium (FA) cation and small amount of Cs and Br anions leading to the so-called triple cation configuration $Cs_{0.05}(MA_{0.17}FA_{0.83})_{0.95}Pb(I_{0.83}Br_{0.17})_3$, that has a wider bandgap and meets both efficiency and stability requirement.[231–233] Beyond the development of new harvesting material, high-performing CTLs is still demanding to achieve high-efficiency devices.[225,226,234,235] The process to produce electricity in these technologies depends, in fact, on the selective contacts between perovskite and the CTL. Engineering of new HTL aims to facilitate the charge transport to the electrodes, block undesired back hole-electron injection, and to improve the crystallinity of the perovskite. These challenges have also required study on band alignment between perovskite and CTLs and charge transfer kinetics.[226]

All-in-all, great experimental and theoretical efforts have focused on the optimization and design of new harvesting materials and CTLs, and strategy to improve the whole performances of the PSCs. In this framework, here, we propose suitable computational strategies for an in-depth understanding of the $CsPbBr_3$ perovskite passivation, charge transfer phenomena at MAPI and triple cation perovskites, and design of new HTLs.

5.1 Zwitterionic Ligand to Effective Passivation of $CsPbBr_3$ Nanocrystals

Introduction. Noteworthy progress to obtain stable Cs lead-based halide perovskite nanocrystals (CsLHP NCs) has been achieved by enhancing the binding of the capping ligands to the NC surface with passivating agents.[236] These capping ligands are frequently added to the NC surface via laborious post-synthetic methods due to their poor availability and/or low solubility under the reaction conditions.[237] Beyond the effective increase of optical features and/or stability of resulting NCs, these post-processes can generate them structural, morphological, and spectroscopic changes.[238] To overcome these problems, Roberto Grisorio (researcher at Politecnico di Bari) developed a straightforward synthetic procedure for passivating $CsPbBr_3$ NCs through in-situ formation of a zwitterionic ligand via the SN2 reaction between an additional halide source (8-bromooctanoic acid) and oleylamine (OLAm) used as the surfactant (Figure 5.1.1a). Together with Grisorio and other experimental groups, we demonstrated that the synergistic interaction between the dialkylammonium and carboxylate functions allows the adhesion of the resulting zwitterionic ligand to the NC surface (Figure 5.1.1b). As a result of this efficient passivation, the NCs are less soluble in nonpolar hexane, making them suitable for use in the purification phases. In the following section, we report our contribution to this case of study, while we refer the interested reader to the published work on the subject for further details on the synthesis and spectroscopic characterizations, carried out by Grisorio and the other experimental collaborators.[239] In order to shed light on the passivation mechanism and binding mode of the zwitterionic ligand, we carried out a computational study on the interface between the (010)-$CsPbBr_3$ surface and the zwitterionic ligand. Furthermore, because experiments highlighted that the polarity of used solvents affects the stability of the zwitterionic ligand with the NC surface, the effects of different solvents were

investigated by the efficient implicit solvation model MPE[99] in non-periodic calculations using large clusters.

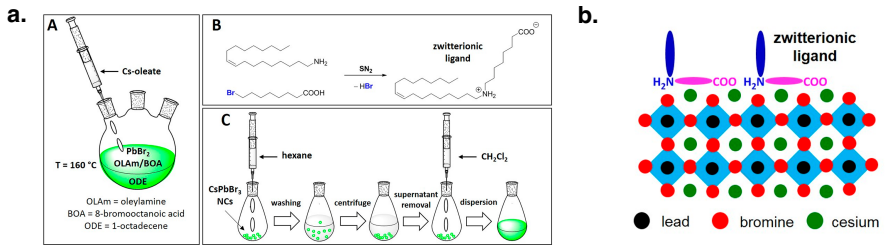

Figure 5.1.1 (a) *(A) Synthetic approach for $CsPbBr_3$ NCs. (B) The formation reaction of the zwitterionic ligand. (C) Schematization of the purification steps of the CsPbBr3 NCs, involving hexane as the washing solvent and DCM as the medium for storing the purified NCs dispersion. (**b**) Schematization of the passivation mode at the NCs CsBr-rich surface involving the zwitterionic ligand.*

Models & computational details. The zwitterionic ligand with the $CsPbBr_3$ NC surfaces was modelled by maintaining the original chain separation (C8) between the dialkylammonium and the carboxylate groups, while introducing a shorter group ($–C_3H_8$) to take into account the oleyl fragment (Figure 5.1.2a). Concerning the NCs, we performed periodic DFT simulation on slab model of (010)-$CsBrPb_3$ surface with 25Å of vacuum along the c direction (Figure 5.1.2c,d). To evaluate the adsorption behaviour and energetics of the molecules at different coverage (Θ) levels, two supercells with different surface areas of the xy plane were considered. The smallest supercell (highest Θ), with neighbouring image zwitterionic molecules ~13 Å/~5 Å apart in the xy plane, is a 5L 2×2 of the (010) unit cell (Figure 5.1.5c). The largest system is a 4L 4×4 supercell with a low Θ of molecules separated by ~ 29 Å/~ 20 Å (Figure 5.1.2d). The (2×2×1) and gamma point (1×1×1) k-point sampling schemes are applied to the small and large supercells, respectively. During geometry optimizations, atoms of the

bottom layers were fixed to their bulk-like positions, while the first layer and the adsorbed molecule were allowed to relax. Our relaxed structures present maximum forces acting on each atom below 0.05 eV/Å. We used the relaxed structures obtained in the smallest cell for single point calculations in the larger cell and cluster calculations. To account for the solvent effect with the MPE approach, we used non-periodic clusters containing atoms from a 4L 3.5×2.5 supercell rotated 45° (Figure 5.1.2e). In particular, we used the PBE[26,27] exchange-correlation functional, including Tkatchenko–Scheffler (TS) correction[41] accounting for van der Waals dispersion forces, as implemented in the Fritz Haber Institute ab initio molecular simulations (FHI-aims) code.[75] In the FHI-aims framework, we employed the light-tier1 basis set of NAO for each atom. For the self-consistency of the electron density, we employed a total energy criterion of 1×10^{-6} eV.

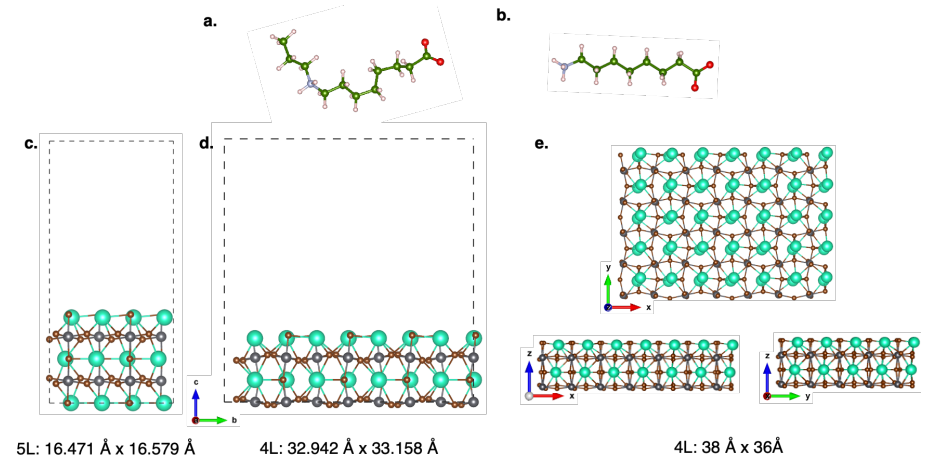

Figure 5.1.2: *Structural models of* ***(a)*** *Zwitterionic molecule,* ***(b)*** *primary amine,* ***(c)*** *5L 2x2 supercell slab of the CsPbBr3 (010) surface, used for high Θ periodic calculations in vacuum* ***(d)*** *4L 4x4 supercell slab of the CsPbBr3 (010) surface, used for low Θ periodic calculations in vacuum* ***(e)*** *4L cluster of the CsPbBr3 (010) surface used for low Θ non-periodic calculations in vacuum, hexane and DCM. Color legend: C (green), H (light pink), O (red), N (light blue), Cs (turquoise), Pb (grey) and Br (brown).*

Zwitterionic ligand at stoichiometric $CsPbBr_2$ interface. To unveil the adhesion feature of the synthesized ligand, we explored the interaction between ligand and stoichiometric perovskite surface by considering all possible bidentate and monodentate binding modes. The former, given by the synergistic interaction between the carboxylate (COO) and dialkylammonium (NH_2) functions, is called COO+NH_2. Meanwhile, monodentate modes through one of them are named COO or NH_2 from the anchoring group. Concerning the COO-binding, on one hand, we also examined a chelating mode in which the zwitterionic molecule is perpendicularly arranged to the NC surface and bound through the two oxygens of the carboxylate group to the cesium atom, denoted as COO(Bi). On the other, the possible opening of zwitterionic mode COO+NH_2 with extraction of Br anion gives the configuration COO(NH_2Br), where the NH_2 group binds the Br^- far from the surface. Finally, we investigated, for comparison, the anchoring mode of a suitable alkylammonium ligand modelling the OLAm surfactant (Figure 5.1.2b), denoted as NH_3. The carboxylate group was introduced to formally preserve charge neutrality. For all these interactions modes featured in Figure 5.1.3, we computed the binding energy as:

$$E_b = E_{surf\text{-}lig} - E_{surf} - E_{lig} \qquad (5.1.1)$$

where $E_{surf\text{-}lig}$, E_{surf} and E_{lig} are the total energies of, respectively, the ligand adsorbed on (010)-$CsPbBr_3$ surface, the pristine perovskite surface, and the isolated molecule.

Analysis of the binding energies by periodic DFT (Table 5.1.1) reveals strong adhesion of the bidentate zwitterionic ligand to the ideal $CsPbBr_3$ surface, mainly at high coverage (Θ). In particular, the bidentate mode COO+NH_2 is significantly more stable at both low and high Θ than the NH_3 binding and corresponding open configuration modes, in which binding occurs through only the carboxylate group via monodentate, COO, or chelated, COO(Bi) anchoring. This can be ascribed to the shorter binding distances between the COO group and surface Cs

cations (Figure 5.1.3a,b), exactly from ~3.0 Å in COO/COO(Bi) to ~2.8 Å in COO+NH_2. Although, monodentate binding with the dialkylammonium group, NH_2, is not stable at high Θ and relaxes to the COO+NH_2 bidentate mode configurations; at low Θ this configuration is quite less stable than COO+ NH_2. Finally, the lower energies of the opened zwitterionic binding (COO(NH_2Br) highlight the doubtful formation of Br anion extraction.

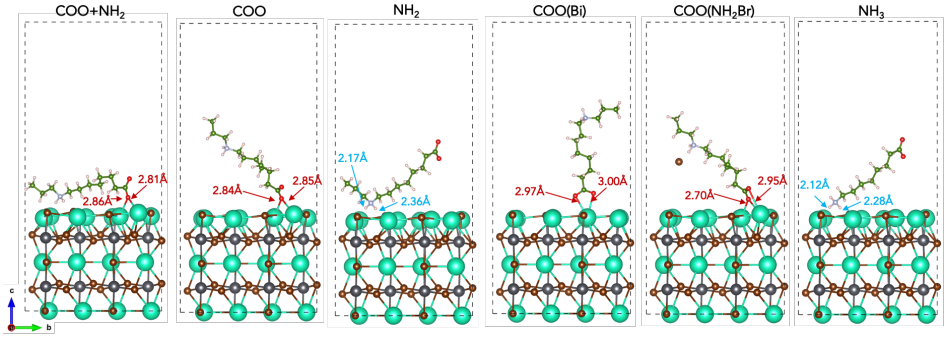

Figure 5.1.3 *Optimized anchoring modes of zwitterionic molecule adsorbed on CsPbBr3 stoichiometric surface. Color code: as Figure 5.1.2, distances O-Cs (red), NH_2-Br (blue).*

Table 5.1.1 *Computed binding energies (E_b) for all anchoring configurations of the zwitterionic molecule on $CsPbBr_3$ stoichiometric surface at different coverages (Θ) and dielectric media.*

E_b (eV)	COO+NH_2	COO	NH_2	COO(Bi)	COO(NH_2Br)	NH_3
High Θ 2x2 Supercell, Vacuum	-4.04	-1.55	Unstable	-0.61	-1.48	-1.10
Low Θ 4x4 Supercell, Vacuum	-2.94	-1.43	-2.87	-2.25	-0.31	-1.31
Low Θ Cluster, Vacuum	-3.40	-1.74	-2.40	-1.24	-2.40	-1.73
Low Θ Cluster, Hexane	-3.30	-1.16	-1.64	-0.86	-164	-1.97
Low Θ Cluster, DCM	-3.81	-0.41	-0.53	-0.32	-0.53	-0.49

To unveil the effect of solvents on monodentate/bidentate binding modes, we considered the DCM and hexane implicit solvents via the cluster approach. First,

to validate this approach we computed the E_b in vacuum (Cluster, vacuum). The resulting E_b and energy trend for the aforementioned configurations are close to periodic DFT values at low Θ, validating our approach. The vacuum energy trend is unchanged in both solvents of different polarities. Nevertheless, we obtained a strong binding energy (E_b = −3.81 eV) for the zwitterionic ligand in the COO+NH_2 binding mode to this perovskite surface in DCM at low Θ, which explains the remarkable stability of the purified $CsPbBr_3$ NCs in such medium. Plus, the less stable, but strong interaction, in hexane accounts for the removal of other possible passivating agents during the washing stages of the NCs.

Zwitterionic ligand at defective $CsPbBr_2$ interface. We also investigated the effect of surface point defects. Defective $CsPbBr_3$ surfaces were generated by removing one Cs and one Br atoms from the first exposed layer. In this case, both surface and subsurface layers were relaxed together with the molecule during geometry optimizations. Analysis of E_b (Table 5.1.2) reveals that defects favour the bidentate anchoring of the zwitterionic ligand (Def-COO+NH_2 in Figure 5.1.4), stable in both DCM (E_b = −5.37 eV) and hexane (E_b = −4.44 eV). Furthermore, efficient passivation of the NC defective surface is given by a different bidentate binding mode, denoted as Def-COO+NH_2(CH_2) in Figure 5.1.4, thanks to the fill of the Cs^+ vacancy by a methylene group of the aliphatic chain and hydrogen bonds between the dialkylammonium group and the adjacent Br atoms. As for the stoichiometric surface, on one hand, the opening of zwitterionic specie with Br^- extraction is not favourite. On the other, the monodentate binding mode (Def-NH_2) evolves at high Θ to the bidentate mode with the dialkylammonium and the carboxylate moieties saturating Cs^+ and Br^- vacancies, respectively, while it is stable at low Θ, mainly in hexane (E_b = −5.67 eV). This zwitterionic ligand in Def-NH_2 binding mode provides a polar surrounding to the NC surface due to the peripheral carboxylate group and could be held responsible for the NC insolubility in hexane.

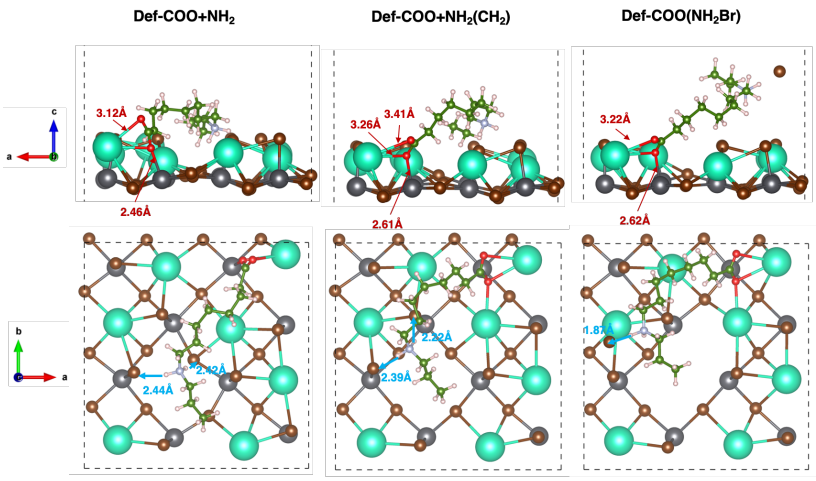

Figure 5.1.4 *Side and top views of the optimized zwitterionic molecule adsorbed on $CsPbBr_3$ defective surfaces. Color code: as in Figure 5.1.3*

Table 5.1.2 *Computed binding energies (E_b) for all configurations of the zwitterionic molecule on $CsPbBr_3$ defective surface at different coverages (Θ) and dielectric media.*

E_b (eV)	Def-COO+NH_2	Def-COO (Def-COO+$NH_2(CH_2)$)	Def-NH_2	Def-COO(NH_2Br)
High Θ 2x2 Supercell, Vacuum	-5.90	-5.50	Unstable	-3.74
Low Θ 4x4 Supercell, Vacuum	-5.96	-5.77	-5.86	-1.19
Low Θ Cluster, Vacuum	-6.11	-3.98	-6.17	-1.12
Low Θ Cluster, Hexane	-4.44	-2.31	-5.67	-1.61
Low Θ Cluster, DCM	-5.37	-3.23	-5.03	-1.02

To sum up, our theoretical studies reinforced the observation of higher NC stability derived by efficient bidentate adhesion of the zwitterionic ligand on the perovskite surfaces, underlying the effect of solvents. Overall, these findings suggest our approach based on modelling large clusters in implicit solvent as a reliable computational strategy to account for the solvent effect.

5.2 Unveil Structure and Electronic Features of SPIRO/Triple Cation Perovskite Interfaces.

Introduction. Understanding the main parameters influencing the charge dynamics at perovskite/CTL interfaces is crucial to design materials and devices with improved efficiency.[9,15,225,226,240] Generally, charge recombination can occur via different pathways at different time scales. Experiments estimated that charge recombination events occur on the nanosecond time scales, while charge extraction at interfaces spans a wide range from sub-femtosecond to nanosecond.[226,227,233,234,240–242] The coexistence of different phenomena lead to difficult interpretation of experimental data, so that computational simulations can be helpful to disentangle timescales of each process and rationalize the underlying mechanism from both structural and electronic point of view. On one hand, the band alignment between perovskite and CTLs can represent the thermodynamic driving force for hole/electron extraction from the perovskite to the ETL/HTL.[226] On the other, unless the expensive AIMD approach[243], one can estimate the electron injection time via a simple donor-acceptor model, based on the projection-operator diabatization (POD) approach.[244–247] Such a method consists in partitioning the Kohn-Sham (or Fock) matrix of the interacting system, expressed in orthonormal basis ($\overline{H}$), into a donor (D) and an acceptor (A) part, and separately diagonalizing of this matrix blocks, as following:

$$\overline{H} = \begin{pmatrix} \varepsilon_{D,1} & \cdots & 0 & & & \\ \vdots & \ddots & \vdots & & \overline{H}_{DA} & \\ 0 & \cdots & \varepsilon_{D,N} & & & \\ & & & \varepsilon_{A,1} & \cdots & 0 \\ & \overline{H}_{AD} & & \vdots & \ddots & \vdots \\ & & & 0 & \cdots & \varepsilon_{A,N} \end{pmatrix} \qquad (5.2.1)$$

where ε_D and ε_A are one-electron energies of donor and acceptor localized diabatic states, respectively, while the off-diagonal blocks ($\overline{\mathrm{H}}_{\mathrm{DA}}$, $\overline{\mathrm{H}}_{\mathrm{AD}}$), with elements $|V_{ad}|$, denote the relative donor-acceptor couplings.

This approach is successfully employed to unveil the ET mechanism at the MAPI interface with the most used ETL, the TiO_2.[246] In this framework, we employed this scheme, as implemented by Futera *et al.*[245] in the CP2K software,[219] to investigate the hole injection dynamics at the interfaces between MAPI and triple cation $Cs_{0.05}(MA_{0.17}FA_{0.83})_{0.95}Pb(I_{0.83}Br_{0.17})_3$ perovskites with one of the state-of-the-art HTL, the Spiro-OMeTAD (SPIRO). Meanwhile, SPIRO/MAPI interfaces have been widely characterized[235,248,249], to the best of our knowledge, this is the first complete structural and electronic characterization of SPIRO/triple cation perovskite interfaces. In particular, we assessed the role of both A cation halide (AX) and the lead halide (PbX_2) surface type terminations, and the effect of Cs atoms on the topmost layer.

Models & computational details. The computational cell of the perovskite $MAPI_3$ and $Cs_{0.05}(FA_{0.83}MA_{0.17})_{0.95}Pb(I_{0.83}Br_{0.17})_3$ consists of 100 $APbX_3$ units (Figure 5.2.1a). This supercell was built by scaling back the $Cs_8FA_{88}MA_{12}Pb_{103}Cd_5I_{269}Br_{55}$ model (108 f.u.) reported by Saidaminov[250], where FA/Cs/MA and I/Br are distributed randomly, and the orientation of the organic cations is determined after NVT molecular dynamics simulations. The lattice constants of optimized bulk structures increase of ~1Å putting in the larger formammidium (FA) and Cs cations. Concerning the electronic structure, the projected density of state (pDOS) are reported in Figure 5.2.1b. Valence (VB) and conduction band (CB) in both perovskites are given by I^- and Pb^{2+} states, respectively. Furthermore, in agreement with literature[231,232], the band gap of triple cation perovskite increases of ~0.09 eV with respect to the MAPI.

Concerning the SPIRO/perovskite interfaces, we build up the structural models for the perovskite surfaces by cleaving the bulk structure with optimized lattice

constants along the (010) plane and then introducing 25Å of a vacuum above the reoriented surface along the c direction (Figure 5.2.2). The resulting 8-layer slabs preserve the stoichiometry of the parent bulk. For adsorption purposes, we considered both AX- and PbX_2- type terminations. Since the cation composition differs within each AX layer due to the random cation distribution, we considered two kinds of AX terminations: one exposing Cs, MA, and FA (CsFAMAX surface) and one exposing only the majority MA and FA cations (FAMAX surface). For the same reason, two PbX_2 – terminations can be distinguished based on the presence of Cs in the subsurface layer. PbX_2 – terminated perovskite surface without and with subsurface Cs are indicated as PbX_2 and PbX_2(Cs) in Figure 5.2.2, respectively. The inclusion of Cs in the surface/subsurface allows to dissect the direct/indirect role of Cs in the adsorption event for AX/PbX_2 termination. Isolated SPIRO (Figure 5.2.2b) was computed in a 30 Å x 30 Å x 30 Å unit cell. During geometry optimizations involving the perovskite surface, atoms of the bottom layers were fixed to their bulk-like positions, while the first layer and the adsorbed molecule were allowed to relax without symmetry constraints. Our relaxed structures present maximum forces acting on each atom below 0.05 eV/Å. Due to large dimensions of the bulk and the surfaces, the gamma point (1×1×1) k-point sampling scheme was applied for all calculations. To optimize bulk structure and spiro/perovskite interfaces, the computational details for our periodic DFT calculations are the same in section 5.1, employing the PBE functional with TS correction.[26,27,41] To investigate the hole injection dynamics at the interfaces between MAPI and triple cation $Cs_{0.05}(FA_{0.83}MA_{0.17})_{0.95}Pb(I_{0.83}Br_{0.17})_3$ perovskite with SPIRO, we computed the donor-acceptor couplings at HSE06-D3BJ[31] level of theory, as implemented in CP2K.[219] We evaluated the spectral function as:

$$\Gamma_n(E) = 2\pi \sum_m |V_{nm}|^2 \delta(E - \varepsilon_m) \qquad (5.2.2)$$

where V_{nm} the electronic coupling matrix element between the diabatic donor n state and the acceptor m state of the perovskite valence band, with energy ε_m.

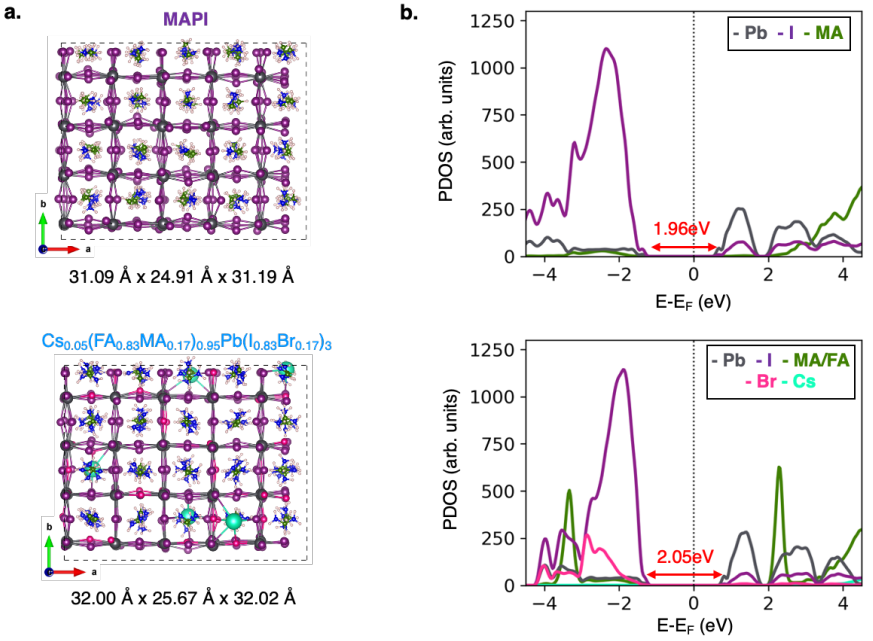

Figure 5.2.1 (a) *Optimized structures and* ***(b)*** *projected density of states (pDOS) at PBE-TS level of theory of perovskite MAPI (top) and* $Cs_{0.05}(FA_{0.83}MA_{0.17})_{0.95}Pb(I_{0.83}Br_{0.17})_3$ *(bottom) bulk. Atomic color code: Color code: Cs (cyan), Br(magenta), I (violet), Pb (gray), C (green), H (pink), N (blue). pDOS color code: Cs (cyan), Br(magenta), I (violet), Pb (gray), MA/FA (green).*

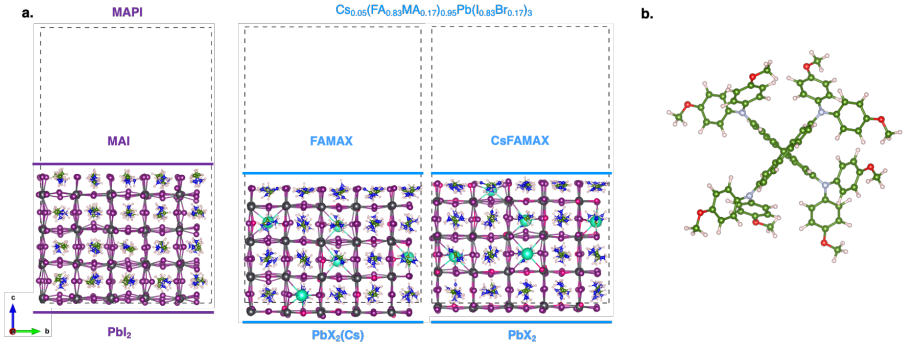

Figure 5.2.2 (a) *Slab models of the surfaces considered for SPIRO adsorption on MAPI: MAI,* PbI_2 *and on triple cation FAMAX,* PbX_2 *(Cs) and CsFAMAX,* PbX_2*.* ***(b).*** *Structure of Spiro-OMeTAD (SPIRO). Color code as in Figure 5.2.1,* N_{Spiro} *(light blue), O (red).*

Structural and energetic characterization of SPIRO/perovskites interfaces. Relaxed optimized structures of SPIRO at interfaces with MAPI and triple cation $Cs_{0.05}$ $(MA_{0.17}FA_{0.83})_{0.95}Pb(I_{0.83}Br_{0.17})_3$ perovskite surfaces are featured in Figure 5.2.3a. Binding energies (E_b) are computed at HSE06-TS level of theory on PBE-TS geometries as follows:

$$E_b = E_{Surf/HTL} - E_{Surf} - E_{HTL} \quad (5.2.3)$$

where $E_{Surf/HTL}$, E_{surf} and E_{HTL} are the energies for each SPIRO/perovskite interface, pristine surfaces, and isolated SPIRO, respectively. The exact values of binding energies are reported in Table 5.2.1, while the overall trend is displayed in Figure 5.2.3b with a further decomposition as follows:

$$E_b = E_a + E_{dM} + E_{dS} \quad (5.2.4)$$

$$E_a = (E_{Surf/HTM} - E_{Surf*} - E_{HTM*}) \quad E_{dM} = (E_{HTM*} - E_{HTM}) \quad E_{dM} = (E_{Surf*} - E_{Surf}) \quad (5.2.5)$$

where E_a, E_{dM} and E_{dS} are the adhesion energy, the distortion energy of SPIRO and the distortion energy of the perovskite surface, respectively. E_a is calculated from the energy of the fully relaxed interface ($E_{surf/HTL}$) and the energies of SPIRO, and the surface distorted at the interface geometry (E_{HTL*} and E_{Surf*}, respectively). E_a thus portrays the pure electronic interaction between SPIRO and the surface. Distortion energies E_{dM} and E_{dS} are calculated as the difference between the energies of each system and the interface geometry and those at their fully relaxed state, and account for the penalty energy needed for each component to change conformation ahead of forming the interface.

The SPIRO adsorption on the MAI surface is preferred for the MAPI, while it is strongly bonded to triple cation PbX_2(Cs) surface. The Cs atom in subsurface layer stabilizes SPIRO/triple cation PbX_2-interface of ~1eV. Similarly, Cs enhances SPIRO/triple cation AX-interfaces, when it is linked to a methoxy group of SPIRO (CsFAMAX(O-Cs) in Figure 5.2.3a). These findings suggest that the Cs atom has a significant rule in SPIRO/perovskite interaction.

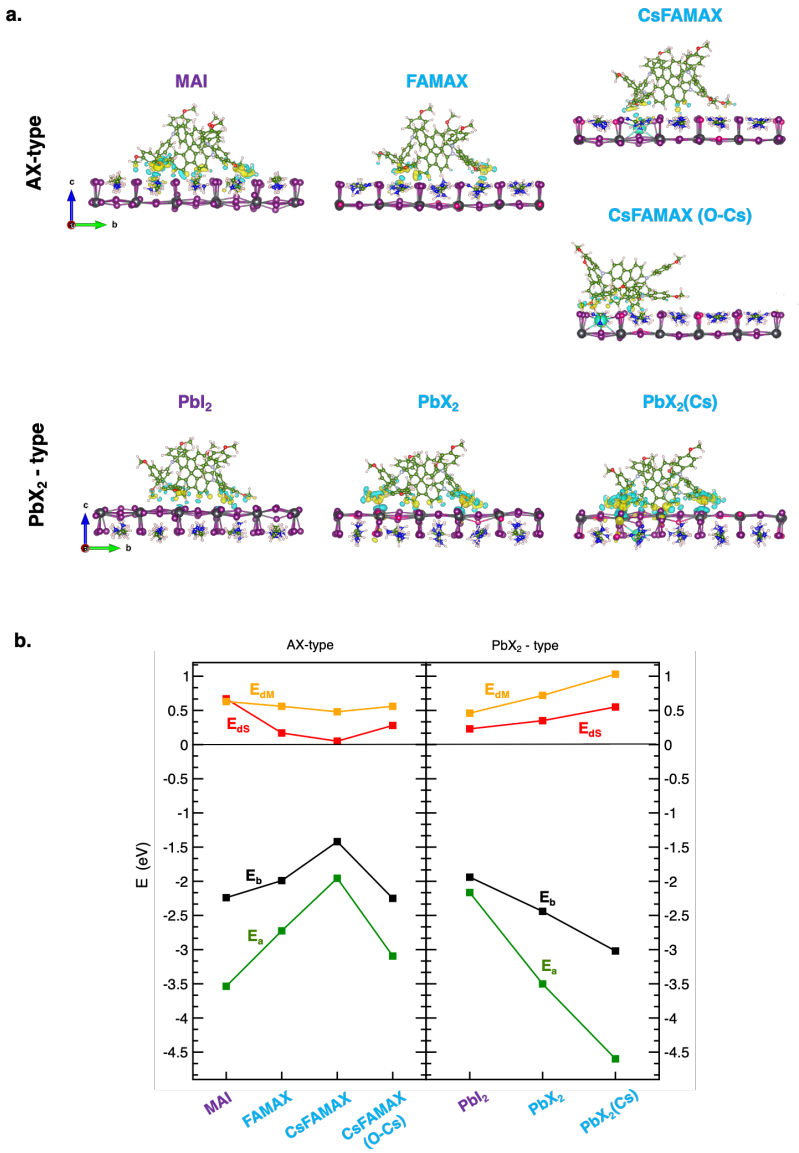

Figure 5.2.3 (a) *Lateral views of relaxed structures of SPIRO/perovskite interfaces considering AX- (top) or PbX_2- (bottom) type terminations of MAPI and triple cation perovskite with the charge density (CD) difference plots (electron gain (yellow), electron loss (cyan); isosurface value 0.001 a.u.).* ***(b)*** *Decompositions of binding energies of SPIRO on surfaces with AX- or PbX_2- type terminations with different compositions at HSE06-TS level of theory. Color code: as in Figure 5.2.1. Graphic color code: E_b (black), E_a (green), E_{dS} (red), E_{dM} (orange).*

The further energetic analysis (Figure 5.2.3b) reveals that adhesion energy (E_a) is the dominant term of E_b for both perovskites and all surface terminations, while surface and molecular distortion energies (E_{dS} and E_{dM}) are overall low and present an opposite trend with regard to E_b. Thus, the favourite adsorption of SPIRO at perovskites interfaces can be ascribed to a strong electronic interaction of SPIRO with perovskite surfaces, also confirmed by charge difference (CD) plots (Figure 5.2.3a)

Table 5.2.1 *Binding energies (E_b) at HSE06-TS level of theory of SPIRO/perovskite interfaces with AX- or PbX_2- type terminations with different compositions, and mean distances along z-axis between SPIRO and surfaces first layer eq 5.2.6 ($\bar{d}_{(Spiro-Surf),z}$).*

AX-type	**MAI**	**FAMAX**	**CsFAMAX**	**CsFAMAX(O-Cs)**
E_b (eV)	-2.24	-1.99	-1.42	-2.25
$\bar{d}_{(Spiro-Surf),z}$(Å)	1.62	2.21	2.39	1.71
PbX_2-type	**PbI_2**	**PbX_2**	**PbX_2(Cs)**	
E_b (eV)	-1.94	-2.44	-3.02	
$\bar{d}_{(Spiro-Surf),z}$(Å)	2.00	1.58	1.50	

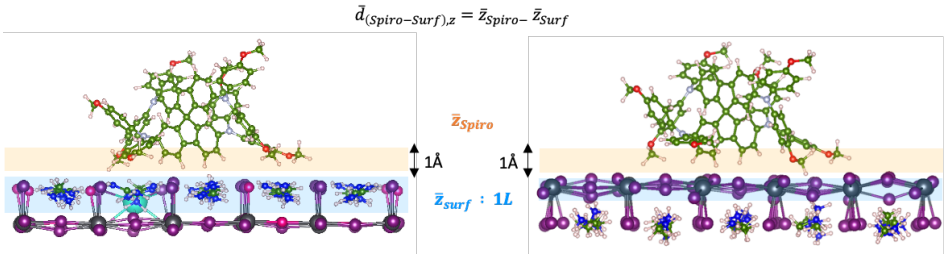

Figure 5.2.4 *Graphical representation of layers that define $\bar{z}_{Surf}$ and $\bar{z}_{Spiro}$*

To unveil the binding/adhesion energies trend, we also analysed the mean distances along z-axis between SPIRO and surfaces first layer ($\bar{d}_{(Spiro-Surf),z}$), defined as following:

$$\bar{d}_{(Spiro-Surf),z} = \bar{z}_{Spiro} - \bar{z}_{Surf} \quad (5.2.6)$$

where $\bar{z}_{Spiro}$ and $\bar{z}_{Surf}$ are the mean values of atomic positions along z-axis of SPIRO atoms included in a layer of 1Å thick closer to surfaces, and of topmost surfaces layer (atoms in the 1L) (Figure 5.2.4), respectively. Resulting values in Table 5.2.1 reveals that more stable SPIRO/perovskites interfaces (more negative binding energies) exhibit the low distances. Thus, this parameter, $\bar{d}_{(Spiro-Surf),z}$, can be correlated to the high interaction between HTM and perovskite. Furthermore, structural analysis of molecule-surface distances (Figure 5.2.5a) reveals that the functional groups -OCH_3 define the main interactions between SPIRO and surface terminations, as already known.[235,248,249] In both perovskite materials, the methoxy-oxygen atoms are mainly bound to the topmost layer MA/FA/Cs and Pb cations of AX- and PbX_2-type surface termination, respectively. On one hand, for the AX-type composition, the SPIRO/CsMAFAX interaction (CsMAFAX(O-Cs)) presents a bond length between Cs and methoxy O atoms of ~3.25Å, that is the typical coordination distances between Cs and O.[251] On the other, for the PbX_2-type surfaces the most stable interface SPIRO/PbX_2(Cs) shows shorter O-Pb distances (~2.8 Å). Therefore, the further stabilization occurring in the PbX_2(Cs) and CsMAFAX interfaces of triple cation perovskite can rely on the stronger O-Pb and O-Cs interactions, respectively. Concerning the distortion energies, the most stable interface, the SPIRO/PbX_2(Cs), has also the higher E_{dS} and E_{dM}. At both perovskite interfaces, the SPIRO undergoes a slight reorganization, with a variation of 2° and 4° for the angles of the main fluorene moiety and the lateral methoxyphenyl chains, respectively, compared to the value in the free SPIRO molecule (Figure 5.2.5b). These structural variations occur with a slight elongation of the methoxy CH_3-O bond of ~0.02/0.03 Å at the most stable SPIRO/PbX_2(Cs) interface (Figure 5.2.5c). Meanwhile, the perovskite surfaces undergo a reorganization of MA/FA cations on the topmost layers (Figure 5.2.6).

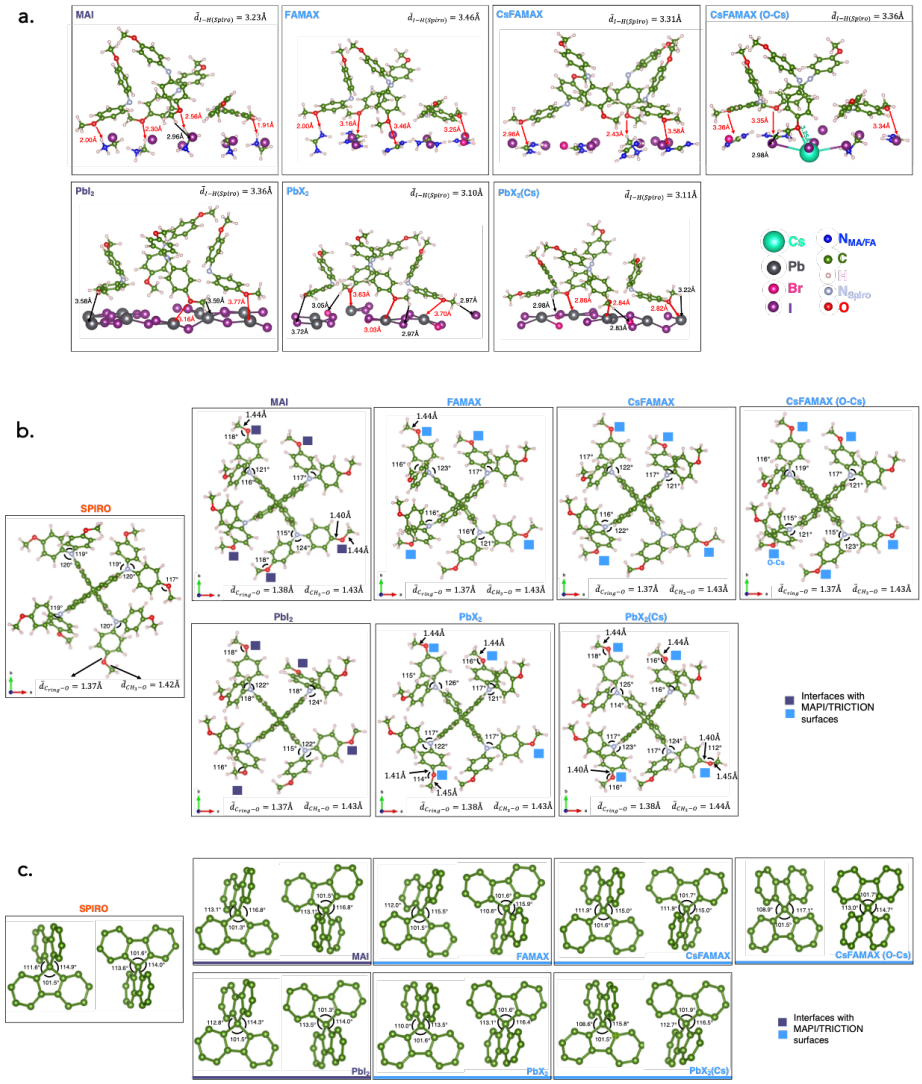

Figure 5.2.5 (a) *Main bond distances between SPIRO and surfaces. Structural variation of SPIRO bond length and angle in main fluorene moiety* ***(b)*** *and lateral groups* ***(c)****. Color code: as in Figure 5.2.1. The violet and blues boxes in b and c indicate residues toward the surfaces.*

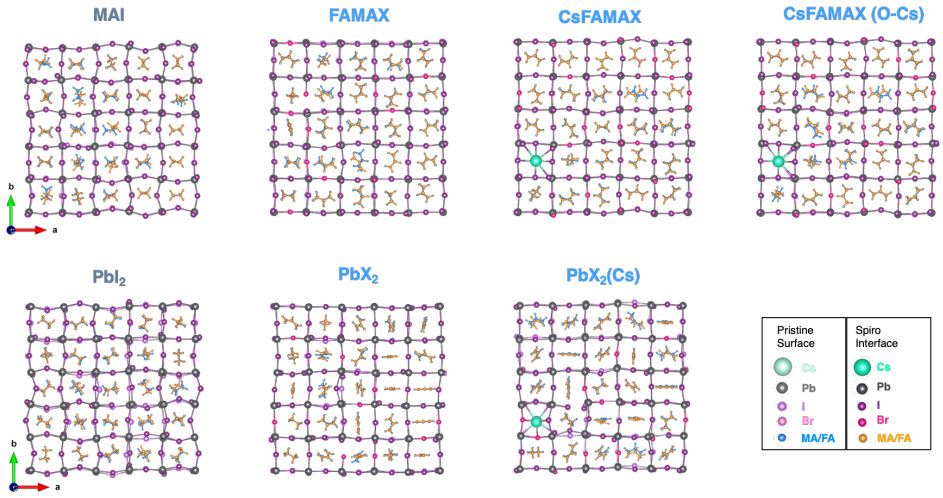

Figure 5.2.6 *Main structural variations of perovskite surface topmost layers. Color code: Pristine surfaces (light color) with MAFA (light blue), SPIRO/surfaces interfaces (dark color) with MA/FA (orange).*

Electronic features of SPIRO/perovskites interfaces. The electronic properties of the investigated SPIRO/perovskite interfaces were also analysed in terms of their projected Density of States (pDOS) at HSE06 level of theory. Comparison of the pDOS by means of FHI-aims and CP2K programs (Figure 5.2.7) showed no significant difference, so that hereafter we employed CP2K for the whole electronic analysis, from pDOS to POD approach. The pDOS allows to evaluate the energy difference of the HTM HOMO and the VB of perovskite, index of the thermodynamic driving force for hole extraction. In a performant HTL, the HOMO should be higher in energy than the perovskite VB for an effective hole extraction. The pDOS in Figure 5.2.7 reveal that the SPIRO presents a very similar electronic behaviour for all the analysed terminations and compositions, with its HOMO well above the perovskite VB, in particular for the PbX_2 termination. Thus, all the considered interfaces possess the required features for hole extraction.

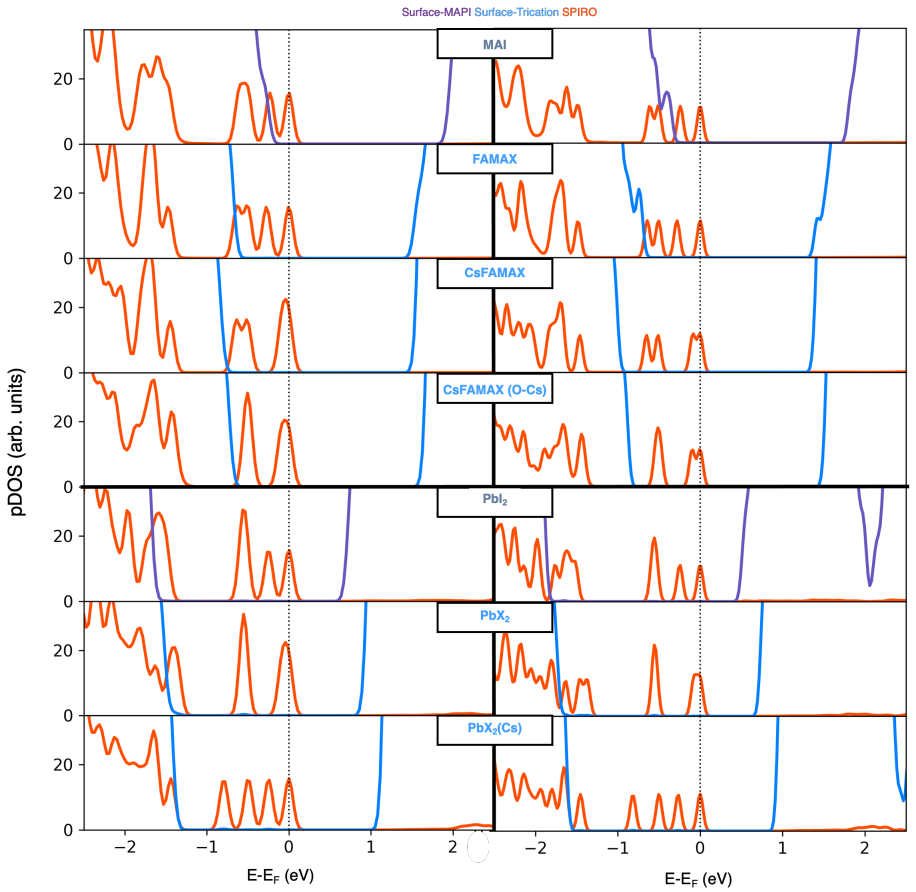

Figure 5.2.7 *pDOS of SPIRO/perovskite interfaces computed by FHI-AIMs (HSE06-TS) (right) and CP2K (HSE06-D3BJ) (left) programs. Color code: MAPI surface (violet), triple cation surfaces (light blue), SPIRO (orange).*

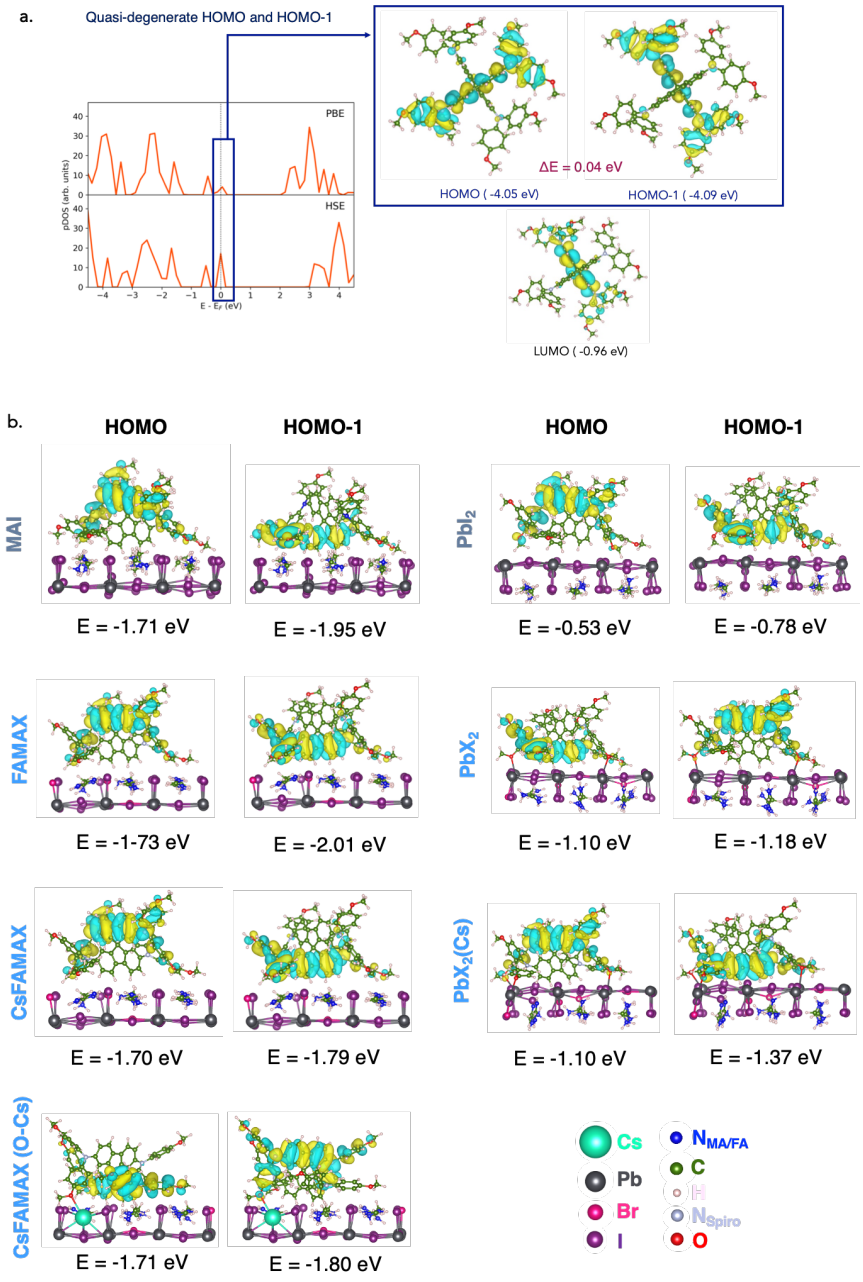

Figure 5.2.8 (a) *Isolated SPIRO pDOS at PBE-D3BJ and HSE06-D3BJ level of theory and molecular orbitals: HOMO, HOMO-1 and LUMO. (**b**) HOMO and HOMO-1 with respective HSE06-D3BJ energies of SPIRO at perovskite interfaces with AX- (left) and PbX_2- (right) type terminations. Color code: Figure 5.2.1*

According to further analysis of the SPIRO molecular orbitals (MOs) in Figure 5.2.8, the degeneracy of HOMO and HOMO-1 in the isolated SPIRO molecule (Figure 5.2.8a) is absent at most interfaces. These two molecular orbitals at perovskite interfaces are differently oriented with respect to the surfaces. The HOMOs point to the vacuum, while the HOMO-1 to the surfaces. This different orientation increases the energy difference between HOMO and HOMO-1 from 0.04 eV in the free molecule to ~ 0.25/0.3 eV at MAI, PbI_2, MAFAX, and PbX_2(Cs) interfaces. The PbX_2 and CsFAMAX (O-Cs) terminations show, indeed, an opposite orientation of these SPIRO MOs and a smaller splitting (ΔE ~0.07/0.09 eV, respectively). At these interfaces, the HOMO is oriented toward the surface, but the HOMO-1 is localized on methoxy O atom strongly bound to Pb and Cs atoms, respectively for PbX_2 and CsFAMAX (O-Cs) terminations. Therefore, both HOMO and HOMO-1 show a great interaction with perovskite surface due to orientation and molecular localization, respectively, decreasing the splitting effect. Overall, according to our calculations, the nature of SPIRO HOMO/HOMO-1 splitting could be ascribed to the different interactions with the perovskite surfaces.

Charge transfer via POD approach. Motivated by Mos analysis, we considered both HOMO and HOMO-1 to investigate the hole injection dynamics at the interfaces between MAPI and triple cation $Cs_{0.05}(MA_{0.17}FA_{0.83})_{0.95}Pb(I_{0.83}Br_{0.17})_3$ perovskites. In the framework of the simple donor-acceptor model [244,245], these two MOs are the donor state, while the acceptor states are the perovskite VB. To reduce the computational cost, we considered the first two layers of perovskites as the acceptor. Figure 5.2.9 features an overview of the computed spectral function and coupling matrix elements $|V_{ad}|$ between the donor (the SPIRO MOs) and a wide range of perovskite VB with respective atomic projected DOS of SPIRO and first two layers of perovskites at HSE06-D3BJ level of theory. The energies of the SPIRO state ($E_{HOMO/HOMO-1}$) are indicated by red lines.

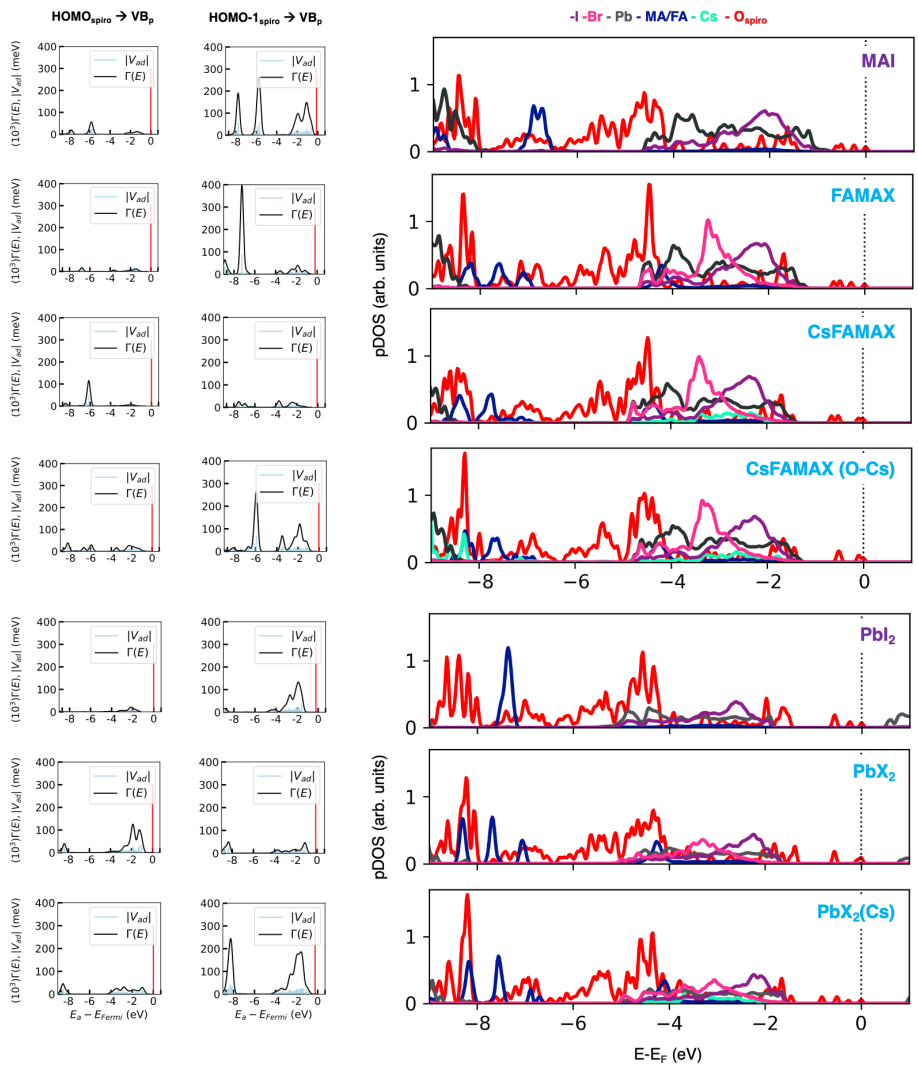

Figure 5.2.9 *HSE06-D3BJ computed spectral function (Γ(E)) and coupling matrix elements $|V_{ad}|$ between donor (the SPIRO HOMO and HOMO-1) and a wide range of perovskite VB (left) with respective pDOS (right) of SPIRO and first two layers of perovskites. The energies of the SPIRO state ($E_{HOMO/HOMO-1}$) are indicated by red lines. From top to bottom: AX-type termination (MAI, FAMAX, CsFAMAX, CsFAMAX(O-Cs)), PbX_2-type termination (PbI_2, PbX_2, PbX_2(Cs)).*

We found a stronger coupling between both SPIRO MOs and inner states of perovskites VB for the AX-type terminations (between -9 and -6 eV), while with the higher VB energy states of PbX_2-type terminations (between -1 and -4 eV). The participation of inner states is also suggested by experiments.[234] Comparison of the pDOS and $|V_{ad}|$ plots reveals that the stronger coupling occurs where the VB state consisted mostly of MA/FA/Cs orbitals and of Pb/I orbitals, respectively for the AX- and PbX_2-type composition. Thus, these results highlight that there is a major probability of charge transfer to perovskites VB states given by a major contribution of the atoms, that have the main interactions with the SPIRO methoxy CH_3-O atom, with a direct role of Cs states in the Cs-exposing surface.

The hole injection time (τ), computed via the relation with the spectral function ($\tau = \hbar/\Gamma$), are reported in Table 5.2.2. The resulting times fall in the range reported for hole extraction from SPIRO at perovskite interfaces, that span the experimental TPL time scale from sub-femtosecond to nanosecond.[226,227,233,234,240–242]

Table 5.2.2. *Hole injection time (τ) in ps between SPIRO HOMO and HOMO-1 and VB perovskite interfaces with AX- or PbX_2- type terminations with different compositions.*

τ(ps): AX-type	**MAI**	**FAMAX**	**CsFAMAX**	**CsFAMAX (O-Cs)**
$HOMO_{spiro}$ → VB_p	11.7	38.7	5.70	16.7
$HOMO\text{-}1_{spiro}$ → VB_p	1.80	1.65	12.9	2.50
τ(ps): PbX_2-type	**PbI_2**	**PbX_2**	**PbX_2(Cs)**	
$HOMO_{spiro}$ → VB_p	31.6	5.24	14.3	
$HOMO\text{-}1_{spiro}$ → VB_p	4.93	13.1	2.68	

According to our results, the τ drop ~10 ps when moving from SPIRO HOMO to HOMO-1 coupling with MAI, FAMAX, CsFAMAX(OCs), PbI_2 and PbX_2(Cs) surfaces, while HOMO hole injection is ~26 ps lower than HOMO-1 for PbI_2 and FAMAX surfaces. This trend could be ascribed to SPIRO HOMO/HOMO-1 orientation and interaction with the different perovskite surfaces (Figure 5.2.8). Comparison of times with MOs orientation highlights that hole injection is faster from MOs oriented toward the surface, generally HOMO-1, and HOMO for the PbX_2 surface. Meanwhile, both SPIRO/triple cation interfaces with Cs on topmost layer show different behaviour. Both computed τ are lower for MOs oriented toward the vacuum, exactly HOMO and HOMO-1 of CsFAMAX and CsFAMAX (O-Cs) interfaces, respectively. Despite the MOs orientation, these SPIRO MOs are localized on terminal methoxy CH_3-O atom, lying closer to the surfaces and bonding to Cs at CsFAMAX and CsFAMAX (O-Cs) systems, respectively (Figure 5.2.10). Strong correlations with perovskite VB are thus established.

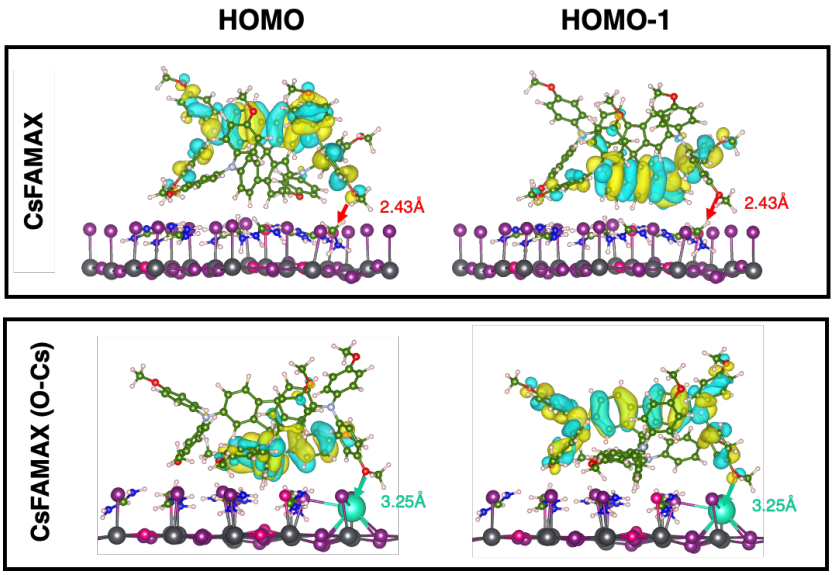

Figure 5.2.10 *SPIRO molecular orbitals at CsFAMAX and CsFAMAX(O-Cs) interfaces.*

Considering the stronger MOs coupled to VB for each interface, the terminations with no Cs in the topmost layer and the PbI_2 surface have a τ of ~5 ps, while the less stable SPIRO/FAMAX interfaces have the lowest hole injection time of ~1.65 ps. A quite similar τ is found for the SPIRO/MAI interfaces (~1.8 ps) and only ~1ps faster than the charge transfer at the most stable triple cation interfaces, the CsFAMAX(O-Cs) and PbX_2(Cs) (2.50 ps and 2.69 ps, respectively). These findings suggest that the hole injection can occur with similar time at both type of surface termination, the AX and PbX_2, of triple cation perovskite.

In conclusion, these results highlight perovskite interfaces can affect the energy difference between SPIRO HOMO and HOMO-1 and relative charge transfer. In particular, the Cs on the topmost layer atoms strengthen the SPIRO/perovskite interaction and decrease the hole injection time, which can involve the inner states of perovskites, as previously suggested.[234] Furthermore, proposed computational strategy appears efficient to characterize the interfaces of harvesting materials.

The manuscript reporting this case of study is under revision.

5.3 New HTLs for Perovskite Solar Cells.

Introduction. Despite its advantages, the widely adopted Spiro-OMeTAD presents critical issues related to its cost, stability, and device lifetimes.[225,249] Thus, the community has commonly focused on the design of new HTLs. Engineering of HTL aims to facilitate the charge transport to the electrodes, block undesired back hole-electron injection, and to improve the crystallinity of the perovskite. A competitive substitute for the conventional SPIRO needs to increase also long-term stability of PSCs under ambient conditions, ensuring low cost, simple synthesis, and minimal damages. Only a thorough understanding of the complex phenomena that occur at the HTL/perovskite interfaces can offer new standards for the development of new HTLs for more stable PSCs. In this framework, by means of the periodic DFT approach, we provided structural, energetic, and electronic features of two new HTLs, named SCF1 and SCF2 (Figure 5.3.1) at triple cation perovskite interfaces (Figure 5.2.2) and compared them with SPIRO. These HTLs were synthetized by the group of Professor Vivo at Tampere University (TAU). In particular, they were obtained by eliminating the orthogonal portion of the SPIRO scaffold to reduce the molecular distortion required for surface anchoring. They differ for the lateral functional groups: $–OCH_3$ or $–CH_3$ for SCF1 and SCF2, respectively. These HTLs showed good thermal stability, hydrophobicity, and comparable hole mobility to undoped SPIRO. Additionally, the device employing SCF1 with $Cs_{0.05}(FA_{0.83}MA_{0.17})_{0.95}Pb(I_{0.83}Br_{0.17})_3$ perovskite displayed a PCE of 13.9 % and exhibited a significantly extended shelf-lifetime and better stability compared to SPIRO. In the following section, we report our contribution to this case of study, while the whole work is object of a manuscript under revision.

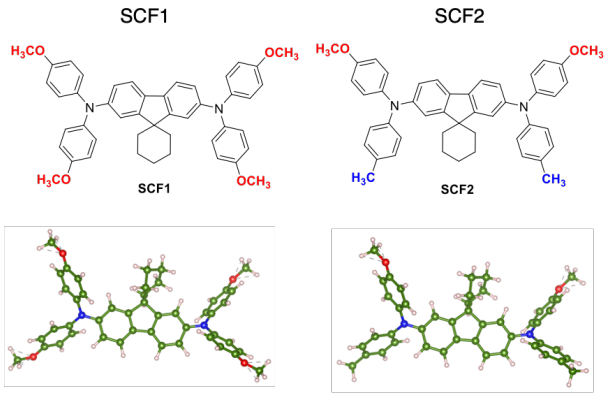

Figure 5.3.1: *Structure of SCF1 and SCF2. Color code: as in Figure 5.2.1*

Models & computational details. Models and computational details for our periodic DFT calculations are the same of section 5.2.

DFT-characterization of SCF-HTMs vs SPIRO. As for SPIRO in section 5.2, we addressed all possible surface terminations of the triple cation perovskite for modeling the HTL/perovskite interactions (Figure 5.2.2). Minimum energy geometries are featured in Figure 5.3.2, with resulting binding energies (E_b, eq 5.2.3) at HSE06-TS level of theory on PBE-TS geometries, and the mean distances along z axis ($\bar{d}_{(Spiro-Surf),z}$ eq. 5.2.6). To consistency, we started with all the HTL at similar distance from surfaces. In this way, we found different minima for SPIRO, which is far from surfaces with regards of section 5.2, and no O-Cs bound are found for CsFAMAX termination. This finding highlights the key rule of AIMD simulations to sample the potential energy surfaces of all possible HTLs/perovskites configurations. Due to dimension of these systems, metadynamics at DFTB level of theory[49,53,217] can be helpful to reduce the computational cost, but to best of our knowledge Slater-Koster files for perovskite are not present. Thus, as future prospective, we suggest to development of a reliable parameter set and further analysis on these intricate interfaces.

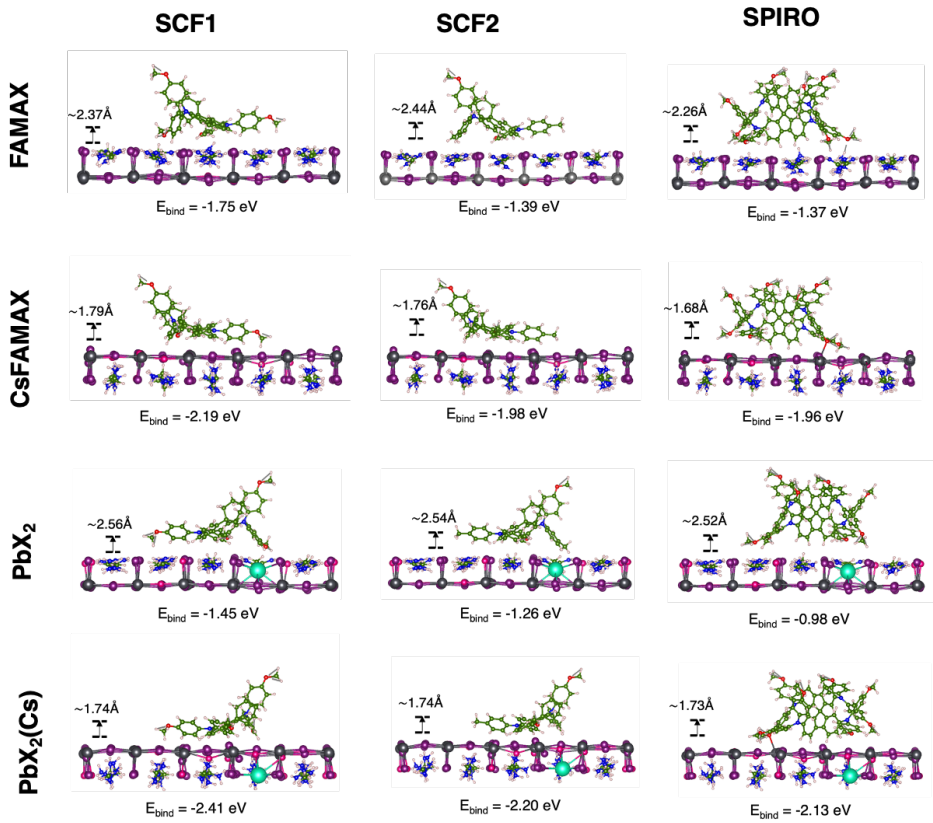

Figure 5.3.2 *Lateral views of minimum-energy structures HTL/triple cation perovskite interfaces considering AX or PbX_2 terminations. Color code as Figure 5.2.2*

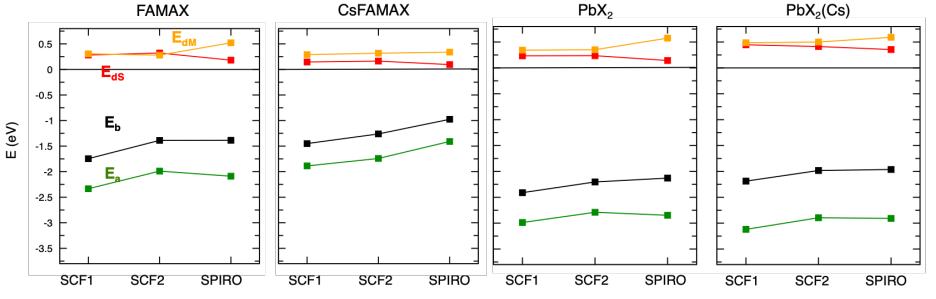

Figure 5.3.3 *Decompositions of binding energies of HTMs SCF1, SCF2 and SPIRO on AX- or PbX_2- surfaces with different compositions.*

Nevertheless, according to the computed binding energies for the minima in Figure 5.3.2, also at these distances from surfaces, the HTL is strongly adsorbed on perovskite. In particular, we found that the SCF1 forms the most stable interface with the perovskite for all terminations and surface compositions, with binding energies stronger up to 0.4 eV with respect to SPIRO and SCF2. Between these two latter HTLs the SCF2/perovskite interactions are slightly more favorable. Overall, this SCF1 enhanced interactions with triple cation perovskite can promote the stability of the corresponding solar cells, as determined via experimental stability studies. To an in-depth understanding of this trend, as in section 5.2, we analyzed the contribution to E_b in terms of adhesion (E_a) and distortion energies (E_{dM} and E_{dS}). Again, the resulting values, plotted in Figure 5.3.3, reveals that E_a is the dominant term. This energy is more negative for SCF1 on all terminations explored, while the surface distortion energies (E_{dS}) are overall low, especially those induced by SPIRO. Concerning the molecular distortion energies (E_{dM}), SCF1 and SCF2 present a lower E_{dM} than SPIRO, explaining the final trend of HTLs/perovskite stabilization: E_b(SCF1)< E_b(SCF2)< E_b(SPIRO). This behavior could rely on the presence of the orthogonal fragment in SPIRO that induce further molecular distortion in the surface anchoring, contrary to the SCF-HTMs.

Concerning the different stability of the two SCFs-HTLs, the $\bar{d}_{(Spiro-Surf),z}$ and detailed structural analysis in Figure 5.3.4 reveal that the SCF1 lies closer to perovskite surfaces and the functional groups -OCH_3 define the main interactions between all HTLs and surface termination. Additionally, the CD plots in Figure 5.3.5 shows a further interaction between fluorene-ring and MA/FA cation in the SCF1-FAMAX interface. Overall, the major number of -OCH_3 terminal-functional groups and further interaction via the main fluorene moiety can explain the most favorite anchoring of SCF1 with respect to SCF2.

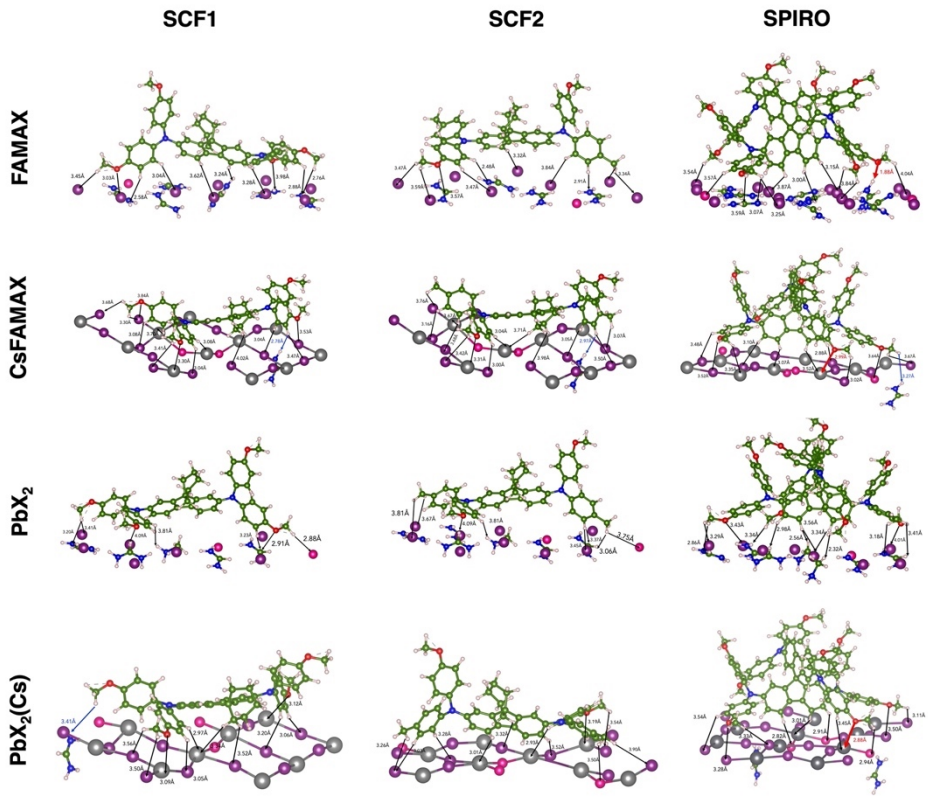

Figure 5.3.4 *Structural analysis of HTL/triple cation perovskite interfaces. Color code as Figure 5.2.2*

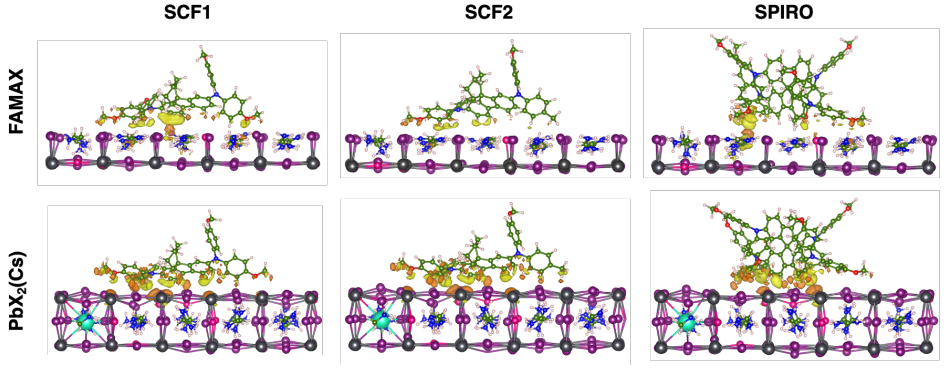

Figure 5.3.5. *Charge difference (CD) plot computed at HSE06-TS level of theory of the most favorite SCF1, SCF2 and SPIRO interfaces: FAMAX or PbX_2(Cs) terminations. Isodensity value: 0.005 a.u. Color code: as Figure 5.2.2, electron gain (yellow), electron loss (orange).*

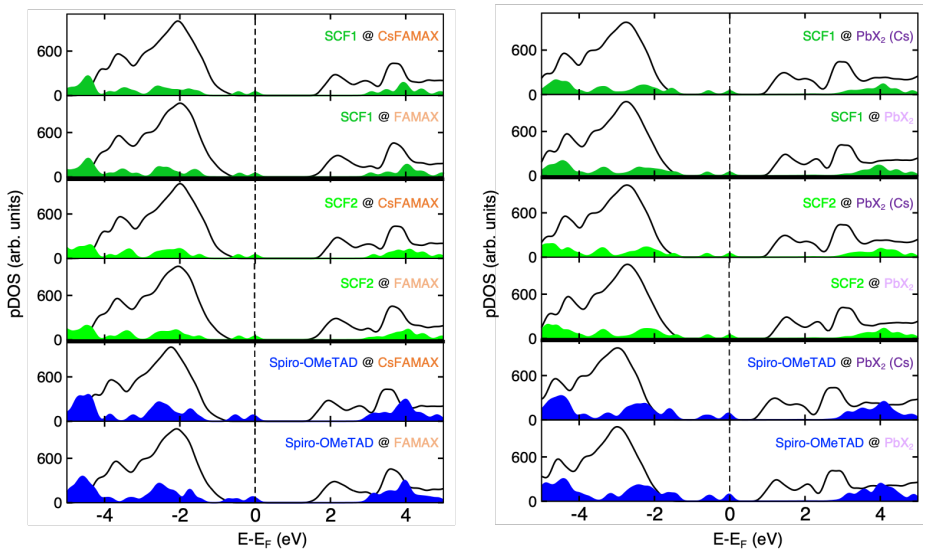

Figure 5.3.6: *Projected density of states (pDOS) of* $Cs_{0.05}(FA_{0.83}\,MA_{0.17})_{0.95}Pb(I_{0.83}Br_{0.17})$ *(black line), SCF1 (solid dark green pattern), SCF2 (solid light green pattern) or Spiro-OMeTAD (solid blue pattern) for HTM adsorption on the different terminations and compositions considered. The Fermi energy (*E_F*) is set to zero.*

To estimate the thermodynamic driving force for hole extraction from the perovskite to the HTL, we also investigated the electronic behavior of HTM/perovskite interfaces through the projected Density of States (pDOS) (Figure 5.3.6). For all the perovskite surfaces terminations, the SCF-HTLs HOMO is well above the perovskite VB. Thus, SCF1 and SCF2 also possess the required features for hole extraction from triple cation perovskite.

In conclusion, theoretical and experimental investigations of the SCF-HTM/triple cation interface highlights the stability of these simplified HTLs, in particular of SCF1 which possesses the highest binding energies and suitable energy levels for charge extraction from the perovskite layer.

This work, group of Professor Vivo (TAU), is object of an article accepted in Chemistry of Materials Journal.

FINAL REMARKS AND FUTURE PERSPECTIVES

An atomistic perspective on complex materials and interfaces is becoming more and more crucial to enable the development and optimization of energy conversion devices so to enhance both stability and performance. Great efforts have been devoted to development and validation of reliable computational strategies to span and disentangle all the main physico-chemical processes, occurring at heterogeneous interfaces, and to design new materials for these devices. But to unveil the complex interfacial phenomena, several aspects in operando condition must not be neglected, and an in-depth understanding of interface reactivity can often require new strategies beyond the current state of the art. To this end, in this thesis, we have identified effective and straightforward computational approaches for several challenges on interface chemistry in the field of the main technologies for production and storage of clean renewable energy, considering next-generation batteries, perovskite solar cells and photoelectrochemical cells.

Considering the case of Na ion uptake at anatase interfaces, we showed the promising application of the sawtooth potential to address electrochemical processes at electrode/electrolyte interface including the electric field effects for mimicking in operando condition. Moreover, the new insights achieved for the corrosive singlet oxygen release at cathode of Li-air battery and the first step of effective SEI formation by vinylene carbonate open-ring reduction at lithium metal anode, as also for the high oxygen evolution barrier at iridium oxide photoanode, provided the validation of embedded cluster approaches, from a simple electrostatic potential to the more complex density functional embedding theory (DFET), paving the route for further application of embedding strategies for challenges related to molecular reactivity at electrode interfaces.

Beyond the electric bias, the effect of the solvent medium is another variable to take into account to bridge the gap between atomistic simulations and lab experiments. Consistency between experimental proposed structure and our results from metadynamic simulations at the convenient DFTB level of theory for the water dynamic at anatase interfaces have proven this approach as reliable and cheap method to unveil the processes occurring at aqueous interfaces, e.g. water structure and reactivity at electrode surfaces, which are crucial in the context of photoelectrochemical cells for water splitting or CO_2 photoreduction.

Additionally, the ab-initio characterization of new zwitterionic ligand on perovskite $CsPbBr_3$ has stronger up this experimental passivating strategy of harvesting materials, also highlighting the efficiency of the cluster approach with implicit solvent model to account for solvent effect.

Overall, accounting experimental variables, e.g. electric field and solvent, we have demonstrated how the computational modelling can be helpful for interpretation of experimental data.

Eventually, for the SPIRO/lead halide perovskite interfaces we have shown the potential of atomistic investigation to unveil the structure-function relationships and to provide new insights on complex physico-chemical processes, also helpful to design new materials, e.g. the proposed SCFs-HTLs. However, these cases of study have also highlighted the key role of molecular HTLs dynamics at perovskite interfaces.

In conclusion, all the suggested atomistic strategies can be helpful to span several phenomena occurring at different time and space scales and to enhance the knowledge of fundamental physico-chemical processes at complex heterogeneous interfaces. Nevertheless, several issues need further investigation, such as the unveiling of whole mechanism for poly(VC) formation in lithium metal batteries SEI, the anatase efficiency as photocatalyst toward CO_2 reduction, the competitive oxo-oxo coupling as oxygen evolution reaction

mechanism at iridium oxide interfaces or sampling of all the possible configurations of molecular HTLs/perovskite interfaces for reliable characterization and design of new sunlight harvesting material. To advance the knowledge of these light-driven and electric processes toward a desired scale-up of these technologies, a future perspective is so to push forward the proposed computational tools, combining post-HF methods with the DFET to address reactivity at heterogeneous interfaces, metadynamic simulations with electric field for solvent dynamics at the electrode-electrolyte interface, and at DFTB level of theory for molecule/solid interfaces, dominated by dispersive interactions. The integration of all these computational tools will provide a new original look at the fundamental (photo-)electrochemical processes that we must control and optimize to take full advantage of all the renewable energies for a bright and sustainable economic development of our global society.

APPENDIX A

We discuss, hereby, the cases of study, not focused on heterogeneous interfaces, carried out in the field of solar energy devices and catalysis. In particular, the following A1 section concerns new harvesting material based on antimony-based perovskite-inspired materials (Sb-PIMs), while in A2 section we present new luminescent solar concentrators (LSCs) based on molecular Ir(III) complexes. Finally, in A3 section we report an unexpected imidazole binding to DiRodium(II) complex, leading to a promising catalyst. All these studies are the result of a collaboration with the experimental groups of Professors Paola Vivo (Tampere University (TAU)), Andrea Pucci (University of Pisa) and Stefano Stagni (University of Bologna), and Antonello Merlino (University of Naples Federico II), respectively. For a full dissertation, we refer to the published works (A1 ref [252], A2 ref [253], A3 ref [254]).

A1. Efficient Mixed Organic-Inorganic Perovskite-Inspired Material for Indoor Photovoltaics

Antimony-based perovskite-inspired materials (Sb-PIMs), with $A_3Sb_2X_9$ stoichiometry, have emerged as alternative harvesting materials for Pb- and Sn-free solar cells.[255] Beyond their optoelectronic properties, good intrinsic stability and low toxicity, Sb-PIMs materials have been particularly promising for indoor photovoltaics (IPVs) due to their bandgaps of ~2eV.

Up to date, the most investigated Sb-PIM is the full inorganic $Cs_3Sb_2I_9$, which presents two polymorphs: the 0D dimer and the 2D layered form.[256,257] The former, easily synthesizable at low temperatures, is not ideal for photovoltaic applications due to indirect band gap and poor charge-carrier transport.[258] Meanwhile, the 2D polymorph enables effective charge transport across the layers and has a nearly direct bandgap.[256,259–261] Unfortunately, it is thermodynamically stable typically at high temperatures.[257,262] Therefore, researchers have recently focused on how to promote the suppression of the 0D phase and the formation of the 2D layered one, also motivated by the discovery of novel 2D Sb-PIM compositions suitable for IPVs.

On one hand, the mix X-site, e.g. mix I/Cl anions, has shown to be a promising strategy to assure a 2D structure, without effect on the bandgap.[262,263] On the other one, engineering the small A-site cation, such as in double A-site cation[264] and methylammonium (MA)-based Sb-PIMs[265], has reported encouraging results in these materials performance. In this framework, we introduced for the first time a triple-cation Sb-based PIM, $Cs_{2.4}MA_{0.5}FA_{0.1}Sb_2I_{8.5}Cl_{0.5}$ (CsMAFA-Sb). In particular, by means of theoretical and experimental tools, we investigated the structural and electronic features of the proposed CsMAFA-Sb, compared with the full inorganic $Cs_3Sb_2I_9$ composition, and the double- and triple mixed A-site cations ($Cs_{2.4}$ $FA_{0.6}Sb_2I_9$, $Cs_{2.4}MA_{0.6}Sb_2I_9$, $Cs_{2.4}MA_{0.5}FA_{0.1}Sb_2I_9$). Experimental

study, carried out by group of Professor Vivo, revealed that solar cells with CsMAFA-Sb material are more performant than the double-cation CsMA-Sb and CsFA-Sb.

By means of periodic DFT approach, we analysed the effect of mix A cation and I/Cl anions on structural and electronic features. Relaxed optimized structures of the inorganic 2D-layered $Cs_3Sb_2I_9$ PIM and its hybrid organic–inorganic derivatives are featured in Figure A1.1. The first significative result is that all minimum-energy structures consist of 2D layer phase of $Cs_3Sb_2I_9$ PIM. Detailed analysis of lattice constant and stacking between 2D layers (Table A1.1) revealed that the double-cation CsFA-Sb presents a lattice elongation of 0.25Å (~3%) along the a-axis, leading to high difference between the a and b lattice constants. These two lattice constants differ of only 0.08Å in the double cation CsMA-Sb PIM, accompanied indeed with an elongation of ~0.5% along the c-axis. Meanwhile, including both organic cation (FA/MA) and Cl-anion, the lattice parameters of inorganic PIMs are quite re-established. This structure also has unchanged stacking between SbI_8 octahedra.

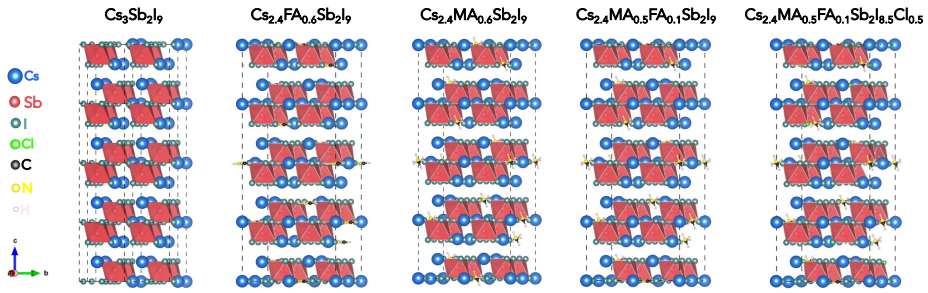

Figure A1.1 *Bulk structure and lattice parameters of the 2D- $A_3Sb_2X_9$ PIMs with A=Cs, FA, MA and X=I, Cl. Color code: Cs (blue), Sb (red), I (teal), Cl (green), C (black), N (yellow), H (light pink).*

Table A1.1 *Lattice parameters, stacking between layers (d_1 and d_2 shown on the left) at PBE level of theory of the optimized 2D- $A_3Sb_2X_9$ PIMs structure. Stacking between layers: d_1 (magenta) and d_2 (orange).*

2D-$A_3Sb_2X_9$	Lattice parameters / f.u. (Å)			Stacking (Å)	
	a	b	c	d_1	d_2
$Cs_3\,Sb_2\,I_9$	8.30	8.30	10.23	6.95	3.28
$Cs_{2.4}\,FA_{0.6}\,Sb_2\,I_9$	8.55	8.37	10.24	6.93	3.31
$Cs_{2.4}\,MA_{0.6}\,Sb_2\,I_9$	8.43	8.35	10.28	6.97	3.31
$Cs_{2.4}\,MA_{0.5}\,FA_{0.1}\,Sb_2\,I_9$	8.45	8.36	10.27	6.96	3.31
$Cs_{2.4}\,MA_{0.5}\,FA_{0.1}\,Sb_2\,I_{8.5}\,Cl_{0.5}$	8.42	8.32	10.24	6.94	3.29

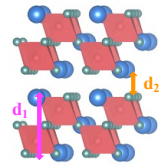

To achieve a high device performance, one should require no effect of mix A and X cation on nature of nearly direct band $Cs_3Sb_2I_9$ gap. On one hand, analysing the projected density of states (pDOS) (Figure A1.2), we found that the valence band mainly consists of the s–p interaction from the hybridization of Sb(5s) and I(5p) atomic orbitals, while the conduction band is given by the strong p–p interactions resulting from the overlap of I(5p)–Sb(5p). Plus, as the Cs-cations, the MA/FA cations give no direct contribution to the valence band maximum (VBM) and conduction band maximum (CBM). These findings are consistent with the electronic structure of the full-inorganic material.[259,266] On the other, the band energy structures in Figure A1.3 highlight that all the mixed inorganic–organic PIMs preserve the quasi-direct band gap. Plus, only the $Cs_{2.4}MA_{0.5}FA_{0.1}Sb_2I_{8.5}Cl_{0.5}$ composition shows a slight increase of ~0.1 eV (~5%) for both direct and indirect band gap, with also a decrease of difference between the two types of gaps (~0.04 eV).

Overall, our DFT results highlight that the triple-cation $Cs_{2.4}MA_{0.5}FA_{0.1}Sb_2I_{8.5}Cl_{0.5}$ Sb-PIM shows both desired structural and electronic features: stable 2D layered phase, closer to the full inorganic material, and also nearly direct band gap, suitable for efficient indoor light-harvesting.

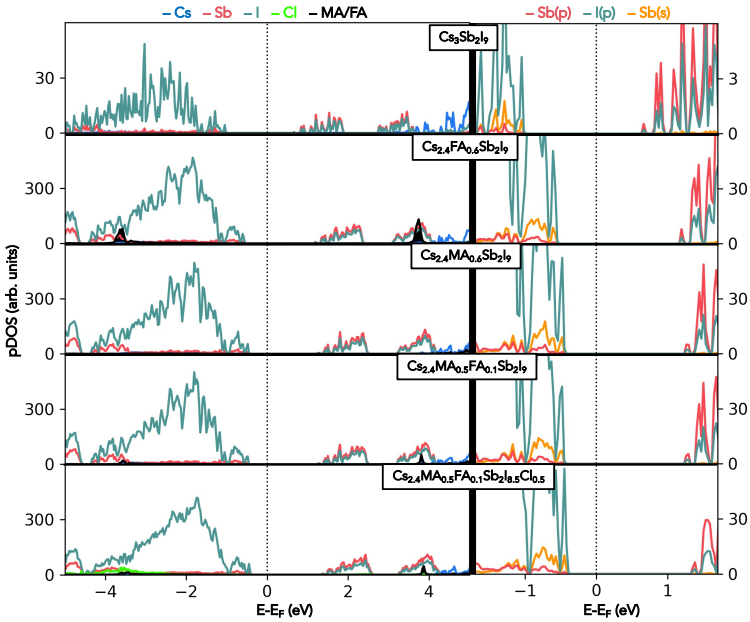

Figure A1.2 *Projected density of states (pDOS) of the 2D- $A_3Sb_2X_9$ PIMs with A = Cs, FA, MA and X = I, Cl. Color code left panel: Cs (blue), Sb (red), I (teal), Cl (green), MA/FA (black) (on left). Color code right panel: p-states Sb (red), s-states Sb (orange), p-states I (teal).*

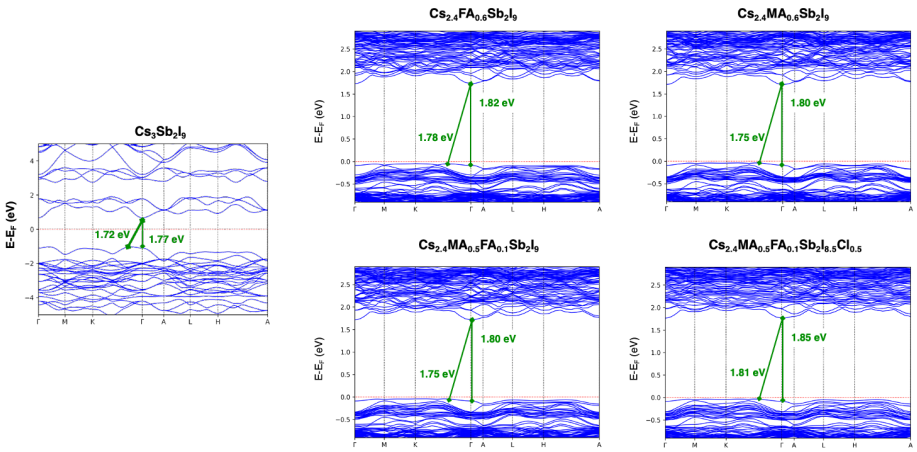

Figure A1.3. *Computed band structure of the full inorganic 2D-$Cs_3Sb_2I_9$ PIMs (left panel) and 2D-$A_3Sb_2X_9$ PIMs with A = Cs, FA, MA and X = I, Cl (right panel). The values of direct and indirect band gaps (green lines) are also reported.*

To sum up, our theoretical and experimental characterization of CsMAFA-Sb highlights the suitable structural and electronic features and high performances of this PIM in solar cells, encouraging future design of harvesting material with low toxicity, high stability, and low defect density for high-performance IPVs.

Computational Details: The hybrid organic-inorganic $A_3Sb_2X_9$ PIM derivatives have been built up by a 2x2x4 supercell of full inorganic material (A=Cs and X=I) containing 16 f.u. In this way, the resulting $Cs_{2.4}MA_{0.5}FA_{0.1}Sb_2I_{8.5}Cl_{0.5}$ supercell delivers the exact stoichiometry of the experimental structures (Figure A1.1). We have performed PBC-DFT calculations employing the light-tier1 basis set of NAO for each atom, as implemented in the FHI-aims code.[75] As self- consistency threshold for electron density convergence, a total energy criterion of 1×10^{-6} eV was employed. The PBE[26,27] exchange-correlation functional was employed for all geometry optimizations including the Tkatchenko–Scheffler (TS) correction[41] accounting for van der Waals dispersion forces. Our relaxed structures present maximum forces acting on each atom below 0.02 eV $Å^{-1}$. For the $Cs_3Sb_2I_9$, the Γ-centered (4×4×4) k-points sampling mesh had been used; these values ensure converged energies within 3 meV/f.u, while the (2×2×1) k-point scheme had been used for all the other structures. The mixed occupancy of Cs/MA/FA was simulated via the special quasi-random structure (SQS) approach as implemented in the Alloy Theoretic Automated Toolkit code.[267,268] The special quasi-random structure (SQS) is a state-of-the-art method to study solid solutions with two or more components and allowed our models to properly account for the configurational entropy by achieving a mixed occupancy. Since the PBE functional usually underestimate the band energy gap, the HSE06 hybrid functional to calculate the projected density of states (pDOS) and the band energy structures on the PBE minimum-energy structures were employed.

A2. New Iridium Complex as Colourless Luminescent Solar Concentrators.

Luminescent solar concentrators (LSCs) can enhance the intensity of incident light in solar cells, also leading an increase of energy production.[269,270] These technologies consist usually of homogeneous dispersion of organic dyes, e.g. red-emitting fluorophore, into a suitable, transparent polymeric matrix. In this framework, the luminescent Ir(III) cyclometalated complexes have emerged as a valid alternative to organic dyes. This latter would involve emission from only the singlet excited states, while the metal complexes can have both singlet and triplet emissive states. This feature can have a key role in development of polymer-based technologies as LSCs.

To this aims, the groups of Professor Pucci and Stagni designed and prepared two new red-emitting Ir(III) tetrazole complexes $[Ir(C^N)_2(iQTZ\text{-}PPG)]^+$ with ppy (2-phenylpyridine) or npy (2-(naphthalen-2-yl)pyridine) as (C^N) ligand (iQTZ-PPG, here, is abbreviation for 1-(2-(prop-2-yn-1-yl)-2*H*-tetrazol-5-yl)isoquinoline) (Figure A2.1a). These two complexes were then physically dispersed into different polymers, resulting in auspicious for the colorless LSCs development. In particular, photophysical characterizations highlight that the corresponding diluted solutions in dichloromethane (CH_2Cl_2) at 298 K display an absorption and red emission peak at λ_{max} ~350 nm and ~600 nm, respectively (Figure A2.1b,c). Plus, the broad, unstructured shape of the emission profiles and susceptibility to dissolved dioxygen suggest the prevalent charge transfer (CT) nature and triplet multiplicity of the emissive excited states.

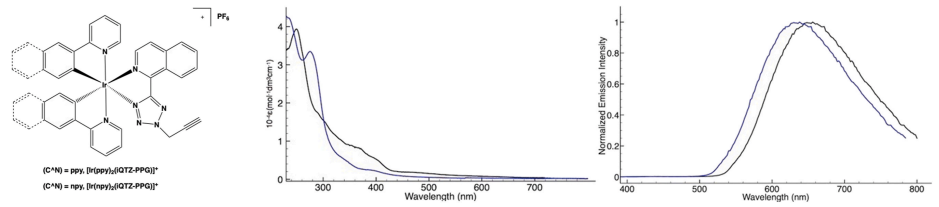

***Scheme A2.1 a**. Ir(III) complexes and relative acronyms employed in the work [..]. **b.** Absorption and **c.** normalized emission (λ_{exc} = 350 nm) profiles of $[Ir(ppy)_2(iQTZ\text{-}PPG)]^+$ (black line) and $[Ir(npy)_2(iQTZ\text{-}PPG)]^+$ (blue line), CH_2Cl_2, 298 K.*

Atomistic investigation can support these experimental results, unveiling the electronic structures of the two proposed complexes. To this aim, we performed DFT and TD-DFT simulations including the implicit effect of solvent.

Consistent with similar Ir(III) tetrazole complexes[271–273], analysis of the molecular orbitals (MOs) of the ground electronic states revealed that both Ir(III) complexes show high-occupied MO (HOMO) levels mainly localized on the metal center and the cyclometalated ligands (ppy and spy), while only the lower-unoccupied MO (LUMO) level is only given by π-conjugated system of the tetrazole ligand (iQTZ-PPG) (Figure A2.2).

Concerning the vertical excitation energies for the spin-allowed electronic transitions (Table A2.1), we found that intense high-energy absorption bands consist of transitions on one ligand (LC), with λ_{cal} = 302/335 and 324/332 nm for $[Ir(ppy)_2(iQTZ\text{-}PPG)]^+$ and $[Ir(npy)_2(iQTZ\text{-}PPG)]^+$, respectively, in remarkable agreement with experimental data. In particular, these LC transitions mostly involve the (npy) ligands into $[Ir(npy)_2(iQTZ\text{-}PPG)]^+$, while in other complex, $[Ir(ppy)_2(iQTZ\text{-}PPG)]^+$, both (ppy) and (iQTZ-PPG). Otherwise, the lower energy bands beyond 400 nm are given by a metal-to-ligand (MLCT and ligand-to-ligand (LLCT) transition.

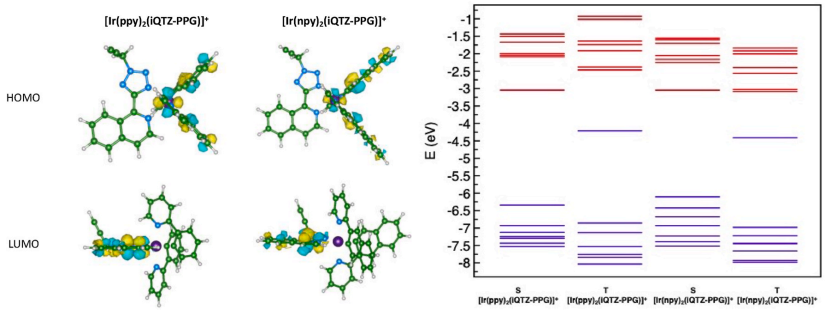

Figure A2.2 *(Left) Minimum-energy geometries and isodensity surface plots of the HOMO and LUMO of* $[Ir(ppy)_2(iQTZ\text{-}PPG)]^+$ *and* $[Ir(npy)_2(iQTZ\text{-}PPG)]^+$ *(isosurface value 0.005 a.u.). Color legend: C (green), N (blu), Ir (purple), H (white); isodensity positive and negative values are in yellow and cyan, respectively; (right) Energy level diagram from HOMO-6 to LUMO+6 for both singlet (S) and triplet (T) optimized geometries: occupied orbital (blue), unoccupied orbital (red).*

Table A2.1 *TD-DFT calculated lowest excited singlet states and character of the transitions for the two complexes. The* ΔE_{calc}, λ_{calc} *and* f *are the main transition energies, the calculated* λ_{max} *and the oscillator strength, respectively. Electron transition assignment derives from analysis of main Khon-Sham orbital contribution to the electronic transition.*

Complex	ΔE_{cal} (eV)	λ_{cal} (nm)	f	Electronic tranisition assignment	Nature of transition
$[Ir(ppy)_2(iQTZ\text{-}PPG)]^+$	4.11	302	0.077	HOMO-1 → LUMO+3 (54%)	LC
				HOMO-2 → LUMO+2 (24%)	
	3.70	335	0.128	HOMO-6 → LUMO (68%)	LC
	3.45	359	0.078	HOMO → LUMO+2 (41%)	MLCT+LLCT
				HOMO-3 → LUMO (37%)	
	3.31	374	0.072	HOMO → LUMO+1 (66%)	MLCT+LC
	2.50	496	0.001	HOMO → LUMO (70%)	MLCT+LLCT
$[Ir(npy)_2(iQTZ\text{-}PPG)]^+$	3..83	324	0.208	HOMO-2 → LUMO+2 (46%)	LC+MLCT
				HOMO → LUMO+6 (43%)	
	3.73	332	0.341	HOMO-2 → LUMO+1 (59%)	LC+MLCT
				HOMO → LUMO+4 (27%)	
	3.49	354	0.191	HOMO-1 → LUMO+1 (50%)	LC+MLCT
				HOMO-5 → LUMO (44%)	
	3.04	407	0.040	HOMO → LUMO+1 (68%)	LC+MLCT
	2.35	526	0.0002	HOMO → LUMO (69%)	MLCT+LLCT

Because the experiment suggests the triplet state as the final excited state, from which emission occurs, we also optimized the two complexes with this spin multiplicity. We found no significant structural variations between singlet and triplet minimum-energy geometries, except for a slight shrinking of distances between one of the two cyclometalated ligands (ppy or npy) and the chelate tetrazole ligand (iQTZ-PPG). The triplet state is mostly localized on this latter ligand, consistently with the positions of the LUMOs in the singlet states. The computed vertical emission transition from this spin state lies in the red region at λ_{em} = 574 and 616 nm for $[Ir(ppy)_2(iQTZ\text{-}PPG)]^+$ and $[Ir(npy)_2(iQTZ\text{-}PPG)]^+$, respectively, and can be ascribed to MLCT-LLCT spin-forbidden transitions, as observed experimentally.

In conclusion, our theoretical investigation supported the experimental findings and unveiled the charge transfer (CT) nature and triplet multiplicity of the emissive excited states. This study, combining theoretical and experimental data, also highlighted the potentiality of these complexes and can pave the route for the design of new hybrid LSCs.

Computational Details: Theoretical calculations were carried out with the Gaussian16 program.[274] The optimization of the geometries for both singlet ground-state and first triplet-excited state was carried out by using the DFT method at the PBE0(D3-BJ).[30,40] We employed the SDD effective core potential and basis sets[275] for Ir and the 6–31++G (d,p) basis set[73] for N, C and H atoms. Such an approach has been recently validated for similar Ir(III) complexes.[276] The absence of negative frequencies in the vibrational analysis was used as a parameter to confirm the reliability of the optimized geometries. Vertical excitation energies have been computed by using the time-dependent DFT (TD-DFT) with the optimized singlet ground-state geometries. In all calculations, we took into account the solvent medium by means of the PCM of implicit solvation[97] with default parameters for dichloromethane (CH_2Cl_2), as implemented in Gaussian16.

Reproduced [253] with permission from Elsevier.

A3. Unusual Coordination between Dirhodium Complex and Imidazole in a Protein Environment.

Dirhodium(II) ($Rh_2(II)$) complexes have emerged as efficient catalysts for several reactions, including H_2 evolution and CO_2 reduction.[277,278] Due to their favorable interaction with peptides and proteins, these complexes have also a key role in the synthesis of metalloenzymes with efficient catalytic properties.[279] In this framework, the group of Professor Merlino characterized the adduct formed upon the reaction of $Rh_2(II)$ tetraacetate complexes ($[Rh_2(\mu\text{-}O_2CCH_3)_4]$) with the protein bovine pancreatic ribonuclease (RNaseA).[280] Plus, to verify the $Rh_2(II)$ complex reactivity upon formation of the complex-protein adduct at the crystal state, they solved the X-ray structure of the reaction product of this $Rh_2(II)$/RNaseA adduct with imidazole (Im). Unexpectedly, they found that the Im reacts with the complex-protein adduct, coordinating the $Rh_2(II)$ center in equatorial position, rather than in the typical axial site.[281] To shed light on the origin of this unusual coordination, by means of DFT approach, we investigated the reactivity and selectivity of the Im molecule with the $Rh_2(II)$/RNaseA adduct.

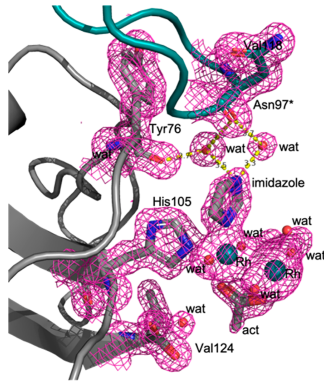

Figure A3.1 *Imidazole (Im) binding site in the structure of RNase A treated with $[Rh_2(\mu\text{-}O_2CCH_3)_4]$ and then with Im. The dirhodium center is coordinated to the side chain of His105. The 2Fo − Fc electron density map is reported at 1.0 σ and colored in pink.*

We started by carving a small cluster of the adduct from the crystal structure, hereafter named Rh_2(His)(μ-O_2CCH_3)(H_2O)$_7$, and characterized the replacement of one H_2O ligand with an Im molecule. In particular, there are three possibilities for the substitution of H_2O: in axial position opposite to His105 (ax), in equatorial to the second Rh atom (r2) or to the Rh atom coordinated with His105 (r). (Figure A3.2a). For a comparison, we also used a minimal model, neglecting the protein environment and replacing the His105 with another Im molecule (Figure A3.2b). Meanwhile, to account for the dielectric properties of the chemical environment, we considered an implicit water solvent, due to the exposition of dirhodium adduct to aqueous solution.

For all of these substitutions (Figure A3.2), we computed the free energies according to:

$$\Delta G = G_p + G_{Im} - G_r - G_{H2O} \qquad (A3.2)$$

where G_{Im} and G_{H2O} are the free energies of isolated imidazole and water molecules, respectively, while G_p and G_r are the free energies of resulting (p) and reactant (r) complexes.

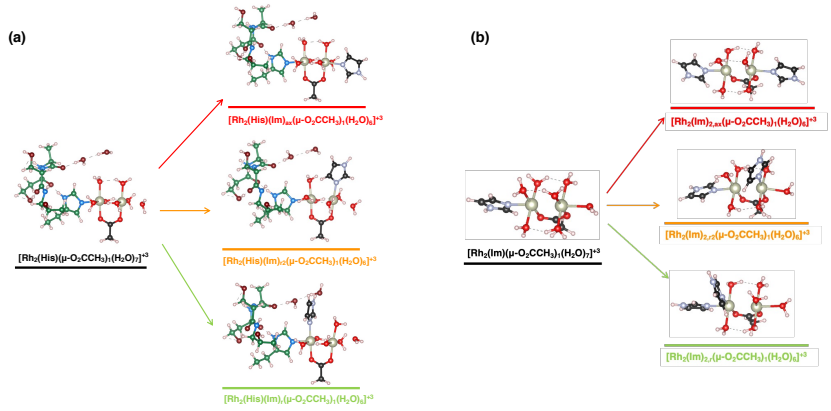

Figure A3.2 *Substitution reactions with inclusion of the second Im molecule for* ***(a)*** *the dirhodium/protein adduct (cluster model) and* ***(b)*** *for the corresponding minimal model. Color code: Rh(silver), O(red), N(blu), C(green/black).*

Table A3.1 *Free-energy variations (ΔG) upon substitution of a water molecule (A3.1) with Im at different coordination sites and relative free energy variations (ΔG_{rel}) with respect to the experimentally found equatorial Site (r)*

		ax	r2	r
ΔG (eV)	**Cluster model**	-0.398	-1.004	-1.173
	Minimal model	-0.482	-0.940	-1.003
ΔG_{rel} (eV)	**Cluster model**	0.776	0.169	0.0
	Minimal model	0.544	0.081	0.0

Comparison of the cluster and minimal models highlights that the protein environment enhances the thermodynamic driving force for coordination of Im at equatorial site (r). Nevertheless, the minimal model predicts the same trend, with equatorial (r) position favorite against the other ones, consistently with experiments. This finding allows to employ this model for further investigation into this unusual coordination.

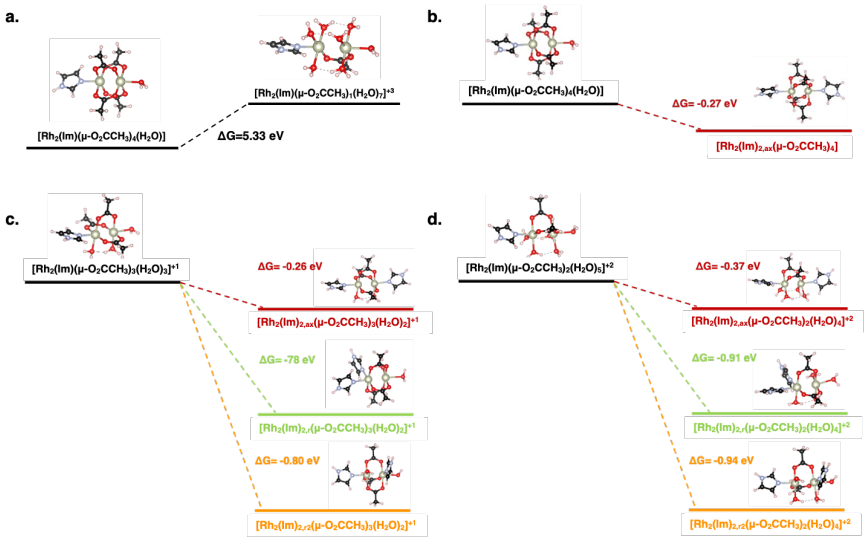

Figure A3.3 *Substitution free energies for water molecules by three μ-O_2CCH_3 (a) and Im on different sites. All possible adducts with f our (b), three (c) and two (d) acetate ligands are considered. Color code: as Figure A3.2*

The effect of degree of hydrolysis is also considered comparing the substitution reactions (from H_2O to Im) on different sites for adducts with four, three, and two acetate ligands (Figure A3.3), with also the highly hydrolyzed [Rh_2(Im)(μ-O_2CCH_3)(H_2O)$_7$] specie. Noteworthy, we found that the formation of isolated hydrated species is not favorite (Figure A3.3a), so that other degrees of hydrolysis, but in the protein, the environment can balance the thermodynamics for this process by providing convenient coordination spots for the leaving acetate groups and extra stabilization via the second-shell hydrogen-bond network. Plus, we found that Im coordination in axial position is less favourite for all hydrolysis degrees, while the (Im)$_{2,r}$ complex becomes the most stable over the other (Im)$_{2,r2}$ only for the adduct with one acetate group.

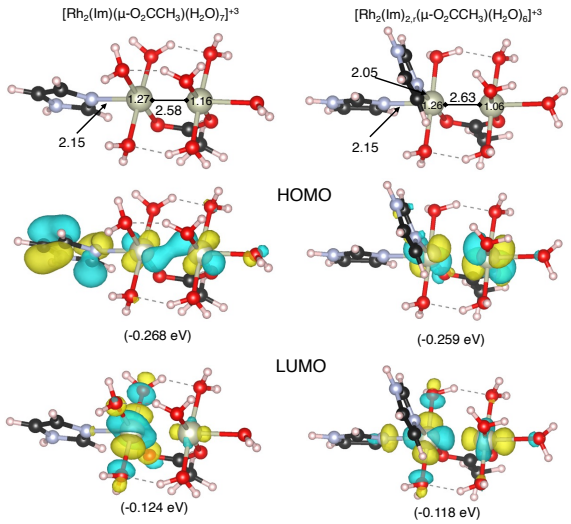

Figure A3.4 *Top panel: Computed Bader charges on rhodium atoms and selected distances for [Rh_2(Im)(μ-O_2CCH_3)(H_2O)$_7$] and [Rh_2(Im)$_{2,r}$(μ-O_2CCH_3)(H_2O)$_6$]. Central (bottom) panel: HOMO (LUMO) of both adducts and corresponding energies. Color code as in Figure A3.2, in which the isodensity surfaces are depicted as yellow and cyan for positive and negative values, respectively. The distances and Bader's effective charges are reported for rhodium in the top panel, and the HOMO and LUMO energies are reported in parentheses.*

Bader charges analysis of the $[Rh_2(Im)(\mu\text{-}O_2CCH_3)(H_2O)_7]$ complex in Figure A3.4 reveals that the two rhodium atoms are not equivalent. The Rh atom bound to Im(His105 in protein adduct) has slightly more positive charge than the other one. This result suggests that this Rh bound to Im can act as a better Lewis acid site for the second Im, leading to the observed product with equatorial Im, $(Im)_r$. Detailed analysis of molecular orbitals (MO) also reveals that the HOMO and LUMO orbitals differ for the $[Rh_2(Im)(\mu\text{-}O_2CCH_3)(H_2O)_7]$ and $[Rh(Im)_{2,r}(\mu\text{-}O_2CCH_3)(H_2O)_6]$ complexes. Contrary to the full hydroxylated complex, the HOMO is not more localized on the axial Im, while the second Rh atom contributes to the LUMO (Figure A3.4). The peculiar electronic features of the resulting $(Im)_r$ complex can also affect the (photo)catalytic activity.

In conclusion, our combined experimental and theoretical results unveiled an unexpected equatorial coordination of imidazole molecule to the adduct of dirhodium(II,II) tetraacetate/RNaseA, that can also affect the metal compound efficacy and reactivity.

Computational Details: DFT calculations were performed with Gaussian16.[274] The TZVP basis set was used for C, N, H and O atoms and the SDD effective core potential (ECP) and basis set for Rh.[275] Structural optimizations, molecular frequencies, and thermochemistry data were obtained at the B3LYP (D3-BJ), level of theory.[28,29,40] The water solvent is considered with the PCM model.[97] We tested also the SMD model[98] of implicit solvation on selected structures and compare it to PCM, but we found no significant differences with PCM, and we kept this last model. The default maximum force and displacement tolerance parameters in Gaussian were considered for the ground-state minimum-energy structures. Molecular frequencies were computed within the harmonic oscillator approximation, and the thermochemical data were computed at room temperature (298 K).

List of Publications

Several cases of study in this Ph.D. thesis are object of the following publications:

- Less is more: simplified fluorene-based dopant-free hole-transport materials promote the long-term ambient stability of perovskite solar cells
*P. Mäkinen, **F. Fasulo**, M. Liu, G. K. Grandhi, D. Conelli, B. Al-Anesi, H. Ali-Löytty, K. Lahtonen, S. Toikkonen, G. P. Suranna, A. B. Muñoz-García, M. Pavone, R. Grisorio, P. Vivo. Paola. Chem. Mater. (2023) Accepted Manuscript.*

- Vinylene carbonate reactivity at lithium metal surface: first-principles insights on the early steps of SEI formation
***F. Fasulo**, A. B. Munoz-Garcia, A. Massaro, O. Crescenzi, C. Huang, M. Pavone. J. Mater. Chem. A (2023) Accepted Manuscript.*

- Triple A-Site Cation Mixing in 2D Perovskite-Inspired Antimony Halide Absorbers for Efficient Indoor Photovoltaics
*N. Lamminen, G. K. Grandhi, **F. Fasulo,** A. Hiltunen, H. Pasanen, M. Liu, B. Al-Anesi, A. Efimov, H. Ali-Löytty, K. Lahtonen, P. Mäkinen, A. Matuhina, A. B. Muñoz-García, M. Pavone, P. Vivo. Adv. Energy Mater. (2022), 2203175.*

- In Situ Formation of Zwitterionic Ligands: Changing the Passivation Paradigms of $CsPbBr_3$ Nanocrystals
*R. Grisorio, **F. Fasulo**, A. B. Muñoz-García, M. Pavone, D. Conelli, E. Fanizza, M. Striccoli, I. Allegretta, R. Terzano, N. Margiotta, P. Vivo, G. P. Suranna. Nano Lett. 22, (2022), 4437–4444.*

- Unexpected Imidazole Coordination to the Dirhodium Center in a Protein Environment: Insights from X-Ray Crystallography and Quantum Chemistry
*D. Loreto, **F. Fasulo**, A.B. Muñoz-García, M. Pavone, A. Merlino. Inorg. Chem. 61, (2022), 8402–8405.*

- Dynamics of Water Dissociative Adsorption on TiO_2 Anatase (101) at Monolayer Coverage and Below
***F. Fasulo,** G. Piccini, A. B. Muñoz-García, M. Pavone, M. Parrinello. J. Phys. Chem. C 126 (2022), 15752–15758.*

- Na Uptake at TiO_2 Anatase Surfaces under Electric Field Control: A First-Principles Study
***F. Fasulo,** A. Massaro, A. B. Muñoz-García, M. Pavone. J. Mater. Res. 37 (2022), 3216–3226.*

- Colourless Luminescent Solar Concentrators Based on Iridium(III)-Phosphors.
*V. Fiorini, N. Monti, G. Vigarani, G. Santi, **F. Fasulo,** M. Massi, L. Giorgini, A.B. Muñoz-García, M. Pavone, A. Pucci, S. Stagni. Dyes and Pigments 2021, 193.*

Bibliography

(1) Schlögl, R. The Role of Chemistry in the Energy Challenge. ChemSusChem 2010, 3 (2), 209–222. https://doi.org/10.1002/cssc.200900183.

(2) Kabeyi, M. J. B.; Olanrewaju, O. A. Sustainable Energy Transition for Renewable and Low Carbon Grid Electricity Generation and Supply. Front Energy Res 2022, 9. https://doi.org/10.3389/fenrg.2021.743114.

(3) Badwal, S. P. S.; Giddey, S. S.; Munnings, C.; Bhatt, A. I.; Hollenkamp, A. F. Emerging Electrochemical Energy Conversion and Storage Technologies. Front Chem 2014, 2. https://doi.org/10.3389/fchem.2014.00079.

(4) Hwang, J.-Y.; Myung, S.-T.; Sun, Y.-K. Sodium-Ion Batteries: Present and Future. Chem Soc Rev 2017, 46 (12), 3529–3614. https://doi.org/10.1039/C6CS00776G.

(5) Dunn, B.; Kamath, H.; Tarascon, J.-M. Electrical Energy Storage for the Grid: A Battery of Choices. Science (1979) 2011, 334 (6058), 928–935. https://doi.org/10.1126/science.1212741.

(6) Menictas, C. M. S.-K. and T. M. L. Advances in Batteries for Medium and Large-Scale Energy Storage: Types and Applications.; Elsevier, 2014.

(7) Mohammad Bagher, A. Types of Solar Cells and Application. American Journal of Optics and Photonics 2015, 3 (5), 94. https://doi.org/10.11648/j.ajop.20150305.17.

(8) Correa-Baena, J.-P.; Saliba, M.; Buonassisi, T.; Grätzel, M.; Abate, A.; Tress, W.; Hagfeldt, A. Promises and Challenges of Perovskite Solar Cells. Science (1979) 2017, 358 (6364), 739–744. https://doi.org/10.1126/science.aam6323.

(9) Park, N.-G.; Grätzel, M.; Miyasaka, T.; Zhu, K.; Emery, K. Towards Stable and Commercially Available Perovskite Solar Cells. Nat Energy 2016, 1 (11), 16152. https://doi.org/10.1038/nenergy.2016.152.

(10) Grätzel, M. Photoelectrochemical Cells. Nature 2001, 414 (6861), 338–344. https://doi.org/10.1038/35104607.

(11) White, J. L.; Baruch, M. F.; Pander, J. E.; Hu, Y.; Fortmeyer, I. C.; Park, J. E.; Zhang, T.; Liao, K.; Gu, J.; Yan, Y.; Shaw, T. W.; Abelev, E.; Bocarsly, A. B. Light-Driven Heterogeneous Reduction of Carbon Dioxide: Photocatalysts and Photoelectrodes. Chem Rev 2015, 115 (23), 12888–12935. https://doi.org/10.1021/acs.chemrev.5b00370.

(12) Wang, M.; Feng, Z. Interfacial Processes in Electrochemical Energy Systems. Chem Comm 2021, 57 (81), 10453–10468. https://doi.org/10.1039/D1CC01703A.

(13) Pham, T. A.; Ping, Y.; Galli, G. Modelling Heterogeneous Interfaces for Solar Water Splitting. Nat Mater 2017, 16 (4), 401–408. https://doi.org/10.1038/nmat4803.

(14) Gao, W.; Hood, Z. D.; Chi, M. Interfaces in Heterogeneous Catalysts: Advancing Mechanistic Understanding through Atomic-Scale Measurements. Acc Chem Res 2017, 50 (4), 787–795. https://doi.org/10.1021/acs.accounts.6b00596.

(15) Shao, S.; Loi, M. A. The Role of the Interfaces in Perovskite Solar Cells. Adv Mater Interfaces 2020, 7 (1), 1901469. https://doi.org/10.1002/admi.201901469.

(16) Shi, S.; Gao, J.; Liu, Y.; Zhao, Y.; Wu, Q.; Ju, W.; Ouyang, C.; Xiao, R. Multi-Scale Computation Methods: Their Applications in Lithium-Ion Battery Research and

Development. Chin Phys B 2016, 25 (1), 018212. https://doi.org/10.1088/1674-1056/25/1/018212.

(17) Verkhovtsev, A. v.; Solov'yov, I. A.; Solov'yov, A. v. Advances in Multiscale Modeling for Novel and Emerging Technologies. The European Physical Journal D 2021, 75 (7), 207. https://doi.org/10.1140/epjd/s10053-021-00213-5.

(18) Pavone, M.; Caspary Toroker, M. Toward Ambitious Multiscale Modeling of Nanocrystal Catalysts for Water Splitting. ACS Energy Lett 2020, 5 (6), 2042–2044. https://doi.org/10.1021/acsenergylett.0c01086.

(19) Attila Szabo, N. S. O. Modern Quantum Chemistry: Introduction to Advanced Electronic Structure Theory; new york: dover publishing, Ed.; 1996.

(20) Roos, B. O.; Taylor, P. R.; Sigbahn, P. E. M. A Complete Active Space SCF Method (CASSCF) Using a Density Matrix Formulated Super-CI Approach. Chem Phys 1980, 48 (2), 157–173. https://doi.org/10.1016/0301-0104(80)80045-0.

(21) Andersson, K.; Malmqvist, P.; Roos, B. O. Second-order Perturbation Theory with a Complete Active Space Self-consistent Field Reference Function. J Chem Phys 1992, 96 (2), 1218–1226. https://doi.org/10.1063/1.462209.

(22) Angeli, C.; Cimiraglia, R.; Evangelisti, S.; Leininger, T.; Malrieu, J.-P. Introduction of n -Electron Valence States for Multireference Perturbation Theory. J Chem Phys 2001, 114 (23), 10252–10264. https://doi.org/10.1063/1.1361246.

(23) Finley, J.; Malmqvist, P.-Å.; Roos, B. O.; Serrano-Andrés, L. The Multi-State CASPT2 Method. Chem Phys Lett 1998, 288 (2–4), 299–306. https://doi.org/10.1016/S0009-2614(98)00252-8.

(24) Dyall, K. G. The Choice of a Zeroth-order Hamiltonian for Second-order Perturbation Theory with a Complete Active Space Self-consistent-field Reference Function. J Chem Phys 1995, 102 (12), 4909–4918. https://doi.org/10.1063/1.469539.

(25) Wolfram Koch and Max C. Holthause. A Chemist's Guide to Density Functional Theory; Wiley-VCH, Ed.; 2001.

(26) Perdew, J. P.; Burke, K.; Ernzerhof, M. Generalized Gradient Approximation Made Simple [Phys. Rev. Lett. 77, 3865 (1996)]. Phys Rev Lett 1997, 78 (7), 1396–1396. https://doi.org/10.1103/PhysRevLett.78.1396.

(27) Perdew, J. P.; Burke, K.; Ernzerhof, M. Generalized Gradient Approximation Made Simple. Phys Rev Lett 1996, 77 (18), 3865–3868. https://doi.org/10.1103/PhysRevLett.77.3865.

(28) Lee, C.; Yang, W.; Parr, R. G. Development of the Colle-Salvetti Correlation-Energy Formula into a Functional of the Electron Density. Phys Rev B 1988, 37 (2), 785–789. https://doi.org/10.1103/PhysRevB.37.785.

(29) Becke, A. D. A New Mixing of Hartree–Fock and Local Density-functional Theories. J Chem Phys 1993, 98 (2), 1372–1377. https://doi.org/10.1063/1.464304.

(30) Adamo, C.; Barone, V. Toward Reliable Density Functional Methods without Adjustable Parameters: The PBE0 Model. J Chem Phys 1999, 110 (13), 6158–6170. https://doi.org/10.1063/1.478522.

(31) Heyd, J.; Scuseria, G. E.; Ernzerhof, M. Hybrid Functionals Based on a Screened Coulomb Potential. J Chem Phys 2003, 118 (18), 8207–8215. https://doi.org/10.1063/1.1564060.

(32) Bao, J. L.; Gagliardi, L.; Truhlar, D. G. Self-Interaction Error in Density Functional Theory: An Appraisal. J Phys Chem Lett 2018, 9 (9), 2353–2358. https://doi.org/10.1021/acs.jpclett.8b00242.

(33) Verma, P.; Truhlar, D. G. Does DFT+U Mimic Hybrid Density Functionals? Theor Chem Acc 2016, 135 (8), 182. https://doi.org/10.1007/s00214-016-1927-4.

(34) Lutfalla, S.; Shapovalov, V.; Bell, A. T. Calibration of the DFT/GGA+U Method for Determination of Reduction Energies for Transition and Rare Earth Metal Oxides of Ti, V, Mo, and Ce. J Chem Theory Comput 2011, 7 (7), 2218–2223. https://doi.org/10.1021/ct200202g.

(35) Anisimov, V. I.; Zaanen, J.; Andersen, O. K. Band Theory and Mott Insulators: Hubbard U Instead of Stoner I. Phys Rev B 1991, 44 (3), 943–954. https://doi.org/10.1103/PhysRevB.44.943.

(36) Wang, L.; Maxisch, T.; Ceder, G. Oxidation Energies of Transition Metal Oxides within the GGA+ U Framework. Phys Rev B 2006, 73 (19), 195107. https://doi.org/10.1103/PhysRevB.73.195107.

(37) Hadjittofis, E.; Das, S. C.; Zhang, G. G. Z.; Heng, J. Y. Y. Interfacial Phenomena. In Developing Solid Oral Dosage Forms; Elsevier, 2017; pp 225–252. https://doi.org/10.1016/B978-0-12-802447-8.00008-X.

(38) Hermann, J.; Tkatchenko, A. Van Der Waals Interactions in Material Modelling. In Handbook of Materials Modeling; Springer International Publishing: Cham, 2018; pp 1–33. https://doi.org/10.1007/978-3-319-42913-7_6-1.

(39) Grimme, S.; Antony, J.; Ehrlich, S.; Krieg, H. A Consistent and Accurate Ab Initio Parametrization of Density Functional Dispersion Correction (DFT-D) for the 94 Elements H-Pu. J Chem Phys 2010, 132 (15), 154104. https://doi.org/10.1063/1.3382344.

(40) Grimme, S.; Ehrlich, S.; Goerigk, L. Effect of the Damping Function in Dispersion Corrected Density Functional Theory. J Comput Chem 2011, 32 (7), 1456–1465. https://doi.org/10.1002/jcc.21759.

(41) Tkatchenko, A.; Scheffler, M. Accurate Molecular Van Der Waals Interactions from Ground-State Electron Density and Free-Atom Reference Data. Phys Rev Lett 2009, 102 (7), 073005. https://doi.org/10.1103/PhysRevLett.102.073005.

(42) Brinck, T.; Murray, J. S.; Politzer, P. Polarizability and Volume. J Chem Phys 1993, 98 (5), 4305–4306. https://doi.org/10.1063/1.465038.

(43) Hirshfeld, F. L. Bonded-Atom Fragments for Describing Molecular Charge Densities. Theor Chim Acta 1977, 44 (2), 129–138. https://doi.org/10.1007/BF00549096.

(44) Bloch, F. Über die Quantenmechanik der Elektronen in Kristallgittern. Zeitschrift für Physik 1929, 52 (7–8), 555–600. https://doi.org/10.1007/BF01339455.

(45) Ashcroft. Solid State Physic; Cengage Learning Emea., Ed.; 2003.

(46) Kratzer, P.; Neugebauer, J. The Basics of Electronic Structure Theory for Periodic Systems. Front Chem 2019, 7. https://doi.org/10.3389/fchem.2019.00106.

(47) Methfessel, M.; Paxton, A. T. High-Precision Sampling for Brillouin-Zone Integration in Metals. Phys Rev B 1989, 40 (6), 3616–3621. https://doi.org/10.1103/PhysRevB.40.3616.

(48) Sun, W.; Ceder, G. Efficient Creation and Convergence of Surface Slabs. Surf Sci 2013, 617, 53–59. https://doi.org/10.1016/j.susc.2013.05.016.

(49) Seifert, G. Tight-Binding Density Functional Theory: An Approximate Kohn−Sham DFT Scheme. J Phys Chem A 2007, 111 (26), 5609–5613. https://doi.org/10.1021/jp069056r.

(50) Spiegelman, F.; Tarrat, N.; Cuny, J.; Dontot, L.; Posenitskiy, E.; Martí, C.; Simon, A.; Rapacioli, M. Density-Functional Tight-Binding: Basic Concepts and Applications to Molecules and Clusters. Adv Phys X 2020, 5 (1), 1710252. https://doi.org/10.1080/23746149.2019.1710252.

(51) Verma, S.; Rivera, M.; Scanlon, D. O.; Walsh, A. Machine Learned Calibrations to High-Throughput Molecular Excited State Calculations. J Chem Phys 2022, 156 (13), 134116. https://doi.org/10.1063/5.0084535.

(52) Lipp, V.; Tkachenko, V.; Stransky, M.; Aradi, B.; Frauenheim, T.; Ziaja, B. Density Functional Tight Binding Approach Utilized to Study X-Ray-Induced Transitions in Solid Materials. Sci Rep 2022, 12 (1), 1551. https://doi.org/10.1038/s41598-022-04775-1.

(53) Lee, K. H.; Schnupf, U.; Sumpter, B. G.; Irle, S. Performance of Density-Functional Tight-Binding in Comparison to Ab Initio and First-Principles Methods for Isomer Geometries and Energies of Glucose Epimers in Vacuo and Solution. ACS Omega 2018, 3 (12), 16899–16915. https://doi.org/10.1021/acsomega.8b02213.

(54) Selli, D.; Fazio, G.; Seifert, G.; di Valentin, C. Water Multilayers on TiO_2 (101) Anatase Surface: Assessment of a DFTB-Based Method. J Chem Theory Comput 2017, 13 (8), 3862–3873. https://doi.org/10.1021/acs.jctc.7b00479.

(55) Luschtinetz, R.; Frenzel, J.; Milek, T.; Seifert, G. Adsorption of Phosphonic Acid at the TiO_2 Anatase (101) and Rutile (110) Surfaces. J Phys Chem C 2009, 113 (14), 5730–5740. https://doi.org/10.1021/jp8110343.

(56) Vitillo, J. G.; Cramer, C. J.; Gagliardi, L. Multireference Methods Are Realistic and Useful Tools for Modeling Catalysis. Isr J Chem 2022, 62 (1–2). https://doi.org/10.1002/ijch.202100136.

(57) Gaggioli, C. A.; Stoneburner, S. J.; Cramer, C. J.; Gagliardi, L. Beyond Density Functional Theory: The Multiconfigurational Approach to Model Heterogeneous Catalysis. ACS Catal 2019, 9 (9), 8481–8502. https://doi.org/10.1021/acscatal.9b01775.

(58) Sun, Q.; Chan, G. K.-L. Quantum Embedding Theories. Acc Chem Res 2016, 49 (12), 2705–2712. https://doi.org/10.1021/acs.accounts.6b00356.

(59) Huang, P.; Carter, E. A. Self-Consistent Embedding Theory for Locally Correlated Configuration Interaction Wave Functions in Condensed Matter. J Chem Phys 2006, 125 (8), 084102. https://doi.org/10.1063/1.2336428.

(60) Kubas, A.; Berger, D.; Oberhofer, H.; Maganas, D.; Reuter, K.; Neese, F. Surface Adsorption Energetics Studied with “Gold Standard” Wave-Function-Based Ab Initio Methods: Small-Molecule Binding to TiO_2 (110). J Phys Chem Lett 2016, 7 (20), 4207–4212. https://doi.org/10.1021/acs.jpclett.6b01845.

(61) Gerhards, L.; Klüner, T. Theoretical Investigation of CH-Bond Activation by Photocatalytic Excited SO_2 and the Effects of C-, N-, S-, and Se-Doped TiO_2. Phys Chem Chem Phys 2022, 24 (4), 2051–2069. https://doi.org/10.1039/D1CP04335H.

(62) Teusch, T.; Klüner, T. Photodesorption Mechanism of Water on WO_3 (001) – a Combined Embedded Cluster, Computational Intelligence and Wave Packet Approach. Phys Chem Chem Phys 2020, 22 (34), 19267–19274. https://doi.org/10.1039/D0CP02809F.

(63) Kunz, A. B. Embedded Cluster Methods for Surface and Chemisorption Studies. Prog Surf Sci 1987, 26 (1–4), 165–174. https://doi.org/10.1016/0079-6816(87)90056-6.

(64) Liao, P.; Carter, E. A. Optical Excitations in Hematite (α-Fe_2O_3) via Embedded Cluster Models: A CASPT2 Study. J Phys Chem C 2011, 115 (42), 20795–20805. https://doi.org/10.1021/jp206991v.

(65) Seijo, L.; Barandiarán, Z. The Ab Initio Model Potential Method: A Common Strategy for Effective Core Potential and Embedded Cluster Calculations; 1999; pp 55–152. https://doi.org/10.1142/9789812815156_0002.

(66) Hay, P. J.; Wadt, W. R. Ab Initio Effective Core Potentials for Molecular Calculations. Potentials for K to Au Including the Outermost Core Orbitals. J Chem Phys 1985, 82 (1), 299–310. https://doi.org/10.1063/1.448975.

(67) Huang, C.; Pavone, M.; Carter, E. A. Quantum Mechanical Embedding Theory Based on a Unique Embedding Potential. J Chem Phys 2011, 134 (15), 154110. https://doi.org/10.1063/1.3577516.

(68) Huang, C.; Carter, E. A. Potential-Functional Embedding Theory for Molecules and Materials. J Chem Phys 2011, 135 (19), 194104. https://doi.org/10.1063/1.3659293.

(69) Libisch, F.; Huang, C.; Carter, E. A. Embedded Correlated Wavefunction Schemes: Theory and Applications. Acc Chem Res 2014, 47 (9), 2768–2775. https://doi.org/10.1021/ar500086h.

(70) Wu, Q.; Yang, W. A Direct Optimization Method for Calculating Density Functionals and Exchange–Correlation Potentials from Electron Densities. J Chem Phys 2003, 118 (6), 2498. https://doi.org/10.1063/1.1535422.

(71) Huang, C.; Muñoz-García, A. B.; Pavone, M. Effective Scheme for Partitioning Covalent Bonds in Density-Functional Embedding Theory: From Molecules to Extended Covalent Systems. J Chem Phys 2016, 145 (24), 244103. https://doi.org/10.1063/1.4972012.

(72) Yu, K.; Carter, E. A. Extending Density Functional Embedding Theory for Covalently Bonded Systems. Proceedings of the National Academy of Sciences 2017, 114 (51). https://doi.org/10.1073/pnas.1712611114.

(73) Schäfer, A.; Horn, H.; Ahlrichs, R. Fully Optimized Contracted Gaussian Basis Sets for Atoms Li to Kr. J Chem Phys 1992, 97 (4), 2571–2577. https://doi.org/10.1063/1.463096.

(74) Dunning, T. H. Gaussian Basis Sets for Use in Correlated Molecular Calculations. I. The Atoms Boron through Neon and Hydrogen. J Chem Phys 1989, 90 (2), 1007–1023. https://doi.org/10.1063/1.456153.

(75) Blum, V.; Gehrke, R.; Hanke, F.; Havu, P.; Havu, V.; Ren, X.; Reuter, K.; Scheffler, M. Ab Initio Molecular Simulations with Numeric Atom-Centered Orbitals. Comput Phys Commun 2009, 180 (11), 2175–2196. https://doi.org/10.1016/j.cpc.2009.06.022.

(76) Balabin, R. M. Enthalpy Difference between Conformations of Normal Alkanes: Intramolecular Basis Set Superposition Error (BSSE) in the Case of n-Butane and n-Hexane. J Chem Phys 2008, 129 (16), 164101. https://doi.org/10.1063/1.2997349.

(77) van Duijneveldt, F. B.; van Duijneveldt-van de Rijdt, J. G. C. M.; van Lenthe, J. H. State of the Art in Counterpoise Theory. Chem Rev 1994, 94 (7), 1873–1885. https://doi.org/10.1021/cr00031a007.

(78) Ireta, J.; Galván, M. Plane Waves Basis Sets in the Description of Diatomic Anions and Valence Charge Density. J Chem Phys 1996, 105 (18), 8231–8236. https://doi.org/10.1063/1.472701.

(79) Kresse, G.; Furthmüller, J. Efficiency of Ab-Initio Total Energy Calculations for Metals and Semiconductors Using a Plane-Wave Basis Set. Comput Mater Sci 1996, 6 (1), 15–50. https://doi.org/10.1016/0927-0256(96)00008-0.

(80) Massobrio, C.; Ruiz, E. Localized Orbitals vs. Pseudopotential-Plane Waves Basis Sets: Performances and Accuracy for Molecular Magnetic Systems. Monatshefte für Chemie / Chemical Monthly 2003, 134 (2), 317–326. https://doi.org/10.1007/s00706-002-0538-z.

(81) Kresse, G.; Joubert, D. From Ultrasoft Pseudopotentials to the Projector Augmented-Wave Method. Phys Rev B 1999, 59 (3), 1758–1775. https://doi.org/10.1103/PhysRevB.59.1758.

(82) Blöchl, P. E. Projector Augmented-Wave Method. Phys Rev B 1994, 50 (24), 17953–17979. https://doi.org/10.1103/PhysRevB.50.17953.

(83) Hamann, D. R. Generalized Norm-Conserving Pseudopotentials. Phys Rev B 1989, 40 (5), 2980–2987. https://doi.org/10.1103/PhysRevB.40.2980.

(84) Mulliken, R. S. Electronic Population Analysis on LCAO–MO Molecular Wave Functions. I. J Chem Phys 1955, 23 (10), 1833–1840. https://doi.org/10.1063/1.1740588.

(85) Löwdin, P. On the Non-Orthogonality Problem Connected with the Use of Atomic Wave Functions in the Theory of Molecules and Crystals. J Chem Phys 1950, 18 (3), 365–375. https://doi.org/10.1063/1.1747632.

(86) Bader, R. F. W. A Quantum Theory of Molecular Structure and Its Applications. Chem Rev 1991, 91 (5), 893–928. https://doi.org/10.1021/cr00005a013.

(87) Henkelman, G.; Arnaldsson, A.; Jónsson, H. A Fast and Robust Algorithm for Bader Decomposition of Charge Density. Comput Mater Sci 2006, 36 (3), 354–360. https://doi.org/10.1016/j.commatsci.2005.04.010.

(88) Niu, X.; Li, Y.; Shu, H.; Yao, X.; Wang, J. Efficient Carrier Separation in Graphitic Zinc Oxide and Blue Phosphorus van Der Waals Heterostructure. J Phys Chem C 2017, 121 (6), 3648–3653. https://doi.org/10.1021/acs.jpcc.6b12613.

(89) Galvez-Aranda, D. E.; Seminario, J. M. Ab Initio Study of the Interface of the Solid-State Electrolyte $Li_9N_2Cl_3$ with a Li-Metal Electrode. J Electrochem Soc 2019, 166 (10), A2048–A2057. https://doi.org/10.1149/2.0211910jes.

(90) Zelený, M.; Hegedüs, J.; Foster, A. S.; Drabold, D. A.; Elliott, S. R.; Nieminen, R. M. Ab Initio Study of Cu Diffusion in α-Cristobalite. New J Phys 2012, 14 (11), 113029. https://doi.org/10.1088/1367-2630/14/11/113029.

(91) Kunc, K.; Resta, R. External Fields in the Self-Consistent Theory of Electronic States: A New Method for Direct Evaluation of Macroscopic and Microscopic Dielectric

Response. Phys Rev Lett 1983, 51 (8), 686–689. https://doi.org/10.1103/PhysRevLett.51.686.

(92) Resta, R.; Kunc, K. Self-Consistent Theory of Electronic States and Dielectric Response in Semiconductors. Phys Rev B 1986, 34 (10), 7146–7157. https://doi.org/10.1103/PhysRevB.34.7146.

(93) Kirtman, B.; Ferrero, M.; Rérat, M.; Springborg, M. Polarization of One-Dimensional Periodic Systems in a Static Electric Field: Sawtooth Potential Treatment Revisited. J Chem Phys 2009, 131 (4), 044109. https://doi.org/10.1063/1.3185727.

(94) Selçuk, S.; Selloni, A. Influence of External Electric Fields on Oxygen Vacancies at the Anatase (101) Surface. J Chem Phys 2014, 141 (8), 084705. https://doi.org/10.1063/1.4893559.

(95) Christopher J. Cramer. Essentials of Computational Chemistry: Theories and Models, Second edition.; John Wiley & Sons Ltd, Ed.; 2014.

(96) Roux, B.; Simonson, T. Implicit Solvent Models. Biophys Chem 1999, 78 (1–2), 1–20. https://doi.org/10.1016/S0301-4622(98)00226-9.

(97) Mennucci, B.; Tomasi, J.; Cammi, R.; Cheeseman, J. R.; Frisch, M. J.; Devlin, F. J.; Gabriel, S.; Stephens, P. J. Polarizable Continuum Model (PCM) Calculations of Solvent Effects on Optical Rotations of Chiral Molecules. J Phys Chem A 2002, 106 (25), 6102–6113. https://doi.org/10.1021/jp020124t.

(98) Marenich, A. v.; Cramer, C. J.; Truhlar, D. G. Universal Solvation Model Based on Solute Electron Density and on a Continuum Model of the Solvent Defined by the Bulk Dielectric Constant and Atomic Surface Tensions. J Phys Chem B 2009, 113 (18), 6378–6396. https://doi.org/10.1021/jp810292n.

(99) Sinstein, M.; Scheurer, C.; Matera, S.; Blum, V.; Reuter, K.; Oberhofer, H. Efficient Implicit Solvation Method for Full Potential DFT. J Chem Theory Comput 2017, 13 (11), 5582–5603. https://doi.org/10.1021/acs.jctc.7b00297.

(100) Paquet, E.; Viktor, H. L. Computational Methods for Ab Initio Molecular Dynamics. Adv Chem 2018, 2018, 1–14. https://doi.org/10.1155/2018/9839641.

(101) Car, R.; Parrinello, M. Unified Approach for Molecular Dynamics and Density-Functional Theory. Phys Rev Lett 1985, 55 (22), 2471–2474. https://doi.org/10.1103/PhysRevLett.55.2471.

(102) Barducci, A.; Bonomi, M.; Parrinello, M. Metadynamics. WIREs Computational Molecular Science 2011, 1 (5), 826–843. https://doi.org/10.1002/wcms.31.

(103) Laio, A.; Parrinello, M. Escaping Free-Energy Minima. Proceedings of the National Academy of Sciences 2002, 99 (20), 12562–12566. https://doi.org/10.1073/pnas.202427399.

(104) Barducci, A.; Bussi, G.; Parrinello, M. Well-Tempered Metadynamics: A Smoothly Converging and Tunable Free-Energy Method. Phys Rev Lett 2008, 100 (2), 020603. https://doi.org/10.1103/PhysRevLett.100.020603.

(105) Lodesani, F.; Tavanti, F.; Menziani, M. C.; Maeda, K.; Takato, Y.; Urata, S.; Pedone, A. Exploring the Crystallization Path of Lithium Disilicate through Metadynamics Simulations. Phys Rev Mater 2021, 5 (7), 075602. https://doi.org/10.1103/PhysRevMaterials.5.075602.

(106) Martoňák, R.; Donadio, D.; Oganov, A. R.; Parrinello, M. Crystal Structure Transformations in SiO2 from Classical and Ab Initio Metadynamics. Nat Mater 2006, 5 (8), 623–626. https://doi.org/10.1038/nmat1696.

(107) Santoro, M.; Gorelli, F. A.; Bini, R.; Ruocco, G.; Scandolo, S.; Crichton, W. A. Amorphous Silica-like Carbon Dioxide. Nature 2006, 441 (7095), 857–860. https://doi.org/10.1038/nature04879.

(108) Aschauer, U.; Bowen, P.; Parker, S. C. Oxygen Vacancy Diffusion in Alumina: New Atomistic Simulation Methods Applied to an Old Problem. Acta Mater 2009, 57 (16), 4765–4772. https://doi.org/10.1016/j.actamat.2009.06.061.

(109) Röder, F.; Braatz, R. D.; Krewer, U. Multi-Scale Simulation of Heterogeneous Surface Film Growth Mechanisms in Lithium-Ion Batteries. J Electrochem Soc 2017, 164 (11), E3335–E3344. https://doi.org/10.1149/2.0241711jes.

(110) Scrosati, B.; Garche, J. Lithium Batteries: Status, Prospects and Future. J Power Sources 2010, 195 (9), 2419–2430. https://doi.org/10.1016/j.jpowsour.2009.11.048.

(111) Nayak, P. K.; Yang, L.; Brehm, W.; Adelhelm, P. From Lithium-Ion to Sodium-Ion Batteries: Advantages, Challenges, and Surprises. Angew Chem, Int Ed Engl 2018, 57 (1), 102–120. https://doi.org/10.1002/anie.201703772.

(112) Eftekhari, A.; Kim, D.-W. Sodium-Ion Batteries: New Opportunities beyond Energy Storage by Lithium. J Power Sources 2018, 395, 336–348. https://doi.org/10.1016/j.jpowsour.2018.05.089.

(113) Vaalma, C.; Buchholz, D.; Weil, M.; Passerini, S. A Cost and Resource Analysis of Sodium-Ion Batteries. Nat Rev Mater 2018, 3 (4), 18013. https://doi.org/10.1038/natrevmats.2018.13.

(114) Muñoz-Márquez, M. Á.; Saurel, D.; Gómez-Cámer, J. L.; Casas-Cabanas, M.; Castillo-Martínez, E.; Rojo, T. Na-Ion Batteries for Large Scale Applications: A Review on Anode Materials and Solid Electrolyte Interphase Formation. Adv Energy Mater 2017, 7 (20), 1700463. https://doi.org/10.1002/aenm.201700463.

(115) Massaro, A.; Muñoz-García, A. B.; Tuccillo, M.; Pavone, M.; Prosini, P. P. An Ab Initio Study of Li/Ni-Doped NaxMeO2 Cathode Material for Na-Ion Batteries. Journal of Energy and Power Technology 2020, 03 (02), 1–1. https://doi.org/10.21926/jept.2102022.

(116) Massaro, A.; Langella, A.; Gerbaldi, C.; Elia, G. A.; Muñoz-García, A. B.; Pavone, M. Ru-Doping of P2-$Na_xMn_{0.75}Ni_{0.25}O_2$ -Layered Oxides for High-Energy Na-Ion Battery Cathodes: First-Principles Insights on Activation and Control of Reversible Oxide Redox Chemistry. ACS Appl Energy Mater 2022, 5 (9), 10721–10730. https://doi.org/10.1021/acsaem.2c01455.

(117) Massaro, A.; Muñoz-García, A. B.; Prosini, P. P.; Gerbaldi, C.; Pavone, M. Unveiling Oxygen Redox Activity in P2-Type $Na_xNi_{0.25}Mn_{0.68}O_2$ High-Energy Cathode for Na-Ion Batteries. ACS Energy Lett 2021, 6 (7), 2470–2480. https://doi.org/10.1021/acsenergylett.1c01020.

(118) Xu, Y.; Memarzadeh Lotfabad, E.; Wang, H.; Farbod, B.; Xu, Z.; Kohandehghan, A.; Mitlin, D. Nanocrystalline Anatase TiO_2: A New Anode Material for Rechargeable Sodium Ion Batteries. Chem Com 2013, 49 (79), 8973. https://doi.org/10.1039/c3cc45254a.

(119) Abraham, K. M.; Jiang, Z. A Polymer Electrolyte-Based Rechargeable Lithium/Oxygen Battery. J Electrochem Soc 1996, 143 (1), 1–5. https://doi.org/10.1149/1.1836378.

(120) Rahman, Md. A.; Wang, X.; Wen, C. A Review of High Energy Density Lithium–Air Battery Technology. J Appl Electrochem 2014, 44 (1), 5–22. https://doi.org/10.1007/s10800-013-0620-8.

(121) Imanishi, N.; Yamamoto, O. Perspectives and Challenges of Rechargeable Lithium–Air Batteries. Mater Today Adv 2019, 4, 100031. https://doi.org/10.1016/j.mtadv.2019.100031.

(122) Ogasawara, T.; Débart, A.; Holzapfel, M.; Novák, P.; Bruce, P. G. Rechargeable Li_2O_2 Electrode for Lithium Batteries. J Am Chem Soc 2006, 128 (4), 1390–1393. https://doi.org/10.1021/ja056811q.

(123) Wang, L.; Zhang, Y.; Liu, Z.; Guo, L.; Peng, Z. Understanding Oxygen Electrochemistry in Aprotic LiO_2 Batteries. Green Energy & Environment 2017, 2 (3), 186–203. https://doi.org/10.1016/j.gee.2017.06.004.

(124) Xu, W.; Wang, J.; Ding, F.; Chen, X.; Nasybulin, E.; Zhang, Y.; Zhang, J.-G. Lithium Metal Anodes for Rechargeable Batteries. Energy Environ. Sci. 2014, 7 (2), 513–537. https://doi.org/10.1039/C3EE40795K.

(125) Wang, R.; Cui, W.; Chu, F.; Wu, F. Lithium Metal Anodes: Present and Future. Journal of Energy Chemistry 2020, 48, 145–159. https://doi.org/10.1016/j.jechem.2019.12.024.

(126) Janek, J.; Zeier, W. G. A Solid Future for Battery Development. Nat Energy 2016, 1 (9), 16141. https://doi.org/10.1038/nenergy.2016.141.

(127) Peled, E.; Menkin, S. Review–SEI: Past, Present and Future. J Electrochem Soc 2017, 164 (7), A1703–A1719. https://doi.org/10.1149/2.1441707jes.

(128) Yu, Z.; Cui, Y.; Bao, Z. Design Principles of Artificial Solid Electrolyte Interphases for Lithium-Metal Anodes. Cell Rep Phys Sci 2020, 1 (7), 100119. https://doi.org/10.1016/j.xcrp.2020.100119.

(129) Song, T.; Paik, U. TiO_2 as an Active or Supplemental Material for Lithium Batteries. J Mater Chem A Mater 2016, 4 (1), 14–31. https://doi.org/10.1039/C5TA06888F.

(130) Madian, M.; Eychmüller, A.; Giebeler, L. Current Advances in TiO_2-Based Nanostructure Electrodes for High Performance Lithium Ion Batteries. Batteries 2018, 4 (1), 7. https://doi.org/10.3390/batteries4010007.

(131) Linsebigler, A. L.; Lu, G.; Yates, J. T. Photocatalysis on TiO_2 Surfaces: Principles, Mechanisms, and Selected Results. Chem Rev 1995, 95 (3), 735–758. https://doi.org/10.1021/cr00035a013.

(132) Ni, M.; Leung, M. K. H.; Leung, D. Y. C.; Sumathy, K. A Review and Recent Developments in Photocatalytic Water-Splitting Using TiO_2 for Hydrogen Production. Renew Sust Energ Rev 2007, 11 (3), 401–425. https://doi.org/10.1016/j.rser.2005.01.009.

(133) Bella, F.; Muñoz-García, A. B.; Meligrana, G.; Lamberti, A.; Destro, M.; Pavone, M.; Gerbaldi, C. Unveiling the Controversial Mechanism of Reversible Na Storage in TiO_2 Nanotube Arrays: Amorphous versus Anatase TiO_2. Nano Res 2017, 10 (8), 2891–2903. https://doi.org/10.1007/s12274-017-1656-6.

(134) Huang, J. P.; Yuan, D. D.; Zhang, H. Z.; Cao, Y. L.; Li, G. R.; Yang, H. X.; Gao, X. P. Electrochemical Sodium Storage of TiO_2(B) Nanotubes for Sodium Ion Batteries. RSC Adv 2013, 3 (31), 12593. https://doi.org/10.1039/c3ra42413h.

(135) Bella, F.; Muñoz-García, A. B.; Colò, F.; Meligrana, G.; Lamberti, A.; Destro, M.; Pavone, M.; Gerbaldi, C. Combined Structural, Chemometric, and Electrochemical Investigation of Vertically Aligned TiO_2 Nanotubes for Na-Ion Batteries. ACS Omega 2018, 3 (7), 8440–8450. https://doi.org/10.1021/acsomega.8b01117.

(136) Longoni, G.; Pena Cabrera, R. L.; Polizzi, S.; D'Arienzo, M.; Mari, C. M.; Cui, Y.; Ruffo, R. Shape-Controlled TiO_2 Nanocrystals for Na-Ion Battery Electrodes: The Role of Different Exposed Crystal Facets on the Electrochemical Properties. Nano Lett 2017, 17 (2), 992–1000. https://doi.org/10.1021/acs.nanolett.6b04347.

(137) Massaro, A.; Muñoz-García, A. B.; Maddalena, P.; Bella, F.; Meligrana, G.; Gerbaldi, C.; Pavone, M. First-Principles Study of Na Insertion at TiO_2 Anatase Surfaces: New Hints for Na-Ion Battery Design. Nanoscale Adv 2020, 2 (7), 2745–2751. https://doi.org/10.1039/D0NA00230E.

(138) Giannozzi, P.; Baseggio, O.; Bonfà, P.; Brunato, D.; Car, R.; Carnimeo, I.; Cavazzoni, C.; de Gironcoli, S.; Delugas, P.; Ferrari Ruffino, F.; Ferretti, A.; Marzari, N.; Timrov, I.; Urru, A.; Baroni, S. Q Quantum ESPRESSO toward the Exascale. J Chem Phys 2020, 152 (15), 154105. https://doi.org/10.1063/5.0005082.

(139) Finazzi, E.; di Valentin, C.; Pacchioni, G.; Selloni, A. Excess Electron States in Reduced Bulk Anatase TiO2: Comparison of Standard GGA, GGA+U, and Hybrid DFT Calculations. J Chem Phys 2008, 129 (15), 154113. https://doi.org/10.1063/1.2996362.

(140) Dal Corso, A. Pseudopotentials Periodic Table: From H to Pu. Comput Mater Sci 2014, 95, 337–350. https://doi.org/10.1016/j.commatsci.2014.07.043.

(141) Bengtsson, L. Dipole Correction for Surface Supercell Calculations. Phys Rev B 1999, 59 (19), 12301–12304. https://doi.org/10.1103/PhysRevB.59.12301.

(142) Bai, Q.; Yang, L.; Chen, H.; Mo, Y. Computational Studies of Electrode Materials in Sodium-Ion Batteries. Adv Energy Mater 2018, 8 (17), 1702998. https://doi.org/10.1002/aenm.201702998.

(143) Kim, K.-T.; Ali, G.; Chung, K. Y.; Yoon, C. S.; Yashiro, H.; Sun, Y.-K.; Lu, J.; Amine, K.; Myung, S.-T. Anatase Titania Nanorods as an Intercalation Anode Material for Rechargeable Sodium Batteries. Nano Lett 2014, 14 (2), 416–422. https://doi.org/10.1021/nl402747x.

(144) Fasulo, F.; Massaro, A.; Muñoz-García, A. B.; Pavone, M. Na Uptake at TiO_2 Anatase Surfaces under Electric Field Control: A First-Principles Study. J Mater Res 2022, 37 (19), 3216–3226. https://doi.org/10.1557/s43578-022-00579-1.

(145) Wandt, J.; Jakes, P.; Granwehr, J.; Gasteiger, H. A.; Eichel, R.-A. Singlet Oxygen Formation during the Charging Process of an Aprotic Lithium-Oxygen Battery. Angew Chem, Int Ed Engl 2016, 55 (24), 6892–6895. https://doi.org/10.1002/anie.201602142.

(146) Mahne, N.; Schafzahl, B.; Leypold, C.; Leypold, M.; Grumm, S.; Leitgeb, A.; Strohmeier, G. A.; Wilkening, M.; Fontaine, O.; Kramer, D.; Slugovc, C.; Borisov, S. M.; Freunberger, S. A. Singlet Oxygen Generation as a Major Cause for Parasitic Reactions during Cycling of Aprotic Lithium–Oxygen Batteries. Nat Energy 2017, 2 (5), 17036. https://doi.org/10.1038/nenergy.2017.36.

(147) Schürmann, A.; Luerßen, B.; Mollenhauer, D.; Janek, J.; Schröder, D. Singlet Oxygen in Electrochemical Cells: A Critical Review of Literature and Theory. Chem Rev 2021, 121 (20), 12445–12464. https://doi.org/10.1021/acs.chemrev.1c00139.

(148) Hassoun, J.; Croce, F.; Armand, M.; Scrosati, B. Investigation of the O_2 Electrochemistry in a Polymer Electrolyte Solid-State Cell. Angew Chem, Int Ed Engl 2011, 50 (13), 2999–3002. https://doi.org/10.1002/anie.201006264.

(149) Mourad, E.; Petit, Y. K.; Spezia, R.; Samojlov, A.; Summa, F. F.; Prehal, C.; Leypold, C.; Mahne, N.; Slugovc, C.; Fontaine, O.; Brutti, S.; Freunberger, S. A. Singlet Oxygen from Cation Driven Superoxide Disproportionation and Consequences for Aprotic Metal–O_2 Batteries. Energy Environ Sci 2019, 12 (8), 2559–2568. https://doi.org/10.1039/C9EE01453E.

(150) Houchins, G.; Pande, V.; Viswanathan, V. Mechanism for Singlet Oxygen Production in Li-Ion and Metal–Air Batteries. ACS Energy Lett 2020, 5 (6), 1893–1899. https://doi.org/10.1021/acsenergylett.0c00595.

(151) Johnson, L.; Li, C.; Liu, Z.; Chen, Y.; Freunberger, S. A.; Ashok, P. C.; Praveen, B. B.; Dholakia, K.; Tarascon, J.-M.; Bruce, P. G. The Role of LiO2 Solubility in O2 Reduction in Aprotic Solvents and Its Consequences for Li–O2 Batteries. Nat Chem 2014, 6 (12), 1091–1099. https://doi.org/10.1038/nchem.2101.

(152) Aurbach, D.; McCloskey, B. D.; Nazar, L. F.; Bruce, P. G. Advances in Understanding Mechanisms Underpinning Lithium–Air Batteries. Nat Energy 2016, 1 (9), 16128. https://doi.org/10.1038/nenergy.2016.128.

(153) Wang, Y.; Lai, N.-C.; Lu, Y.-R.; Zhou, Y.; Dong, C.-L.; Lu, Y.-C. A Solvent-Controlled Oxidation Mechanism of Li_2O_2 in Lithium-Oxygen Batteries. Joule 2018, 2 (11), 2364–2380. https://doi.org/10.1016/j.joule.2018.07.021.

(154) Petit, Y. K.; Mourad, E.; Prehal, C.; Leypold, C.; Windischbacher, A.; Mijailovic, D.; Slugovc, C.; Borisov, S. M.; Zojer, E.; Brutti, S.; Fontaine, O.; Freunberger, S. A. Mechanism of Mediated Alkali Peroxide Oxidation and Triplet versus Singlet Oxygen Formation. Nat Chem 2021, 13 (5), 465–471. https://doi.org/10.1038/s41557-021-00643-z.

(155) Mo, Y.; Ong, S. P.; Ceder, G. First-Principles Study of the Oxygen Evolution Reaction of Lithium Peroxide in the Lithium-Air Battery. Phys Rev B 2011, 84 (20), 205446. https://doi.org/10.1103/PhysRevB.84.205446.

(156) Pierini, A.; Brutti, S.; Bodo, E. Study of the Electronic Structure of Alkali Peroxides and Their Role in the Chemistry of Metal–Oxygen Batteries. J Phys Chem A 2021, 125 (42), 9368–9376. https://doi.org/10.1021/acs.jpca.1c07255.

(157) Zaichenko, A.; Schröder, D.; Janek, J.; Mollenhauer, D. Pathways to Triplet or Singlet Oxygen during the Dissociation of Alkali Metal Superoxides: Insights by Multireference Calculations of Molecular Model Systems. Chem Eur J 2020, 26 (11), 2395–2404. https://doi.org/10.1002/chem.201904110.

(158) Kresse, G.; Hafner, J. Ab Initio Molecular-Dynamics Simulation of the Liquid-Metal–Amorphous-Semiconductor Transition in Germanium. Phys Rev B 1994, 49 (20), 14251–14269. https://doi.org/10.1103/PhysRevB.49.14251.

(159) Kresse, G.; Furthmüller, J. Efficiency of Ab-Initio Total Energy Calculations for Metals and Semiconductors Using a Plane-Wave Basis Set. Comput Mater Sci 1996, 6 (1), 15–50. https://doi.org/10.1016/0927-0256(96)00008-0.

(160) Kresse, G.; Furthmüller, J. Efficient Iterative Schemes for Ab Initio Total-Energy Calculations Using a Plane-Wave Basis Set. Phys Rev B 1996, 54 (16), 11169–11186. https://doi.org/10.1103/PhysRevB.54.11169.

(161) Fdez. Galván, I.; Vacher, M.; Alavi, A.; Angeli, C.; Aquilante, F.; Autschbach, J.; Bao, J. J.; Bokarev, S. I.; Bogdanov, N. A.; Carlson, R. K.; Chibotaru, L. F.; Creutzberg, J.; Dattani, N.; Delcey, M. G.; Dong, S. S.; Dreuw, A.; Freitag, L.; Frutos, L. M.; Gagliardi, L.; Gendron, F.; Giussani, A.; González, L.; Grell, G.; Guo, M.; Hoyer, C. E.; Johansson, M.; Keller, S.; Knecht, S.; Kovačević, G.; Källman, E.; Li Manni, G.; Lundberg, M.; Ma, Y.; Mai, S.; Malhado, J. P.; Malmqvist, P. Å.; Marquetand, P.; Mewes, S. A.; Norell, J.; Olivucci, M.; Oppel, M.; Phung, Q. M.; Pierloot, K.; Plasser, F.; Reiher, M.; Sand, A. M.; Schapiro, I.; Sharma, P.; Stein, C. J.; Sørensen, L. K.; Truhlar, D. G.; Ugandi, M.; Ungur, L.; Valentini, A.; Vancoillie, S.; Veryazov, V.; Weser, O.; Wesołowski, T. A.; Widmark, P.-O.; Wouters, S.; Zech, A.; Zobel, J. P.; Lindh, R. OpenMolcas: From Source Code to Insight. J Chem Theory Comput 2019, 15 (11), 5925–5964. https://doi.org/10.1021/acs.jctc.9b00532.

(162) Müller, T.; Dallos, M.; Lischka, H.; Dubrovay, Z.; Szalay, P. G. A Systematic Theoretical Investigation of the Valence Excited States of the Diatomic Molecules B_2 , C_2 , N_2 and O_2. Theor Chem Acc: Theory, Computation, and Modeling (Theoretica Chimica Acta) 2001, 105 (3), 227–243. https://doi.org/10.1007/s002140000210.

(163) Hummelshøj, J. S.; Luntz, A. C.; Nørskov, J. K. Theoretical Evidence for Low Kinetic Overpotentials in Li-O_2 Electrochemistry. J Chem Phys 2013, 138 (3). https://doi.org/10.1063/1.4773242.

(164) Ota, H.; Shima, K.; Ue, M.; Yamaki, J. Effect of Vinylene Carbonate as Additive to Electrolyte for Lithium Metal Anode. Electrochim Acta 2004, 49 (4), 565–572. https://doi.org/10.1016/j.electacta.2003.09.010.

(165) Zhang, B.; Metzger, M.; Solchenbach, S.; Payne, M.; Meini, S.; Gasteiger, H. A.; Garsuch, A.; Lucht, B. L. Role of 1,3-Propane Sultone and Vinylene Carbonate in Solid Electrolyte Interface Formation and Gas Generation. J Phys Chem C 2015, 119 (21), 11337–11348. https://doi.org/10.1021/acs.jpcc.5b00072.

(166) Pritzl, D.; Solchenbach, S.; Wetjen, M.; Gasteiger, H. A. Analysis of Vinylene Carbonate (VC) as Additive in Graphite/$LiNi_{0.5}Mn_{1.5}O_4$ Cells. J Electrochem Soc 2017, 164 (12), A2625–A2635. https://doi.org/10.1149/2.1441712jes.

(167) Lee, H.-H.; Wang, Y.-Y.; Wan, C.-C.; Yang, M.-H.; Wu, H.-C.; Shieh, D.-T. The Function of Vinylene Carbonate as a Thermal Additive to Electrolyte in Lithium Batteries. J Appl Electrochem 2005, 35 (6), 615–623. https://doi.org/10.1007/s10800-005-2700-x.

(168) Michan, A. L.; Parimalam, Bharathy. S.; Leskes, M.; Kerber, R. N.; Yoon, T.; Grey, C. P.; Lucht, B. L. Fluoroethylene Carbonate and Vinylene Carbonate Reduction: Understanding Lithium-Ion Battery Electrolyte Additives and Solid Electrolyte Interphase Formation. Chem Mater 2016, 28 (22), 8149–8159. https://doi.org/10.1021/acs.chemmater.6b02282.

(169) Chai, J.; Liu, Z.; Ma, J.; Wang, J.; Liu, X.; Liu, H.; Zhang, J.; Cui, G.; Chen, L. In Situ Generation of Poly(Vinylene Carbonate) Based Solid Electrolyte with Interfacial Stability for $LiCoO_2$ Lithium Batteries. Adv Sci 2017, 4 (2), 1600377. https://doi.org/10.1002/advs.201600377.

(170) Ushirogata, K.; Sodeyama, K.; Okuno, Y.; Tateyama, Y. Additive Effect on Reductive Decomposition and Binding of Carbonate-Based Solvent toward Solid Electrolyte Interphase Formation in Lithium-Ion Battery. J Am Chem Soc 2013, 135 (32), 11967–11974. https://doi.org/10.1021/ja405079s.

(171) Soto, F. A.; Ma, Y.; Martinez de la Hoz, J. M.; Seminario, J. M.; Balbuena, P. B. Formation and Growth Mechanisms of Solid-Electrolyte Interphase Layers in Rechargeable Batteries. Chem Mater 2015, 27 (23), 7990–8000. https://doi.org/10.1021/acs.chemmater.5b03358.

(172) Wang, Y.; Nakamura, S.; Tasaki, K.; Balbuena, P. B. Theoretical Studies to Understand Surface Chemistry on Carbon Anodes for Lithium-Ion Batteries: How Does Vinylene Carbonate Play Its Role as an Electrolyte Additive? J Am Chem Soc 2002, 124 (16), 4408–4421. https://doi.org/10.1021/ja017073i.

(173) Wang, J.; Wang, S.-Q. Surface Energy and Work Function of fcc and bcc Crystals: Density Functional Study. Surf Sci 2014, 630, 216–224. https://doi.org/10.1016/j.susc.2014.08.017.

(174) Vydrov, O. A.; Scuseria, G. E.; Perdew, J. P. Tests of Functionals for Systems with Fractional Electron Number. J Chem Phys 2007, 126 (15), 154109. https://doi.org/10.1063/1.2723119.

(175) Perdew, J. P.; Burke, K.; Ernzerhof, M. Generalized Gradient Approximation Made Simple [Phys. Rev. Lett. 77, 3865 (1996)]. Phys Rev Lett 1997, 78 (7). https://doi.org/10.1103/PhysRevLett.78.1396.

(176) White, W. F.; Boggs, J. E. Microwave Spectra of ^{13}C- and ^{18}O-Containing Species and the Structure of Vinylene Carbonate. J Chem Phys 1971, 54 (11), 4714–4717. https://doi.org/10.1063/1.1674745.

(177) Huang, C. Extending the Density Functional Embedding Theory to Finite Temperature and an Efficient Iterative Method for Solving for Embedding Potentials. J Chem Phys 2016, 144 (12), 124106. https://doi.org/10.1063/1.4944464.

(178) Fuchs, M.; Scheffler, M. Ab Initio Pseudopotentials for Electronic Structure Calculations of Poly-Atomic Systems Using Density-Functional Theory. Comput Phys Commun 1999, 119 (1), 67–98. https://doi.org/10.1016/S0010-4655(98)00201-X.

(179) Ebadi, M.; Brandell, D.; Araujo, C. M. Electrolyte Decomposition on Li-Metal Surfaces from First-Principles Theory. J Chem Phys 2016, 145 (20), 204701. https://doi.org/10.1063/1.4967810.

(180) Brennan, M. D.; Breedon, M.; Best, A. S.; Morishita, T.; Spencer, M. J. S. Surface Reactions of Ethylene Carbonate and Propylene Carbonate on the Li(001) Surface. Electrochim Acta 2017, 243, 320–330. https://doi.org/10.1016/j.electacta.2017.04.163.

(181) Lau, K. C.; Curtiss, L. A.; Greeley, J. Density Functional Investigation of the Thermodynamic Stability of Lithium Oxide Bulk Crystalline Structures as a Function of Oxygen Pressure. J Phys Chem C 2011, 115 (47), 23625–23633. https://doi.org/10.1021/jp206796h.

(182) Goodenough, J. B.; Kim, Y. Challenges for Rechargeable Li Batteries. Chem Mater 2010, 22 (3), 587–603. https://doi.org/10.1021/cm901452z.

(183) Henkelman, G.; Uberuaga, B. P.; Jónsson, H. A Climbing Image Nudged Elastic Band Method for Finding Saddle Points and Minimum Energy Paths. J Chem Phys 2000, 113 (22), 9901–9904. https://doi.org/10.1063/1.1329672.

(184) Fasulo, F.; Munoz-Garcia, A. B.; Massaro, A.; Crescenzi, O.; Huang, C.; Pavone, M. Vinylene Carbonate Reactivity at Lithium Metal Surface: First-Principles Insights on the Early Steps of SEI Formation. J Mater Chem A Mater 2023. https://doi.org/10.1039/D2TA08772C.

(185) Naito, T.; Shinagawa, T.; Nishimoto, T.; Takanabe, K. Recent Advances in Understanding Oxygen Evolution Reaction Mechanisms over Iridium Oxide. Inorg Chem Front 2021, 8 (11), 2900–2917. https://doi.org/10.1039/D0QI01465F.

(186) Wu, H.; Wang, Y.; Shi, Z.; Wang, X.; Yang, J.; Xiao, M.; Ge, J.; Xing, W.; Liu, C. Recent Developments of Iridium-Based Catalysts for the Oxygen Evolution Reaction in Acidic Water Electrolysis. J Mater Chem A Mater 2022, 10 (25), 13170–13189. https://doi.org/10.1039/D1TA10324E.

(187) Lončar, A.; Escalera-López, D.; Cherevko, S.; Hodnik, N. Inter-relationships between Oxygen Evolution and Iridium Dissolution Mechanisms. Angew Chem, Int Ed Engl 2022, 61 (14). https://doi.org/10.1002/anie.202114437.

(188) Fujishima, A.; Honda, K. Electrochemical Photolysis of Water at a Semiconductor Electrode. Nature 1972, 238 (5358), 37–38. https://doi.org/10.1038/238037a0.

(189) Saveleva, V. A.; Wang, L.; Teschner, D.; Jones, T.; Gago, A. S.; Friedrich, K. A.; Zafeiratos, S.; Schlögl, R.; Savinova, E. R. Operando Evidence for a Universal Oxygen Evolution Mechanism on Thermal and Electrochemical Iridium Oxides. J Phys Chem Lett 2018, 9 (11), 3154–3160. https://doi.org/10.1021/acs.jpclett.8b00810.

(190) Pfeifer, V.; Jones, T. E.; Velasco Vélez, J. J.; Arrigo, R.; Piccinin, S.; Hävecker, M.; Knop-Gericke, A.; Schlögl, R. In Situ Observation of Reactive Oxygen Species Forming on Oxygen-Evolving Iridium Surfaces. Chem Sci 2017, 8 (3), 2143–2149. https://doi.org/10.1039/C6SC04622C.

(191) Ping, Y.; Nielsen, R. J.; Goddard, W. A. The Reaction Mechanism with Free Energy Barriers at Constant Potentials for the Oxygen Evolution Reaction at the IrO_2 (110) Surface. J Am Chem Soc 2017, 139 (1), 149–155. https://doi.org/10.1021/jacs.6b07557.

(192) Velasco-Vélez, J.-J.; Carbonio, E. A.; Chuang, C.-H.; Hsu, C.-J.; Lee, J.-F.; Arrigo, R.; Hävecker, M.; Wang, R.; Plodinec, M.; Wang, F. R.; Centeno, A.; Zurutuza, A.; Falling, L. J.; Mom, R. V.; Hofmann, S.; Schlögl, R.; Knop-Gericke, A.; Jones, T. E. Surface Electron-Hole Rich Species Active in the Electrocatalytic Water Oxidation. J Am Chem Soc 2021, 143 (32), 12524–12534. https://doi.org/10.1021/jacs.1c01655.

(193) Schweinar, K.; Gault, B.; Mouton, I.; Kasian, O. Lattice Oxygen Exchange in Rutile IrO_2 during the Oxygen Evolution Reaction. J Phys Chem Lett 2020, 11 (13), 5008–5014. https://doi.org/10.1021/acs.jpclett.0c01258.

(194) Zagalskaya, A.; Alexandrov, V. Role of Defects in the Interplay between Adsorbate Evolving and Lattice Oxygen Mechanisms of the Oxygen Evolution Reaction in RuO_2 and IrO_2. ACS Catal 2020, 10 (6), 3650–3657. https://doi.org/10.1021/acscatal.9b05544.

(195) Geppert, J.; Röse, P.; Czioska, S.; Escalera-López, D.; Boubnov, A.; Saraçi, E.; Cherevko, S.; Grunwaldt, J.-D.; Krewer, U. Microkinetic Analysis of the Oxygen Evolution Performance at Different Stages of Iridium Oxide Degradation. J Am Chem Soc 2022, 144 (29), 13205–13217. https://doi.org/10.1021/jacs.2c03561.

(196) Sargeant, E.; Illas, F.; Rodríguez, P.; Calle-Vallejo, F. Importance of the Gas-Phase Error Correction for O_2 When Using DFT to Model the Oxygen Reduction and Evolution Reactions. Journal of Electroanalytical Chemistry 2021, 896, 115178. https://doi.org/10.1016/j.jelechem.2021.115178.

(197) Radoń, M.; Pierloot, K. Binding of CO, NO, and O_2 to Heme by Density Functional and Multireference Ab Initio Calculations. J Phys Chem A 2008, 112 (46), 11824–11832. https://doi.org/10.1021/jp806075b.

(198) Kurashige, Y.; Saitow, M.; Chalupský, J.; Yanai, T. Radical O–O Coupling Reaction in Diferrate-Mediated Water Oxidation Studied Using Multireference Wave Function Theory. Phys. Chem. Chem. Phys. 2014, 16 (24), 11988–11999. https://doi.org/10.1039/C3CP55225J.

(199) Neese, F.; Wennmohs, F.; Becker, U.; Riplinger, C. The ORCA Quantum Chemistry Program Package. J Chem Phys 2020, 152 (22), 224108. https://doi.org/10.1063/5.0004608.

(200) González, D.; Heras-Domingo, J.; Sodupe, M.; Rodríguez-Santiago, L.; Solans-Monfort, X. Importance of the Oxyl Character on the IrO_2 Surface Dependent Catalytic Activity for the Oxygen Evolution Reaction. J Catal 2021, 396, 192–201. https://doi.org/10.1016/j.jcat.2021.02.026.

(201) Tilocca, A.; Selloni, A. Vertical and Lateral Order in Adsorbed Water Layers on Anatase TiO_2 (101). Langmuir 2004, 20 (19), 8379–8384. https://doi.org/10.1021/la048937r.

(202) Tilocca, A.; Selloni, A. Structure and Reactivity of Water Layers on Defect-Free and Defective Anatase TiO_2 (101) Surfaces. J Phys Chem B 2004, 108 (15), 4743–4751. https://doi.org/10.1021/jp037685k.

(203) Cheng, H.; Selloni, A. Hydroxide Ions at the Water/Anatase TiO_2 (101) Interface: Structure and Electronic States from First Principles Molecular Dynamics. Langmuir 2010, 26 (13), 11518–11525. https://doi.org/10.1021/la100672f.

(204) Vittadini, A.; Selloni, A.; Rotzinger, F. P.; Grätzel, M. Structure and Energetics of Water Adsorbed at TiO_2 Anatase (101) and (001) Surfaces. Phys Rev Lett 1998, 81 (14), 2954–2957. https://doi.org/10.1103/PhysRevLett.81.2954.

(205) Calegari Andrade, M. F.; Ko, H.-Y.; Car, R.; Selloni, A. Structure, Polarization, and Sum Frequency Generation Spectrum of Interfacial Water on Anatase TiO_2. J Phys Chem Lett 2018, 9 (23), 6716–6721. https://doi.org/10.1021/acs.jpclett.8b03103.

(206) Calegari Andrade, M. F.; Ko, H.-Y.; Zhang, L.; Car, R.; Selloni, A. Free Energy of Proton Transfer at the Water–TiO_2 Interface from Ab Initio Deep Potential Molecular Dynamics. Chem Sci 2020, 11 (9), 2335–2341. https://doi.org/10.1039/C9SC05116C.

(207) Nadeem, I. M.; Treacy, J. P. W.; Selcuk, S.; Torrelles, X.; Hussain, H.; Wilson, A.; Grinter, D. C.; Cabailh, G.; Bikondoa, O.; Nicklin, C.; Selloni, A.; Zegenhagen, J.; Lindsay, R.; Thornton, G. Water Dissociates at the Aqueous Interface with Reduced Anatase TiO_2 (101). J Phys Chem Lett 2018, 9 (11), 3131–3136. https://doi.org/10.1021/acs.jpclett.8b01182.

(208) Selli, D.; Fazio, G.; Seifert, G.; di Valentin, C. Water Multilayers on TiO_2 (101) Anatase Surface: Assessment of a DFTB-Based Method. J Chem Theory Comput 2017, 13 (8), 3862–3873. https://doi.org/10.1021/acs.jctc.7b00479.

(209) Sumita, M.; Hu, C.; Tateyama, Y. Interface Water on TiO_2 Anatase (101) and (001) Surfaces: First-Principles Study with TiO_2 Slabs Dipped in Bulk Water. J Phys Chem C 2010, 114 (43), 18529–18537. https://doi.org/10.1021/jp105364z.

(210) Herman, G. S.; Dohnálek, Z.; Ruzycki, N.; Diebold, U. Experimental Investigation of the Interaction of Water and Methanol with Anatase−TiO_2 (101). J Phys Chem B 2003, 107 (12), 2788–2795. https://doi.org/10.1021/jp0275544.

(211) Nadeem, I. M.; Harrison, G. T.; Wilson, A.; Pang, C. L.; Zegenhagen, J.; Thornton, G. Bridging Hydroxyls on Anatase TiO_2 (101) by Water Dissociation in Oxygen Vacancies. J Phys Chem B 2018, 122 (2), 834–839. https://doi.org/10.1021/acs.jpcb.7b06955.

(212) Jackman, M. J.; Thomas, A. G.; Muryn, C. Photoelectron Spectroscopy Study of Stoichiometric and Reduced Anatase TiO_2 (101) Surfaces: The Effect of Subsurface Defects on Water Adsorption at Near-Ambient Pressures. J Phys Chem C 2015, 119 (24), 13682–13690. https://doi.org/10.1021/acs.jpcc.5b02732.

(213) Raju, M.; Kim, S.-Y.; van Duin, A. C. T.; Fichthorn, K. A. ReaxFF Reactive Force Field Study of the Dissociation of Water on Titania Surfaces. J Phys Chem C 2013, 117 (20), 10558–10572. https://doi.org/10.1021/jp402139h.

(214) Patrick, C. E.; Giustino, F. Structure of a Water Monolayer on the Anatase TiO_2 (101) Surface. Phys Rev Appl 2014, 2 (1), 014001. https://doi.org/10.1103/PhysRevApplied.2.014001.

(215) Walle, L. E.; Borg, A.; Johansson, E. M. J.; Plogmaker, S.; Rensmo, H.; Uvdal, P.; Sandell, A. Mixed Dissociative and Molecular Water Adsorption on Anatase TiO_2 (101). J Phys Chem C 2011, 115 (19), 9545–9550. https://doi.org/10.1021/jp111335w.

(216) Martinez-Casado, R.; Mallia, G.; Harrison, N. M.; Pérez, R. First-Principles Study of the Water Adsorption on Anatase(101) as a Function of the Coverage. J Phys Chem C 2018, 122 (36), 20736–20744. https://doi.org/10.1021/acs.jpcc.8b05081.

(217) O'Carroll, D.; English, N. A DFTB-Based Molecular Dynamics Investigation of an Explicitly Solvated Anatase Nanoparticle. Appl Sci 2022, 12 (2), 780. https://doi.org/10.3390/app12020780.

(218) Luschtinetz, R.; Frenzel, J.; Milek, T.; Seifert, G. Adsorption of Phosphonic Acid at the TiO_2 Anatase (101) and Rutile (110) Surfaces. J Phys Chem C 2009, 113 (14), 5730–5740. https://doi.org/10.1021/jp8110343.

(219) Kühne, T. D.; Iannuzzi, M.; del Ben, M.; Rybkin, V. v.; Seewald, P.; Stein, F.; Laino, T.; Khaliullin, R. Z.; Schütt, O.; Schiffmann, F.; Golze, D.; Wilhelm, J.; Chulkov, S.; Bani-Hashemian, M. H.; Weber, V.; Borštnik, U.; Taillefumier, M.; Jakobovits, A. S.; Lazzaro, A.; Pabst, H.; Müller, T.; Schade, R.; Guidon, M.; Andermatt, S.; Holmberg, N.; Schenter, G. K.; Hehn, A.; Bussy, A.; Belleflamme, F.; Tabacchi, G.; Glöß, A.; Lass, M.; Bethune, I.; Mundy, C. J.; Plessl, C.; Watkins, M.; VandeVondele, J.; Krack, M.; Hutter, J. CP2K: An Electronic Structure and Molecular Dynamics Software Package - Quickstep: Efficient and Accurate Electronic Structure Calculations. J Chem Phys 2020, 152 (19), 194103. https://doi.org/10.1063/5.0007045.

(220) Tribello, G. A.; Bonomi, M.; Branduardi, D.; Camilloni, C.; Bussi, G. PLUMED 2: New Feathers for an Old Bird. Comput Phys Commun 2014, 185 (2), 604–613. https://doi.org/10.1016/j.cpc.2013.09.018.

(221) Bussi, G.; Donadio, D.; Parrinello, M. Canonical Sampling through Velocity Rescaling. J Chem Phys 2007, 126 (1), 014101. https://doi.org/10.1063/1.2408420.

(222) Uehara, K.; Mizuno, N. Heterolytic Dissociation of Water Demonstrated by Crystal-to-Crystal Core Interconversion from (μ-Oxo)Divanadium to Bis(μ-Hydroxo)Divanadium Substituted Polyoxometalates. J Am Chem Soc 2011, 133 (6), 1622–1625. https://doi.org/10.1021/ja108245g.

(223) Ishikawa, Y.; Diaz-Morales, R. R.; Perez, A.; Vilkas, M. J.; Cabrera, C. R. A Density-Functional Study of the Energetics of H_2O Dissociation on Bimetallic Pt/Ru Nanoclusters. Chem Phys Lett 2005, 411 (4–6), 404–410. https://doi.org/10.1016/j.cplett.2005.05.128.

(224) Fasulo, F.; Piccini, G.; Muñoz-García, A. B.; Pavone, M.; Parrinello, M. Dynamics of Water Dissociative Adsorption on TiO_2 Anatase (101) at Monolayer Coverage and Below. J Phys Chem C 2022, 126 (37), 15752–15758. https://doi.org/10.1021/acs.jpcc.2c03077.

(225) Malinkiewicz, O.; Yella, A.; Lee, Y. H.; Espallargas, G. M.; Graetzel, M.; Nazeeruddin, M. K.; Bolink, H. J. Perovskite Solar Cells Employing Organic Charge-Transport Layers. Nat Photonics 2014, 8 (2), 128–132. https://doi.org/10.1038/nphoton.2013.341.

(226) Jiménez-López, J.; Cambarau, W.; Cabau, L.; Palomares, E. Charge Injection, Carriers Recombination and HOMO Energy Level Relationship in Perovskite Solar Cells. Sci Rep 2017, 7 (1), 6101. https://doi.org/10.1038/s41598-017-06245-5.

(227) Ponseca, C. S.; Hutter, E. M.; Piatkowski, P.; Cohen, B.; Pascher, T.; Douhal, A.; Yartsev, A.; Sundström, V.; Savenije, T. J. Mechanism of Charge Transfer and Recombination Dynamics in Organo Metal Halide Perovskites and Organic Electrodes, PCBM, and Spiro-OMeTAD: Role of Dark Carriers. J Am Chem Soc 2015, 137 (51), 16043–16048. https://doi.org/10.1021/jacs.5b08770.

(228) Snaith, H. J. Perovskites: The Emergence of a New Era for Low-Cost, High-Efficiency Solar Cells. J Phys Chem Lett 2013, 4 (21), 3623–3630. https://doi.org/10.1021/jz4020162.

(229) Protesescu, L.; Yakunin, S.; Bodnarchuk, M. I.; Krieg, F.; Caputo, R.; Hendon, C. H.; Yang, R. X.; Walsh, A.; Kovalenko, M. v. Nanocrystals of Cesium Lead Halide Perovskites ($CsPbX_3$, X = Cl, Br, and I): Novel Optoelectronic Materials Showing Bright Emission with Wide Color Gamut. Nano Lett 2015, 15 (6), 3692–3696. https://doi.org/10.1021/nl5048779.

(230) Stranks, S. D.; Snaith, H. J. Metal-Halide Perovskites for Photovoltaic and Light-Emitting Devices. Nat Nanotechnol 2015, 10 (5), 391–402. https://doi.org/10.1038/nnano.2015.90.

(231) Saliba, M.; Matsui, T.; Seo, J.-Y.; Domanski, K.; Correa-Baena, J.-P.; Nazeeruddin, M. K.; Zakeeruddin, S. M.; Tress, W.; Abate, A.; Hagfeldt, A.; Grätzel, M. Cesium-Containing Triple Cation Perovskite Solar Cells: Improved Stability, Reproducibility and High Efficiency. Energy Environ Sci 2016, 9 (6), 1989–1997. https://doi.org/10.1039/C5EE03874J.

(232) Xu, J.; Boyd, C. C.; Yu, Z. J.; Palmstrom, A. F.; Witter, D. J.; Larson, B. W.; France, R. M.; Werner, J.; Harvey, S. P.; Wolf, E. J.; Weigand, W.; Manzoor, S.; van Hest, M. F. A. M.; Berry, J. J.; Luther, J. M.; Holman, Z. C.; McGehee, M. D. Triple-Halide Wide–Band Gap Perovskites with Suppressed Phase Segregation for Efficient Tandems. Science (1979) 2020, 367 (6482), 1097–1104. https://doi.org/10.1126/science.aaz5074.

(233) Pydzińska-Białek, K.; Drushliak, V.; Coy, E.; Załęski, K.; Flach, J.; Idígoras, J.; Contreras-Bernal, L.; Hagfeldt, A.; Anta, J. A.; Ziółek, M. Understanding the Interfaces between Triple-Cation Perovskite and Electron or Hole Transporting Material. ACS Appl Mater Interfaces 2020, 12 (27), 30399–30410. https://doi.org/10.1021/acsami.0c07095.

(234) Droseros, N.; Dänekamp, B.; Tsokkou, D.; Boix, P. P.; Banerji, N. Charge Injection and Trapping at Perovskite Interfaces with Organic Hole Transporting Materials of Different Ionization Energies. APL Mater 2019, 7 (4), 041115. https://doi.org/10.1063/1.5086692.

(235) Wang, Q.; Mosconi, E.; Wolff, C.; Li, J.; Neher, D.; de Angelis, F.; Suranna, G. P.; Grisorio, R.; Abate, A. Rationalizing the Molecular Design of Hole-Selective Contacts to Improve Charge Extraction in Perovskite Solar Cells. Adv Energy Mater 2019, 9 (28), 1900990. https://doi.org/10.1002/aenm.201900990.

(236) Smock, S. R.; Chen, Y.; Rossini, A. J.; Brutchey, R. L. The Surface Chemistry and Structure of Colloidal Lead Halide Perovskite Nanocrystals. Acc Chem Res 2021, 54 (3), 707–718. https://doi.org/10.1021/acs.accounts.0c00741.

(237) Haydous, F.; Gardner, J. M.; Cappel, U. B. The Impact of Ligands on the Synthesis and Application of Metal Halide Perovskite Nanocrystals. J Mater Chem A Mater 2021, 9 (41), 23419–23443. https://doi.org/10.1039/D1TA05242J.

(238) Fanizza, E.; Cascella, F.; Altamura, D.; Giannini, C.; Panniello, A.; Triggiani, L.; Panzarea, F.; Depalo, N.; Grisorio, R.; Suranna, G. P.; Agostiano, A.; Curri, M. L.; Striccoli, M. Post-Synthesis Phase and Shape Evolution of $CsPbBr_3$ Colloidal Nanocrystals: The Role of Ligands. Nano Res 2019, 12 (5), 1155–1166. https://doi.org/10.1007/s12274-019-2371-2.

(239) Grisorio, R.; Fasulo, F.; Muñoz-García, A. B.; Pavone, M.; Conelli, D.; Fanizza, E.; Striccoli, M.; Allegretta, I.; Terzano, R.; Margiotta, N.; Vivo, P.; Suranna, G. P. In Situ Formation of Zwitterionic Ligands: Changing the Passivation Paradigms of $CsPbBr_3$ Nanocrystals. Nano Lett 2022, 22 (11), 4437–4444. https://doi.org/10.1021/acs.nanolett.2c00937.

(240) Khan, J. I.; Isikgor, F. H.; Ugur, E.; Raja, W.; Harrison, G. T.; Yengel, E.; Anthopoulos, T. D.; de Wolf, S.; Laquai, F. Charge Carrier Recombination at Perovskite/Hole Transport Layer Interfaces Monitored by Time-Resolved Spectroscopy. ACS Energy Lett 2021, 6 (12), 4155–4164. https://doi.org/10.1021/acsenergylett.1c01931.

(241) Piatkowski, P.; Cohen, B.; Javier Ramos, F.; di Nunzio, M.; Nazeeruddin, M. K.; Grätzel, M.; Ahmad, S.; Douhal, A. Direct Monitoring of Ultrafast Electron and Hole Dynamics in Perovskite Solar Cells. Phys Chem Chem Phys 2015, 17 (22), 14674–14684. https://doi.org/10.1039/C5CP01119A.

(242) Leng, J.; Liu, J.; Zhang, J.; Jin, S. Decoupling Interfacial Charge Transfer from Bulk Diffusion Unravels Its Intrinsic Role for Efficient Charge Extraction in Perovskite

Solar Cells. J Phys Chem Lett 2016, 7 (24), 5056–5061. https://doi.org/10.1021/acs.jpclett.6b02309.

(243) Long, R.; Prezhdo, O. v. Dopants Control Electron–Hole Recombination at Perovskite–TiO_2 Interfaces: Ab Initio Time-Domain Study. ACS Nano 2015, 9 (11), 11143–11155. https://doi.org/10.1021/acsnano.5b05843.

(244) Kondov, I.; Čížek, M.; Benesch, C.; Wang, H.; Thoss, M. Quantum Dynamics of Photoinduced Electron-Transfer Reactions in Dye−Semiconductor Systems: First-Principles Description and Application to Coumarin 343−TiO_2. J Phys Chem C 2007, 111 (32), 11970–11981. https://doi.org/10.1021/jp072217m.

(245) Futera, Z.; Blumberger, J. Electronic Couplings for Charge Transfer across Molecule/Metal and Molecule/Semiconductor Interfaces: Performance of the Projector Operator-Based Diabatization Approach. J Phys Chem C 2017, 121 (36), 19677–19689. https://doi.org/10.1021/acs.jpcc.7b06566.

(246) Haruyama, J.; Sodeyama, K.; Hamada, I.; Han, L.; Tateyama, Y. First-Principles Study of Electron Injection and Defects at the TiO_2 /$CH_3NH_3PbI_3$ Interface of Perovskite Solar Cells. J Phys Chem Lett 2017, 8 (23), 5840–5847. https://doi.org/10.1021/acs.jpclett.7b02622.

(247) Xie, Y.; Sun, H.; Zheng, Q.; Zhao, J.; Ren, H.; Lan, Z. Diabatic Hamiltonian Construction in van Der Waals Heterostructure Complexes. J Mater Chem A Mater 2019, 7 (48), 27484–27492. https://doi.org/10.1039/C9TA09434B.

(248) Coppola, C.; Pecoraro, A.; Muñoz-García, A. B.; Infantino, R.; Dessì, A.; Reginato, G.; Basosi, R.; Sinicropi, A.; Pavone, M. Electronic Structure and Interfacial Features of Triphenylamine- and Phenothiazine-Based Hole Transport Materials for Methylammonium Lead Iodide Perovskite Solar Cells. Phys Chem Chem Phys 2022, 24 (24), 14993–15002. https://doi.org/10.1039/D2CP01270G.

(249) Torres, A.; Rego, L. G. C. Surface Effects and Adsorption of Methoxy Anchors on Hybrid Lead Iodide Perovskites: Insights for Spiro-MeOTAD Attachment. J Phys Chem C 2014, 118 (46), 26947–26954. https://doi.org/10.1021/jp510595s.

(250) Saidaminov, M. I.; Kim, J.; Jain, A.; Quintero-Bermudez, R.; Tan, H.; Long, G.; Tan, F.; Johnston, A.; Zhao, Y.; Voznyy, O.; Sargent, E. H. Suppression of Atomic Vacancies via Incorporation of Isovalent Small Ions to Increase the Stability of Halide Perovskite Solar Cells in Ambient Air. Nat Energy 2018, 3 (8), 648–654. https://doi.org/10.1038/s41560-018-0192-2.

(251) Leclaire, A. The Caesium Oxygen Interactions in the Crystalline Solids. J Solid State Chem 2008, 181 (9), 2338–2345. https://doi.org/10.1016/j.jssc.2008.05.038.

(252) Lamminen, N.; Grandhi, G. K.; Fasulo, F.; Hiltunen, A.; Pasanen, H.; Liu, M.; Al-Anesi, B.; Efimov, A.; Ali-Löytty, H.; Lahtonen, K.; Mäkinen, P.; Matuhina, A.; Muñoz-García, A. B.; Pavone, M.; Vivo, P. Triple A-Site Cation Mixing in 2D Perovskite-Inspired Antimony Halide Absorbers for Efficient Indoor Photovoltaics. Adv Energy Mater 2022, 2203175. https://doi.org/10.1002/aenm.202203175.

(253) Fiorini, V.; Monti, N.; Vigarani, G.; Santi, G.; Fasulo, F.; Massi, M.; Giorgini, L.; Muñoz-García, A. B.; Pavone, M.; Pucci, A.; Stagni, S. Colourless Luminescent Solar Concentrators Based on Iridium(III)-Phosphors. Dyes and Pigments 2021, 193, 109532. https://doi.org/10.1016/j.dyepig.2021.109532.

(254) Loreto, D.; Fasulo, F.; Muñoz-García, A. B.; Pavone, M.; Merlino, A. Unexpected Imidazole Coordination to the Dirhodium Center in a Protein Environment: Insights from X-Ray Crystallography and Quantum Chemistry. Inorg Chem 2022, 61 (22), 8402–8405. https://doi.org/10.1021/acs.inorgchem.2c01370.

(255) Glück, N.; Bein, T. Prospects of Lead-Free Perovskite-Inspired Materials for Photovoltaic Applications. Energy Environ Sci 2020, 13 (12), 4691–4716. https://doi.org/10.1039/D0EE01651A.

(256) Saparov, B.; Hong, F.; Sun, J.-P.; Duan, H.-S.; Meng, W.; Cameron, S.; Hill, I. G.; Yan, Y.; Mitzi, D. B. Thin-Film Preparation and Characterization of $Cs_3Sb_2I_9$: A Lead-Free Layered Perovskite Semiconductor. Chemistry of Materials 2015, 27 (16), 5622–5632. https://doi.org/10.1021/acs.chemmater.5b01989.

(257) Yamada, K.; Sera, H.; Sawada, S.; Tada, H.; Okuda, T.; Tanaka, H. Reconstructive Phase Transformation and Kinetics of $Cs_3Sb_2I_9$ by Means of Rietveld Analysis of X-Ray Diffraction and ^{127}I NQR. J Solid State Chem 1997, 134 (2), 319–325. https://doi.org/10.1006/jssc.1997.7562.

(258) Hebig, J.-C.; Kühn, I.; Flohre, J.; Kirchartz, T. Optoelectronic Properties of $(CH_3NH_3)_3Sb_2I_9$ Thin Films for Photovoltaic Applications. ACS Energy Lett 2016, 1 (1), 309–314. https://doi.org/10.1021/acsenergylett.6b00170.

(259) Geng, T.; Ma, Z.; Chen, Y.; Cao, Y.; Lv, P.; Li, N.; Xiao, G. Bandgap Engineering in Two-Dimensional Halide Perovskite $Cs_3Sb_2I_9$ Nanocrystals under Pressure. Nanoscale 2020, 12 (3), 1425–1431. https://doi.org/10.1039/C9NR09533K.

(260) Berri, S. Theoretical Analysis of the Structural, Electronic, Optical and Thermodynamic Properties of Trigonal and Hexagonal $Cs_3Sb_2I_9$ Compound. Eur Phys J B 2020, 93 (10), 191. https://doi.org/10.1140/epjb/e2020-10143-1.

(261) Correa-Baena, J.-P.; Nienhaus, L.; Kurchin, R. C.; Shin, S. S.; Wieghold, S.; Putri Hartono, N. T.; Layurova, M.; Klein, N. D.; Poindexter, J. R.; Polizzotti, A.; Sun, S.; Bawendi, M. G.; Buonassisi, T. A -Site Cation in Inorganic $A_3Sb_2I_9$ Perovskite Influences Structural Dimensionality, Exciton Binding Energy, and Solar Cell Performance. Chem Mater 2018, 30 (11), 3734–3742. https://doi.org/10.1021/acs.chemmater.8b00676.

(262) Umar, F.; Zhang, J.; Jin, Z.; Muhammad, I.; Yang, X.; Deng, H.; Jahangeer, K.; Hu, Q.; Song, H.; Tang, J. Dimensionality Controlling of $Cs_3Sb_2I_9$ for Efficient All-Inorganic Planar Thin Film Solar Cells by HCl-Assisted Solution Method. Adv Opt Mater 2019, 7 (5), 1801368. https://doi.org/10.1002/adom.201801368.

(263) Jiang, F.; Yang, D.; Jiang, Y.; Liu, T.; Zhao, X.; Ming, Y.; Luo, B.; Qin, F.; Fan, J.; Han, H.; Zhang, L.; Zhou, Y. Chlorine-Incorporation-Induced Formation of the Layered Phase for Antimony-Based Lead-Free Perovskite Solar Cells. J Am Chem Soc 2018, 140 (3), 1019–1027. https://doi.org/10.1021/jacs.7b10739.

(264) Choi, Y. K.; Heo, J. H.; Hong, K.-H.; Im, S. H. Dual-Site Mixed Layer-Structured $FA_xCs_{3-x}Sb_2I_6Cl_3$ Pb-Free Metal Halide Perovskite Solar Cells. RSC Adv 2020, 10 (30), 17724–17730. https://doi.org/10.1039/D0RA00787K.

(265) Jian, W.; Jia, R.; Zhang, H.-X.; Bai, F.-Q. Arranging Strategies for A-Site Cations: Impact on the Stability and Carrier Migration of Hybrid Perovskite Materials. Inorg Chem Front 2020, 7 (8), 1741–1749. https://doi.org/10.1039/D0QI00102C.

(266) Liu, Y.-L.; Yang, C.-L.; Wang, M.-S.; Ma, X.-G.; Yi, Y.-G. Theoretical Insight into the Optoelectronic Properties of Lead-Free Perovskite Derivatives of $Cs_3Sb_2I_9$ (X = Cl, Br, I). J Mater Sci 2019, 54 (6), 4732–4741. https://doi.org/10.1007/s10853-018-3162-y.

(267) van de Walle, A.; Asta, M.; Ceder, G. The Alloy Theoretic Automated Toolkit: A User Guide. Calphad 2002, 26 (4), 539–553. https://doi.org/10.1016/S0364-5916(02)80006-2.

(268) van de Walle, A.; Sun, R.; Hong, Q.-J.; Kadkhodaei, S. Software Tools for High-Throughput CALPHAD from First-Principles Data. Calphad 2017, 58, 70–81. https://doi.org/10.1016/j.calphad.2017.05.005.

(269) Debije, M. G.; Verbunt, P. P. C. Solar Concentrators: Thirty Years of Luminescent Solar Concentrator Research: Solar Energy for the Built Environment (Adv. Energy Mater. 1/2012). Adv Energy Mater 2012, 2 (1), 1–1. https://doi.org/10.1002/aenm.201290003.

(270) Griffini, G.; Levi, M.; Turri, S. Thin-Film Luminescent Solar Concentrators: A Device Study towards Rational Design. Renew Energy 2015, 78, 288–294. https://doi.org/10.1016/j.renene.2015.01.009.

(271) Stagni, S.; Colella, S.; Palazzi, A.; Valenti, G.; Zacchini, S.; Paolucci, F.; Marcaccio, M.; Albuquerque, R. Q.; de Cola, L. Essential Role of the Ancillary Ligand in the Color Tuning of Iridium Tetrazolate Complexes. Inorg Chem 2008, 47 (22), 10509–10521. https://doi.org/10.1021/ic801157k.

(272) Monti, N.; Zacchini, S.; Massi, M.; Hochkoeppler, A.; Giorgini, L.; Fiorini, V.; Stefan, A.; Stagni, S. Antibacterial Activity of a New Class of Tris Homoleptic Ru(II)-complexes with Alkyl-tetrazoles as Diimine-type Ligands. Appl Organomet Chem 2020, 34 (9). https://doi.org/10.1002/aoc.5806.

(273) Fiorini, V.; Zanoni, I.; Zacchini, S.; Costa, A. L.; Hochkoeppler, A.; Zanotti, V.; Ranieri, A. M.; Massi, M.; Stefan, A.; Stagni, S. Methylation of Ir(III)-Tetrazolato Complexes: An Effective Route to Modulate the Emission Outputs and to Switch to Antimicrobial Properties. Dalton Trans 2017, 46 (36), 12328–12338. https://doi.org/10.1039/C7DT02352A.

(274) Frisch, M. J.; Trucks, G. W.; Schlegel, H. B.; Scuseria, G. E.; Robb, M. A.; Cheeseman, J. R.; Scalmani, G.; Barone, V.; Petersson, G. A.; Nakatsuji, H.; Li, X.; Caricato, M.; Marenich, A. v; Bloino, J.; Janesko, B. G.; Gomperts, R.; Mennucci, B.; Hratchian, H. P.; Ortiz, J. v; Izmaylov, A. F.; Sonnenberg, J. L.; Williams-Young, D.; Ding, F.; Lipparini, F.; Egidi, F.; Goings, J.; Peng, B.; Petrone, A.; Henderson, T.; Ranasinghe, D.; Zakrzewski, V. G.; Gao, J.; Rega, N.; Zheng, G.; Liang, W.; Hada, M.; Ehara, M.; Toyota, K.; Fukuda, R.; Hasegawa, J.; Ishida, M.; Nakajima, T.; Honda, Y.; Kitao, O.; Nakai, H.; Vreven, T.; Throssell, K.; Montgomery Jr., J. A.; Peralta, J. E.; Ogliaro, F.; Bearpark, M. J.; Heyd, J. J.; Brothers, E. N.; Kudin, K. N.; Staroverov, V. N.; Keith, T. A.; Kobayashi, R.; Normand, J.; Raghavachari, K.; Rendell, A. P.; Burant, J. C.; Iyengar, S. S.; Tomasi, J.; Cossi, M.; Millam, J. M.; Klene, M.; Adamo, C.; Cammi, R.; Ochterski, J. W.; Martin, R. L.; Morokuma, K.; Farkas, O.; Foresman, J. B.; Fox, D. J. Gaussian 16 Revision C.01. 2016.

(275) Bergner, A.; Dolg, M.; Küchle, W.; Stoll, H.; Preuß, H. Ab Initio Energy-Adjusted Pseudopotentials for Elements of Groups 13–17. Mol Phys 1993, 80 (6), 1431–1441. https://doi.org/10.1080/00268979300103121.

(276) Criscuolo, V.; Prontera, C. T.; Pavone, M.; Crescenzi, O.; Maglione, M. G.; Tassini, P.; Lettieri, S.; Maddalena, P.; Borriello, C.; Minarini, C.; Manini, P. Luminescent Cis-Iridium(III) Complex Based on a Bis(6,7-Dimethoxy-3,4-Dihydroisoquinoline) Platform Featuring an Unusual Cis Orientation of the C∧N Ligands: From a Theoretical Approach to a Deep Red LEEC Device. ACS Omega 2019, 4 (1), 2009–2018. https://doi.org/10.1021/acsomega.8b02859.

(277) Huang, J.; Sun, J.; Wu, Y.; Turro, C. Dirhodium(II,II)/NiO Photocathode for Photoelectrocatalytic Hydrogen Evolution with Red Light. J Am Chem Soc 2021, 143 (3), 1610–1617. https://doi.org/10.1021/jacs.0c12171.

(278) Millet, A.; Xue, C.; Turro, C.; Dunbar, K. R. Unsymmetrical Dirhodium Single Molecule Photocatalysts for H 2 Production with Low Energy Light. Chem Comm 2021, 57 (16), 2061–2064. https://doi.org/10.1039/D0CC08248A.

(279) Loreto, D.; Merlino, A. The Interaction of Rhodium Compounds with Proteins: A Structural Overview. Coord Chem Rev 2021, 442, 213999. https://doi.org/10.1016/j.ccr.2021.213999.

(280) Loreto, D.; Ferraro, G.; Merlino, A. Unusual Structural Features in the Adduct of Dirhodium Tetraacetate with Lysozyme. Int J Mol Sci 2021, 22 (3), 1496. https://doi.org/10.3390/ijms22031496.

(281) Jaźwiński, J.; Kamieński, B. Adducts of Rhodium(II) Tetraacetate with Some Nitrogenous Organic Ligands: Application of Natural Abundance ^{15}N and ^{13}C CPMAS NMR Spectroscopy. Solid State Nucl Magn Reson 2007, 32 (2), 25–33. https://doi.org/10.1016/j.ssnmr.2007.07.005.